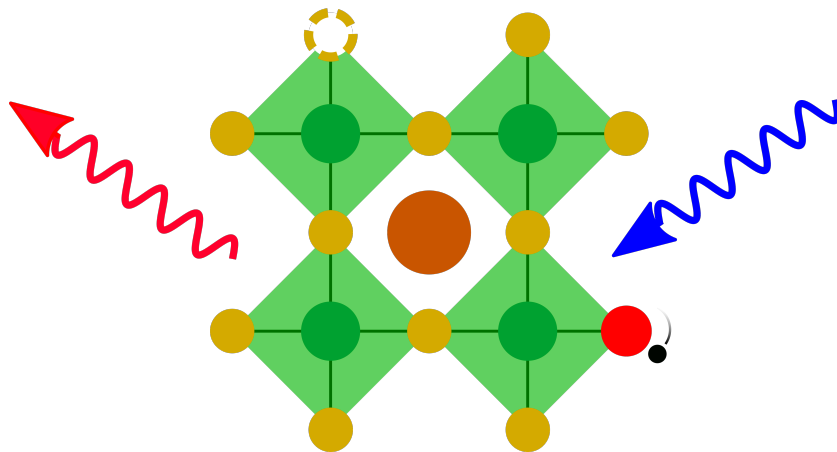

Shining a light on the photochemistry of methylammonium lead iodide perovskite for solar cell applications



Emmanuel V. PÉAN

Submitted to Swansea University in fulfilment of the requirements for the Degree of
Doctor of Philosophy

Swansea University

2020

Abstract

Since their first use in solar cells in 2009, lead halide perovskites have been employed in a wide variety of solar cell architectures leading to an impressive 25.5 % power conversion efficiency in 2020. However, the complex properties of perovskite materials as well as their instability in ambient atmosphere is impeding their development. In particular, trap states, through their formation and passivation, are believed to be responsible for the instability and subsequent degradation of the perovskite, as well as decreasing the device performances. In this work, 3 aspects of the methylammonium lead iodide (MAPI) perovskite are investigated. First, the steady-state photoluminescence and degradation of MAPI were investigated using fluorescence spectroscopy, microscopy, and X-ray diffractometry. Photobrightening, due to the passivation of trap states, and photodarkening, due to the degradation of the perovskite by moisture and oxygen, are found to be competing processes, making the onset of degradation difficult to accurately determine. Second, two models used to simulate charge carrier recombination and time-resolved photoluminescence (TRPL) in perovskite materials, and extract information related to trap states are investigated. The importance of the excitation fluence and repetition period used is highlighted. The models are then used to fit TRPL decays of a MAPI thin-film and a bimolecular rate constant of $\sim 50 \times 10^{-20} \text{ cm}^3/\text{ns}$ is obtained. Finally, the optical, morphological, photoluminescence and crystallographic properties, and stability of MAPI and 5-aminovaleric acid iodide-modified MAPI (AVA-MAPI) infiltrated in mesoporous carbon perovskite solar cells are investigated. Superoxide formation was measured using the dihydroethidium fluorescence probe and AVA-MAPI is shown to generate less superoxide than MAPI when infiltrated in mesoporous layers (ZrO_2 , $\text{TiO}_2/\text{ZrO}_2$ and $\text{TiO}_2/\text{ZrO}_2/\text{C}$). This is partially explained by the presence of a uniform capping layer in AVA-MAPI, hindering oxygen diffusion in the film hence reducing superoxide formation.

Declarations

This work has not previously been accepted in substance for any degree and is not being concurrently submitted in candidature for any degree.



March 2020

This thesis is the result of my own investigations, except where otherwise stated. Other sources are acknowledged by footnotes giving explicit references. A bibliography is



March 2020

I hereby give consent for my thesis, if accepted, to be available for photocopying and for inter-library loan, and for the title and summary to be made available to outside



March 2020

Authorship statement 1

Shining a light on the photoluminescence behaviour of methylammonium lead iodide perovskite: investigating the competing photobrightening and photodarkening processes

DOI: 10.1016/j.matlet.2019.01.103

Located in Chapter 3

Candidate contributed: Sample fabrication (100 %), sample characterisation (100 %), discussion (34 %) and writing (50 %)

Catherine S. De Castro contributed: Discussion (33 %) and writing (25 %)

Matthew L. Davies contributed: Discussion (33 %) and writing (25 %)

We the undersigned agree with the above stated “proportion of work undertaken” for each of the above published peer-reviewed manuscripts contributing to this thesis:

Signed Candidate 

Catherine S. De Castro 

Matthew L. Davies 

Authorship statement 2

Interpreting Time-Resolved Photoluminescence of Perovskite Materials

DOI: 10.1039/D0CP04950F

Located in Chapter 4

Candidate contributed: Calculations (100 %), discussion (60 %) and writing (60 %)

Stoichko Dimitrov contributed: Discussion (20 %) and writing (15 %)

Catherine S. De Castro contributed: Discussion (10 %) and writing (15 %)

Matthew L. Davies contributed: Discussion (10 %) and writing (10 %)

We the undersigned agree with the above stated “proportion of work undertaken” for each of the above published peer-reviewed manuscripts contributing to this thesis:

Signed Candidate

Stoichko Dimitrov

Catherine S. De Castro

Matthew L. Davies

Authorship statement 3

Investigating the Superoxide Formation and Stability in Mesoporous Carbon Perovskite Solar Cells with an Aminovaleric Acid Additive!

DOI:10.1002/adfm.201909839

Located in Chapter 5

Candidate contributed: Sample fabrication (31 %), sample characterisation (100 %), discussion (25 %) and writing (35 %)

Jenny Baker contributed: Sample fabrication (23 %) and writing (5 %)

Matthew L. Davies contributed: Discussion (25 %) and writing (15 %)

Catherine S. De Castro contributed: Discussion (25 %) and writing (15 %)


Francesca De Rossi contributed: Sample fabrication (23 %) and writing (5 %)

Stoichko Dimitrov contributed: Discussion (25 %) and writing (15 %)

Simone Meroni contributed: Sample fabrication (23 %) and writing (5 %)

Trystan Watson contributed: Writing (5 %)

We the undersigned agree with the above stated “proportion of work undertaken” for each of the above published peer-reviewed manuscripts contributing to this thesis:

Signed Candidate 

Jenny Baker 

Matthew L. Davies 

Catherine S. De Castro 

Francesca De Rossi 

Stoichko Dimitrov 

Simone Meroni 

Trystan Watson 

Contents

Abstract	2
Declarations	3
Authorship statement 1	4
Authorship statement 2	5
Authorship statement 3	6
Acknowledgements	11
Abbreviations	12
Research as Art	17
1 Introduction	23
1.1 General introduction	25
1.1.1 State of the world energy supply	25
1.1.2 Generality on photovoltaic solar cells	26
1.2 Photoluminescence principles	29
1.2.1 Generality on photoluminescence	29
1.2.2 Photoluminescence of semiconductors	32
1.3 Theory of solar cells and perovskite solar cells	34
1.3.1 Solar cells working principle	34
A Solar cells architectures	34
B Solar cells properties	37
C Solar cells photoluminescence	37
1.3.2 Perovskite solar cells	38
A Generality on perovskite solar cells	38

	B	History of perovskite solar cells	38
1.4		Methylammonium lead iodide perovskite	40
	1.4.1	Structural, electronic and optical properties of methylammonium lead iodide	40
	1.4.2	Instability and defect properties	41
	A	Oxygen	43
	B	Water	44
	C	Frenkel pair annihilation under illumination	46
	D	Iodide vacancy and uncoordinated lead formation under illumination	46
	E	Defect formation and passivation due to lead iodide	48
	F	Uncoordinated lead passivation by hydrogen peroxide	48
	G	Defect formation and passivation due to iodine	49
1.5		Thesis overview	52
1.6		References	52
2		Experimental details	62
	2.1	Ultraviolet-visible absorption spectroscopy	63
	2.2	Photoluminescence spectroscopy	64
		2.2.1 Fluorometry	64
		2.2.2 Fluorescence microscopy	65
		2.2.3 Time-correlated single photon counting	67
	2.3	Microscopy and images analysis	68
	2.4	X-ray diffractometry	68
	2.5	Profilometry and power measurements	70
	2.6	Data analysis	70
		2.6.1 Data post-processing	70
		2.6.2 Error and averaging	71
		2.6.3 Curve fitting	72
		2.6.4 Background subtraction	72
	2.7	References	73
3		Optical properties of methylammonium lead iodide thin-films	75
	3.1	Introduction	76
	3.2	Methodology	77
		3.2.1 Sample fabrication	77

3.2.2	Photoluminescence spectroscopy	77
3.2.3	X-ray diffractometry	78
3.2.4	Absorbance spectroscopy and optical microscopy	79
3.3	Results and discussions	79
3.3.1	Photoluminescence properties of methylammonium lead iodide	79
3.3.2	Crystallographic properties of methylammonium lead iodide .	85
3.4	Conclusion	88
3.5	References	89

4 Modelling charge carrier recombination and time-resolved photoluminescence of methylammonium lead iodide perovskite 92

4.1	Introduction	94
4.1.1	Recombination processes	96
A	Bimolecular recombinations	96
B	Trap-mediated recombinations	97
4.1.2	TRPL kinetic models	99
A	Bimolecular-trapping model	99
B	Bimolecular-trapping-detraping model	101
4.1.3	Chapter outline	103
4.2	Methodology	103
4.2.1	Simulations	103
4.2.2	Fitting	108
4.2.3	Sample manufacturing & instrumentation	110
4.3	Results & Discussions	110
4.3.1	Bimolecular-trapping model	112
A	Fluence regimes	112
B	Carrier accumulation	116
C	Experimental decay fitting	120
4.3.2	Bimolecular-trapping-detraping model	122
A	Fluence regimes	122
B	Carrier accumulation	128
C	Experimental decay fitting	130
4.3.3	Comparison of the models and discussions	135
4.4	Conclusion	137
4.5	References	139

5	Superoxide formation and stability in mesoporous carbon perovskite solar cells with an aminovaleric acid additive	144
5.1	Introduction	146
5.2	Methodology	148
5.2.1	Sample fabrication	148
5.2.2	Microscopy and morphology	149
5.2.3	Ultraviolet-Visible spectrophotometry	149
5.2.4	X-ray diffractometry measurements	150
5.2.5	Photoluminescence measurements	151
5.2.6	Superoxide yield measurements	152
5.3	Results and discussions	154
5.3.1	Properties of MAPI and AVA-MAPI perovskites on different substrates	154
A	Morphology properties	154
B	Optical properties	159
C	Photoluminescence properties	163
D	Crystallographic properties	169
5.3.2	Stability of MAPI and AVA-MAPI perovskites on different substrates	171
A	Ambient stability under illumination	171
B	Superoxide formation in MAPI and AVA-MAPI perovskites	173
5.4	Conclusion	183
5.5	Bibliography	185
6	Conclusions	188
6.1	Optical properties of methylammonium lead iodide thin-films	188
6.2	Modelling charge carrier recombination and time-resolved photoluminescence of methylammonium lead iodide perovskite	190
6.3	Superoxide formation and stability in mesoporous carbon perovskite solar cells with an aminovaleric acid additive	192

Acknowledgements

I am grateful for the generous financial support of the Zienkiewicz Scholarship from Swansea University, the Sêr Cymru Solar initiative and the Material and Manufacturing Academy (M2A), without which this project would not have been possible. I would also like to thank the Royal Society of Chemistry for funding some of my travels to the conferences and seminar I attended, as well as the AIM facility for allowing me to use their equipment.

I would like to express my deep gratitude to Dr Matthew Davies and Prof. James Durrant for allowing me to carry out my PhD in the Applied Photochemistry group at Swansea University. I am particularly thankful for Matthew's supervision, guidance and constant optimism over the past 3.5 years. I am grateful to Dr Catherine De Castro and Dr Stoichko Dimitrov for their assistance and support to my work. I greatly appreciate Catherine's trainings and help with different experiments, always ready to give a hand and having new ideas. Stoichko has been of a great help to understand and discuss scientific topics and I greatly enjoyed our discussions.

A great part of this thesis could not have been done without the help and advices of fellow colleagues of the SPECIFIC PV team and in particular the Applied Photochemistry group. I am thankful for the collaborative work done with Dr Catherine De Castro, Dr Stoichko Dimitrov, Dr Matthew Davies, Dr Francesca De Rossi, Dr Simone Meroni, Dr Jenny Baker and Prof. Trystan Watson. Fellow doctoral student, James Carlos, has been of a great help to design some of the sample holders used in this work and I am highly grateful for his help. I am also grateful to Dr Emily Speller for helping me with fluorescence probe experiments and Dr Tom Dunlop for helping with X-ray diffractometry and electron microscopy.

A doctorate is not an easy task, all the more for a foreigner moving in a unknown city. I cannot imagine myself where I am now without the friends I made in Swansea: Catherine De Castro, Harry Lakhiani, James Mcgettrick, James Carlos, Jeremy Barbe, Michael Newman, Phil Ansell, Ruth Bowley and Stoichko Dimitrov.

Finally, I would like to thank my parents for their constant support and their interest in my work.

Abbreviations

0-9

- 5-AVA: 5-aminovaleric acid
- 5-AVAI: 5 aminovaleric acid iodide

A

- A : absorptance
- A : absorbance
- A_i : parameters of the model associated with curve i
- AVA-MAPI: aminovaleric acid methylammonium lead iodide

B

- B_n : bimolecular contribution to the change in the carrier concentration
- B_{PL} : bimolecular contribution to the change in the TRPL intensity
- B_A : substitution of A by B
- B_i : interstitial B
- BT: bimolecular-trapping (model)
- BTD: bimolecular-trapping-detraping (model)

C

- c : concentration
- CB: conduction band
- CBM: conduction band minimum
- CA: carrier accumulation
- cm: centimetre
- %CA: difference between the single and multiple pulse approximations

D

- D : film thickness
- D_n : detrapping contribution to the change in the carrier concentration
- D_{PL} : detrapping contribution to the change in the TRPL intensity
- d : distance between neighbouring crystallographic plans
- DFT: density functional theory
- DMF: dimethylformamide
- DMSO: dimethylsulfoxide
- DSSC: dye-sensitised solar cell
- dt : small period of time

E

- E : energy
- E_F : Fermi energy
- E_g : band-gap energy
- EDX: energy dispersive X-ray spectroscopy
- ETL: electron transport layer
- eV: electron-volt

F

- F : fitting model
- FAPI: formamidinium lead iodide
- fs: femtosecond
- FTO: fluorine doped tin oxide
- FWHM: full width at half maximum

G

- GBL: gamma-butyrolactone
- GGA: generalised gradient approximation
- GIXRD: grazing-incidence x-ray diffractometry

H

- h: hour
- h : Planck constant
- HTL: hole transport layer

I

- I : intensity
- I_0 : incident intensity
- I_{max} : maximum photoluminescence intensity
- I_A : absorbed intensity
- I_R : reflected intensity
- I_T : transmitted intensity
- I_{TRPL}^p : time-resolved photoluminescence intensity after excitation pulse p
- I_{TRPL} : time-resolved photoluminescence intensity experimentally measured after **P** excitation pulses
- $I(t)/I(0)$: superoxide yield

K

- K : shape factor
- K: Kelvin
- k_T : trapping rate constant
- k_B : bimolecular recombination rate constant
- k_D : detrapping rate constant
- k_N : non-radiative bimolecular recombination rate constant
- k_R : band-to-band recombination rate constant
- kJ: kilojoule
- KRICT: Korean Research Institute of chemical technology

L

- L : crystallite domain mean size
- l : light path

M

- M : number of curves fitted
- m : integer
- MAI: methylammonium iodide
- MAPBr: methylammonium lead bromide
- MAPI: methylammonium lead iodide
- MAPIC: methylammonium lead iodide/chloride
- mCPSC: mesoporous carbon perovskite solar cell
- meV: millielectron volt
- min: minute
- mm: millimetre
- mol: mole
- MSSC: meso-superstructured solar cell
- mV: millivolt
- mW: milliwatt

N

- N : number of points of a curve
- n : charge carrier concentration
- n_e : free electron concentration
- n_h : free hole concentration
- N_0 : charge carrier concentration generated by an excitation pulse
- n_0 : N-type doping concentration
- N_T : trap states concentration
- n_t : trapped electron concentration
- nm: nanometer

P

- P : number of excitation pulses used to measure TRPL
- P : power
- p_0 : P-type doping concentration
- PCE: power conversion efficiency
- PL: photoluminescence
- PMMA: polymethyl methacrylate
- PMT: photomultiplier tube
- ppm: parts per million
- PSC: perovskite solar cell
- PTFE: polytetrafluoroethylene

R

- R : reflectance
- R^2 : coefficient of determination
- RH: relative humidity
- RP : repetition period
- rpm: rotation per minute

S

- S : area of the sample
- s: second
- SS_{res} : sum of the square difference between 2 sets of curves
- SS_{total} : sum of the square difference between each points and the average of all the curves
- SEM: secondary electron microscopy
- SOC: spin-orbit coupling
- spiro-OMeTAD: 2,2',7,7'- Tetrakis[N,N-di(4-methoxyphenyl)amino]-9,9'-spirobifluorene
- ss-DSSC: solid-state dye-sensitised solar cell
- S/N: signal to noise ratio

T

- T : transmittance
- T_n : trapping contribution to the change in the carrier concentration
- T_{PL} : trapping contribution to the change in the TRPL intensity
- t : time
- TRMC: time-resolved microwave conductivity
- TRPL: time-resolved photoluminescence
- TWy: terawatt-year

U

- UV-Vis: ultraviolet-visible

V

- V_A : A vacancy
- VB: valence band
- VBM: valence band maximum
- V_{OC} : open-circuit voltage

W

- w : weight

X

- XRD: X-ray diffractometry

Y

- $y_{i,j}$: intensity associated with point x_j of curve i
- \bar{y} : average of all the curves
- yr: year

#

- α : absorption coefficient
- β : superoxide yield correction factor
- ε : molar attenuation coefficient
- Δn_e : photoexcited electron concentration
- Δn_h : photoexcited hole concentration
- $\Delta \lambda_{em}$: emission wavelength slitwidth
- $\Delta \lambda_{exc}$: excitation wavelength slitwidth
- η_{esc} : photon escape probability
- θ : angle
- λ : wavelength
- λ_{em} : emission wavelength
- λ_{exc} : excitation wavelength
- λ_{max} : maximum emission wavelength
- μM : micromolar
- μm : micrometer
- v : speed of light
- \AA : angstrom

Research as Art

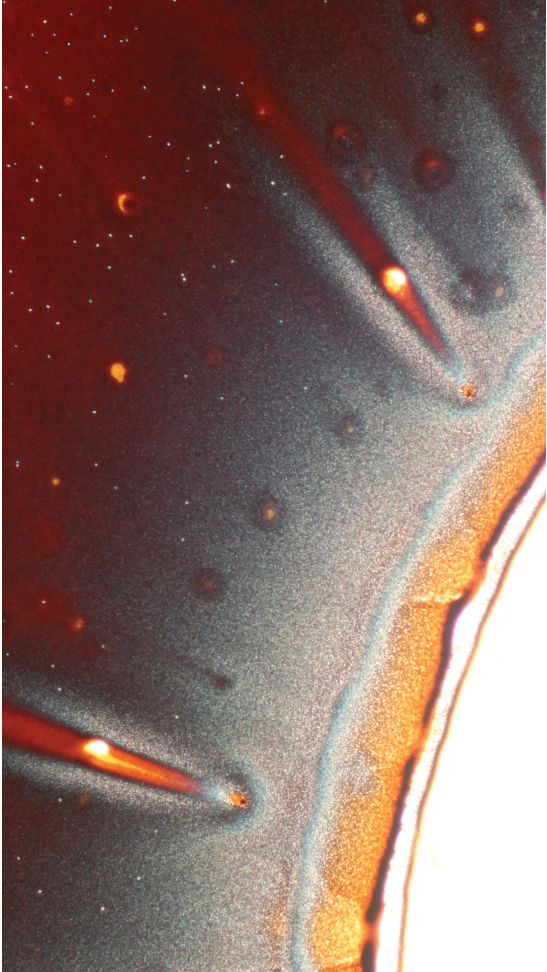
Research as Art is a photo competition open to university students, researchers and staff members. 6 pictures were submitted between 2016 and 2019 with the collaboration of researchers at Swansea University.

**SWANSEA UNIVERSITY
RESEARCH FORUM**
Research as Art Competition 2017

**AWARD FOR
"IMAGINATION"**

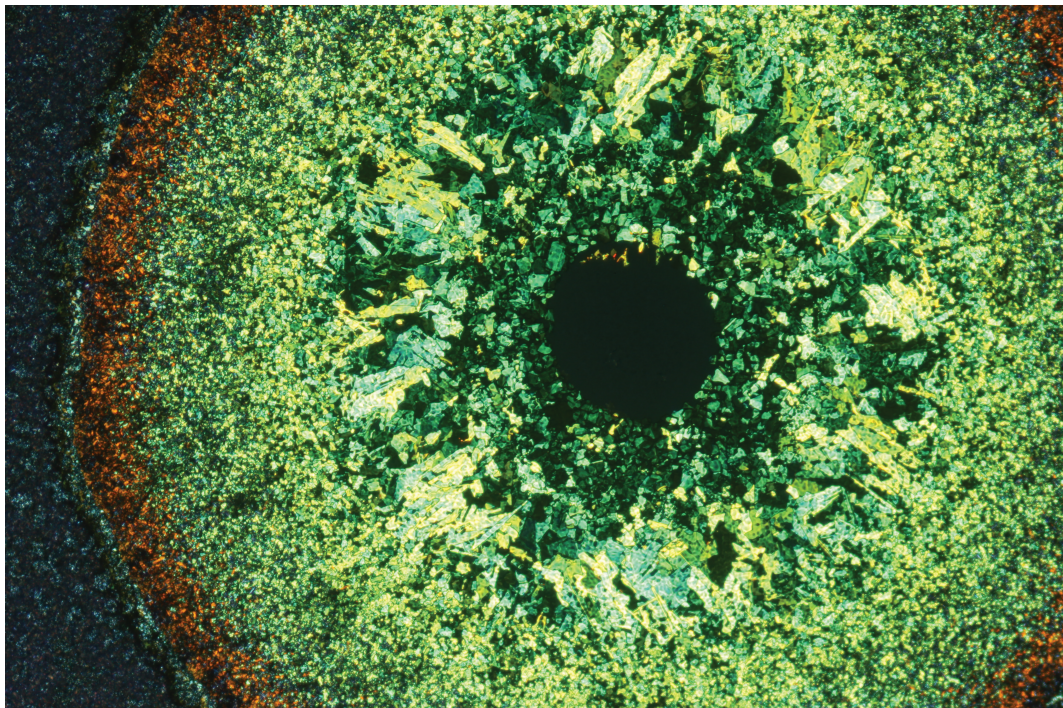
Author:

Emmanuel Péan
College of Engineering
SPECIFIC project
In collaboration with
Catherine Sueme de Castro,
Ashley Purslove
Funded by: Zienkiewicz scholarship



Title: Beauty in Failure

This photo, taken with an optical microscope, is the result of a perovskite sample that went wrong. This could have been caused by incorrect deposition of ethyl acetate, which should have improved the crystallisation of the perovskite layer on the substrate.
The resulting picture looks like meteors (middle of the image) crashing onto a sun (left bottom corner). Those "meteors" and their "tails" may have been formed by the presence of impurities on the sample. In contrast, the "sun" might have resulted from an inhomogeneous diffusion of ethyl acetate into the perovskite sublayer. Finally, the white spots in the darkest region (right top corner) seem like distant stars.
To conclude, scientific research is not always fruitful, however, it is when you make mistakes that you learn the most and have the most fun.



I SEE A GREEN FUTURE

EMMANUEL V. PÉAN - COLLEGE OF ENGINEERING, SPECIFIC

In collaboration with: Catherine S. De Castro (SPECIFIC), James McGettrick (SPECIFIC), Tamara McFarlane (SPECIFIC)

Funded by: Zienkiewicz Scholarship and Sêr Solar

This is a photograph of a thin perovskite layer magnified 10 times using an optical microscope. Perovskite materials are good candidates for inexpensive solar panels although their lifetime still requires improvement. Initially this sample did not present any remarkable features, however, following several weeks in storage striking details began to emerge. This image most likely arose from the presence of impurities in the perovskite layer or from degradation of the material over time. The resulting structure resembles an eye with a vivid green crystalline iris surrounding an ebony pupil.

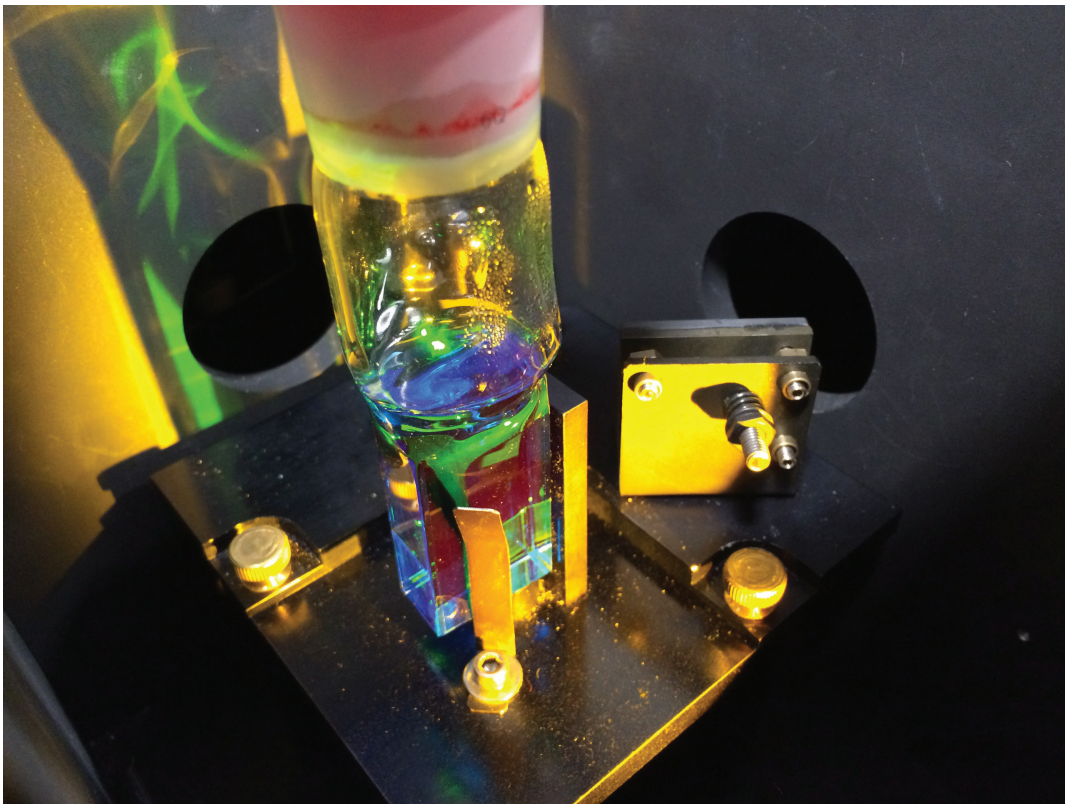
RWY'N GWELD DYFODOL GWYRDD

EMMANUEL V. PÉAN - COLEG PEIRIANNEG, SPECIFIC

Mewn cydweithrediad gyda: Catherine S. De Castro (SPECIFIC), James McGettrick (SPECIFIC), Tamara McFarlane (SPECIFIC)

Ariennir gan: Zienkiewicz Scholarship a Sêr Solar

Dyma lun o haen perovskite tenau wedi'i chwyddo 10 gwaith gan ddefnyddio microsgop optegol. Mae deunyddiau perovskite yn ddeunydd posibl da ar gyfer paneli solar rhad er bod angen gwella eu hoes o hyd. I ddechrau, nid oedd y sampl hwn yn dangos unrhyw nodweddion rhyfeddol, ond ar ôl ei storio am sawl wythnos dechreuodd manylion trawiadol ddod i'r amlwg. Mae'n debygol mai oherwydd amhureddau yn yr haen perovskite neu oherwydd i'r deunydd ddirywio dros amser y digwyddodd y llun hwn. Mae'r strwythur canlyniadol yn debyg i lygad gydag iris werdd risialaidd o amgylch cannyll ebony.



SINGLE(T) RAINBOW

EMMANUEL V. PÉAN - COLLEGE OF ENGINEERING, SPECIFIC

In collaboration with: Tamara McFarlane (SPECIFIC), Michael Newman (SPECIFIC)

Funded by: Zienkiewicz Scholarship and Sêr Solar

Singlet oxygen is a reactive form of oxygen capable of degrading solar panels thus limiting their lifetime. It is possible to monitor it using a probe emitting light which is then measured via the two openings shown here. The probe can be tested using methylene blue (which acquires its name from its electric blue colour as pictured in the cuvette) that generates singlet oxygen under illumination. When combined, the two chemicals are illuminated with red, yellow and green light merging into an orange light which can be observed around the cuvette. Methylene blue absorbs red and yellow light leaving only the green light to be transmitted which can be observed on the walls surrounding the cuvette.

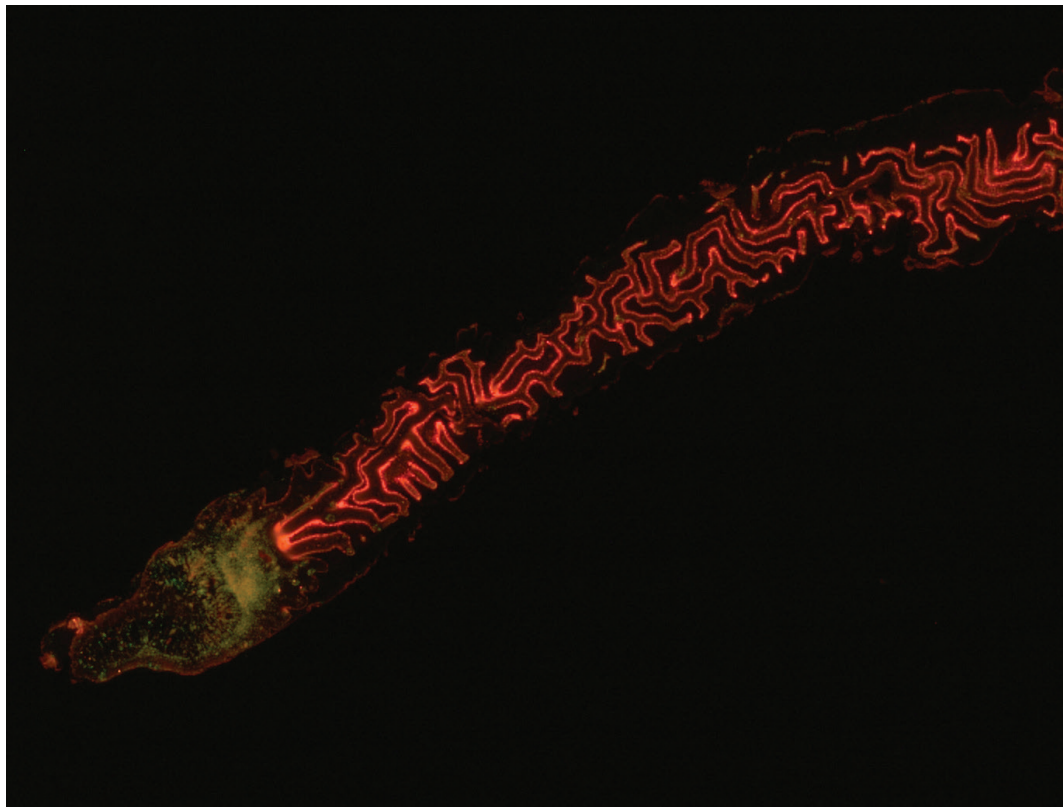
ENFYS SINGLED

EMMANUEL V. PÉAN - COLEG PEIRIANNEG, SPECIFIC

Mewn cydweithrediad gyda: Tamara McFarlane (SPECIFIC), Michael Newman (SPECIFIC)

Ariennir gan: Zienkiewicz Scholarship a Sêr Solar

Mae ocsigen singled yn ffurf adweitheddol ar ocsigen a all ddiraddio paneli solar ac felly cyfyngu ar eu hoes. Mae'n bosibl ei fonitro trwy ddefnyddio profiedydd sy'n gollwng golau a gaiff ei fesur wedyn trwy'r ddau agoriad a ddangosir yma. Gellir profi'r profiedydd gan ddefnyddio 'methylene glas (sy'n cael ei enw o'r lliw glas llachar fel y dangosir yn y ddysgl) sy'n cynhyrchu ocsigen singled o dan olau. Pan gânt eu cyfuno, caiff y ddau gemegyn eu goleuo â golau coch, melyn a gwyrdd gan uno'n olau oren y gellir ei weld o amgylch y ddysgl. Mae glas methylen yn amsugno golau coch a melyn gan adael dim ond y golau gwyrdd i gael ei drosglwyddo a gellir ei weld ar y waliau o amgylch y ddysgl.



ENLIGHTENING SNAKE

EMMANUEL V. PÉAN - COLLEGE OF ENGINEERING, SPECIFIC

In collaboration with: Catherine S. De Castro (SPECIFIC), James McGettrick (SPECIFIC), Tamara McFarlane (SPECIFIC)

Funded by: Zienkiewicz Scholarship and Sêr Solar

Fluorescence microscopy involves illuminating an object to observe the resultant light it emits, which is then captured with a camera. Here, we have photographed a thin layer of perovskite material deposited on glass. Perovskites are very promising candidates for inexpensive and efficient solar panels, however, they tend to degrade over time, thus limiting the panel's lifetime. The uneven deposition of the material caused the formation of hairline features such as this one, which strikingly resembles a snake. The "body" emits the red light characteristics of the perovskite whereas the "head" exhibits green light, likely due to degradation at that location. Ultimately, this image enlightens us on the processes taking place in this material.

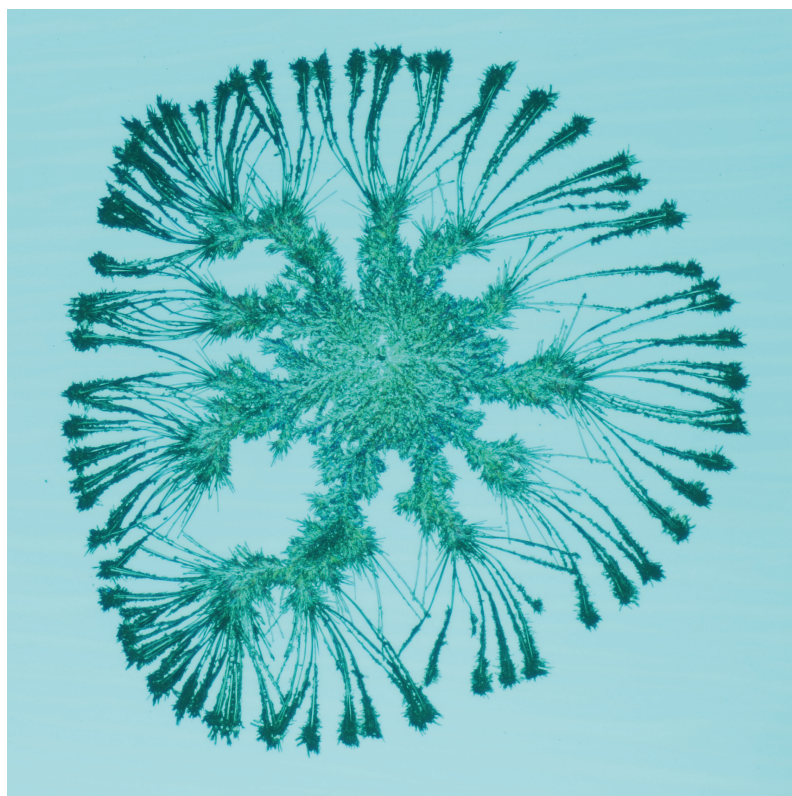
NEIDR SY'N GOLEUO

EMMANUEL V. PÉAN - COLEG PEIRIANNEG, SPECIFIC

Mewn cydweithrediad gyda: Catherine S. De Castro (SPECIFIC), James McGettrick (SPECIFIC), Tamara McFarlane (SPECIFIC)

Ariennir gan: Zienkiewicz Scholarship a Sêr Solar

Mae microsgop fflworoleuedd yn golygu goleuo gwrthrych i arsylwi'r golau y mae'n ei allyrru wedyn, sydd yna yn cael ei ddal gan gamera. Yma, rydym wedi tynnu lluniau haen denau o ddeunydd perovskite a adneuwyd ar wydr. Mae perovskitau yn ymgeiswyr addawol iawn ar gyfer paneli solar rhad ac effeithlon, fodd bynnag, maent yn tueddu i ddiraddio dros amser, gan gyfyngu ar hyd oes y panel. Achosodd dyddodiad anwastad y deunydd ffurfio nodweddion llinell wallt fel hon, sy'n drawiadol o debyg i neidr. Mae'r "corff" yn gollwng nodweddion golau coch y perovskite tra bod y "pen" yn dangos golau gwyrdd, mae'n debyg oherwydd diraddio yn y lleoliad hwnnw. Yn y pen draw, mae'r ddelwedd hon yn ein goleuo am y prosesau sy'n digwydd yn y deunydd hwn.



DEVELOPING A BLUEPRINT TO ADVANCE PEROVSKITE TECHNOLOGY

**EMMANUEL V. PÉAN - SWANSEA UNIVERSITY,
SCHOOL OF ENGINEERING, SPECIFIC**

In Collaboration with: Matthew L. Davies

Funded by: Sêr Solar and Zienkiewicz Scholarship

This photo, taken with an optical microscope, is the result of the degradation of a perovskite. Perovskites are very promising materials for low-cost, efficient solar panels, however, they tend to degrade when exposed to oxygen and light. The image is reminiscent of cyanotype photographs (blueprints) which were used in the first ever published illustrative books containing photographic images namely; "Photographs of British Algae: Cyanotype Impressions" (Anna Atkins 1843) and "The Pencil of Nature" (William Henry Fox Talbot 1844). Excitement generated by the invention of new technologies is true for both cases; cyanotypes allowed the publication of photographs for the first time using a low-cost method dependent on light-matter interactions, can perovskite solar panels mimic this and be the solar technology of the future? This similarity to a cyanotype reminds us of the fundamental beauty in science and the importance of capturing and displaying photographs to the world.

DATBLYGU GLASBRINT I DDATBLYGU TECHNOLEG PEROVSKITE

**EMMANUEL V. PÉAN - PRIFYSGOL ABERTAWE,
COLEG PEIRIANNEG, SPECIFIC**

Mewn cydweithrediad â: Matthew L. Davies

Ariannwyd gan: Sêr Solar ac Ysgoloriaeth Zienkiewicz

Tynnwyd y llun yma â microsgop optig, a dyma ganlyniad dirywiad perovskite. Mae perovskites yn ddeunyddiau addawol iawn ar gyfer paneli solar effeithlon a rhad, ond maen nhw'n dueddol o ddirywio pan maen nhw'n dod i gysylltiad ag ocsigen a goleuni. Mae'r darlun yma'n dwyn lluniau syanoteip (glasbrint) i gof, a ddefnyddiwyd yn y llyfrau darluniadol cyntaf a gyhoeddwyd gyda lluniau ffotograffaid, yn benodol; "Photographs of British Algae: Cyanotype Impressions" (Anna Atkins 1843) a "The Pencil of Nature" (William Henry Fox Talbot 1844). Mae cyffro drwy ddyfeisio technolegau newydd yn berthnasol yn y ddau achos. Roedd syanoteipiau'n golygu bod modd cyhoeddi lluniau am y tro cyntaf gan ddefnyddio dull rhad a oedd yn dibynnu ar ryngweithiadau gwrthrych-goleuni. A all paneli solar perovskite ail-greu hyn, a dod yn dechnoleg solar y dyfodol? Mae'r tebygrwydd yma i syanoteip yn ein hatgoffa o harddwch cynhenid gwyddoniaeth, a phwysigrwydd cipio ffotograffau a'u harddangos i'r byd.



GROWING CRYSTALS FROM SCRATCH

EMMANUEL V. PÉAN - SWANSEA UNIVERSITY,
SCHOOL OF ENGINEERING, SPECIFIC

Funded by: Sêr Solar and Zienkiewicz Scholarship

This is an image time-lapse (from left to right, top to bottom) of the growth of perovskite crystals. A solution containing compounds A and B dissolved in a solvent is heated to 100°C. As the temperature of the solution increases, the bonding between compounds A and B and the solvent weakens and A and B reacts with each other to form the AB compound. Here, we observe the growth of 2 perovskite crystals over 11 minutes. Perovskites are very promising materials for solar panels as they are cheap and easy to manufacture.

TYFU CRISIALAU O'R DECHRAU

EMMANUEL V. PÉAN - PRIFYSGOL ABERTAW, COLEG PEIRIANNEG, SPECIFIC

Ariannwyd gan: Sêr Solar ac Ysgoloriaeth Zienkiewicz

Dyma lun treigl amser (o'r chwith i'r dde, o'r top i'r gwaelod) o dwf crisialau perovskite. Caiff toddiant yn cynnwys cyfansoddiadau A a B hydawdd ei wresogi i 100°C. Wrth i dymheredd y toddiant gynyddu, mae'r bond rhwng cyfansoddiadau A a B a'r toddiant yn gwanhau, ac mae A a B yn adweithio â'i gilydd i ffurfio'r cyfansoddiad AB. Yma, gwelwn dwf dau grisial perovskite dros 11 munud. Mae perovskites yn ddeunyddiau addawol ar gyfer paneli solar, gan eu bod yn rhad ac yn hawdd eu gweithgynhyrchu.

Chapter 1

Introduction

Since their first use in dye sensitized solar cells in 2009, perovskites have been extensively employed in various solar cell architectures [1]. Perovskite solar cells (PSCs) can be thin [2], flexible [3], and made from abundant materials [4] and easy manufacturing processes [5]. In particular, the methylammonium lead iodide (MAPI) perovskite has been used in numerous high efficiency PSCs due to its high absorption coefficient [6], solution processability [6], almost optimum band-gap energy [6], [7] and high charge carrier mobilities [8]. However, instability of the perovskite layer is hindering the commercialisation of PSCs [9]. Furthermore, fluctuations of the PSC properties (*e.g.* photoluminescence variation over time under illumination) impede their study and development [10]. Light, oxygen and moisture have been shown to be responsible for affecting the perovskite electronic properties as well as degrading it [11], [12]. Understanding the photochemical properties of MAPI, and perovskites in general, is therefore of great importance to help tackle these problems. In this chapter, the electronic and photoluminescence properties of materials for solar energy conversion and background on solar cell operation are discussed. An overview of the reported intrinsic and extrinsic instability of MAPI is then examined.

Contents

1.1	General introduction	25
1.1.1	State of the world energy supply	25
1.1.2	Generality on photovoltaic solar cells	26
1.2	Photoluminescence principles	29
1.2.1	Generality on photoluminescence	29
1.2.2	Photoluminescence of semiconductors	32
1.3	Theory of solar cells and perovskite solar cells	34
1.3.1	Solar cells working principle	34
A	Solar cells architectures	34
B	Solar cells properties	37
C	Solar cells photoluminescence	37
1.3.2	Perovskite solar cells	38
A	Generality on perovskite solar cells	38
B	History of perovskite solar cells	38
1.4	Methylammonium lead iodide perovskite	40
1.4.1	Structural, electronic and optical properties of methylammonium lead iodide	40
1.4.2	Instability and defect properties	41
A	Oxygen	43
B	Water	44
C	Frenkel pair annihilation under illumination	46
D	Iodide vacancy and uncoordinated lead formation under illumination	46
E	Defect formation and passivation due to lead iodide	48
F	Uncoordinated lead passivation by hydrogen peroxide	48
G	Defect formation and passivation due to iodine	49
1.5	Thesis overview	52
1.6	References	52

1.1 General introduction

1.1.1 State of the world energy supply

Energy, whether in the form of electricity or fuel, is a very important aspect of our civilisation, used for heating, lightning, manufacturing goods and transport amongst others. The current world energy supply is primarily based on a mix of oil (31 %), coal (26 %) and gas (22 %) (**Figure 1.1a**) [13]. However, the combustion of these compounds generates carbon dioxide (CO₂). As a consequence, since the industrial revolution (*ca.* 1760-1840), the atmospheric CO₂ concentration has increased by 45 % from 280 ppm to 405 ppm in 2019 (**Figure 1.1b**) [14]. Due to its ability to scatter back outgoing infrared radiation from the Earth, CO₂ is a major contributor to global warming leading to sea rise, ocean acidification and more frequent extreme weather phenomenon [15]. While a 1°C increase in global average temperature has been measured since 1880 [16], [17] (**Figure 1.1b**), up to an additional 3.8°C increase by the end of the 21st century has been projected [18]. Furthermore, coal, oil and gas are finite resources while the world's energy demand is continuously increasing (**Figure 1.1a**). Based on the International Energy Agency's new policies scenario [19], predicting a 0.12 TWy yearly increase of fossil fuels consumption, coal, petroleum, gas and uranium resources could be exhausted in approximately 70 years. There is thus an urgent necessity to develop, deploy and utilise a greater amount of renewable energy technologies.

Solar energy is by far the dominant source of renewable energy with 23,000 TWy incident upon the earth's continents each year, compared to the remaining 1,570 TWy of coal, petroleum, gas and uranium (**Figure 1.1c**) [20]. In about 7 hours, the Sun provides Earth enough energy to sustain the world's current energy consumption for an entire year (19 TWy in 2018 [13])¹. Equivalently, capturing only 0.08 % of the incident solar energy would meet our current energy needs. However, this abundance is counterbalanced by intermittency of the solar illumination due to the rotation of the earth and the weather conditions. It is also not possible to generate energy from solar cells on demand which thus requires the use of storage devices.

¹Equivalently, over the duration of this thesis (3.5 years), the Sun provided Earth enough energy to sustains the world's energy consumption for the next 782 years (assuming a 0.21 TWy yearly energy demand increase).

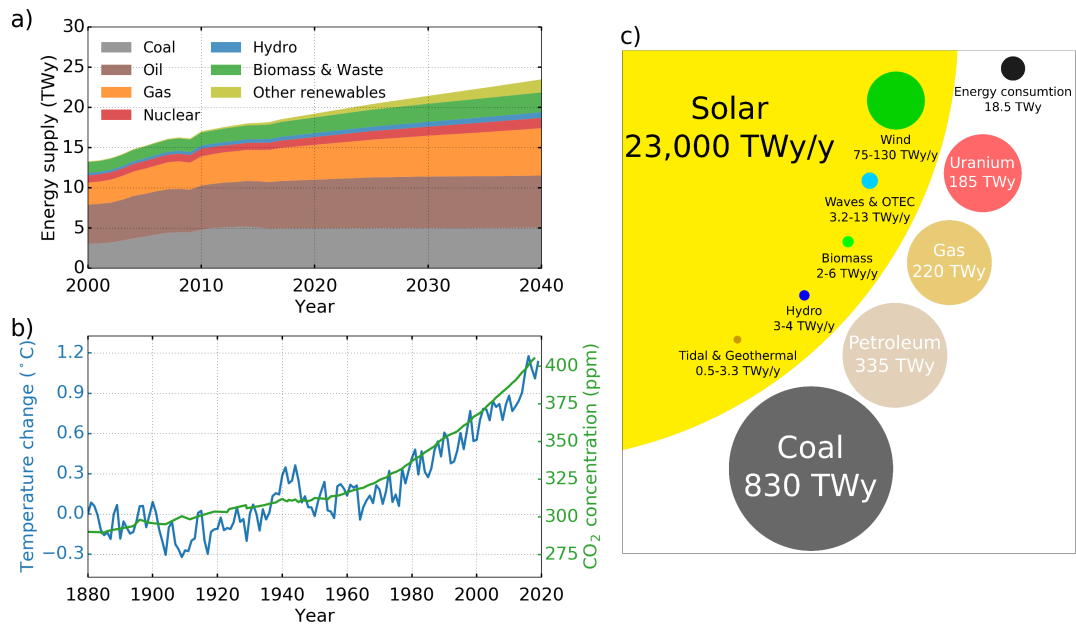


Figure 1.1: **a)** Evolution of the world's energy supply between 2000 and 2018, and the predicted supply up to 2040 according to the International Energy Agency new policies scenario [19]. **b)** Relative temperature variation with respect to 1880 [16], [17] and carbon dioxide (CO₂) concentration variation [14] between 1880 and 2018. **c)** World's energy reserves in 2015 (adapted from [20]). The area of each circle is proportional to the associated energy reserve. For renewable energies, the potential yearly energy is shown while for finite resources the overall estimated energy reserve is shown. Note that solar energy is not entirely shown due to its massive area and only includes incident energy on continents.

1.1.2 Generality on photovoltaic solar cells

The first solar cell, able to generate an electric current from light, was developed by Aleksandr Shtoletov in 1891 [21]. Since then, photovoltaic solar cells have been extensively investigated in order to improve their ability to convert light into electricity, cost, weight and durability, leading to a large variety of solar cell technologies. Record power conversion efficiencies (PCE) of laboratory (small scale) devices are given in **Figure 1.2** [22].

Solar cells are often classified into 3 generations; first generation monocrystalline and polycrystalline (or multicrystalline) silicon solar cells; second generation thin-film semiconductor solar cells and; third generation of various technologies which are solution processable (**Table 1.1**). The first silicon solar cell was presented by Bell Labs in 1954 and had a 6 % efficiency [23]. Since then, the PCE of silicon solar cells has increased up to 26.1 % [22] and they accounted for 95 % of the total

production of solar panels in 2017 [24]. Although silicon is an abundant material in the earth's crust [25], it requires complex processing and relatively high energy to purify it to 99.999999 % to obtain such high PCE [26]. Furthermore, due to the low light absorption coefficient of silicon, relatively thick layers (*ca.* 100 μm) are required to obtain high efficiencies. As a consequence, silicon solar cells are relatively heavy and not flexible, hindering their possible uses. These problems were addressed through the development of the second generation: thin-film solar cells. By using materials with a direct band-gap (see **Section 1.2.2**) and a high light absorption coefficient, it was possible to reduce the thickness of the layer from *ca.* 100 μm down to *ca.* 100 nm, allowing thin-film solar cells to be flexible and lightweight. Second generation solar cells have a higher efficiency/price ratio than the first generation, making their energy payback of about 0.6 years compared to 2 years for the first generation [27]. Finally, the third generation includes all the new technologies currently under development and is sometime referred as the printable solar cell generation. It includes organic solar cells, perovskite solar cells (PSCs), dye sensitised solar cells (DSSCs), CZTSSe solar cells and quantum dots solar cells. These technologies use less expensive compounds than the second generation and are showing promises in matching the efficiency of the first generation. Amongst the third generation of solar cells, PSCs are extremely promising, almost matching the PCE of market-leading PV silicon solar cells after only 11 years of development (25.5 % and 26.1 % respectively). PSCs can be solution processed [28], work well under low light levels [29], have low manufacturing cost and a short energy payback time [27].

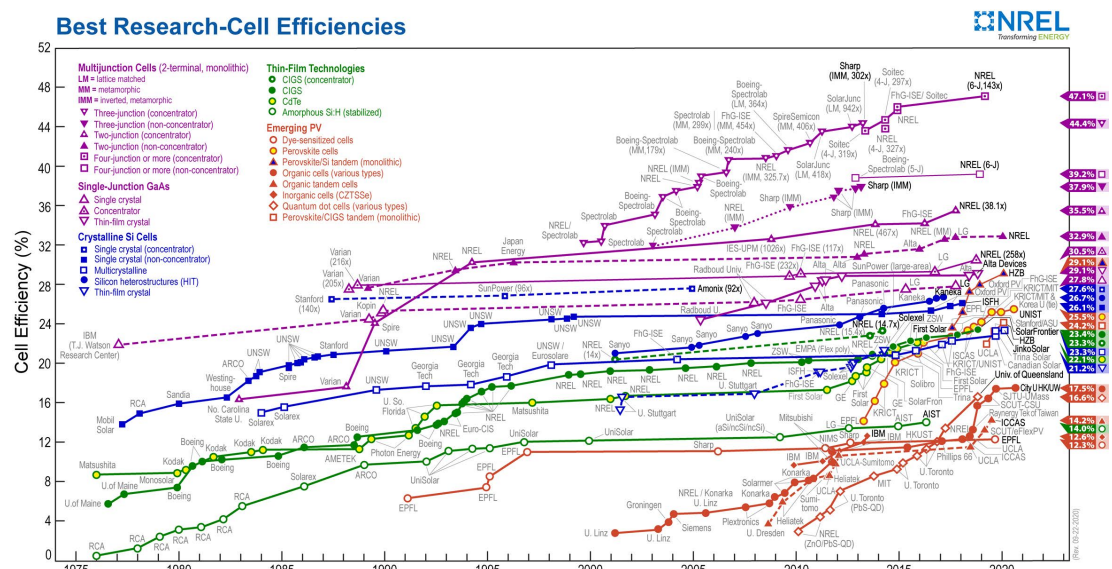


Figure 1.2: Best research-scale photovoltaic device efficiencies [22].

Table 1.1: Summary of the advantages, disadvantages and record power conversion efficiency (PCE) of the main single-junction solar cell technologies. Blue: first generation, Green: second generation, Orange: third generation. Record PCEs are shown for each technology without the use of concentrators [22].

Technology	Advantages	Disadvantages	PCE (%)
Monocrystalline silicon	Cheap material [25] High efficiency	Energy intense processing[26] Long payback time [30] Heavy and nonflexible	26.1
Polycrystalline silicon	Cheap material [25] Good efficiency	Long payback time [30] Heavy and non-flexible	23.3
Amorphous silicon	Cheap material [25] Lightweight/flexible Works with low light levels [31]	Low efficiency	14.0
CIGS	Good efficiency Lightweight/flexible	Low availability of materials [25]	23.4
GaAs	High efficiency Lightweight/flexible	Expensive materials [26]	29.1
CdTe	Good efficiency Low module cost [26] Lightweight/flexible	Toxicity of Cd [32] Low availability of Te [25] High processing temperature [26]	22.1
Organic	Solution-processable [33] Uses abundant elements [26] Low production cost[33] Works well with low light [34] Lightweight/flexible	Medium efficiency Poor stability [35]	17.5
DSSC	Simple manufacturing [36] Semi-transparent [36] Works well with low light [37]	Low efficiency Liquid electrolyte [36] High cost of Ru [26]	12.3
CZTSSe	Uses abundant and non-toxic elements[25] Lightweight/flexible	Low efficiency	12.6
Perovskite	Good efficiency Solution processible [28] Works well with low light [29] Lightweight/flexible Short payback time [27]	Stability issues with oxygen, moisture and light [9]	25.5

1.2 Photoluminescence principles

1.2.1 Generality on photoluminescence

Photoluminescence (PL) (from the Greek word *photo* [light] and the Latin word *lumen* [light]) is the process in which a system (*e.g.* an atom or molecule) emits light following the absorption of light. An electron is excited from its ground state (*a.k.a.* energy level) to a higher energy state, an excited state, through the absorption of a photon with energy equal to the energy difference between the ground and excited states (**Figure 1.3**). PL occurs when an excited state electron moves to a lower electronic energy state by releasing the energy difference in the form of a photon (also described as the radiative depopulation of the excited state). Depending on the spin of the excited electron with another electron which shared the same ground state, two PL processes are distinguished: phosphorescence (from the Ancient Greek word *phōsphoros* [the bearer of light]) and fluorescence (from the mineral name fluorite, the Middle English word *spar* [beam] and the Latin word *escens* [process or state]) (**Figure 1.3**). Fluorescence occurs when the spin of the excited electron is opposite to the spin of the electron in the ground state (the excited electron is then said to occupy a singlet state), this tends to be a fast process, typically pico-nanoseconds [38]. Phosphorescence occurs when the spin of the excited electron is the same as the spin of the electron in the ground state (the excited electron then occupies a triplet state). Phosphorescence is typically a slower process (of the order of the second) due to the forbidden nature of this transition as per the Pauli exclusion principle which states that two electrons with identical spin cannot occupy the same energy level, thus the transition back to the ground state must involve a change of spin [38]. A third but rarer PL process is delayed fluorescence which is of the order of the microsecond and is caused by triplet-triplet annihilation, during which 2 triplet states lead to the creation of a single state.

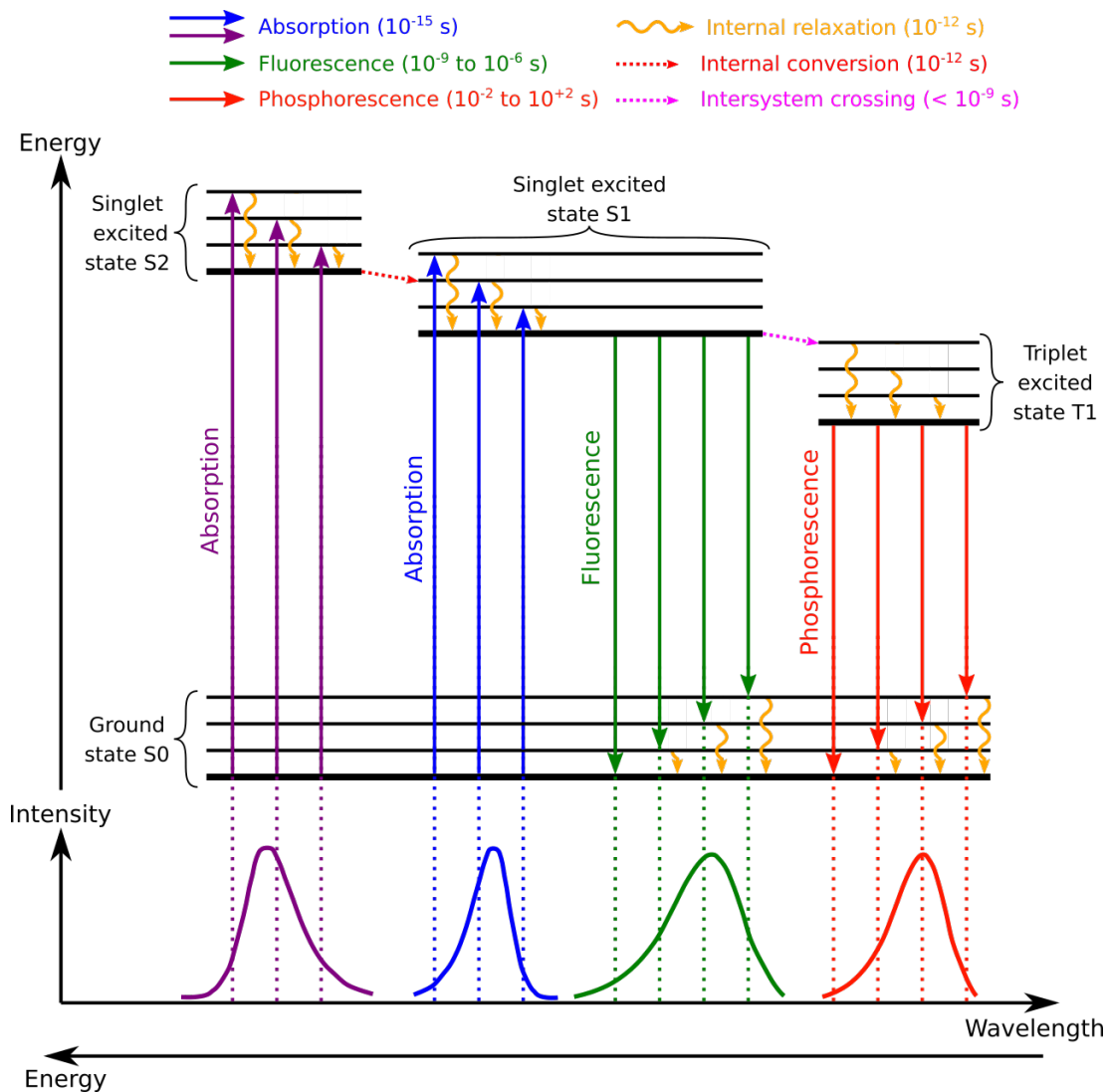


Figure 1.3: Jablonski diagram illustrating the electronic transitions between the energy states of a molecular system. Each electronic state is associated with multiple vibrational and rotational levels. The average time of each event is shown in seconds. Corresponding absorption and emission spectra are also shown. Adapted from [38], [39]

The electronic structure of atoms is only composed of electronic levels while molecules have vibrational and rotational energy levels as well due to their ability to vibrate and rotate. These energy levels are located within a few meV from the electronic energy levels (**Figure 1.3**). While atoms can only absorb photons with very specific energy equal to the energy difference between ground and excited electronic levels, molecules can absorb photons with energy higher than this energy difference due to the presence of the vibrational and rotational levels. When an electron occupies a rotational or vibrational level, it relaxes down to the associated electronic level through the emission of phonons (*a.k.a.* thermal relaxation). As the excited

electron can recombine with any vibrational or rotational empty energy level in the ground state, the energy of the photons emitted by a molecule spans over a range of energies while they have discrete energies for atoms. PL is therefore a good indicator of the chemical nature of a system as the energy of the emitted photons depend on *e.g.* its atomic composition, the bonds type and its environment. Recombination during which the energy is not released as a photon are termed “non-radiative” and are further discussed in **Section 1.2.2** and **Chapter 4**.

Two types of PL measurement can be distinguished: steady-state and time-resolved. During steady-state measurements, the system is continuously illuminated with an excitation wavelength λ_{exc} while the PL intensity is measured at an emission wavelength λ_{em} . Steady-state emission spectra show the system PL intensity at different emission wavelengths from illumination using a specific excitation wavelength (**Figure 1.4a**). Conversely, excitation spectra are a measure of the PL emission at a specific emission wavelength from excitation at different excitation wavelengths (**Figure 1.4b**). It is worth noting that due to the low probability of phosphorescence emission at room temperature and the fast scanning rate of this type of measurements, only fluorescence is usually measured. Combining emission and excitation measurements allows one to obtain maps showing the system PL emission over a wide range of excitation and emission wavelengths. In time-resolved measurements, the system is excited with short light pulses of constant wavelength λ_{exc} and the PL emission decay is measured at λ_{em} over a few nanoseconds to a few microseconds for fluorescence and delayed fluorescence, and up to a few seconds for phosphorescence (note that these order of magnitudes can highly vary depending on the system measured) (**Figure 1.4c**). Steady-state and time-resolved PL (TRPL) are further discussed in **Chapters 3** and **4** respectively.

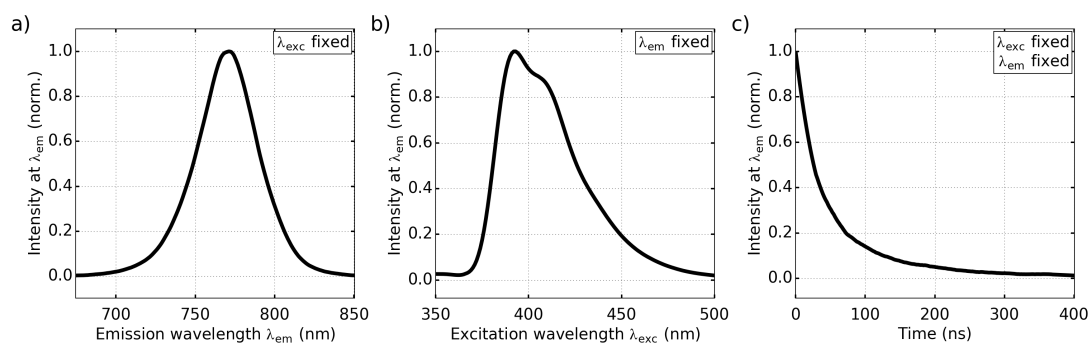


Figure 1.4: Example of steady-state **a)** emission and **b)** excitation spectra, and **c)** time-resolved photoluminescence decay.

1.2.2 Photoluminescence of semiconductors

Due to the high concentration of atoms per volume in crystals, the Pauli exclusion principle leads to the build-up of energy levels which are very close in energy terms, forming almost continuous energy bands. At equilibrium (*i.e.* at 0 K temperature, no perturbation), the highest energy band filled by electrons is called valence band (VB) while the lowest energy band empty of electrons is called conduction band (CB) (**Figure 1.5**). The void of energetic states between these two bands is called band-gap which energy (E_g) is defined as the energy difference between the CB minimum (CBM) energy and the VB maximum (VBM) energy. In the case where the CBM and VBM have the same momentum, the band-gap is said to be “direct”, otherwise, it is said “indirect”. Indirect band-gap materials usually have lower light absorption coefficients than direct band-gap materials as absorption of photons may require a phonon to match the momentum difference between the CBM and VBM.

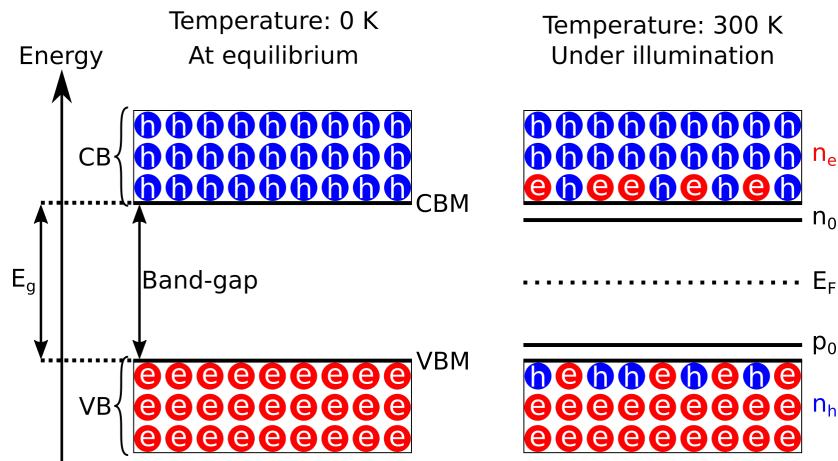


Figure 1.5: Band diagram of an intrinsic semiconductor at equilibrium (*left*) and an extrinsic semiconductor under illumination (*right*). E_F is the Fermi energy and corresponds to the last energy level occupied at 0 K temperature. (CB: conduction band, CBM: conduction band minimum, VB: Valence band, VBM: Valence band minimum, n_e : free electron concentration, n_h : free hole concentration, n_0 : dark electron concentration p_0 : dark hole concentration, E_g : band-gap energy).

At equilibrium and at 0 K, crystals with a non-zero band-gap energy cannot conduct electricity as the electrons cannot move in the VB due to the absence of free energy states. However, if electrons are excited from the VB to the CB, the presence of available energy levels (*i.e.* holes) in the VB allows the movement of the electrons while the high concentration of holes in the CB allows the movement of electrons in it, and the crystals can thus conduct electricity. Semiconductors are a specific class of

crystal in which the VB is separated from the CB by only a few eV. At room temperature, such low band-gap energy allows a very small concentration of electrons to be thermally excited into the CB, enabling the conduction of electricity, hence its name: semiconductor. For the same reason, visible light ($1.7 \text{ eV} < E < 3.3 \text{ eV}$) can excite (*i.e.* photoexcite) electrons into the CB allowing the conduction of electricity.

In an intrinsic semiconductor (which does not present any additional holes or electrons from external sources), the free (*i.e.* excited) electron n_e and hole n_h concentrations are equal. In reality, semiconductors are usually extrinsic due to the presence of extra holes or electrons called “dark” holes or electrons. Impurities and point defects (such as an atom vacancy, interstitial or substitution) can create localised energy levels in the band-gap (**Figure 1.5**). In the case where these energy levels are located next to the VBM or CBM, they are said “shallow”, and “deep” in the opposite case. Shallow level occupied by electrons and located next to the CBM are called “donor” as the electrons can be thermally excited in the CB, adding n_0 dark electrons to the total free electron concentration. Similarly, shallow levels occupied by holes and located next to the VBM are called “acceptor” as these levels can be thermally populated by electrons from the VB hence adding p_0 dark holes to the total free hole concentration. Semiconductors presenting donor energy levels are qualified of “N-type” while semiconductors with acceptor energy levels are “P-type”.

PL in semiconductors arise when a photoexcited electron, from the absorption of a photon which energy is higher than E_g , directly recombines with a hole through band-to-band recombination (**Figure 1.6**). In the case of direct band-gap semiconductors with a high absorption coefficient and a small Stoke shift (small difference between emission and absorption maxima), it has been shown that emitted photons can be re-absorbed through a phenomenon called photon recycling [11], [40]–[43]. Defect-induced localised energy levels in the band-gap can act as non-radiative recombination centres through the trapping and detrapping of the carriers and are usually called “trap states”. If the semiconductor is in contact with a crystal which CBM (VBM) energy is lower (higher) than the semiconductor CBM (VBM) energy, electrons (holes) can be injected (*a.k.a.* extracted) from the perovskite to the adjacent crystal. Recombination processes in the MAPI perovskite are further discussed in **Chapter 4**.

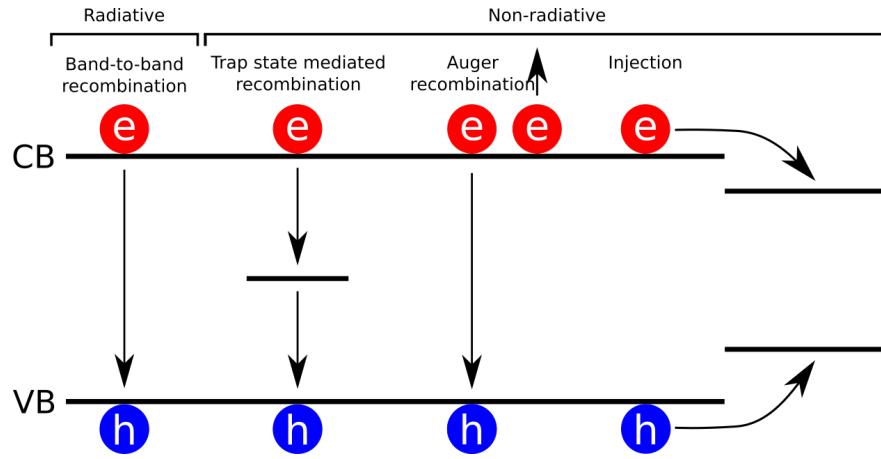


Figure 1.6: Possible recombination processes in semiconductors. If the semiconductor is in contact with a crystal which CBM (VBM) energy is lower (higher) than its own CBM (VBM) energy, electrons (holes) can be injected into the crystal.

The PL of a semiconductor can provide useful information regarding its electronic properties; The maximum PL intensity (I_{max}) is a good indicator of the contribution of radiative recombinations. The maximum emission wavelength (λ_{max}) is linked to the band-gap energy. The full width at half maximum (FWHM), also simply called linewidth, is equal to the sum of contributions arising from lattice defects (FWHM_D), scattering off of phonons (FWHM_P) and scattering off ionised impurities within the lattice (FWHM_I) [44].

$$FWHM = FWHM_D + FWHM_P + FWHM_I \quad (1.1)$$

1.3 Theory of solar cells and perovskite solar cells

1.3.1 Solar cells working principle

A Solar cells architectures

A “photovoltaic cell” or “solar cell” is a device which can convert light into an electric current. Solar cells are composed of an active material which absorbs incident light. The photoexcited electron/hole pair is then separated and collected on each side of the solar cell, at charge selective contacts. The electron travels to an external load, until it recombines with the hole, generating an electric current and voltage [45]. There exist different ways to separate the photoexcited charge carriers after absorption (**Figure 1.7**) [46]. Silicon solar cells are based on the contact of a N and P-type

silicon semiconductors. Due to the mismatch of the CBM and VBM energies between the two semiconductor, such contact leads to the diffusion of the dark electrons from the N-type to the P-type and the dark holes from the P-type to the N-type. The ionised donor and acceptor ions left next to the interface create an electric field that sweeps any carrier away from the interface and creates a charge carrier depletion zone. When light is absorbed (usually in the P-type layer due to it being thicker than the N-type layer), the photoexcited electron diffuses toward the depletion zone where the electric field drives it towards the anode. The photoexcited hole diffusion towards the depletion zone is counterbalanced by the electric field and the hole drifts towards the cathode (**Figure 1.7a**). The use of direct band-gap and high absorption coefficient semiconductors, such as GaAs, allows the use of thinner P and N-type semiconductor layers which increases the chance of light absorption in the depletion zone where the electric field assists charge carrier separation (**Figure 1.7b**). More recent technologies such as PSCs introduces an intrinsic layer between the P-type and N-type materials, in this case the perovskite material, serving as the absorbing material (**Figure 1.7c**). The presence of the intrinsic layer increases the contact area of the P-N junction thus extending the depletion zone, and therefore the electric field, over a wider region thus potentially increasing charge carrier collection. Heterojunction solar cells such as CdTe use the combination of a wide band-gap semiconductor transparent to visible light (*e.g.* CdS) and a smaller band-gap absorber layer (*e.g.* CdTe) to generate a depletion zone and thus an electric field (**Figure 1.7d**). DSSCs consist of a mesoporous TiO₂ scaffold sensitised with a dye and filled with an electrolyte (**Figure 1.7e**). When a photon is absorbed by the dye, the excited electron is injected into the mesoporous TiO₂, travels to the anode and in the external load until it reaches the cathode. After losing the electron, the ground state of the dye is immediately replenished through reduction by the electrolyte. The electrolyte diffuses towards the counter electrode where it is reduced thus completing the cycle. Organic solar cells are based on the mixture of an electron donor and acceptor materials (**Figure 1.7f**). The energy difference between the two materials leads to the separation of the electron-hole pair at the materials interface which are then driven toward the anode and the cathode respectively. The material with the lower CBM and VBM energies (*e.g.* N-type in P-N and P-i-N junctions) is usually called electron transport layer (ETL) as it drives the electrons toward the anode and prevents the holes to do the

same. For similar reasons, the material with the higher CBM and VBM energies (e.g. P-type in P-N and P-i-N junctions) is called the hole transport layer (HTL).

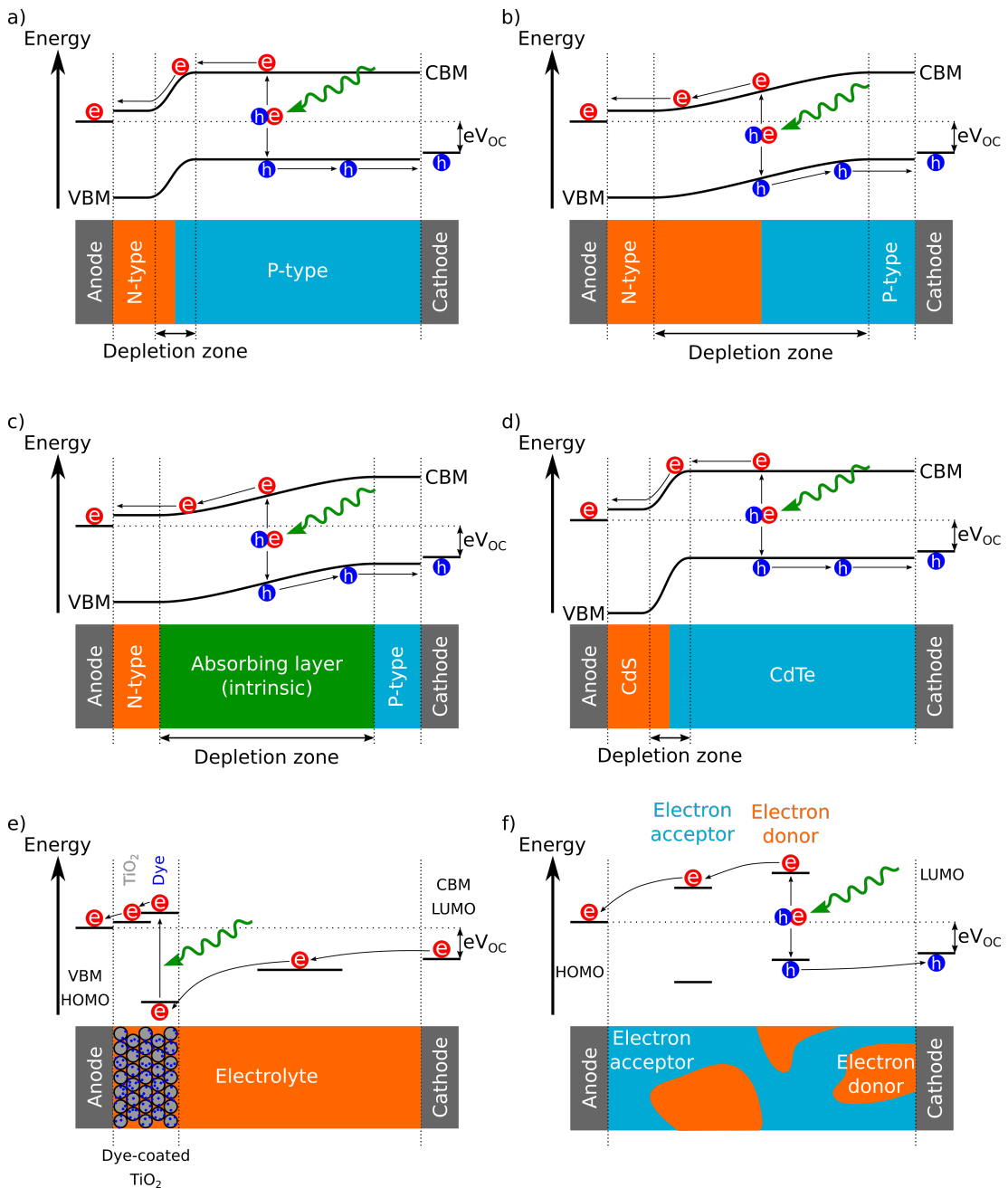


Figure 1.7: Working principle of a) P-N junction, b) thin-film P-N junction, c) P-i-N junction, d) heterojunction, e) dye-sensitized and f) organic solar cell. In all architectures, a photon with energy higher than the band-gap energy creates a hole-electron pair. The mismatch of the conduction band minimum (CBM) (or the lowest unoccupied molecular orbital - LUMO) and the valence band maximum (VBM) (or highest occupied molecular orbital - HOMO) of the layers leads to the formation of an electric field which drives the carriers towards the device's contacts. Adapted from [46]

B Solar cells properties

The PCE of a solar cell, *i.e.* the ratio of electric energy generated to the solar energy received, depends on the voltage and the current generated by the device. The short circuit current (V_{OC}) corresponds to the voltage difference between the photoexcited electron and hole after they have reached the solar cell contacts (**Figure 1.7**). The short circuit current is the maximum electric current obtained from a solar cell at zero voltage. It highly depends on the device ability to absorb light, the mobility of the charge carriers, the carrier injection rates from layer to layer and the carrier recombination rate.

Any photon with energy higher than the band-gap energy can photoexcite electrons into the CB which then thermally relaxes down to the CBM. Hence, every photon absorbed lead to the same open circuit voltage while the energy difference is lost. As a consequence, the optimum PCE can be achieved with a ~ 1.3 eV band-gap energy as per the Shockley-Queissar limit [7]. It is possible to limit this energy loss by using multi-junction solar cells composed of a junction with a high energy band-gap generating a high V_{OC} and a junction with a smaller band-gap energy absorbing lower energy photons.

C Solar cells photoluminescence

PL and electric current generation are similar processes in solar cells and both originate from the excitation of carriers through the absorption of light. While PL is a measure of the radiative recombinations happening in the absorber layer, the current and voltage of the solar cells are indicative of the ability of the solar cell to separate holes and electrons and to extract these charges away from the absorber layer. They are therefore competing processes; extraction of charge carriers preventing them from radiatively recombining and reciprocally. PL emission of solar cells is therefore lower when operating in short-circuit condition due to the extraction of the charge carriers away from the absorber layer, than in open-circuit condition in which the extraction is limited. Both processes are competing with non-radiative recombinations.

1.3.2 Perovskite solar cells

A Generality on perovskite solar cells

The word “perovskite” was first used to designate the CaTiO_3 mineral discovered by the German mineralogist Gustav Rose in 1893 and named after the Russian mineralogist, Lev Perovski [47]. Nowadays, this term labels the class of compounds which share a close similar crystal structure to CaTiO_3 . To be labelled perovskite, a compound must obey a set of 3 rules [48]:

1. The material must follow the stoichiometry ratio ABX_3 ;
2. The B cations and X anions needs to form a (distorted) octahedral coordination;
3. These octahedras should occupy every corner of the unit cell.

Perovskite materials can be found in different crystallographic systems (cubic, tetragonal, orthorhombic, trigonal or monoclinic) depending on the tilting and the rotation of the BX_6 octahedras (*e.g.* **Figure 1.8**), and may present insulating (*e.g.* BaTiO_3), metallic (*e.g.* LaTiO_3), magnetic (*e.g.* LaCoO_3) and superconducting (*e.g.* SrTiO_3 N-type) properties [49], [50].

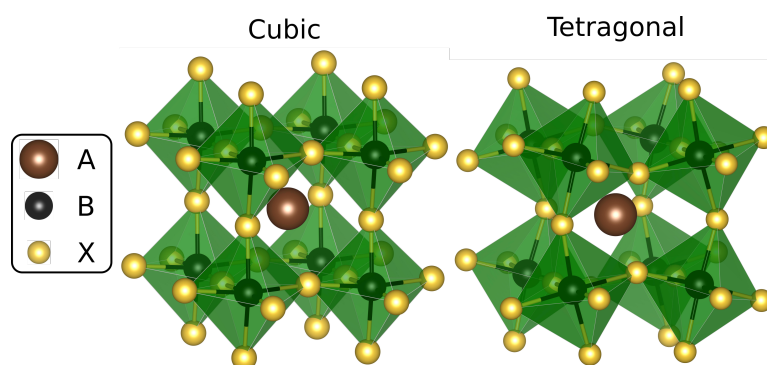


Figure 1.8: Representation of the perovskite structure ABX_3 in the cubic and tetragonal systems. Drawn with Vesta [51].

B History of perovskite solar cells

In an effort to improve the PCE of DSSCs, perovskites were used in a solar cell for the first time by A. Kojima *et al.* in 2009 [52]. Substituting the dye with methylammonium lead iodide ($\text{CH}_3\text{NH}_3\text{PbI}_3$ - MAPI) and methylammonium lead bromide ($\text{CH}_3\text{NH}_3\text{PbBr}_3$ - MAPBr) perovskites lead to 3.8 % and 3.1 % PCE respectively [52]. J-H. Im *et al.* further improved this device and reported a 6.5 %

PCE in 2011 [53]. Perovskite sensitised solar cells were, however, very unstable as the electrolyte dissolved the perovskite material, leading to the development of perovskite solid-state devices analogous to solid state dye sensitised solar cells (ss-DSSCs), where the electrolyte was replaced by a solid material. This evolution of PSCs is highlighted in **Figure 1.9**.

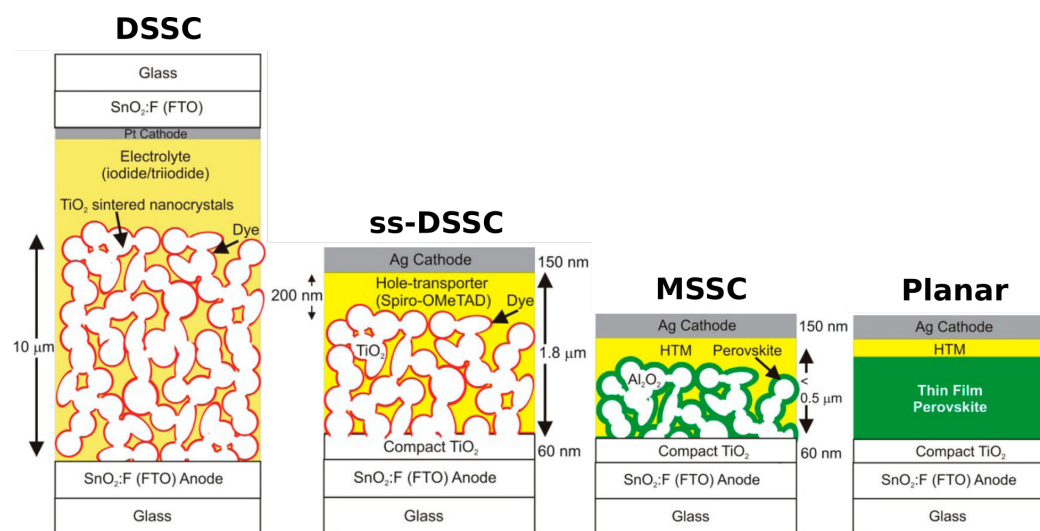


Figure 1.9: Types of perovskite solar cells. DSSC: dye-sensitised solar cell, ss-DSSC: solid-state dye-sensitised solar cell, MSSC: meso-superstructured solar cell. Adapted from [1].

This transition was further motivated by the fact that the mesoporous and absorber layer in ss-DSSCs is limited to *ca.* 2 μm and 3 μm to allow sufficient penetration of the HTL while the dye requires a thickness of *ca.* 10 μm for a monolayer of dye (coated on TiO_2) to absorb enough light [54]. The high absorption coefficient of perovskites allows them to absorb *ca.* 99 % of visible light with a layer thickness of *ca.* 500 nm, thus making them an excellent fit to replace the dyes in ss-DSSCs [1]. By replacing the dye with a perovskite material in a ss-DSSC using 2,2',7,7'-Tetrakis [N,N-di(4-methoxyphenyl)amino]-9,9' -spirobifluorene (spiro-OMeTAD) as HTL, H-S. Kim *et al.* obtained a 9.7 % PCE [55]. It was then demonstrated that perovskites present faster charge carrier transport than the TiO_2 ETL (from 10 to 70 times faster depending on the carrier concentration) [56]. Replacing the mesoporous TiO_2 layer with a mesoporous Al_2O_3 layer enabled a V_{OC} gain up to 300 mV and a 10.9 % PCE [56]. These cells were then renamed meso-superstructured solar cells (MSSCs) to reflect the fact that the mesoporous Al_2O_3 layer act as a scaffold for the perovskite without playing a role in the charge carrier transport [1]. Further research on the electron transport properties

of perovskites lead to the development of planar PSCs where the mesoporous layer is removed, and the perovskite layer ensures efficient carrier transport. M. Lee *et al.* obtained a 1.8 % PCE in 2012 with such architecture [56], but their efficiency quickly increased to 12.0 % [57] up to 15.0 % [58] in 2013. The same year, J. Burschka *et al.* developed a two-step deposition technique for the perovskite layer achieving a 15.0 % PCE [59]. N. J. Jeon and colleagues greatly participated to the improvement of the efficiency of PSCs, first in 2014 when they presented a 16.2 % PCE using a MAPI-MAPBr mix [60] then in 2015, with a 17.9 % PCE using a mix of MAPBr and formamidinium lead iodide (FAPbI₃) [61] and finally in 2016 with a certified 19.7 % PCE by incorporating amount of PbI₂ into the MAPI perovskite layer and even an impressive 20.1 % PCE by adding PbI₂ to the mix MAPBr-FAPbI₃ [62]. M. Saliba and co-workers presented cells with a 21.6 % PCE in 2016 [63]. The same year, the Korean Research Institute of Chemical Technology (KRICT) & the Ulsan National Institute of Science and Technology (UNIST) presented a 22.1 % PCE [64]. The latest efficiency improvements were made by the KRICT and the Minnesota Institute of Technology in 2019 and by UNIST in 2020 with a 25.2 % and 25.5 % PCE respectively [22].

1.4 Methylammonium lead iodide perovskite

The MAPI perovskite was used in the first PSC developed by A. Kojima *et al.* [52] and is still used in high efficiency [62] and relatively stable devices such as mesoporous carbon perovskite solar cells [65].

1.4.1 Structural, electronic and optical properties of methylammonium lead iodide

The MAPI crystallographic cell is composed of a CH₃NH₃⁺ cation surrounded by 4 PbI₆ octahedras. At temperatures lower than 165 K, MAPI can be found in the orthorhombic system (P4/mbm), in the tetragonal system (I4/mcm) between 165 K and 327 K, and in the cubic system (Pm-3m) at higher temperatures [66]. The tetragonal and cubic phases coexist between 300 K and 330 K and present very similar structures leading to similar x-ray diffraction (XRD) patterns (**Figure 1.10**) [67].

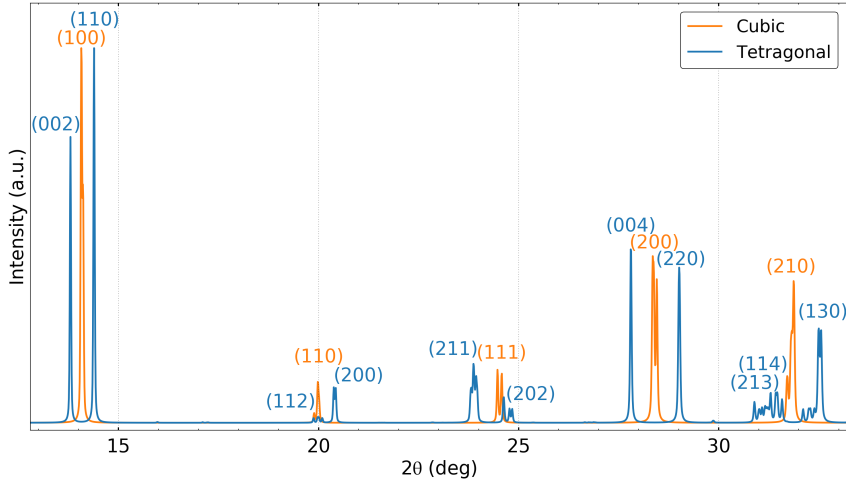


Figure 1.10: Theoretical X-ray diffraction pattern of MAPI in the cubic and tetragonal phases calculated from density functional theory calculations [68] and Vesta’s diffraction pattern simulation tool [51].

For simplicity purposes, only the cubic and tetragonal phases are discussed here as these phases are more likely to be observed at room temperature. In both phases, the VBM of MAPI is mainly composed of lead 6s and iodide 5p orbitals while the CBM is composed of lead 6p and iodide 5p antibonding orbitals [69]–[72]. MAPI has a direct band-gap with energy between 1.63 eV and 1.66 eV in the tetragonal phase and 1.57 eV in the cubic phase determined using density functional theory (DFT), and consistent with the reported *ca.* 1.6 eV from experimental measurements at room temperature [73], [74].

1.4.2 Instability and defect properties

Colin Humphreys once said “*Crystals are like people: it is the defects in them which tend to make them interesting*”. This statement seems particularly apt for lead-halide perovskites as they are believed to contain a number of point defects in their structure [75]. Hereafter, the Kröger-Vink notation is used where a point defect is noted A_S^C , with A the species (*e.g.* atom, vacancy V), S the site occupied by the species (*e.g.* atom site, interstitial i) and C the charge of the defect. In particular, V_A is the A species vacancy, A_B is the substitution of B species by A species and A_i is the A species located at an interstitial site. *Ab initio* calculations have been used to calculate the formation of defects in perovskites. DFT calculations carried using the generalised gradient approximation (GGA) exchange-correlation functional and

without considering spin-orbit coupling (SOC) have been shown to give a value of the band-gap energy close to the one experimentally measured which was explained by a cancellation of the error induced by these two approximations [74], [76]. However, the point defect formation energies as well as position of the defect-induced trap states have been shown to highly depend on the exchange-correlation functional used and whether or not SOC was considered [75], [77]. For example, interstitial iodides I_i have been shown to induce deep electron traps with the Perdew-Burke-Ernzhof functional and SOC in [78] while it has been shown to induce a shallow transition level with the GGA functional without SOC in [76]. Using the precise hybrid functional HSE06 and considering SOC, the Fermi level was found to lie slightly below the middle of the band-gap indicating a slight P-type doping of MAPI in medium-iodine condition (**Figure 1.11b**) [75].

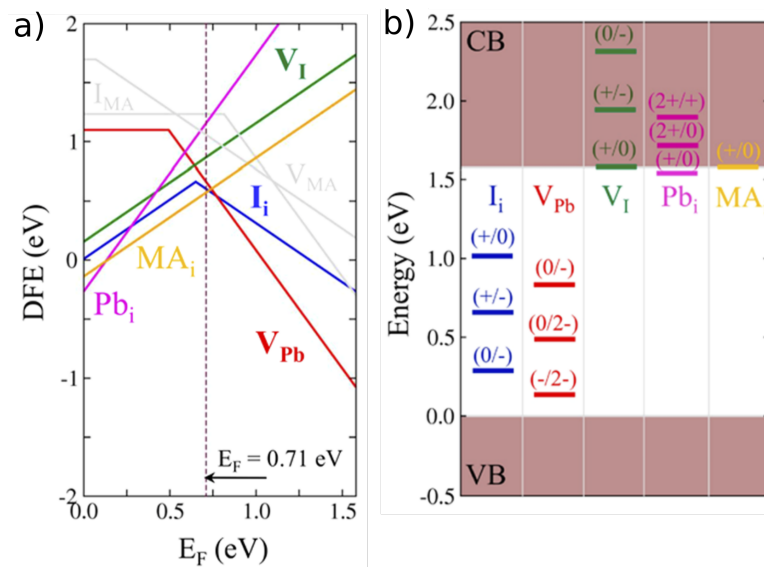


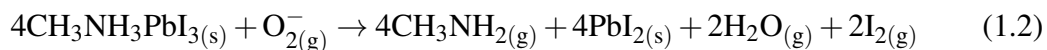
Figure 1.11: a) Defect formation energy (DFE) of different defects in MAPI in iodine-medium condition and b) associated transition levels. Adapted from [75]

In iodine-rich condition, the Fermi level shifts closer to the VB indicating a higher P-type doping while in a iodine-poor condition, the Fermi level is closer to the CB indicating N-type doping [75]. In the iodine-medium condition, MA_i^+ , I_i^- and V_{Pb}^{2-} are the most stable defects and their concentration is expected to be of the order of magnitude of 10^{12} cm^{-3} while I_i^+ has a slightly higher formation energy and therefore an expected concentration of about 10^{10} cm^{-3} (**Figure 1.11a**) [75]. Lead vacancies V_{Pb} are unstable in P-type region and may lead to the formation of I_i^+ and V_I^+ . Iodide vacancies V_I present a shallow transition level near the CB and is always stable in its positive charged state, thus allowing it to form a Frenkel pair with I_i^- (**Figure 1.11b**)

[75]. Both V_{pb} and I_{i} present deep transition levels with possible short lived hole trapping by I_{i}^- and long lived electron trapping by I_{i}^+ [75]. Defects can be formed or passivated from perturbation such as light absorption and reaction with oxygen and moisture and are intrinsically linked with the instability of MAPI.

A Oxygen

Molecular oxygen (O_2) has a relatively high diffusion rate in perovskites (*ca.* $10^{-7} - 10^{-9} \text{ cm}^2/\text{s}$), and can completely diffuse into a $2 \mu\text{m}$ perovskite film in less than 20 s [11], [12], [79]–[86]. Within the perovskite, O_2 can be reduced by excited electrons to form superoxide O_2^- [12]. Iodide vacancies, which tend to be found at surface of grains [76], [87], have been shown to be energetically favourable sites for the formation of superoxide when occupied by a trapped electron [80], [84], [85]. The π -antibonding orbital of O_2 which is located in the middle of band-gap of MAPI shifts down into the perovskite's VB when O_2 occupies an iodide vacancy filled with a trapped electron, thus making the reaction energetically favourable [80], [84]. The reaction between superoxide and MAPI is energetically favourable and happens through deprotonation of the methylammonium cation leading to the formation of lead iodide PbI_2 , gaseous water and iodine I_2 (**Table 1.2**) [80]:



It has also been proposed that deprotonation of MAI by superoxide can lead to the formation of the hydroperoxyl radical HO_2^\bullet [88]. By reacting either with another hydroperoxyl, with water or undergoing reduction, HO_2^\bullet can form hydrogen peroxide H_2O_2 which can then passivate uncoordinated lead (see **Section 1.4.2F**) [88].

Film morphology has been shown to affect superoxide formation as smaller grains tend to generate more superoxide than larger grains [80]. Surface vacancies which are well known to be more reactive than bulk vacancies have been estimated to be around 2.5 times more concentrated in smaller crystallites than larger ones due to their higher surface/volume ratio ($6.0 \times 10^{17} \text{ cm}^{-3}$ and $2.4 \times 10^{17} \text{ cm}^{-3}$ respectively) [80]. Furthermore, it was estimated that the concentration of iodide vacancies in the bulk is around 10^{22} cm^{-3} making it a significant contributor to superoxide formation [68]. Due to the shorter diffusion length in smaller crystallites, O_2 molecules can reach the

bulk defects faster in these crystallites. Denser grain distributions as well as smaller unit cells may limit oxygen penetration in the film and thus limit superoxide formation [86], [89]. The adjacent layers to the perovskite also influence superoxide formation in the perovskite [12]. If the perovskite is deposited on a semiconductor which CBM energy is lower than the perovskite's CBM energy, (*e.g.* TiO₂), the excited electrons can be extracted from the perovskite hence reducing the probability of trapping and reaction with molecular oxygen (**Figure 1.12**) [12]. If the perovskite is deposited on a semiconductor where the CBM energy is higher than the perovskite's CBM energy (*e.g.* Al₂O₃), the excited electrons remain in the perovskite's CBM until radiative recombination with a hole or trapping occurs, potentially leading to superoxide formation in the latter case [12].

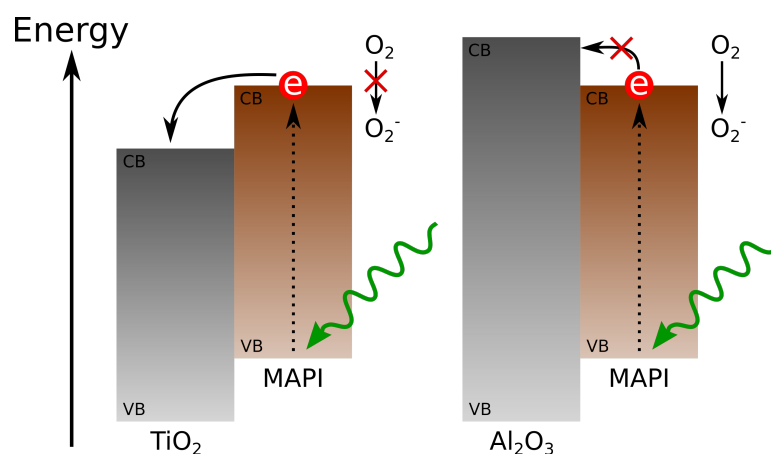
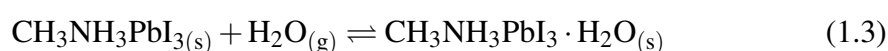


Figure 1.12: Schematic of the possible reactions of photoexcited electrons with molecular oxygen in MAPI, either deposited on TiO₂ or Al₂O₃. Adapted from [12].

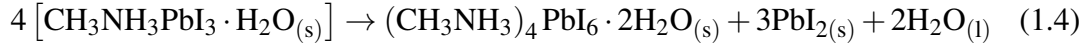
B Water

Water has been shown to be more stable inside the MAPI crystal than at its surface by 0.2 – 0.3 eV and can easily migrate within the crystal due to its low associated energy barrier (0.28 eV) [90]. Water can intercalate in the perovskite lattice and form hydrogen bonds with the ammonia part of the methylammonium cation and the I atoms of the PbI₆ octahedras [90], [91]. The presence of intercalated water has been shown to improve diffusion of iodide I⁻ and methylammonium MA⁺ ions [90]. The formation of the monohydrate CH₃NH₃PbI₃ · H₂O is a favourable reaction [85] (**Table 1.2**) and is more stable than the intercalation of water in the perovskite unit cell [90].



This hydration process is believed to be isotropic through the entire film, likely due to the diffusion of water through grain boundaries [92]. The reaction can easily be reverted by keeping the hydrated perovskite in a low humidity atmosphere [92], [93]. The migration barrier of I^- and MA^+ in the monohydrate is higher than when water is intercalated in MAPI but remains slightly lower than the pure perovskite suggesting that water may enhance defect formation and passivation as discussed hereafter [90].

A second hydration occurs when the perovskite is hydrated with 2 water molecules per formula unit leading to the formation of the dihydrate phase $(CH_3NH_3)_4PbI_6 \cdot 2H_2O$, PbI_2 and liquid water [92], [94], [95]:



This reaction is only partially reversible due to the phase segregation that occurs [92], [93]. The dihydrate phase can be further degraded into PbI_2 and methylammonium iodide (CH_3NH_3I) through reaction with liquid water [92].

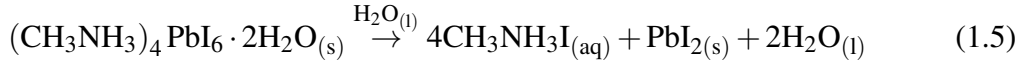


Table 1.2: Enthalpy of reaction of different degradation processes calculated using density functional theory [85].

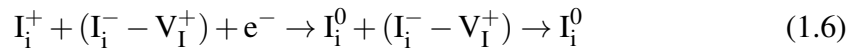
Reaction	Energy (kJ/mol)
$CH_3NH_3PbI_3_{(s)} \xrightarrow{\text{light}} PbI_{2(s)} + CH_3NH_3I_{(s)}$	-54
$CH_3NH_3PbI_3_{(s)} \xrightarrow{\text{light}} PbI_{2(s)} + CH_3NH_2_{(g)} + HI_{(g)}$	+153
$CH_3NH_3PbI_3_{(s)} + H_2O_{(g)} \leftrightarrow CH_3NH_3PbI_3 \cdot H_2O_{(s)}$	-16
$4CH_3NH_3PbI_3 + 2H_2O_{(g)} \rightarrow (CH_3NH_3)_4PbI_6 \cdot 2H_2O_{(s)} + 3PbI_{2(s)}$	-49
$4CH_3NH_3PbI_3_{(s)} + O_{2(g)} \xrightarrow{\text{light}} 4CH_3NH_2_{(g)} + 4PbI_{2(s)} + 2H_2O_{(g)} + 2I_{2(g)}$	-74

Water can passivate defects through the degradation of the perovskites into PbI_2 and PbO [92], [96]. It can also assist the conversion of superoxide to hydrogen peroxide and hence helps passivating uncoordinated lead defects (see **Section 1.4.2F**). On the other hand, the MAPI hydrated phases are less likely to form superoxide

compared to MAPI, potentially due to their higher band-gap energy which prevent formation of excited states through absorption of visible light [85].

C Frenkel pair annihilation under illumination

As previously discussed, MAPI is believed to present numerous point defects and in particular, iodide vacancies V_I^+ and iodide interstitials I_i^+ and I_i^- . Electron trapping by I_i^+ has been shown to increase the energy barrier for the formation of the $I_i^- - V_I^+$ Frenkel pair from 0.55 eV up to 0.86 eV [97]. Due to the low diffusion energy barrier (~ 0.1 eV [98]) and the long lived state of trapped electrons in I_i^+ , I_i^- can diffuse toward V_I^+ leading to their annihilation [97], [99] (**Figure 1.13a**).



The resulting iodide atom I_i^0 can react with another iodide atom to form iodine I_2 .



Iodine can then passivate or form defects in the perovskite as discussed in **Sections 1.4.2E & G**.

D Iodide vacancy and uncoordinated lead formation under illumination

In MAPI, the loss of an electron through the oxidation of an iodide atom by a photoexcited hole has been suggested to reduce its size allowing it to leave its lattice site to an interstitial site and hence creating an iodide Frenkel pair $V_I^+ - I_i^+$ (**Figure 1.13b**) [100], [101]. Two interstitials I_i^+ can react with each other to form I_2 , leaving two iodide vacancies [101].



An iodide vacancy can then reduce atomic lead through the trapping of an electron [101].



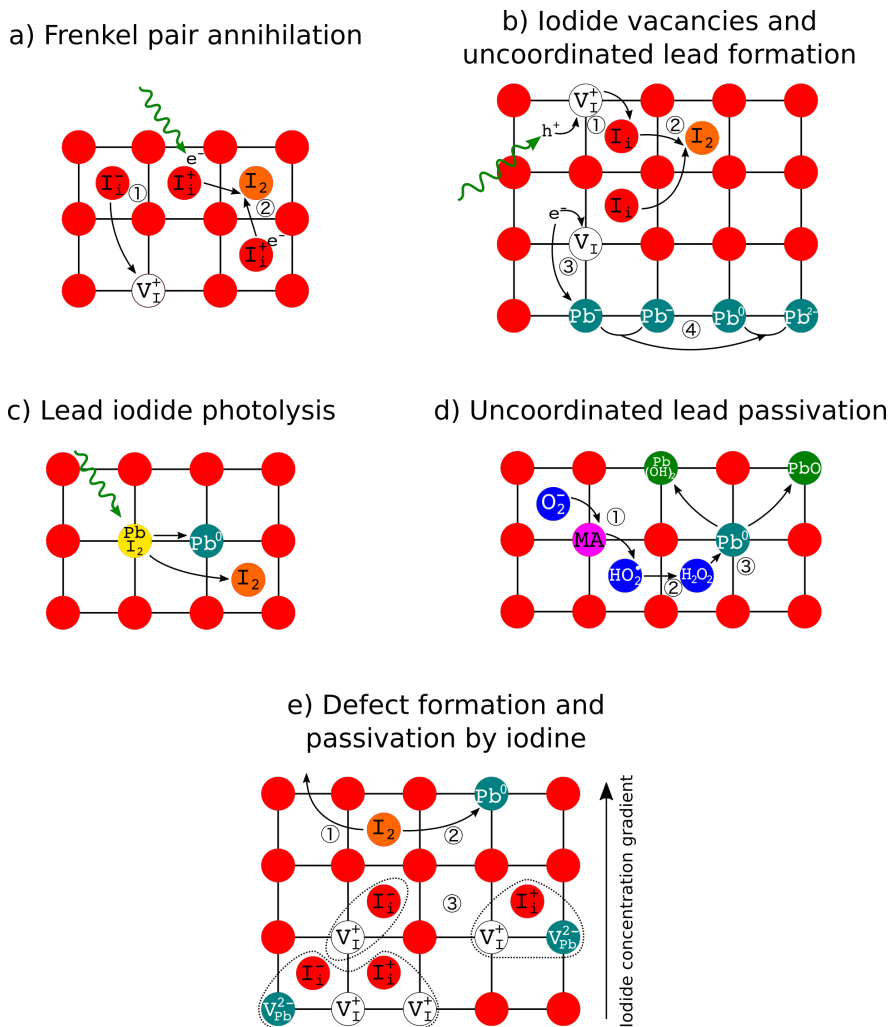


Figure 1.13: Schematic representation of some of the processes leading to formation and passivation of defects in MAPI. **a)** Frenkel pair annihilation ① A photoexcited electron reduces an iodide interstitial I_i^+ , lowering the energy barrier to the annihilation of the Frenkel pair ($I_i^- - V_I^+$) through the migration of I_i^- ② Uncoordinated iodide interstitial can react with each other to form iodine I_2 . **b)** Uncoordinated lead and iodide vacancies formation ① A photoexcited hole lead to the migration of an iodide atom away from its site to an interstitial site ② Interstitial iodide atoms react to form iodine ③ An iodide vacancy reduces lead through the trapping of an electron ④ Lead anion Pb^{2-} and uncoordinated lead Pb^0 are formed through disproportionation of two lead anions. **c)** Lead iodide photolysis leading to the formation of uncoordinated lead and iodine. **d)** Uncoordinated lead passivation ① Superoxide can react with methylammonium MA to form an hydroperoxyl radical. ② The hydroperoxyl radical can react with water or another hydroperoxyl to form hydrogen peroxide ③ Hydrogen peroxide reacts with uncoordinated lead to form either PbO or $Pb(OH)_2$. **e)** Defect formation and passivation by iodine: iodine formed from **a)**, **b)** or **c)** migrates toward the grains surface where it can either ① escape the perovskite as a gas or ② bind to surface sites such as Pb^0 where it acts as an electron trap or form PbI_2 ③ The resulting iodine concentration gradient leads to the formation of defect complexes in the bulk.

The lead anion Pb^{2-} and uncoordinated lead Pb^0 can be formed through disproportionation of two lead anions, consistent with the reported measurement of Pb^0 [102]:



Pb^0 has been experimentally shown to act as a quencher [103] however, this is inconsistent with *ab initio* calculations [88]. It has been postulated that the passivation of Pb^0 may lead to a migration of the iodide interstitials toward the associated vacancies leading to their annihilation [88], consistent with the previous report [103].

E Defect formation and passivation due to lead iodide

Photons with a wavelength lower than 520 nm can photolyse PbI_2 into I_2 which can then lead to the creation of more defects as well as the degradation of the perovskite as discussed in **Section 1.4.2G (Figure 1.13c)** [10].



Excess PbI_2 has also been shown to affect the trap state concentration by changing the chemical potential condition which thus affects the formation energy of the defects [104] (see **Section 1.4.2**). Furthermore, when located at the perovskite and HTL (ETL) interfaces, PbI_2 forms an energy barrier preventing the recombination of holes (electron) within the HTL (ETL) with electrons (holes) in the perovskites [105]. If the PbI_2 is located within the perovskite, it can prevent recombination of carriers located within different grains [105].

F Uncoordinated lead passivation by hydrogen peroxide

Uncoordinated lead can react with hydrogen peroxide H_2O_2 to form PbO and $\text{Pb}(\text{OH})_2$ leading to its passivation and a decrease of non-radiative recombinations (**Figure 1.13d**) [88].

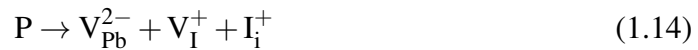


However it is not clear yet if this is directly linked to a passivation of the trap states associated with Pb^0 , or if the iodide vacancies are the quenching species and the passivation of Pb^0 induce an electric field driving the Frenkel pair annihilation [88].

As discussed in **Section 1.4.2A**, superoxide can react with organic cations such as methylammonium or formamidinium cations to form the hydroperoxyl radical HO_2^\bullet [88]. By reacting either with another hydroperoxyl, with water or undergoing reduction, HO_2^\bullet can form hydrogen peroxide H_2O_2 which can then passivate Pb^0 [88].

G Defect formation and passivation due to iodine

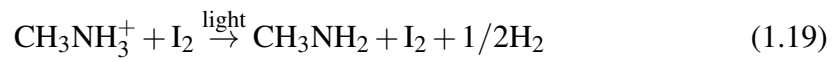
Iodine (either formed according to **Equation 1.7, 1.8** or **1.11**) can migrate to the surface of perovskite grains where it can bind to surface sites and act as an electron trap [97] (**Figure 1.13e**). Furthermore, the iodine concentration gradient created by the diffusion of I_2 leads to the formation of more defects such as V_{Pb} , V_{I} and I_i in the grains bulk in order to balance the iodide concentration [97]:



where P corresponds to the pristine lattice structure. It has been hypothesised that saturation of surface sites by I_2 can lead to the release of I_2 and form PbI_2 [97], consistent with the measurement of iodine gas [106].

Iodine can be photolysed by light of wavelength *ca.* $\lambda < 500$ nm into iodide atoms I which can then react with iodide anion I^- of the perovskite crystal to form I_2^- . This anion can then react with the methylammonium cation to form methylamine and molecular hydrogen, and the regeneration of iodine [107]:





All these defect formation and passivation processes discussed in this section are intrinsically linked. For example, light-mediated iodide Frenkel pair annihilation can lead to the formation of iodine. Iodine can then react with uncoordinated lead to form lead iodide. Lead iodide can then be photolysed to form uncoordinated lead and iodine. An attempt to summarise the complex relations between these processes is shown in **Figure 1.14**.

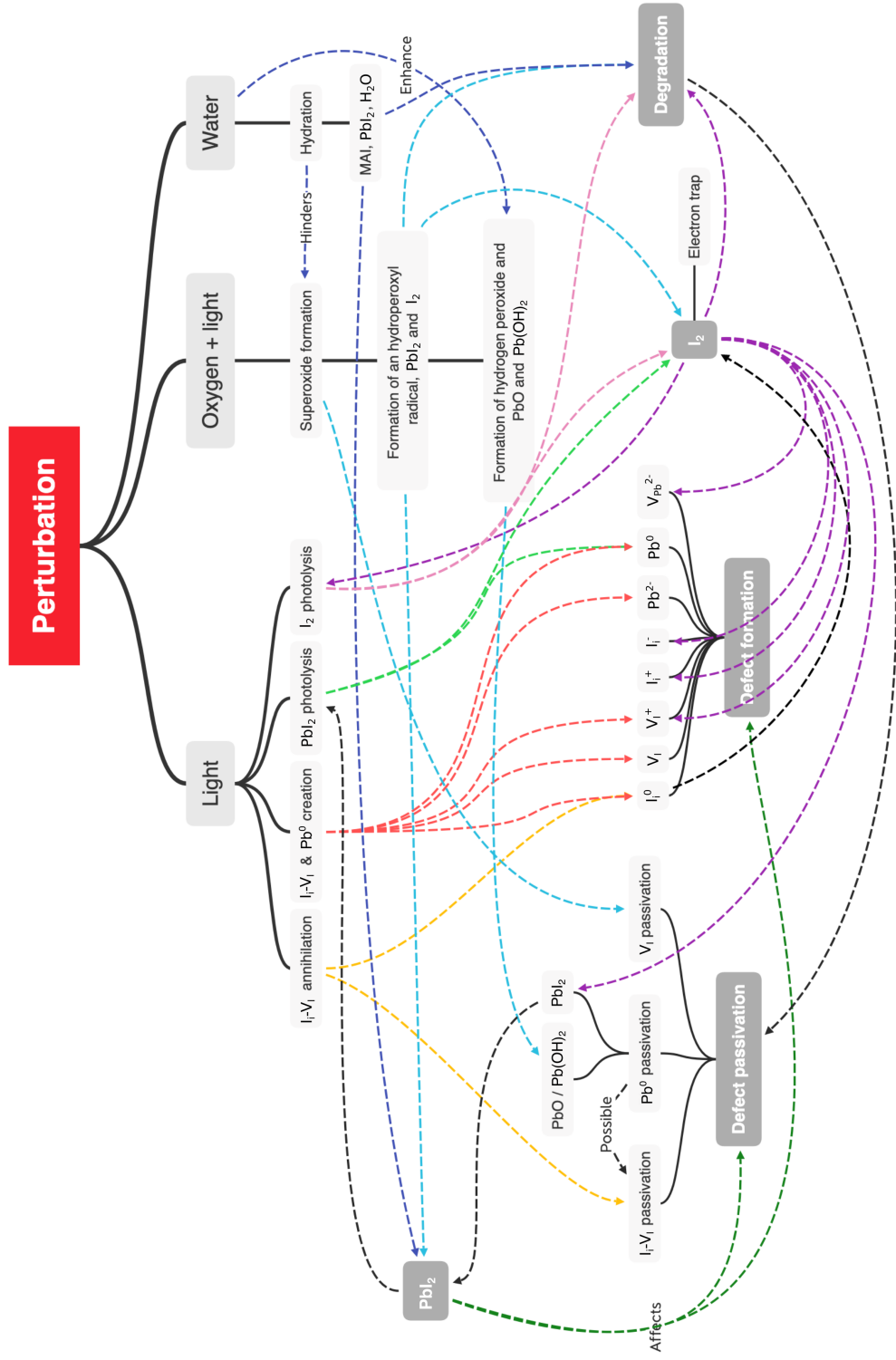


Figure 1.14: Non exhaustive summary of the processes happening in MAPI under different perturbations (light, oxygen and water). The arrows indicate the consequences of each process and highlights their complex relationship.

1.5 Thesis overview

Point defects, light, oxygen and moisture have been shown to be linked to the excited state nature of MAPI and are responsible for its instability. This work aims to photochemically characterise the MAPI perovskite. Although more complex perovskites such as mixed cation perovskites now yield higher efficiencies, MAPI is still used in very stable architectures and is an easier material to investigate, making it a great starting ground. **Chapter 2** describes the experimental techniques used in this work. In **Chapter 3**, photobrightening and photodarkening are investigated using fluorescence microscopy and XRD. In **Chapter 4**, the interpretation and measurement of TRPL as well as charge carrier recombination in MAPI are discussed. Finally, the stability and the formation of superoxide in MAPI and 5-aminovaleric acid iodide modified MAPI infiltrated in mesoporous carbon perovskite solar cells and mesoporous substrates such as ZrO₂ are investigated in **Chapter 5**.

1.6 References

- [1] H. J. Snaith, “Perovskites: The emergence of a new era for low-cost, high-efficiency solar cells”, *Journal of Physical Chemistry Letters*, vol. 4, no. 21, pp. 3623–3630, Nov. 2013. DOI: 10.1021/jz4020162.
- [2] S. Kang *et al.*, “Ultrathin, lightweight and flexible perovskite solar cells with an excellent power-per-weight performance”, *Journal of Materials Chemistry A*, vol. 7, no. 3, pp. 1107–1114, Jan. 2019. DOI: 10.1039/C8TA10585E.
- [3] H. S. Jung *et al.*, “Flexible perovskite solar cells”, *Joule*, vol. 3, no. 8, pp. 1850–1880, 2019. DOI: <https://doi.org/10.1016/j.joule.2019.07.023>.
- [4] C. Feng *et al.*, “Theoretical design for the non-toxic and earth-abundant perovskite solar cell absorber materials”, *Frontiers in Materials*, vol. 7, p. 168, Jun. 2020. DOI: 10.3389/fmats.2020.00168.
- [5] J. Baker *et al.*, “High throughput fabrication of mesoporous carbon perovskite solar cells”, *Journal of Materials Chemistry A*, vol. 5, no. 35, pp. 18 643–18 650, Sep. 2017. DOI: 10.1039/C7TA05674E.
- [6] Y. Li *et al.*, “Direct observation of long electron-hole diffusion distance in ch₃nh₃pbi₃ perovskite thin film”, *Scientific Reports*, vol. 5, no. 1, p. 14 485, Nov. 2015. DOI: 10.1038/srep14485.

- [7] S. Rühle, “Tabulated values of the shockley–queisser limit for single junction solar cells”, *Solar Energy*, vol. 130, pp. 139–147, 2016. DOI: <https://doi.org/10.1016/j.solener.2016.02.015>.
- [8] L. M. Herz, “Charge-carrier mobilities in metal halide perovskites: fundamental mechanisms and limits”, *ACS Energy Letters*, vol. 2, no. 7, pp. 1539–1548, Jul. 2017. DOI: [10.1021/acsenergylett.7b00276](https://doi.org/10.1021/acsenergylett.7b00276).
- [9] R. Wang *et al.*, “A review of perovskites solar cell stability”, *Advanced Functional Materials*, vol. 29, no. 47, p. 1808843, 2019. DOI: [10.1002/adfm.201808843](https://doi.org/10.1002/adfm.201808843).
- [10] W. A. Quitsch *et al.*, “The Role of excitation energy in photobrightening and photodegradation of halide perovskite thin films”, *Journal of Physical Chemistry Letters*, vol. 9, no. 8, pp. 2062–2069, Apr. 2018. DOI: [10.1021/acs.jpcllett.8b00212](https://doi.org/10.1021/acs.jpcllett.8b00212).
- [11] R. Brenes *et al.*, “Metal halide perovskite polycrystalline films exhibiting properties of single crystals”, *Joule*, vol. 1, no. 1, pp. 155–167, Sep. 2017. DOI: [10.1016/j.joule.2017.08.006](https://doi.org/10.1016/j.joule.2017.08.006).
- [12] N. Aristidou *et al.*, “The role of oxygen in the degradation of methylammonium lead trihalide perovskite photoactive layers”, *Angewandte Chemie - International Edition*, vol. 54, no. 28, pp. 8208–8212, Jul. 2015. DOI: [10.1002/anie.201503153](https://doi.org/10.1002/anie.201503153).
- [13] International Energy Agency, “IEA webstore. Global energy & CO₂ status report 2018”, Tech. Rep., 2019.
- [14] C. MacFarling Meure *et al.*, “Law dome CO₂, CH₄ and N₂O ice core records extended to 2000 years BP”, *Geophysical Research Letters*, vol. 33, no. 14, p. L14810, Jul. 2006. DOI: [10.1029/2006GL026152](https://doi.org/10.1029/2006GL026152).
- [15] R. K. Pachauri *et al.*, “Climate change 2014 synthesis report”, Intergovernmental Panel on Climate Change, Tech. Rep., 2015.
- [16] GISTEMP Team. (2020). GISS surface temperature analysis (GISTEMP), version 4, [Online]. Available: <https://data.giss.nasa.gov/gistemp/> (visited on 04/02/2020).
- [17] N. Lenssen *et al.*, “Improvements in the gistemp uncertainty model”, *J. Geophys. Res. Atmos.*, vol. 124, no. 12, pp. 6307–6326, 2019. DOI: [10.1029/2018JD029522](https://doi.org/10.1029/2018JD029522).
- [18] T. Stocker, “Climate change 2013 : the physical science basis”, Intergovernmental Panel on Climate Change, Tech. Rep., 2013, p. 1535.

- [19] International Energy Agency. (2019). World Energy Outlook, [Online]. Available: <https://www.iea.org/reports/world-energy-outlook-2019> (visited on 22/04/2019).
- [20] M. Perez *et al.*, “Update 2015 - a fundamental look at supply side energy reserves for the planet”, Tech. Rep., 2015.
- [21] P. Gevorkian, *Sustainable energy systems engineering : the complete green building design resource*. McGraw-Hill, 2007, p. 568.
- [22] National Renewable Energy Laboratory. (2019). Best research-cell efficiency chart, [Online]. Available: <https://www.nrel.gov/pv/cell-efficiency.html> (visited on 04/03/2019).
- [23] D. M. Chapin *et al.*, “A new silicon p-n junction photocell for converting solar radiation into electrical power”, *Journal of Applied Physics*, vol. 25, no. 5, pp. 676–677, May 1954. DOI: 10.1063/1.1721711.
- [24] Fraunhofer Institute for Solar Energy *et al.*, “Photovoltaics report”, Tech. Rep., 2019.
- [25] Kenneth Barbalace. (2020). Periodic table of elements 1995 - 2019, [Online]. Available: <https://environmentalchemistry.com/yogi/periodic/> (visited on 22/04/2019).
- [26] J. Jean *et al.*, “Pathways for solar photovoltaics”, *Energy and Environmental Science*, vol. 8, no. 4, pp. 1200–1219, Apr. 2015. DOI: 10.1039/c4ee04073b.
- [27] J. Gong *et al.*, “Perovskite photovoltaics: Life-cycle assessment of energy and environmental impacts”, *Energy and Environmental Science*, vol. 8, no. 7, pp. 1953–1968, Jul. 2015. DOI: 10.1039/c5ee00615e.
- [28] J. M. Ball *et al.*, “Low-temperature processed meso-superstructured to thin-film perovskite solar cells”, *Energy & Environmental Science*, vol. 6, no. 6, p. 1739, May 2013. DOI: 10.1039/c3ee40810h.
- [29] J. Dagar *et al.*, “Highly efficient perovskite solar cells for light harvesting under indoor illumination via solution processed SnO₂/MgO composite electron transport layers”, *Nano Energy*, vol. 49, pp. 290–299, Jul. 2018. DOI: 10.1016/J.NANOEN.2018.04.027.
- [30] US Department of Energy - Energy Efficiency and Renewable Energy, “What is the energy payback for PV?”, *International Journal*, pp. 1–2, 2004. DOI: DOE/G0-102004-1847.
- [31] A. Sahay *et al.*, “A comparative study of attributes of thin film and crystalline photovoltaic cells”, Tech. Rep., 2013.

- [32] V. Fthenakis *et al.*, “CdTe PV: real and perceived EHS risks”, NREL, Tech. Rep., 2003.
- [33] J. Nelson, “Polymer:fullerene bulk heterojunction solar cells”, *Materials Today*, vol. 14, no. 10, pp. 462–470, Oct. 2011. DOI: 10.1016/S1369-7021(11)70210-3.
- [34] R. Steim *et al.*, “Organic photovoltaics for low light applications”, *Solar Energy Materials and Solar Cells*, vol. 95, no. 12, pp. 3256–3261, Dec. 2011. DOI: 10.1016/J.SOLMAT.2011.07.011.
- [35] M. Jørgensen *et al.*, “Stability/degradation of polymer solar cells”, *Solar Energy Materials & Solar Cells*, vol. 92, no. 7, pp. 686–714, Jul. 2008. DOI: 10.1016/j.solmat.2008.01.005.
- [36] B. O’Regan *et al.*, “A low-cost, high-efficiency solar-cell based on dye-Sensitized colloidal TiO₂ films”, *Nature*, vol. 353, no. 6346, pp. 737–740, Oct. 1991. DOI: 10.1038/353737a0.
- [37] C.-Y. Chen *et al.*, “Performance characterization of dye-sensitized photovoltaics under indoor lighting”, *The Journal of Physical Chemistry Letters*, vol. 8, no. 8, pp. 1824–1830, Apr. 2017. DOI: 10.1021/acs.jpcllett.7b00515.
- [38] U. Noomnarm *et al.*, “Fluorescence lifetimes: fundamentals and interpretations”, *Photosynthesis Research*, vol. 101, no. 2-3, pp. 181–194, Sep. 2009. DOI: 10.1007/s11120-009-9457-8.
- [39] J. Lee, *Bioluminescence, the nature of the light*. University of Georgia, Jun. 2017.
- [40] J. M. Richter *et al.*, “Enhancing photoluminescence yields in lead halide perovskites by photon recycling and light out-coupling”, *Nature Communications*, vol. 7, no. 1, p. 13941, Dec. 2016. DOI: 10.1038/ncomms13941.
- [41] D. W. DeQuilettes *et al.*, “Charge-carrier recombination in halide perovskites”, *Chemical Reviews*, pp. 11007–11019, Sep. 2019. DOI: 10.1021/acs.chemrev.9b00169.
- [42] T. W. Crothers *et al.*, “Photon reabsorption masks intrinsic bimolecular charge-carrier recombination in CH₃NH₃PbI₃ perovskite”, *Nano Letters*, vol. 17, no. 9, pp. 5782–5789, Sep. 2017. DOI: 10.1021/acs.nanolett.7b02834.
- [43] L. M. Pazos-Outón *et al.*, “Photon recycling in lead iodide perovskite solar cells”, *Science*, vol. 351, no. 6280, pp. 1430–1433, Mar. 2016. DOI: 10.1126/SCIENCE.AAF1168.

- [44] K. P. Goetz *et al.*, “Shining light on the photoluminescence properties of metal halide perovskites”, *Advanced Functional Materials*, vol. 30, no. 23, p. 1910004, 2020. DOI: 10.1002/adfm.201910004.
- [45] J. Bisquert, *The physics of solar cells : perovskites, organics, and photovoltaic fundamentals*. CRC Press, Nov. 2017.
- [46] T. Markvart *et al.*, “Principles of solar cell operation”, in *McEvoy’s Handbook of Photovoltaics: Fundamentals and Applications*, Academic Press, Jan. 2018, pp. 3–28. DOI: 10.1016/B978-0-12-809921-6.00001-X.
- [47] G. Rose, “Ueber einige neue Mineralien des Urals”, *Journal fur Praktische Chemie*, vol. 19, no. 1, pp. 459–468, Jan. 1840. DOI: 10.1002/prac.18400190179.
- [48] J. Breternitz *et al.*, “What defines a perovskite?”, *Advanced Energy Materials*, vol. 8, no. 34, p. 1802366, Dec. 2018. DOI: 10.1002/aenm.201802366.
- [49] T. Wolfram *et al.*, *Electronic and optical properties of d-band perovskites*. Cambridge University Press, 2006.
- [50] A. M. Glazer *et al.*, “The classification of tilted octahedra in perovskites”, *Acta Crystallographica Section B*, vol. 28, no. 11, pp. 3384–3392, Nov. 1972. DOI: 10.1107/S0567740872007976.
- [51] K. Momma *et al.*, “Vesta 3 for three-dimensional visualization of crystal, volumetric and morphology data”, *Journal of Applied Crystallography*, vol. 44, no. 6, pp. 1272–1276, Dec. 2011. DOI: 10.1107/S0021889811038970.
- [52] A. Kojima *et al.*, “Organometal halide perovskites as visible-light sensitizers for photovoltaic cells”, *Journal of the American Chemical Society*, vol. 131, no. 17, pp. 6050–6051, May 2009. DOI: 10.1021/ja809598r.
- [53] J.-H. Im *et al.*, “6.5% efficient perovskite quantum-dot-sensitized solar cell”, *Nanoscale*, vol. 3, no. 10, p. 4088, Oct. 2011. DOI: 10.1039/c1nr10867k.
- [54] L. Schmidt-Mende *et al.*, “Efficiency improvement in solid-state-dye-sensitized photovoltaics with an amphiphilic Ruthenium-dye”, *Applied Physics Letters*, vol. 86, no. 1, p. 013504, Jan. 2005. DOI: 10.1063/1.1844032.
- [55] H.-S. Kim *et al.*, “Lead iodide perovskite sensitized all-solid-state submicron thin film mesoscopic solar cell with efficiency exceeding 9%”, *Scientific Reports*, vol. 2, no. 1, p. 591, 2012. DOI: 10.1038/srep00591.
- [56] M. M. Lee *et al.*, “Efficient hybrid solar cells based on meso-superstructured organometal halide perovskites”, *Science*, vol. 338, no. 6107, pp. 643–647, Nov. 2012. DOI: 10.1126/science.1228604.

- [57] O. Malinkiewicz *et al.*, “Perovskite solar cells employing organic charge-transport layers”, *Nature Photonics*, vol. 8, no. 2, pp. 128–132, Dec. 2013. DOI: 10.1038/nphoton.2013.341.
- [58] M. Liu *et al.*, “Efficient planar heterojunction perovskite solar cells by vapour deposition”, *Nature*, vol. 501, no. 7467, pp. 395–398, Sep. 2013. DOI: 10.1038/nature12509.
- [59] J. Burschka *et al.*, “Sequential deposition as a route to high-performance perovskite-sensitized solar cells”, *Nature*, vol. 499, no. 7458, pp. 316–319, Jul. 2013. DOI: 10.1038/nature12340.
- [60] N. J. Jeon *et al.*, “Solvent engineering for high-performance inorganic–organic hybrid perovskite solar cells”, *Nature Materials*, vol. 13, no. 9, pp. 897–903, Sep. 2014. DOI: 10.1038/nmat4014.
- [61] N. J. Jeon *et al.*, “Compositional engineering of perovskite materials for high-performance solar cells”, *Nature*, vol. 517, no. 7535, pp. 476–480, Jan. 2015. DOI: 10.1038/nature14133.
- [62] Y. C. Kim *et al.*, “Beneficial effects of PbI₂ incorporated in organo-lead halide perovskite solar cells”, *Advanced Energy Materials*, vol. 6, no. 4, pp. 1–8, Feb. 2016. DOI: 10.1002/aenm.201502104.
- [63] M. Saliba *et al.*, “Incorporation of rubidium cations into perovskite solar cells improves photovoltaic performance.”, *Science*, vol. 354, no. 6309, pp. 206–209, Oct. 2016. DOI: 10.1126/science.aah5557.
- [64] W. S. Yang *et al.*, “Iodide management in formamidinium-lead-halide-based perovskite layers for efficient solar cells”, *Science*, vol. 356, no. 6345, pp. 1376–1379, Jun. 2017. DOI: 10.1126/science.aan2301.
- [65] G. Grancini *et al.*, “One-year stable perovskite solar cells by 2D/3D interface engineering”, *Nature Communications*, vol. 8, p. 15684, Jun. 2017. DOI: 10.1038/ncomms15684.
- [66] M. T. Weller *et al.*, “Complete structure and cation orientation in the perovskite photovoltaic methylammonium lead iodide between 100 and 352 K”, *Chemical Communications*, vol. 51, no. 20, pp. 4180–4183, Feb. 2015. DOI: 10.1039/C4CC09944C.
- [67] P. S. Whitfield *et al.*, “Structures, phase transitions and tricritical behavior of the hybrid perovskite methylammonium lead iodide”, *Scientific Reports*, vol. 6, no. 1, p. 35685, Dec. 2016. DOI: 10.1038/srep35685.
- [68] A. Walsh *et al.*, “Self-regulation mechanism for charged point defects in hybrid halide perovskites”, *Angewandte Chemie International Edition*, vol. 54, no. 6, pp. 1791–1794, Feb. 2015. DOI: 10.1002/anie.201409740.

- [69] R. A. Jishi *et al.*, “Modeling of lead halide perovskites for photovoltaic applications”, *The Journal of Physical Chemistry C*, vol. 118, no. 49, pp. 28 344–28 349, Dec. 2014. DOI: 10.1021/jp5050145.
- [70] T. Zhao *et al.*, “Intrinsic and extrinsic charge transport in $\text{CH}_3\text{NH}_3\text{PbI}_3$ perovskites predicted from first-principles”, *Scientific Reports*, vol. 7, p. 19 968, Jan. 2016. DOI: 10.1038/srep19968.
- [71] A. Buin *et al.*, “Halide-dependent electronic structure of organolead perovskite materials”, *Chemistry of Materials*, vol. 27, no. 12, pp. 4405–4412, Jun. 2015. DOI: 10.1021/acs.chemmater.5b01909.
- [72] A. Buin *et al.*, “Materials processing routes to trap-free halide perovskites”, *Nano Letters*, vol. 14, no. 11, pp. 6281–6286, Oct. 2014. DOI: 10.1021/nl502612m.
- [73] M. A. Green *et al.*, “Optical properties of photovoltaic organic-inorganic lead halide perovskites”, *The Journal of Physical Chemistry Letters*, vol. 6, no. 23, pp. 4774–4785, Dec. 2015. DOI: 10.1021/acs.jpcllett.5b01865.
- [74] E. Mosconi *et al.*, “First-principles modeling of mixed halide organometal perovskites for photovoltaic applications”, *The Journal of Physical Chemistry C*, vol. 117, no. 27, pp. 13 902–13 913, Jul. 2013. DOI: 10.1021/jp4048659.
- [75] D. Meggiolaro *et al.*, “Iodine chemistry determines the defect tolerance of lead-halide perovskites”, *Energy Environ. Sci.*, vol. 11, pp. 702–713, 3 2018. DOI: 10.1039/C8EE00124C.
- [76] W.-J. Yin *et al.*, “Unusual defect physics in $\text{CH}_3\text{NH}_3\text{PbI}_3$ perovskite solar cell absorber”, *Applied Physics Letters*, vol. 104, no. 6, p. 063 903, Feb. 2014. DOI: 10.1063/1.4864778.
- [77] M. H. Du, “Density functional calculations of native defects in $\text{CH}_3\text{NH}_3\text{PbI}_3$: Effects of spin - orbit coupling and self-interaction error”, *Journal of Physical Chemistry Letters*, vol. 6, no. 8, pp. 1461–1466, Apr. 2015. DOI: 10.1021/acs.jpcllett.5b00199.
- [78] E. Mosconi *et al.*, “Light-induced annihilation of Frenkel defects in organolead halide perovskites”, *Energy and Environmental Science*, vol. 9, no. 10, pp. 3180–3187, Oct. 2016. DOI: 10.1039/c6ee01504b.
- [79] D. Bryant *et al.*, “Light and oxygen induced degradation limits the operational stability of methylammonium lead triiodide perovskite solar cells”, *Energy & Environmental Science*, vol. 9, no. 5, pp. 1655–1660, 2016. DOI: 10.1039/C6EE00409A.
- [80] N. Aristidou *et al.*, “Fast oxygen diffusion and iodide defects mediate oxygen-induced degradation of perovskite solar cells”, *Nature Communications*, vol. 8, p. 15 218, May 2017. DOI: 10.1038/ncomms15218.

- [81] C.-T. Lin *et al.*, “Evidence for surface defect passivation as the origin of the remarkable photostability of unencapsulated perovskite solar cells employing aminovaleric acid as a processing additive”, *Journal of Materials Chemistry A*, vol. 7, no. 7, pp. 3006–3011, Feb. 2019. DOI: 10.1039/C8TA11985F.
- [82] S. Pont *et al.*, “Tuning $\text{CH}_3\text{NH}_3\text{Pb}(\text{I}_{1-x}\text{Br}_x)_3$ perovskite oxygen stability in thin films and solar cells”, *Journal of Materials Chemistry A*, vol. 5, no. 20, pp. 9553–9560, 2017. DOI: 10.1039/C7TA00058H.
- [83] K. Jemli *et al.*, “Using low temperature photoluminescence spectroscopy to investigate $\text{CH}_3\text{NH}_3\text{PbI}_3$ hybrid perovskite degradation”, *Molecules*, vol. 21, no. 7, p. 885, Jul. 2016. DOI: 10.3390/molecules21070885.
- [84] R. Brenes *et al.*, “The impact of atmosphere on the local luminescence properties of metal halide perovskite grains”, *Advanced Materials*, vol. 30, no. 15, p. 1706208, Apr. 2018. DOI: 10.1002/adma.201706208.
- [85] N. Aristidou *et al.*, “Insights into the increased degradation rate of $\text{CH}_3\text{NH}_3\text{PbI}_3$ solar cells in combined water and O_2 environments”, *Journal of Materials Chemistry A*, vol. 5, no. 48, pp. 25469–25475, Dec. 2017. DOI: 10.1039/c7ta06841g.
- [86] A. Aziz *et al.*, “Understanding the enhanced stability of bromide substitution in lead Iodide perovskites”, *Chemistry of Materials*, vol. 32, no. 1, pp. 400–409, Jan. 2020. DOI: 10.1021/acs.chemmater.9b04000.
- [87] J. Haruyama *et al.*, “Termination dependence of tetragonal $\text{CH}_3\text{NH}_3\text{PbI}_3$ surfaces for perovskite solar cells”, *The Journal of Physical Chemistry Letters*, vol. 5, no. 16, pp. 2903–2909, Aug. 2014. DOI: 10.1021/jz501510v.
- [88] J. S. Godding *et al.*, “Oxidative passivation of metal halide perovskites”, *Joule*, vol. 3, no. 11, pp. 2716–2731, 2019. DOI: 10.1016/j.joule.2019.08.006.
- [89] E. V. Péan *et al.*, “Investigating the superoxide formation and stability in mesoporous carbon perovskite solar cells with an aminovaleric acid additive”, *Advanced Functional Materials*, p. 1909839, Feb. 2020. DOI: 10.1002/adfm.201909839.
- [90] U.-G. Jong *et al.*, “Influence of water intercalation and hydration on chemical decomposition and ion transport in methylammonium lead halide perovskites”, *J. Mater. Chem. A*, vol. 6, pp. 1067–1074, 3 2018. DOI: 10.1039/C7TA09112E.
- [91] C. Müller *et al.*, “Water Infiltration in Methylammonium Lead Iodide Perovskite: Fast and Inconspicuous”, *Chemistry of Materials*, vol. 27, no. 22, pp. 7835–7841, Nov. 2015. DOI: 10.1021/acs.chemmater.5b03883.
- [92] A. Leguy *et al.*, “Reversible hydration of $\text{CH}_3\text{NH}_3\text{PbI}_3$ in films, single crystals and solar cells”, *Chemistry of Materials*, vol. 27, pp. 3397–3407, 2015. DOI: 10.1021/acs.chemmater.5b00660.

- [93] F. Hao *et al.*, “Controllable perovskite crystallization at a gas–solid interface for hole conductor-free solar cells with steady power conversion efficiency over 10%”, *Journal of the American Chemical Society*, vol. 136, no. 46, pp. 16411–16419, Nov. 2014. DOI: 10.1021/ja509245x.
- [94] J. Yang *et al.*, “Investigation of CH₃NH₃PbI₃ degradation rates and mechanisms in controlled humidity environments using *in situ* techniques”, *ACS Nano*, vol. 9, no. 2, pp. 1955–1963, Feb. 2015. DOI: 10.1021/nm506864k.
- [95] J. A. Christians *et al.*, “Transformation of the excited state and photovoltaic efficiency of CH₃NH₃PbI₃ perovskite upon controlled exposure to humidified air”, *Journal of the American Chemical Society*, vol. 137, no. 4, pp. 1530–1538, Feb. 2015. DOI: 10.1021/ja511132a.
- [96] Z. Andaji-Garmaroudi *et al.*, “Photobrightening in lead halide perovskites: Observations, mechanisms, and future potential”, *Advanced Energy Materials*, vol. 10, no. 13, p. 1903109, 2020. DOI: 10.1002/aenm.201903109.
- [97] S. G. Motti *et al.*, “Controlling competing photochemical reactions stabilizes perovskite solar cells”, *Nature Photonics*, p. 1, May 2019. DOI: 10.1038/s41566-019-0435-1.
- [98] D. Meggiolaro *et al.*, “Modeling the interaction of molecular iodine with mapbi₃: A probe of lead-halide perovskites defect chemistry”, *ACS Energy Letters*, vol. 3, no. 2, pp. 447–451, Feb. 2018. DOI: 10.1021/acsenergylett.7b01244.
- [99] D. W. DeQuilettes *et al.*, “Photo-induced halide redistribution in organic–inorganic perovskite films”, *Nature Communications*, vol. 7, no. May, p. 11683, May 2016. DOI: 10.1038/ncomms11683.
- [100] W. Li *et al.*, “Hole trapping by iodine interstitial defects decreases free carrier losses in perovskite solar cells: A time-domain ab initio study”, *ACS Energy Lett.*, vol. 2, no. 6, pp. 1270–1278, Jun. 2017. DOI: 10.1021/acsenergylett.7b00183.
- [101] J. F. Verwey, *Photochemical Processes in lead halides*. Bronder-Offset (Goudsesingel 260), 1967.
- [102] A. J. Ramadan *et al.*, “Processing solvent-dependent electronic and structural properties of cesium lead triiodide thin films”, *J. Phys. Chem. Lett.*, vol. 8, no. 17, pp. 4172–4176, Sep. 2017. DOI: 10.1021/acs.jpcllett.7b01677.

- [103] H. Cho *et al.*, “Overcoming the electroluminescence efficiency limitations of perovskite light-emitting diodes”, *Science*, vol. 350, no. 6265, pp. 1222–1225, 2015. DOI: 10.1126/science.aad1818. eprint: <https://science.sciencemag.org/content/350/6265/1222.full.pdf>.
- [104] Y. Chen *et al.*, “Mechanism of PbI₂ in situ passivated perovskite films for enhancing the performance of perovskite solar cells”, *ACS Applied Materials & Interfaces*, vol. 11, no. 47, pp. 44 101–44 108, Nov. 2019. DOI: 10.1021/acsami.9b13648.
- [105] B. Shi *et al.*, “Unraveling the passivation process of PbI₂ to enhance the efficiency of planar perovskite solar cells”, *The Journal of Physical Chemistry C*, vol. 122, no. 37, pp. 21 269–21 276, Sep. 2018. DOI: 10.1021/acs.jpcc.8b08075.
- [106] G. Y. Kim *et al.*, “Large tunable photoeffect on ion conduction in halide perovskites and implications for photodecomposition”, *Nature Materials*, vol. 17, no. 5, pp. 445–449, 2018.
- [107] S. Wang *et al.*, “Accelerated degradation of methylammonium lead iodide perovskites induced by exposure to iodine vapour”, *Nature Energy*, vol. 2, no. 1, p. 16 195, Jan. 2017. DOI: 10.1038/nenergy.2016.195.

Chapter 2

Experimental details

General experimental techniques are reported in this chapter. Detailed description of the materials, samples, experimental parameters and methodology used are given in the relevant result chapters.

Contents

2.1	Ultraviolet-visible absorption spectroscopy	63
2.2	Photoluminescence spectroscopy	64
2.2.1	Fluorometry	64
2.2.2	Fluorescence microscopy	65
2.2.3	Time-correlated single photon counting	67
2.3	Microscopy and images analysis	68
2.4	X-ray diffractometry	68
2.5	Profilometry and power measurements	70
2.6	Data analysis	70
2.6.1	Data post-processing	70
2.6.2	Error and averaging	71
2.6.3	Curve fitting	72
2.6.4	Background subtraction	72
2.7	References	73

2.1 Ultraviolet-visible absorption spectroscopy

A *Perkin Elmer Lambda 750* and *Lambda 9* ultraviolet-visible (UV-Vis) spectrophotometers were used in this work. Both instruments use a double grating monochromator to filter deuterium and tungsten halogen light sources [1]. The beam is split into two parts, one used as a reference and one used for measuring the sample properties, both measured by *Hamamatsu R928* PMTs [1]. Total reflectance R and transmittance T were measured with the *Lambda 750* with a 100 mm integrating sphere (Figure 2.1). Custom *Labsphere spectralon* mask were used to reduce the aperture of the integrating sphere in order to measure small samples. Prior to the measurements, 100 % and 0 % baselines were carried out. The total absorbance A was calculated with:

$$A = 1 - R - T \quad (2.1)$$

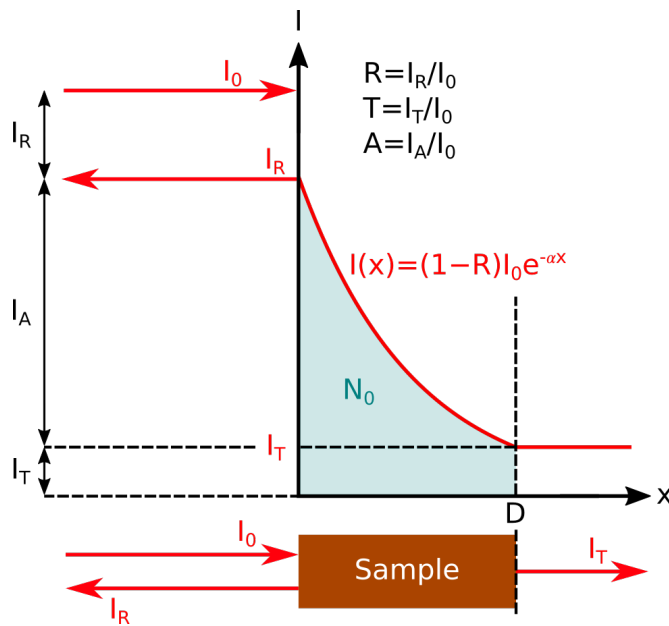


Figure 2.1: Schematic of the intensity reflected (I_R), transmitted (I_T) and absorbed (I_A) in a sample of thickness D upon incidence of a beam of intensity I_0 . After reflection, the intensity exponentially decreases in the sample (the sample is assumed homogeneous and reflection inside it are negligible). R is the reflectance, T is the transmittance, A is the absorbance and α is the absorption coefficient.

The absorption coefficient α is defined as:

$$\alpha = -\frac{1}{D} \log_e \left(\frac{T}{1-R} \right) \quad (2.2)$$

The absorbance \mathbf{A} is defined as:

$$\mathbf{A} = -\log_{10}(T) \quad (2.3)$$

It is worth noting that scattering can lead to losses of light which are not accounted in the reflected, transmitted or absorbed light. The amount of scattered light highly depends on the sample morphology and thickness.

2.2 Photoluminescence spectroscopy

2.2.1 Fluorometry

In this work, a *Horiba Fluoromax-4* and *Edinburgh Instruments FS5* steady-state spectrofluorometers were used to measure PL. The samples were continuously illuminated with an excitation wavelength λ_{exc} selected from a 150 W ozone-free xenon arc lamp source (**Figure 2.2**) and the PL intensity was measured at wavelength λ_{em} . The excitation slitwidth $\Delta\lambda_{exc}$ determines the width of the excitation peak while the emission slitwidth $\Delta\lambda_{em}$ determines the range of wavelength around the emission wavelength over which the PL intensity is averaged *i.e.*:

$$I(\lambda_{em}) = \int_{\lambda_{em}-\Delta\lambda_{em}/2}^{\lambda_{em}+\Delta\lambda_{em}/2} I(\lambda) \cdot d\lambda \quad (2.4)$$

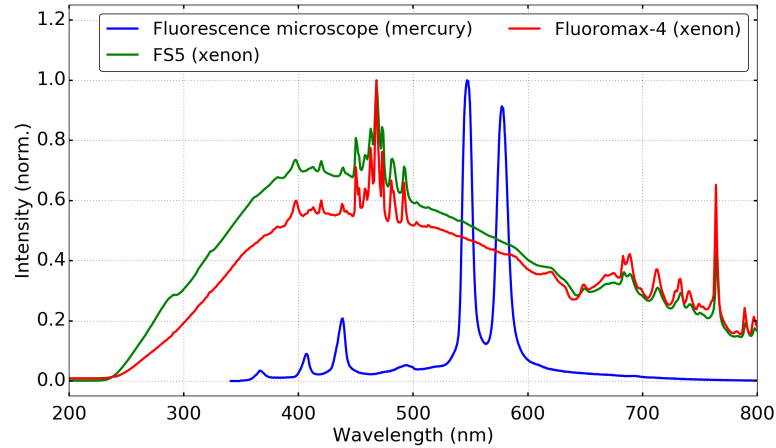


Figure 2.2: Emission spectra of the different lamps used.

Both *Fluoromax-4* and *FS5* use Czerny-Turner monochromators with 1200 grooves/nm gratings to select the excitation and emission wavelengths (**Figure 2.3**) [2], [3]. An *Hamamatsu R928P* photomultiplier tube (PMT) and a photodiode measure the sample emission intensity and the reference excitation intensity respectively [2], [3]. The reference and emission signals were respectively corrected for the lamp intensity and PMT sensitivity using corrections provided by the manufacturers. The instruments were calibrated using the water Raman peak at 397 nm.

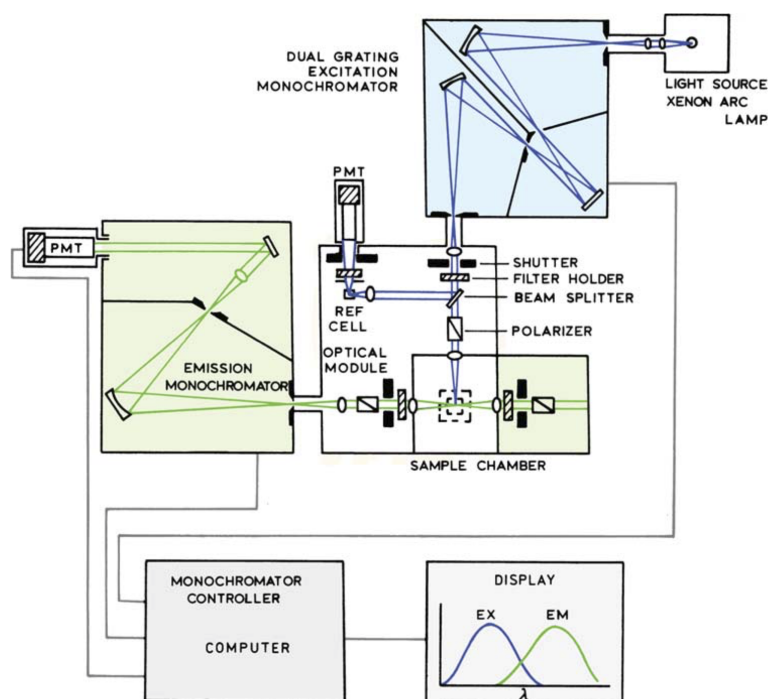


Figure 2.3: Schematic diagram of a spectrofluorometer. The excitation wavelength is selected from the xenon lamp emission using a monochromator and is then split into two beams. One is used as a reference to measure the excitation intensity while the second excites the sample. The sample emission is selected with a monochromator and its intensity is measured using a photomultiplier tube (PMT). From [4].

2.2.2 Fluorescence microscopy

The fluorescence microscopy setup used in this work was constituted of an *Olympus BX51* microscope complemented with an *Olympus U-LH100HG* mercury light source (powered by an *Olympus U-RFL-T* power supply) (**Figure 2.4a**). An excitation wavelength of $\lambda_{exc} = 559$ nm ($\Delta\lambda_{exc} = \pm 17$ nm) was obtained using a *Thorlabs MF559-34* excitation filter, a *Thorlabs FGL665* emission filter and a *Thorlabs MD588* dichroic mirror (**Figure 2.4b**, unfiltered lamp spectra is shown in **Figure 2.2**).

As per the Abbe diffraction limit, this excitation wavelength limits the resolution to *ca.* 200 nm. An *Olympus XC10* camera placed on top of the microscope was used to capture and record videos of the sample PL. An *OceanOptics USB2000+* spectrophotometer in one of the eyepieces recorded the PL emission spectra. An *ASEQ LRI* spectrophotometer placed underneath the sample holder was used to measure the transmitted intensity of the excitation light. Measurements in N₂ atmosphere were performed using a *Linkam THMS600* environmental chamber coupled with a *Brooks 1250 Sho Rate* flowmeter. For measurements in ambient atmosphere, an *EasyLog EL-USB-2LCD* was used to record the temperature and humidity of the room.

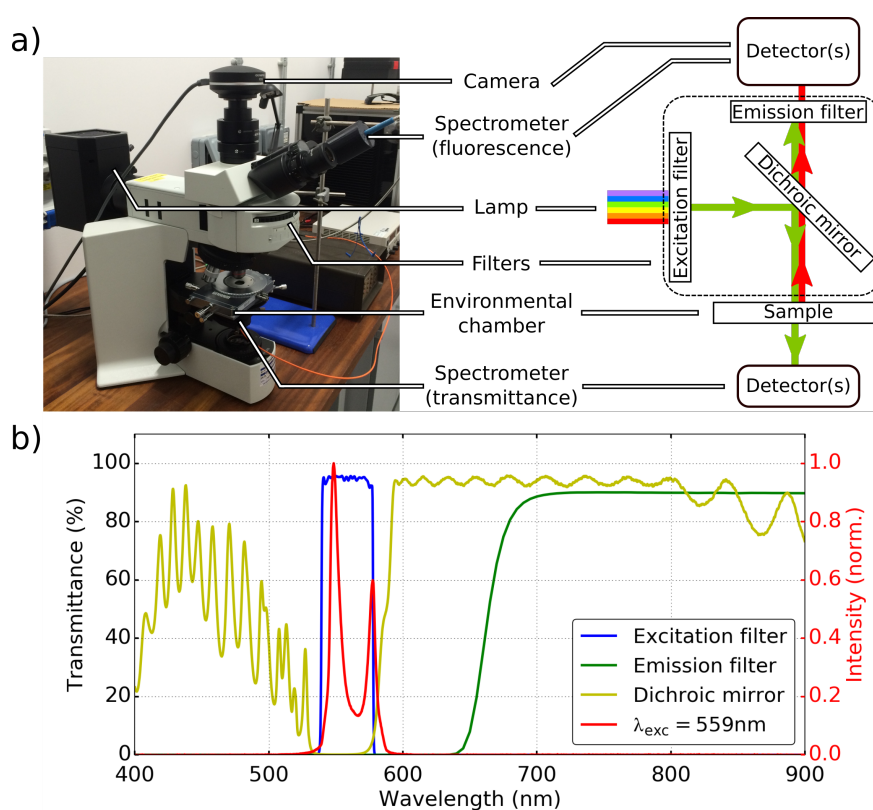


Figure 2.4: Fluorescence microscopy setup. **a)** Photography and schematic of the setup. The excitation wavelength is selected from a mercury light source using a band-pass filter. The light beam is then reflected by a dichroic mirror and is focused on the sample. The PL and some of the excitation light reflected by the sample go through a dichroic mirror and are filtered using a band-pass filter to remove the reflected excitation light. **b)** Transmittance of the filters used and corresponding filtered lamp spectrum (red curve).

2.2.3 Time-correlated single photon counting

An *Edinburgh Instruments Lifespec II* time-correlated single photon counting (TCSPC) operating in reverse mode was used with an *Edinburgh Instruments EPL405* picoseconds pulsed diode laser ($\lambda_{exc} = 405$ nm, $\Delta\lambda_{exc} = \pm 5$ nm, energy per pulse 9.46 pJ for a laser repetition period $RP = 1 \mu s$, pulse width ~ 62.7 ps, as provided by the manufacturer) (**Figure 2.5**). The sample emission is measured using a double monochromator and a *Hamamatsu* micro-channel plate PMT. More details about this instrument and the measurement methodology are given in **Chapter 4**.

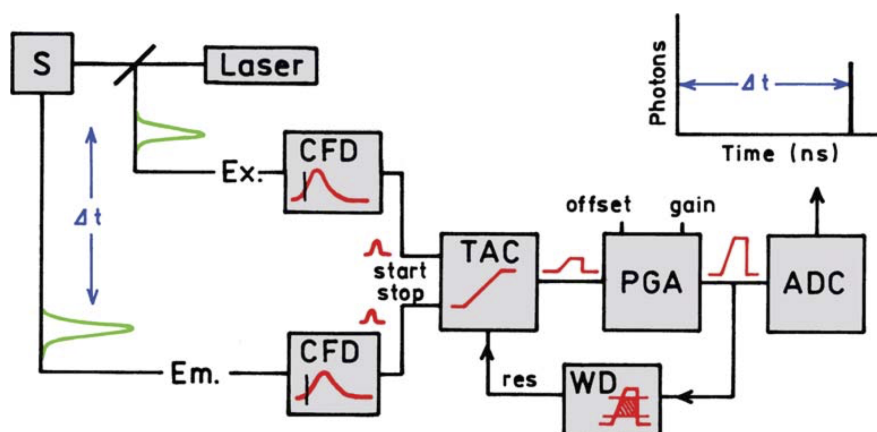


Figure 2.5: Schematic principle of time-correlated single photon counting. The short laser pulse is measured by a constant function discriminator (CFD) which starts a linear voltage ramp controlled by a time-to-amplitude-converter (TAC). When an emitted photon from the sample is measured by the CFD after a certain time, the voltage ramp increase is stopped [4]. The measured voltage difference may then be amplified by a programmable gain amplifier (PGA) while a window discriminator (WD) prevents false reading by limiting the range of the voltage. Finally, an analog-to-digital converter (ADC) converts the voltage signal to the time difference between the excitation pulse and the emission of a photon from the material. The TAC requires a short amount of time to reset after measuring a photon. Therefore, at high excitation repetition rates (*i.e.* short excitation repetition period), some of the excitation pulse events may be ignored by the TAC. This can be solved by operating in reverse mode during which the emission pulse starts the TAC while the excitation pulse stops it. Since *ca.* 1 emitted photon per 100 excitation pulse is measured, the time between two consecutive emitted photons is long enough for the TAC to reset. From [4].

2.3 Microscopy and images analysis

Optical microscopy was performed using an *Olympus BH2* bright field microscope coupled with a *Canon EOS 6D* camera. Surface coverage was calculated from the images using thresholding (**Figure 2.6**). Scanning electron microscopy (SEM) and energy dispersive X-ray spectroscopy (EDX) were carried using a *Zeiss Evo LS25* electron microscope. Because the contrast of electron microscopy images depends on orientation of the grains with respect to the electron beam, thresholding cannot be applied to distinguish grains situated in parallel plans. Instead, grains surface coverage from SEM images was calculated using the *Zeiss ZEN Intellesis trainable image segmentation* software (**Figure 2.6**).

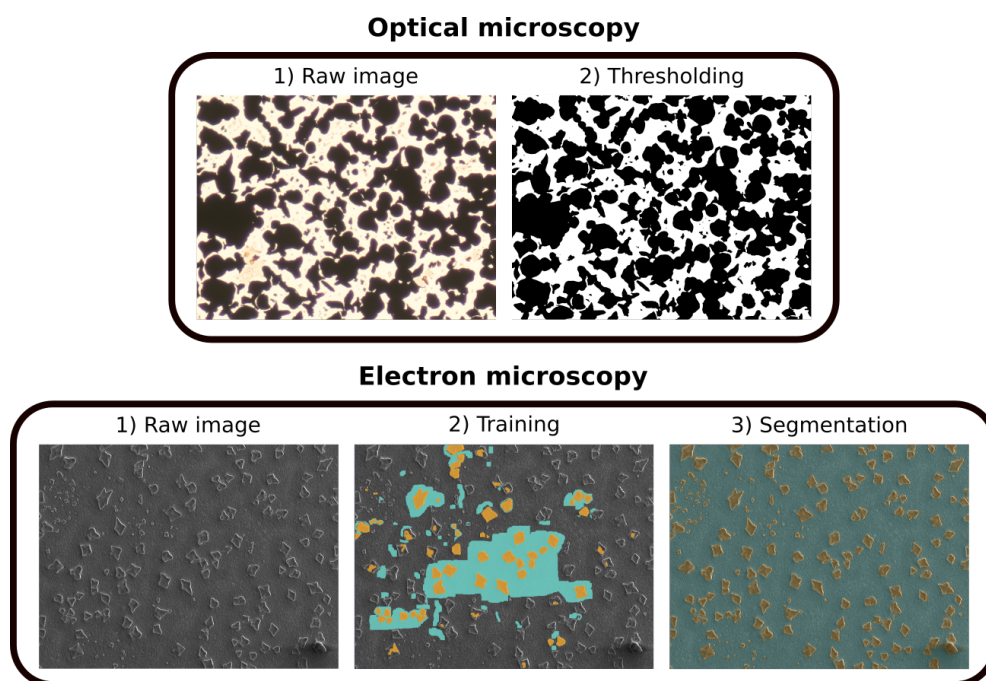


Figure 2.6: Optical microscopy image thresholding and electron microscopy image segmentation processes. The *Zeiss trainable image segmentation* software was trained to distinguish larger grains (yellow) and smaller grains (green).

2.4 X-ray diffractometry

XRD and grazing incidence XRD (GIXRD) measurements were carried using a *Bruker D8 Discover* diffractometer. X-rays of wavelength $\lambda = 1.5418 \text{ \AA}$ from a copper source were focused onto the samples with a Goebel mirror and measured with an angular opening of 2.17° . As per Bragg's law, constructive interferences of the X-rays can be related to the plans formed by the sample crystal structure (**Figure 2.7**).

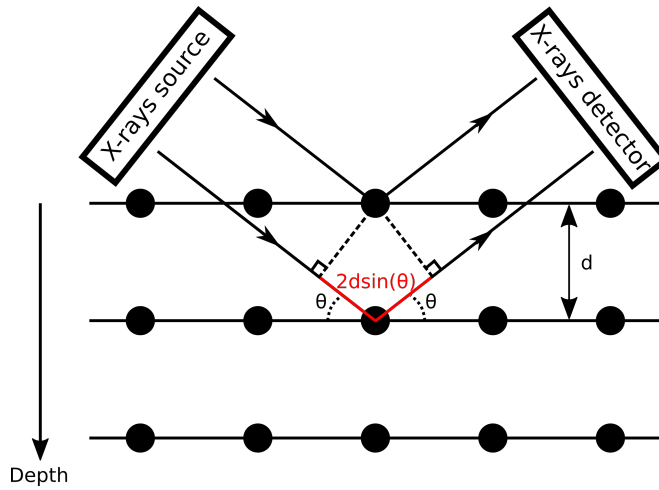


Figure 2.7: Schematic of Bragg's diffraction. The interference between the two X-rays is constructive when the path difference $2d \sin(\theta)$ is equal to a multiple of the wavelength of the X-rays.

The interference between two X-rays incident with an angle θ on two atomic planes separated by a distance d is constructive when the path difference $2d \sin(\theta)$ is proportional to the wavelength of the X-rays λ :

$$2d \sin(\theta) = m \cdot \lambda \quad (2.5)$$

where m is an integer. The peaks observed in a diffraction pattern thus correspond to the distance between two parallel atomic planes. The crystallite domain mean size L was estimated using the Scherrer equation [5]:

$$L = K \frac{\lambda}{FWHM \cdot \cos(\theta)} \quad (2.6)$$

where K is a shape factor whose value is close to unity. The Scherrer equation is only valid for domains smaller than $0.1 \mu\text{m}$ and negligible broadening of the FWHM originating from the instrument and strains in the sample is assumed. The weight ratio of mixed compounds A and B can be estimated through the ratio of the intensities of the peaks associated with these compounds [6]:

$$\frac{I_A}{I_B} \propto \frac{w_A}{w_B} \quad (2.7)$$

where w_A (w_B) is the weight of compound A (B) and I_A (I_B) is the intensity of the peak associated with compound A (B). *in situ* illumination of the samples was carried using a *LedLenser M7R* torch (**Figure 2.8**).

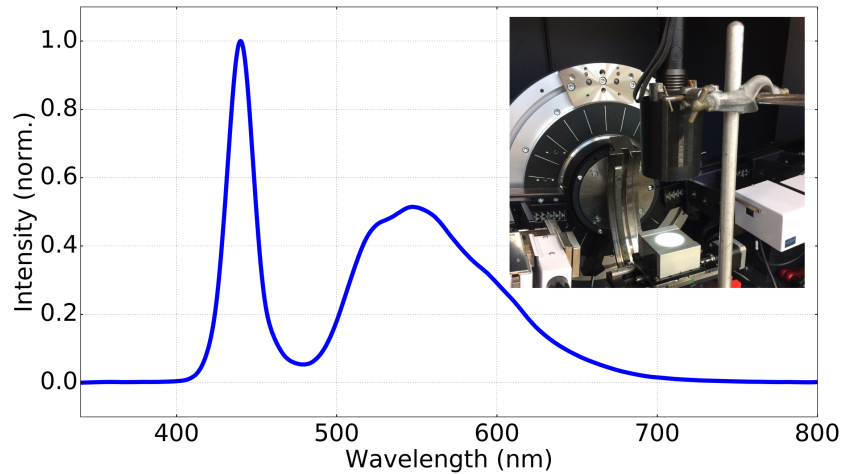


Figure 2.8: Emission spectra of the *LedLenser M7R* torch. Inset: experimental setup. The light of the torch was focused onto the sample using a lens and a 3D printed frame.

2.5 Profilometry and power measurements

A *Dektak 6M* profilometer operating in contact mode was used to measure the thickness of thin-films.

The power of the various light sources used in this work was measured with a *Thorlabs PM100D* power meter and a *Thorlabs S410C* sensor.

2.6 Data analysis

2.6.1 Data post-processing

Data processing and analysis were carried using Python [7], and the Matplotlib [8], Scipy [9], Numpy [10], Scikit-image [11] and Open-CV [12] packages. The Savitzky-Golay [13] filter was used to smooth the measured data (**Figure 2.9a**). The FWHM was calculated by 1) finding the peak maximum 2) finding the peak minimum on each side of the peak 3) calculating the half height of the peak for each and 4) finding the point closest to this value on each side. In some cases, cubic interpolation was used to improve the determination of the curve maximum point (**Figure 2.9c**) and linear interpolation was used for the FWHM calculation (**Figure 2.9b**). Area under a curve was calculated using the trapezoidal rule (**Figure 2.9d**). The background area was calculated from the first and last point and was subtracted from the total area to obtain the curve area.

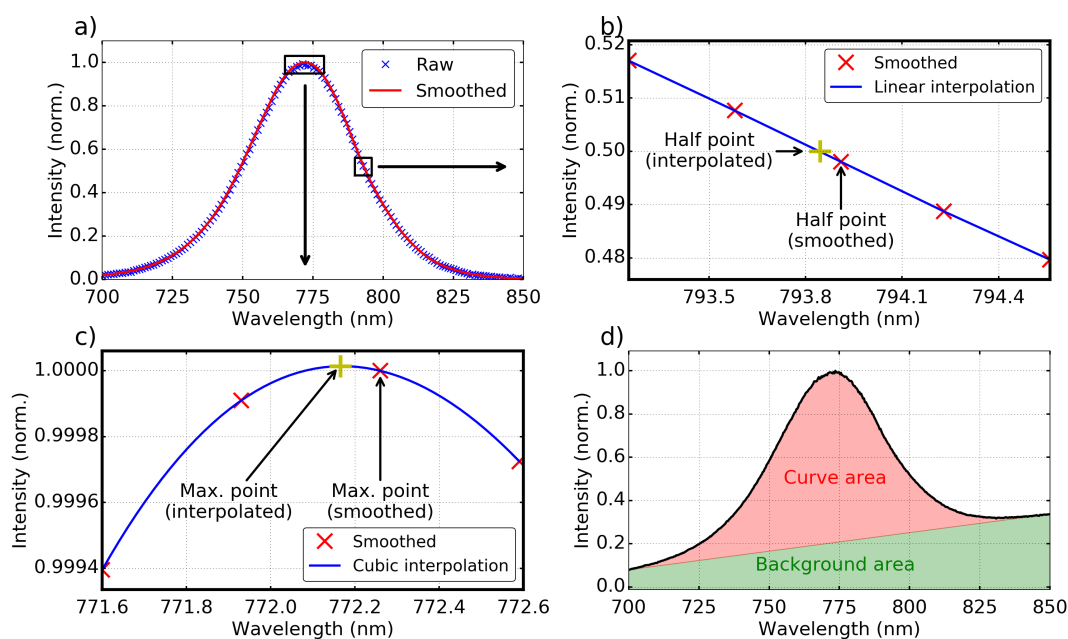


Figure 2.9: Data post-processing **a)** Smoothing using a Savitzky-Golay filter, **b)** linear interpolation of the half intensity point, **c)** cubic interpolation of the maximum intensity point and **d)** area calculation.

2.6.2 Error and averaging

In order to ensure reproducibility of the results, most experiments were repeated multiple times on identical samples. In this work, the error of a measurement is displayed as a coloured area calculated from the maxima and minima of all the repeats of the same experiment (**Figure 2.10**).

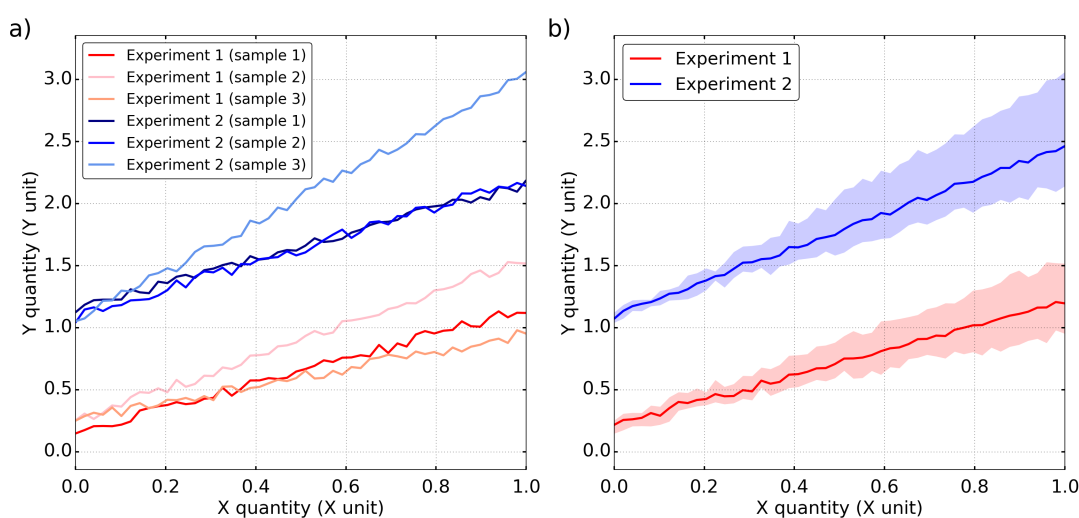


Figure 2.10: **a)** Distinct signal for each sample of two different experiments and **b)** corresponding signals where the average is shown as a solid curve and the error is displayed by the associated coloured area.

2.6.3 Curve fitting

Curve fitting was carried using the least-square method. For a dataset containing M curves, each containing N points, the residue SS_{res} is:

$$SS_{res} = \sum_i^M \sum_j^N (y_j^i - F(x_j, A_i))^2 \quad (2.8)$$

where y_j^i is the intensity associated with x_j of curve i , F is the fit model and A_i are the parameters associated with curve i . The quality of the fit is estimated using the coefficient of determination R^2 :

$$R^2 = 1 - \frac{SS_{res}}{SS_{total}} \quad (2.9)$$

where SS_{total} is the sum of the squared difference between each point and the average of all the curves \bar{y} :

$$SS_{total} = \sum_i^M \sum_j^N (y_n^i - \bar{y})^2 \quad (2.10)$$

2.6.4 Background subtraction

Background intensity was removed using two methods:

1. Average baseline: the average intensity over a range of point is taken as the background intensity and the whole curve is negatively shifted by this amount (**Figure 2.11a**).
2. Linear baseline: the intensity measured at two points is used to calculate a linear baseline which is then subtracted to the data (**Figure 2.11b**).

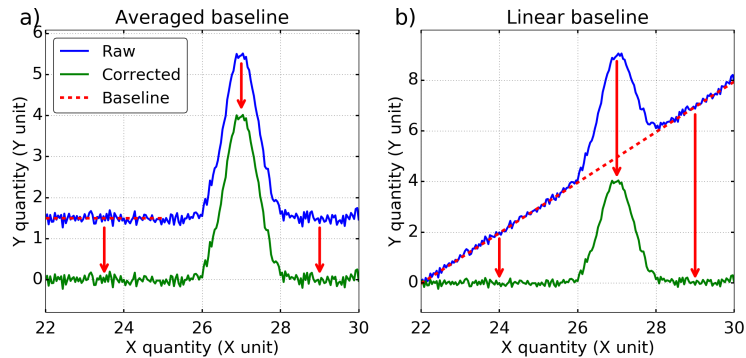


Figure 2.11: Example of an **a**) averaged baseline calculated between $X = 22$ and $X = 25$, and **b**) linear baseline calculated at $X = 22$ and $X = 30$.

2.7 References

- [1] Perkin Elmer. (2007). Lambda 750 UV/Vis/NIR spectrophotometer, [Online]. Available: https://www.perkinelmer.com/lab-solutions/resources/docs/BRO_LAMBDA-750-UV-Brochure.pdf (visited on 26/02/2020).
- [2] HORIBA. (2012). FluoroMax-4 & FluoroMax-4P with USB operation manual, [Online]. Available: https://www.horiba.com/fileadmin/uploads/Scientific/Downloads/UserArea/Fluorescence/Manuals/FluoroMax4_4P_Manual_USB.pdf (visited on 26/02/2020).
- [3] Edinburgh Instruments. (2015). FS5 spectrofluorometer features, [Online]. Available: https://www.edinst.com/wp-content/uploads/2015/07/FS5-Datasheet_Technical-Specification.pdf (visited on 26/02/2020).
- [4] J. R. Lakowicz, *Principles of fluorescence spectroscopy*. Boston, MA: Springer US, 2006. DOI: 10.1007/978-0-387-46312-4.
- [5] P. Scherrer, “Bestimmung der grÖÙe und der inneren struktur von kolloidteilchen mittels röntgenstrahlen”, *Nachrichten von der Gesellschaft der Wissenschaften zu Göttingen, Mathematisch-Physikalische Klasse*, vol. 1918, pp. 98–100, 1918.
- [6] A. Monshi *et al.*, “Ratio of slopes method for quantitative X-ray diffraction analysis”, *Journal of Materials Science*, vol. 26, no. 13, pp. 3623–3627, 1991. DOI: 10.1007/BF00557154.
- [7] G. V. Rossum *et al.*, “Python tutorial”, Centrum voor Wiskunde en Informatica, Tech. Rep., May 1995.
- [8] J. D. Hunter, “Matplotlib: a 2D graphics environment”, *Computing in Science & Engineering*, vol. 9, no. 3, pp. 90–95, 2007. DOI: 10.1109/MCSE.2007.55.
- [9] P. Virtanen *et al.*, “SciPy 1.0: fundamental algorithms for scientific computing in Python”, *Nature Methods*, vol. 17, pp. 261–272, 2020. DOI: <https://doi.org/10.1038/s41592-019-0686-2>.
- [10] S. Van Der Walt *et al.*, “The NumPy array: a structure for efficient numerical computation”, *Computing in Science and Engineering*, vol. 13, no. 2, pp. 22–30, Mar. 2011. DOI: 10.1109/MCSE.2011.37.
- [11] S. van der Walt *et al.*, “Scikit-image: image processing in Python”, *PeerJ*, vol. 2, e453, Jun. 2014. DOI: 10.7717/peerj.453.
- [12] G. Bradski, “The OpenCV Library”, *Dr. Dobb’s Journal of Software Tools*, 2000.

- [13] A. Savitzky *et al.*, “Smoothing and differentiation of data by simplified least squares procedures”, *Analytical Chemistry*, vol. 36, no. 8, pp. 1627–1639, Jul. 1964. DOI: 10.1021/ac60214a047.

Chapter 3

Optical properties of methylammonium lead iodide thin-films

Contents

3.1	Introduction	76
3.2	Methodology	77
3.2.1	Sample fabrication	77
3.2.2	Photoluminescence spectroscopy	77
3.2.3	X-ray diffractometry	78
3.2.4	Absorbance spectroscopy and optical microscopy	79
3.3	Results and discussions	79
3.3.1	Photoluminescence properties of methylammonium lead iodide	79
3.3.2	Crystallographic properties of methylammonium lead iodide	85
3.4	Conclusion	88
3.5	References	89

3.1 Introduction

Photobrightening and photodarkening (the increase and decrease of the PL of a sample induced by illumination, respectively) have been observed numerous times in perovskite materials, in ambient, O₂, N₂ and vacuum environments [1]–[6]. Their intensity and trend appears to be highly dependent on the sample studied (*e.g.* perovskite chemical structure and fabrication method) and the measurement conditions (*e.g.* atmosphere, excitation wavelength, excitation fluence and excitation repetition rate) [1], [6]–[8]. Photobrightening is believed to be caused by the passivation of defects-induced trap states which can mediate non-radiative charge carrier recombination. Multiple processes have been proposed to explain photobrightening: passivation through superoxide formation [9] (**Section 1.4.2A**), Frenkel pair annihilation [8] (**Section 1.4.2C**), uncoordinated lead passivation [10] (**Section 1.4.2F**) and moisture degradation [11]–[13] (**Section 1.4.2B**). Photodarkening is believed to be caused by the formation of trap states through lead iodide photolysis [7] (**Section 1.4.2E**), formation of uncoordinated lead and iodide vacancies [10], [14] (**Section 1.4.2D**), iodine diffusion-mediated defect formation [8] (**Section 1.4.2G**) and the general degradation of the perovskite by moisture and oxygen [12] (**Sections 1.4.2A & B**). The kinetic between photodarkening and photobrightening can be controlled by favouring some processes over other. For example, high repetition rates can lead to photodarkening due to the favoured formation of I₂ compared to the annihilation of iodide Frenkel pairs [8]. Similarly, excitation energies lower than the PbI₂ photolysis energy have been shown to lead to photobrightening while higher energies lead to photodarkening [8]. Photobrightening and photodarkening thus appear intrinsically linked, however it is not clear if these processes and perovskite degradation happen simultaneously or sequentially.

In this chapter, the photobrightening and photodarkening kinetics are investigated by monitoring the PL and XRD pattern of MAPI thin-films over time under continuous illumination. The PL properties measured with a fluorescence microscope in ambient and N₂ atmospheres are first discussed. This is then compared to the degradation kinetic measured in ambient atmosphere under illumination using *in situ* XRD.

3.2 Methodology

A description of the samples, as well as the experimental procedures used in this chapter is given here. More details about the instruments used can be found in **Chapter 2**.

3.2.1 Sample fabrication

The MAPI precursor solution was prepared from a 1.25 : 1.25 M solution of lead iodide (PbI_2 , *Sigma-Aldrich* 99 %) and methylammonium iodide (MAI, *Dyesol*) in 4:1 (v:v) dimethylformamide (DMF, *Sigma-Aldrich*, ≥ 99.8 %): dimethylsulfoxide (DMSO, *Sigma-Aldrich*, ≥ 99.9 %) in a N_2 glovebox. The solution was heated at 60°C until dissolution and then filtered with a $0.45\ \mu\text{m}$ polytetrafluoroethylene (PTFE) filter. Glass substrates were cleaned using *Hellmanex III*, acetone and isopropanol consecutively. The substrates were cleaned in a O_2 plasma for 5 min just before spin-coating to improve the wetting of the substrate surface. For each sample, $100\ \mu\text{L}$ of MAPI precursor solution was spin-coated at 4000 rpm (4000 rpm/s acceleration) for 30 s on the glass substrate in a N_2 glovebox. Finally, the films were annealed at 100°C for 10 min on a hotplate. These samples are not representative of the state of the art which uses an anti-solvent method in order to improve the crystallisation of the perovskite [15]. However, such fabrication step highly increases variability of the samples obtained and was therefore ignored in order to improve reproducibility. The samples were carefully kept in N_2 atmosphere, in the dark and over a short period of time between manufacturing and the measurements in order to avoid any changes to their properties from exposure to oxygen, moisture, light, or intrinsic processes.

3.2.2 Photoluminescence spectroscopy

PL of the samples was measured from the sample's film side with excitation through the same side.

In **Section 3.3.1**, PL measurements were carried out with an *Olympus BX51* microscope with an excitation wavelength of $\lambda_{exc} = 559\ \text{nm}$ ($\Delta\lambda_{exc} = \pm 17\ \text{nm}$) and a 4 X magnification (power $P \sim 200\ \text{mW}/\text{cm}^2$) (a 50 X magnification with power $P \sim 33\ \text{W}/\text{cm}^2$ was used in **Figure 3.1**) (see **Section 2.2.2** for more details). The

emission spectrum was measured using an *OceanOptics USB2000+* spectrophotometer every 4 s with a 4 s integration time. The PL spectra were corrected with the fluorescence microscope filter transmittance. The background intensity was removed using an averaged baseline calculated between 670 nm and 675 nm (see **Section 2.6.1** for more details) and the spectra were then smoothed using a Savitzky-Golay filter. The peak maximum and the FWHM were calculated as described in **Section 2.6.1** using cubic and linear interpolation. The transmitted excitation light spectrum was measured with an *ASEQ LRI* spectrophotometer every 4 s with a 2 s integration time. Due to incomplete filtering of the excitation light by the microscope filters, some of it was measured in the spectra measured with the *OceanOptics UBS2000+* spectrophotometer and was used to monitor the sample reflectance. The reflected (I_R) and transmitted (I_T) intensity were calculated from the reflected and transmitted excitation light at 576.3 nm. A *Linkam THMS600* environmental chamber coupled with a *Brooks 1250 Sho Rate* flowmeter were used to measure samples in N_2 atmosphere.

In **Section 3.3.2**, the PL was measured between 650 nm and 850 nm every 23 min with a *Horiba Fluoromax-4* with an excitation wavelength of $\lambda_{exc} = 530$ nm ($\Delta\lambda_{exc} = \pm 1$ nm, $\Delta\lambda_{em} = \pm 1$ nm, 0.2 nm step, 0.1 s integration time, $P \sim 0.13$ mW/cm²). Spectra were smoothed with a Savitzky-Golay filter.

3.2.3 X-ray diffractometry

XRD and GIXRD patterns were collected with a *Bruker D8* diffractometer (see **Section 2.4** for more details). XRD scans between 10° and 35° were carried with a 0.0047° step and a 0.1 s integration time. The XRD pattern between 11.8° and 14.5° was measured every 23 min with a 0.0008° step and a 0.1 s integration time. GIXRD scans were measured with a 0.5 s integration and a 0.002° step between 12° and 14.5° every 11 min. Samples were illuminated with a *LedLenser M7* torch during *in situ* (GI)XRD ($P \sim 60$ mW/cm²). XRD and GIXRD patterns measured between 11.8° and 14.5° were smoothed using a Savitzky-Golay filter. The maximum point and FWHM of each peak were calculated as per **Section 2.6.1** using cubic and linear interpolation respectively. In order to limit noise in the determination of the peak positions and FWHM, the GIXRD scans were averaged every 2 scans. Crystallite

sizes were estimated using the Scherrer equation (**Equation 2.6**) using an arbitrary shape factor $K = 1$ and the lattice parameter d was retrieved using **Equation 2.5**.

3.2.4 Absorbance spectroscopy and optical microscopy

Absorbance of the films was measured every 23 min with a *Perkin Elmer Lambda 9 UV-Vis* spectrophotometer at 480 nm/min (1 nm step) (see **Section 2.1** for more details). A 100 % transmittance baseline was performed before measurement. The spectra were smoothed using a Savitzky-Golay filter. Optical imaging was performed with an *Olympus BH2* bright field microscope with a 40 X objective.

3.3 Results and discussions

3.3.1 Photoluminescence properties of methylammonium lead iodide

The PL of MAPI thin-films is first investigated under illumination over time in ambient and N_2 atmospheres in order to understand how photobrightening and photodarkening happens in these samples. **Figure 3.1** shows the PL and absorbance of a MAPI thin-film.

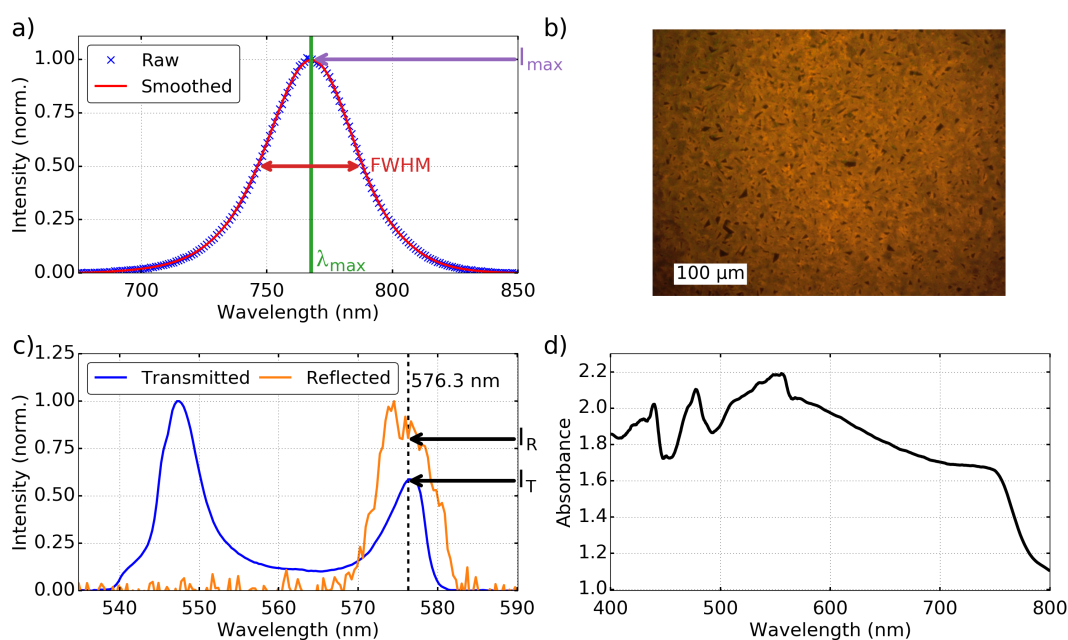


Figure 3.1: Optical properties of a MAPI thin-film on glass. PL **a)** spectrum and **b)** image (50 X magnification). **c)** Transmitted and reflected intensity of the fluorescence microscope excitation light. **d)** Absorbance.

The sample presents a PL peak with a maximum intensity at $\lambda_{max} = 768 \text{ nm} \approx 1.6 \text{ eV}$, consistent with the band edge observed around this wavelength (**Figure 3.1a & d**) and in agreement with the band-gap energy previously reported [16], [17]. PL imaging shows that the perovskite formed micrometric grains with few pinholes (**Figure 3.1b**). The reflected intensity was measured from the excitation light reflected by the sample while the transmitted intensity was measured from the excitation light transmitted by the sample (**Figure 3.1c**).

Sample variability. The PL properties (peak position, FWHM and maximum intensity) of 6 MAPI thin-films before illumination are similar but present slight variations (**Figure 3.2a & b**). This could be explained by the intrinsic variability of MAPI but also by an involuntary exposition of the samples to ambient atmosphere and light that could have altered them before the experiment, even with the great care taken to avoid it. In ambient atmosphere, the room relative humidity (RH) was measured between 60 % and 64 % at the start of each measurement and between 55 % and 75 % during the measurements as shown in **Figure 3.2c**, with samples Ambient (1), (2) and (3) respectively being exposed to an average 58 %, 63 % and 69 % RH. The properties of the samples are monitored under illumination (**Figure 3.3**).

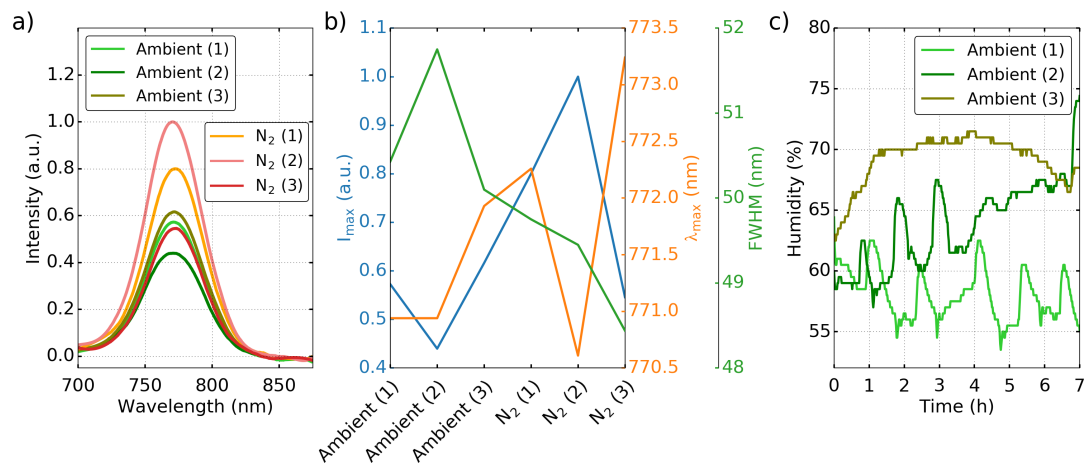


Figure 3.2: a) PL spectra of the samples studied before illumination, b) maximum intensity I_{max} , emission wavelength λ_{max} and FWHM, and c) relative humidity of the room during the measurements.

Maximum intensity. As previously reported in [1]–[5], [18], the PL intensity of the MAPI thin-films fluctuates over time under illumination in both atmospheres studied. In ambient atmosphere, the 3 samples measured behave similarly with an

homogeneous increase of the grains PL intensity (*i.e.* photobrightening) observed over the first ~ 4 h, followed by a more heterogeneous decrease (*i.e.* photodarkening) over the next ~ 2 h (**Figures 3.3a & c**). Depending on the sample and measurement conditions, slightly different kinetics are observed with different rates and quantities of photobrightening and photodarkening. Samples Ambient (2) and (3) almost fully photodarken after 6 h while sample Ambient (1) displays no emission (complete photodarkening) after 6.8 h. Samples Ambient (1) and (3) attain similar maximum intensity while sample Ambient (2) is more emissive although its initial emission is lower than the other two (**Figure 3.3a**). After 7 h, the illuminated spots were yellow in colour, characteristic of degraded MAPI and the formation of lead-iodide.

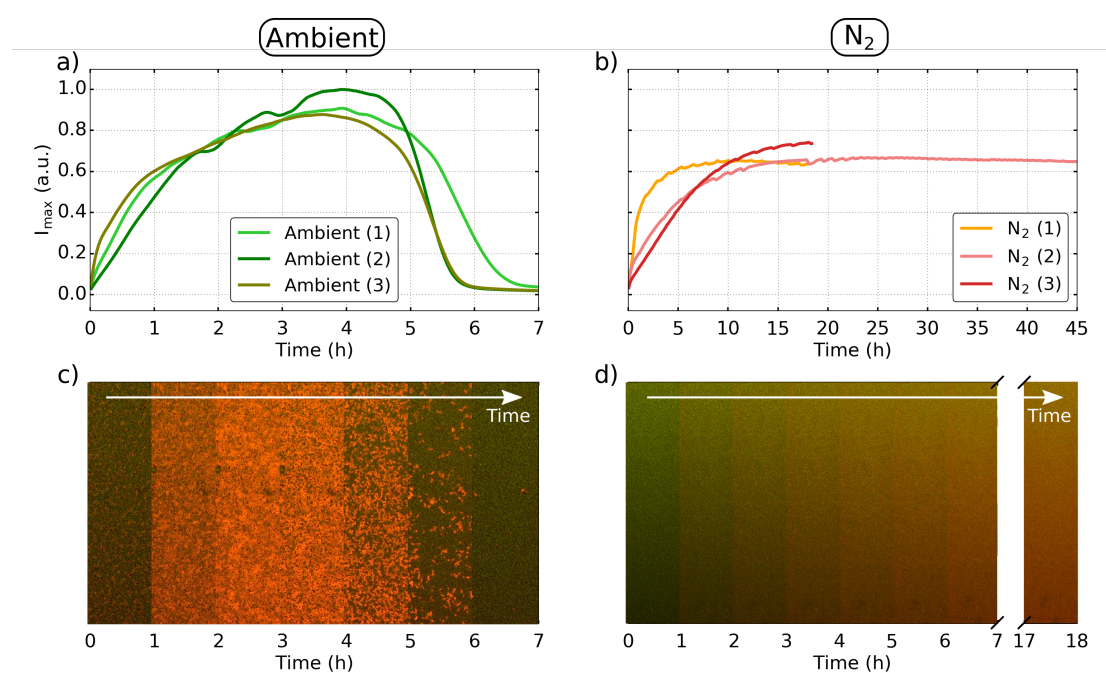


Figure 3.3: PL **a) & b)** maximum intensity I_{max} and **c) & d)** images of MAPI thin-films under illumination measured in an **a) & c)** ambient and **b) & d)** N₂ atmosphere.

In N₂ atmosphere, all the samples photobrighten at a much slower rate than in ambient atmosphere and the maximum emission reached is lower (**Figure 3.3b**). A higher degree of variability between samples is observed compared to those measured in an ambient atmosphere. The photobrightening rate is very dependent on the sample studied with sample N₂ (1) reaching its maximum intensity after 10 h while sample N₂ (3) did not reach its maximum emission even after 18 h. Both sample N₂ (1) and (2) show a very slight photodarkening phase after the initial photobrightening phase with N₂ (1) photodarkening faster than N₂ (2). This is surprising as humidity, which is a common source of variability (*e.g.* **Figure 3.2c**), was not present in the N₂ atmosphere.

However, even with the great care taken to avoid exposition of the samples to ambient atmosphere and light, it is possible that traces of oxygen, moisture and light could have altered the samples before the start of the experiment. This may demonstrate the degree of sensitivity to oxygen and moisture even at very low concentrations.

Photobrightening has been previously linked to the passivation of defect-induced trap states that can mediate non-radiative recombination of charge carriers in perovskites (see **Section 1.4.2**). These defects can be passivated through light-mediated iodide Frenkel pair annihilation (see **Section 1.4.2C**). This process (among others) leads to the formation of an iodide interstitial I_i^0 which can react between another iodide interstitial to form iodine which can then react with uncoordinated lead Pb^0 to form PbI_2 thus passivating it. In ambient atmosphere, these processes are aided by oxygen-mediated passivation of iodide vacancies and uncoordinated lead, and water-mediated passivation through enhancement of oxygen-mediated passivation and favourable degradation of the surface of perovskite grains.

Photodarkening likely arises from degradation and trap state formation in the perovskite. Frenkel pair and uncoordinated lead formation is likely the only defect formation process that can occur in N_2 atmosphere as the excitation wavelength (559 nm) did not allow photolysis of I_2 and PbI_2 [7]. However, iodine formed during the previously mentioned trap passivation and formation processes can migrate toward the grain surface where it can act as a trap state thus leading to photodarkening. Furthermore, the iodine concentration gradient leads to the formation of more defects within the grain bulk which may act as trap states and lead to photodarkening. In ambient atmosphere, this is aided by the reaction of oxygen and moisture with the perovskite into lead iodide and other degradation products leading to the observed photodarkening. The much slower photodarkening observed in N_2 could originate from intrinsic defect formation process although the presence of traces of oxygen and moisture in the sample or in the N_2 used could explain it as well [19]. A higher concentration of oxygen and/or moisture respectively in samples N_2 (1), (2) and (3) would be consistent with the faster photobrightening and photodarkening observed (**Figure 3.3b**). Similarly, the higher RH of samples Ambient (2) and (3) could explain their faster photodarkening compared to Ambient (1) (although Ambient (3) would be expected to photodarken faster than Ambient (2) in this case) (**Figure 3.3a**).FWHM

In both atmospheres, a decrease of the PL spectra FWHM is observed suggesting a decrease of the FWHM contribution from lattice defects, scattering off of phonons and/or scattering off of ionised impurities [20], [21] (**Figure 3.4a**). This is consistent with the passivation of point defects and therefore the associated trap states. In ambient atmosphere the FWHM decreases by ~ 11 nm over the first 5.5 h. In particular, the FWHM of samples Ambient (2) and (3) decrease down to ~ 39.5 nm while the FWHM of sample Ambient (1) decreases to 40.1 nm. This is consistent with the higher RH of Ambient (2) and (3) that would increase passivation of trap states by moisture. An increase of the FWHM is observed halfway during photodarkening and could be due to the formation of defects. This inflexion point happens 5.2 h after the start of the experiment for sample Ambient (2) and (3) and 0.6 h later for sample Ambient (1) and correlates well with the middle of the photodarkening phase. In N_2 atmosphere, defect passivation is limited to light-mediated processes, consistent with the smaller and slower decrease by ~ 4 nm of the FWHM over 18 h and slower photobrightening of the samples measured in this atmosphere. In particular, the FWHM of sample N_2 (1) decreases faster than the other samples consistent with the faster photobrightening rate observed for this sample compared to N_2 (2) and (3). This would be consistent with the presence of oxygen or moisture in this sample that would catalyse defect passivation. No increase of the FWHM is observed in N_2 atmosphere, even after 45 h illumination.

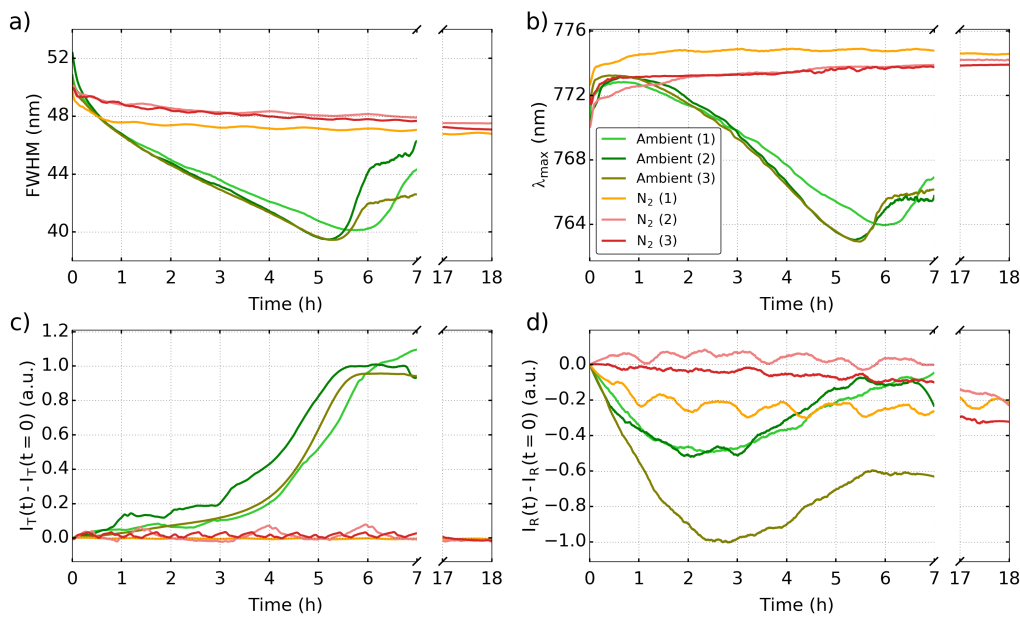


Figure 3.4: Optical properties of MAPI thin-films deposited on glass under illumination in an ambient and a N_2 atmosphere over 18 h. **a)** FWHM and **b)** maximum emission wavelength λ_{max} of the PL spectra, and relative variation of the **d)** transmittance I_T and **e)** reflectance I_R at 576.3 nm.

Emission wavelength. In ambient atmosphere, a red-shift of the the PL spectra is observed during the first 20 – 40 min, followed by a blue-shift (**Figure 3.4b**). Another red-shift is later observed ~ 0.2 h after the inflexion point of the FWHM previously discussed. In N_2 , the spectra initially red-shift over the first 2 – 3 h of illumination, followed by either stabilisation of the emission wavelength (sample N_2 (3)) which can be followed by a very slow blue-shift (sample N_2 (1) and (2)). Such changes in the emission wavelength could indicate a potential change of the band-gap energy. This could be caused by the formation and passivation of defects as well as the presence of reaction by-products such as I_2 and PbI_2 within the perovskite lattice which may affect the unit cell and therefore the band-gap. Photon recycling has been previously shown to lead to a red-shifting of the emission spectra due to the higher escape probability of longer wavelength photons compared to shorter wavelength photons [22]. An increase of the escape probability at longer wavelength, due to *e.g.* a decrease of the absorption coefficient, would then be consistent with the red-shift and photobrightening observed here [22]. The blue-shift may originates from a decrease of the grain size explained by a distortion of the Pb-I bond which affects the band-gap energy [23]–[25]. This is consistent with the degradation kinetic of MAPI by oxygen and moisture during which the surface of the grains is expected to be degraded first. The much slower blue-shift observed in N_2 may be due to the presence of trace of oxygen as previously discussed.

Transmittance and reflectance. An increase of the samples transmittance is observed in ambient atmosphere with larger variations happening during the photodarkening phase (between 4 and 6 h) while no change is observed for samples measured in N_2 atmosphere (**Figure 3.4c**). This increase is likely due to the disappearance of the perovskite absorption front caused by the degradation of the perovskite by water and moisture. In ambient atmosphere, such transmittance changes are associated with a decrease of the sample reflectance for the first 2.5 h, followed by an increase over the next 4 h (**Figure 3.4d**). This is consistent with the degradation kinetic of the perovskite where the grain surface is first degraded, leading to changes in its reflectance. Such changes could also lead to a change of the photon escape probability and therefore could participate to photobrightening and/or photodarkening. Conversely, a very slow decrease of the reflectance is observed in N_2 without any increase even after 45 h. In particular, sample N_2 (1) shows an initial

higher reflectance decrease than other samples measured in N_2 . This is consistent with the possible presence of trace of oxygen and/or moisture in this sample.

3.3.2 Crystallographic properties of methylammonium lead iodide

Figure 3.5 shows the XRD pattern of a MAPI thin-film deposited on glass before (fresh) and after (aged) illumination over 20 hours in an ambient atmosphere.

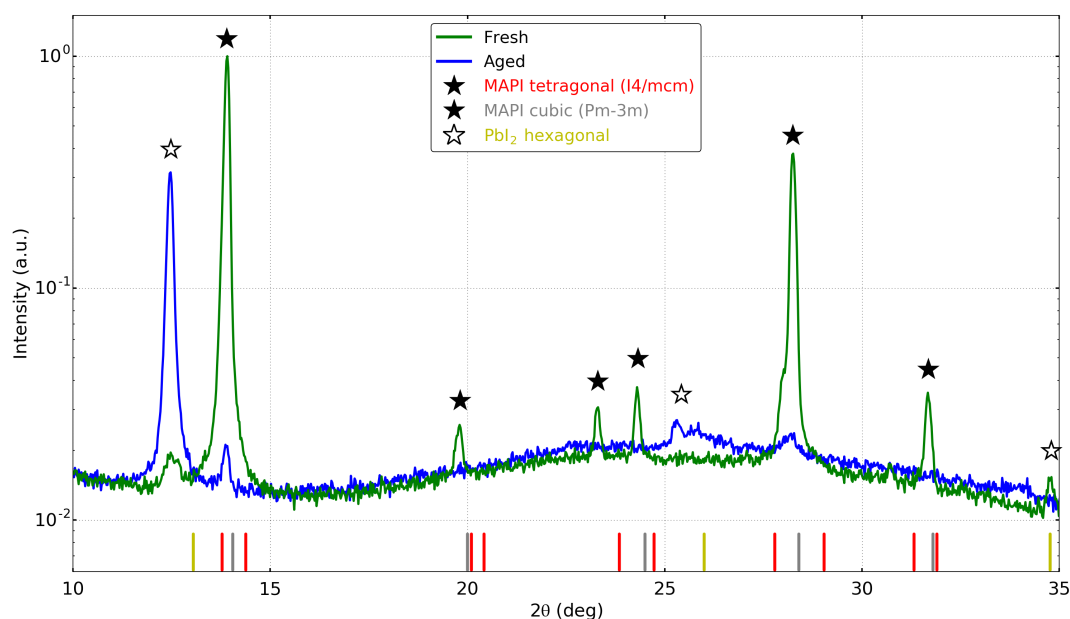


Figure 3.5: XRD pattern of a MAPI thin-film deposited on glass before (fresh) and after (aged) illumination in an ambient atmosphere over 20 hours. The coloured lines correspond to theoretical peak locations calculated from the structures while the stars indicate if the experimental peaks are associated with MAPI or PbI_2 .

Although the fresh perovskite film presents some of the diffraction peaks of the cubic phase of MAPI ((100) at 14.1° and (200) at 28.3°), it is more likely that the perovskite is in the tetragonal system as the film was measured at room temperature. This discrepancy can be explained by the proximity of the tetragonal system's (002) and (110) diffraction peaks at 13.79° and 14.37° respectively, leading to the merging of the two tetragonal peaks leaving a unique peak at 14.1° . This is also observed with the (004) and (220) peaks at 27.8° and 29.0° of the tetragonal phase, however these peaks are further apart and can be partially distinguished from each other. Furthermore, the XRD pattern presents a peak at 23.3° which exist in the tetragonal phase but not in the cubic phase. The shift between the theoretical and measured position of the peaks could be explained by the sample surface roughness leading to differences in

the X-rays focus and refraction angle. After degradation by illumination in an ambient atmosphere, the sample appears yellow and presents diffraction peaks matching the ones of lead iodide (**Figure 3.5**). The MAPI and lead iodide diffraction peaks between 12° and 14.5° were continuously monitored under illumination in ambient atmosphere (**Figure 3.6**).

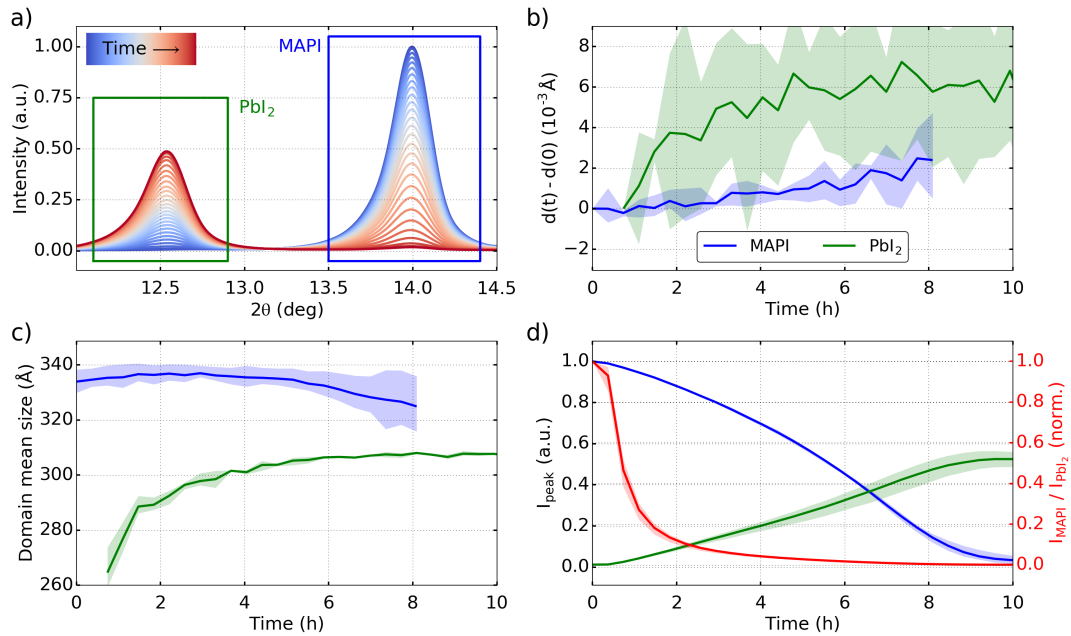


Figure 3.6: Crystallographic properties of MAPI thin-films under illumination for 10 h in an ambient atmosphere (3 samples averaged) **a)** GIXRD pattern, **b)** relative variation of the lattice parameter d , **c)** crystal domain mean size and, **d)** MAPI and PbI₂ peak intensities and intensity ratio. The lattice parameter and domain mean size for PbI₂ are only shown after 0.7 h as the peak intensity is too low to measure these quantities accurately. For the same reason, these quantities for MAPI are not shown after 8.1 h.

The MAPI peak intensity decreases while the lead iodide peak intensity increases over time indicating the degradation of the perovskite into lead iodide (**Figure 3.6a & d**). This is accompanied by a slight shift of the MAPI and lead iodide peak positions which could be either due to an increase of the crystal lattice parameters or a change in the sample surface roughness due to the degradation of the surface of the MAPI grains into lead-iodide (**Figure 3.6b**). Such deformation of the MAPI crystal structure could explain the change of the band-gap energy observed with the fluorescence microscope. The domain mean sizes were calculated using the Scherrer equation and are within the applicability limits of this model (see **Section 2.7** for more details) (**Figure 3.6c**). A slight increase and then decrease of the MAPI domain size are observed over the course

of the experiment. Due to their higher surface defect concentration, it is expected that smaller MAPI grains degrade first leading to an increase of the mean grain size. The decrease of the domain size observed after 3 h likely happens as the larger grains starts degrading and is consistent with the blue-shift of the PL emission peak previously observed. These changes of the diffraction peak FWHM are however very small and could originate from lattice strain change over time and should therefore be considered carefully. The lead iodide domain size increases consistent with the growth of lead iodide grains from MAPI. The degradation of the film is quantified using **Equation 2.7 (Figure 3.6d)**. No monohydrate or dihydrate phases is observed between 7.5° and 15° where their main diffraction peaks should be located [12] (not shown here) and it is thus assumed that only lead iodide and MAPI were present in the film. The degradation rate appears exponential with a very fast conversion of MAPI to lead iodide at the start of the illumination which slows down as more perovskite is degraded thus limiting reaction sites for oxygen and moisture. This experiment was repeated with the PL and absorbance of the sample measured between each XRD measurement (**Figure 3.7**).

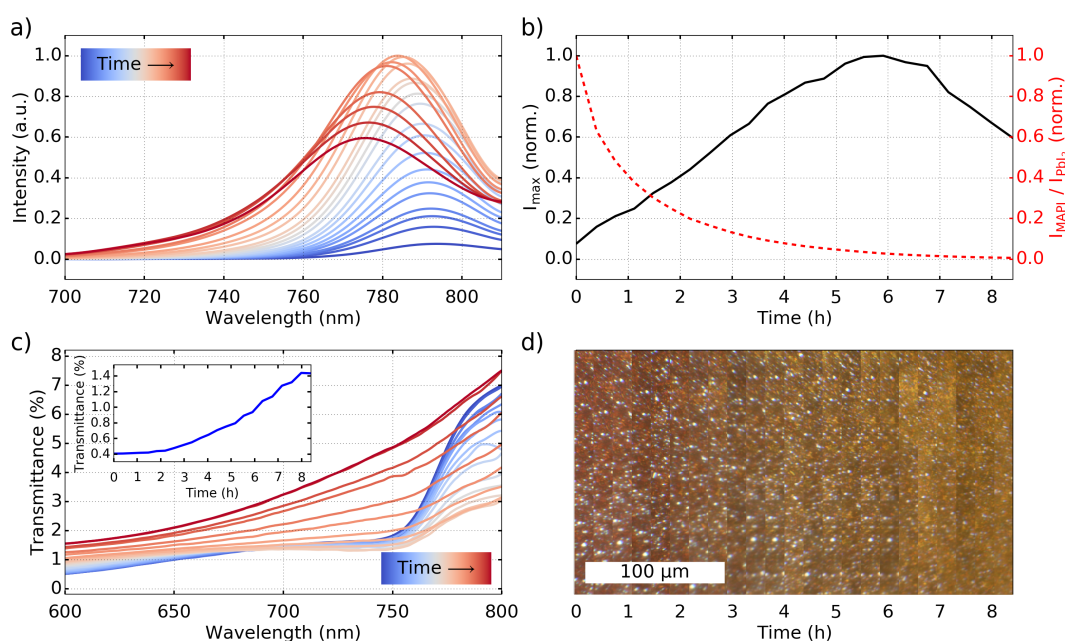


Figure 3.7: **a)** PL spectra, **b)** PL maximum intensity I_{max} and diffraction peak intensity ratio, **c)** absorbance (inset: transmittance at 576.5 nm) and **d)** optical microscopy images of a MAPI thin-film under illumination in an ambient atmosphere for 8.2 h.

As with the fluorescence microscopy setup, photobrightening and photodarkening of the sample are observed with the fluorometer (**Figure 3.7a & b**). The transmittance front around 760 nm disappears over time consistent with the degradation of the

perovskite (**Figure 3.7c**). The transmittance at 576.5 nm follows the same trend as observed with the fluorescence microscopy setup. Most of the perovskite is converted to lead iodide after 3 h according the XRD peak intensity ratio while optical microscopy shows a colour change of the sample which is only noticeable after 3 h (**Figure 3.7d**). The maximum PL intensity of the sample is reached after 5.8 h while most of the perovskite had been degraded. Since photodarkening results from degradation of the perovskite, it is clear that photobrightening and photodarkening are competing processes in this sample. While some of the perovskite layer is degraded into lead iodide, trap states in the remaining perovskite are passivated. The PL intensity after photobrightening, without degradation/photodarkening could thus be potentially much higher.

3.4 Conclusion

The PL and crystallographic properties of MAPI thin-films deposited on glass have been studied in ambient and N₂ atmospheres under illumination. The perovskite is found in the tetragonal I4/mcm phase and presents a 1.6 eV band-gap energy consistent with values previously reported in the literature. Observed photobrightening and photodarkening happen sequentially in ambient atmosphere under illumination before the degradation of the perovskite into lead iodide. The photobrightening observed in N₂ atmosphere is slower and little to no photodarkening is observed. Photobrightening is associated with the passivation of point defects and the associated trap states through light-mediated iodide Frenkel pair annihilation, aided by oxygen, moisture and PbI₂ (originating from moisture and oxygen degradation of the perovskite) passivation in ambient atmosphere. This is consistent with a decrease of the FWHM and red-shift of the PL spectra indicating changes to the samples crystallinity. Given the very slow photodarkening observed in N₂, it is likely that it is caused here by the degradation of the perovskite by oxygen and moisture (although defect formation processes such as Frenkel pair creation and iodine migration should not be overlooked). The blue-shift of the PL spectra observed in ambient atmosphere is linked to a decrease of the perovskite grain size, likely affecting the band-gap energy by altering the Pb-I bond as previously reported. The sample transmittance changes are only observed in ambient atmosphere and are associated with the disappearance of the perovskite absorption front due to

degradation while the reflectance changes are likely due to favourable degradation of the grain surface, hence affecting light reflection at their interface with air. The sample reflectance was found to vary more than its transmittance which thus seem a better indicator of perovskite degradation.

By monitoring the main diffraction peaks of MAPI and PbI_2 , degradation of the perovskite is found to occur during the whole experiment leading to the growth of PbI_2 within MAPI. Most of the degradation happens during the first 3 h of illumination although no noticeable visible change of the perovskite is noted. The maximum photobrightening is observed as most of the perovskite was converted to PbI_2 as indicated by the almost total disappearance of the MAPI (110) diffraction peak and the intense PbI_2 peak. Degradation (and therefore photodarkening) can thus occur at the same time as photobrightening before an obvious colour change of the film. This suggests that degradation may occur earlier than previously thought as it is “masked” by photobrightening.

These results highlight that care should be taken when studying the PL of perovskites. There are a number of competing processes occurring at the same time which can be seen by the variation of the PL maximum intensity, position and FWHM over time. This can lead to large variability which in turn impacts the understanding of these materials. Monitoring the PL over time should thus be favoured over single measures. Measurements in inert atmosphere may also be preferred as they inhibit the degradation of the perovskite as well as photobrightening, hence limiting the PL variations.

3.5 References

- [1] J. F. Galisteo-López *et al.*, “Environmental effects on the photophysics of organic-inorganic halide perovskites”, *The Journal of Physical Chemistry Letters*, vol. 6, no. 12, pp. 2200–2205, Jun. 2015. DOI: 10.1021/acs.jpcllett.5b00785.
- [2] D. W. DeQuilettes *et al.*, “Photo-induced halide redistribution in organic–inorganic perovskite films”, *Nature Communications*, vol. 7, no. May, p. 11 683, May 2016. DOI: 10.1038/ncomms11683.
- [3] R. Brenes *et al.*, “Metal halide perovskite polycrystalline films exhibiting properties of single crystals”, *Joule*, vol. 1, no. 1, pp. 155–167, Sep. 2017. DOI: 10.1016/j.joule.2017.08.006.

- [4] R. Brenes *et al.*, “The impact of atmosphere on the local luminescence properties of metal halide perovskite grains”, *Advanced Materials*, vol. 30, no. 15, p. 1706208, Apr. 2018. DOI: 10.1002/adma.201706208.
- [5] Y. Tian *et al.*, “Mechanistic insights into perovskite photoluminescence enhancement: Light curing with oxygen can boost yield thousandfold”, *Physical Chemistry Chemical Physics*, vol. 17, no. 38, pp. 24978–24987, Sep. 2015. DOI: 10.1039/c5cp04410c.
- [6] Z. Andaji-Garmaroudi *et al.*, “Photobrightening in lead halide perovskites: Observations, mechanisms, and future potential”, *Advanced Energy Materials*, vol. 10, no. 13, p. 1903109, 2020. DOI: 10.1002/aenm.201903109.
- [7] W. A. Quitsch *et al.*, “The Role of excitation energy in photobrightening and photodegradation of halide perovskite thin films”, *Journal of Physical Chemistry Letters*, vol. 9, no. 8, pp. 2062–2069, Apr. 2018. DOI: 10.1021/acs.jpcllett.8b00212.
- [8] S. G. Motti *et al.*, “Controlling competing photochemical reactions stabilizes perovskite solar cells”, *Nature Photonics*, p. 1, May 2019. DOI: 10.1038/s41566-019-0435-1.
- [9] N. Aristidou *et al.*, “Fast oxygen diffusion and iodide defects mediate oxygen-induced degradation of perovskite solar cells”, *Nature Communications*, vol. 8, p. 15218, May 2017. DOI: 10.1038/ncomms15218.
- [10] J. S. Godding *et al.*, “Oxidative passivation of metal halide perovskites”, *Joule*, vol. 3, no. 11, pp. 2716–2731, 2019. DOI: 10.1016/j.joule.2019.08.006.
- [11] U.-G. Jong *et al.*, “Influence of water intercalation and hydration on chemical decomposition and ion transport in methylammonium lead halide perovskites”, *J. Mater. Chem. A*, vol. 6, pp. 1067–1074, 3 2018. DOI: 10.1039/C7TA09112E.
- [12] A. Leguy *et al.*, “Reversible hydration of $\text{CH}_3\text{NH}_3\text{PbI}_3$ in films, single crystals and solar cells”, *Chemistry of Materials*, vol. 27, pp. 3397–3407, 2015. DOI: 10.1021/acs.chemmater.5b00660.
- [13] F. Hao *et al.*, “Controllable perovskite crystallization at a gas–solid interface for hole conductor-free solar cells with steady power conversion efficiency over 10%”, *Journal of the American Chemical Society*, vol. 136, no. 46, pp. 16411–16419, Nov. 2014. DOI: 10.1021/ja509245x.
- [14] J. F. Verwey, *Photochemical Processes in lead halides*. Bronder-Offset (Goudsesingel 260), 1967.
- [15] J. Troughton *et al.*, “Humidity resistant fabrication of $\text{CH}_3\text{NH}_3\text{PbI}_3$ perovskite solar cells and modules”, *Nano Energy*, vol. 39, pp. 60–68, Sep. 2017. DOI: 10.1016/J.NANOEN.2017.06.039.

- [16] M. A. Green *et al.*, “Optical properties of photovoltaic organic-inorganic lead halide perovskites”, *The Journal of Physical Chemistry Letters*, vol. 6, no. 23, pp. 4774–4785, Dec. 2015. DOI: 10.1021/acs.jpcllett.5b01865.
- [17] E. Mosconi *et al.*, “First-principles modeling of mixed halide organometal perovskites for photovoltaic applications”, *The Journal of Physical Chemistry C*, vol. 117, no. 27, pp. 13 902–13 913, Jul. 2013. DOI: 10.1021/jp4048659.
- [18] E. Mosconi *et al.*, “Light-induced annihilation of Frenkel defects in organo-lead halide perovskites”, *Energy and Environmental Science*, vol. 9, no. 10, pp. 3180–3187, Oct. 2016. DOI: 10.1039/c6ee01504b.
- [19] M. Anaya *et al.*, “Origin of light-induced photophysical effects in organic metal halide perovskites in the presence of oxygen”, *The Journal of Physical Chemistry Letters*, vol. 9, no. 14, pp. 3891–3896, Jul. 2018. DOI: 10.1021/acs.jpcllett.8b01830.
- [20] S. Rudin *et al.*, “Temperature-dependent exciton linewidths in semiconductors”, *Phys. Rev. B*, vol. 42, pp. 11 218–11 231, 17 Dec. 1990. DOI: 10.1103/PhysRevB.42.11218.
- [21] K. P. Goetz *et al.*, “Shining light on the photoluminescence properties of metal halide perovskites”, *Advanced Functional Materials*, vol. 30, no. 23, p. 1 910 004, 2020. DOI: 10.1002/adfm.201910004.
- [22] L. M. Pazos-Outón *et al.*, “Photon recycling in lead iodide perovskite solar cells”, *Science*, vol. 351, no. 6280, pp. 1430–1433, Mar. 2016. DOI: 10.1126/SCIENCE.AAF1168.
- [23] G. Grancini *et al.*, “The impact of the crystallization processes on the structural and optical properties of hybrid perovskite films for photovoltaics”, *The Journal of Physical Chemistry Letters*, vol. 5, no. 21, pp. 3836–3842, Nov. 2014. DOI: 10.1021/jz501877h.
- [24] M. R. Filip *et al.*, “Steric engineering of metal-halide perovskites with tunable optical band gaps.”, eng, *Nat Commun*, vol. 5, p. 5757, Dec. 2014. DOI: 10.1038/ncomms6757.
- [25] V. D’Innocenzo *et al.*, “Tuning the light emission properties by band gap engineering in hybrid lead halide perovskite”, *Journal of the American Chemical Society*, vol. 136, no. 51, pp. 17 730–17 733, Dec. 2014. DOI: 10.1021/ja511198f.

Chapter 4

Modelling charge carrier recombination and time-resolved photoluminescence of methylammonium lead iodide perovskite

Contents

4.1	Introduction	94
4.1.1	Recombination processes	96
A	Bimolecular recombinations	96
B	Trap-mediated recombinations	97
4.1.2	TRPL kinetic models	99
A	Bimolecular-trapping model	99
B	Bimolecular-trapping-detrapping model	101
4.1.3	Chapter outline	103
4.2	Methodology	103
4.2.1	Simulations	103
4.2.2	Fitting	108
4.2.3	Sample manufacturing & instrumentation	110
4.3	Results & Discussions	110
4.3.1	Bimolecular-trapping model	112
A	Fluence regimes	112
B	Carrier accumulation	116
C	Experimental decay fitting	120
4.3.2	Bimolecular-trapping-detrapping model	122
A	Fluence regimes	122
B	Carrier accumulation	128
C	Experimental decay fitting	130
4.3.3	Comparison of the models and discussions	135
4.4	Conclusion	137
4.5	References	139

In solar cells, and in particular in PSCs, charge carrier (electron and hole) recombination prevents their extraction into the electron and hole transport layers, and therefore limit the device's PCE [1]. In particular, defect-induced trap states are more detrimental as they can quickly trap carriers, thus preventing their extraction. These trap states, through their formation and passivation, are also believed to be responsible for the instability and subsequent degradation of the perovskite layer [2]–[6]. Extracting information related to recombination processes and trap states is thus essential to the improvement of perovskite solar cells.

4.1 Introduction

TRPL spectroscopy is a powerful technique to study charge carrier recombination kinetics of photoluminescent materials [7]–[9]. TRPL measures the radiative electron-hole recombinations after absorption of a short light excitation pulse (typically of the order of the ps). The TRPL decay obtained is affected by the different competing radiative and non-radiative recombination processes happening in a system, as well as its environment, and is therefore useful for extracting information related to these processes. TRPL is usually measured using time-correlated single photon counting (TCSPC) in which the sample is periodically excited by a pulsed laser and the sample emission is measured at the desired wavelength. Ideally, after each excitation pulse, 0 or 1 photon is measured, thus generally requiring millions to billions of excitation pulses to obtain an adequate signal to noise ratio (S/N). The TRPL intensity I_{TRPL} measured after \mathbf{P} pulses is thus proportional to the sum of the TRPL intensity I_{TRPL}^p after each excitation pulse p :

$$I_{TRPL}(t) \propto \sum_{p=1}^{\mathbf{P}} I_{TRPL}^p(t) \quad (4.1)$$

TRPL decays have been classically fitted with a sum of n exponential decays $A_i e^{-t/\tau_i}$ (A_i and τ_i are respectively the amplitude and lifetime of component i) [10]:

$$I_{TRPL}(t) = \sum_i^n A_i e^{-t/\tau_i} \quad (4.2)$$

When applied to perovskite materials, a bi-exponential ($n = 2$) fit is generally done and the two components are usually assigned to trap-mediated recombination (shorter lifetime τ_1) and radiative recombination (longer lifetime τ_2) [11]–[14]. For perovskite

layers in contact with an electron or hole transport material, the faster component has been linked to charge carrier extraction from the perovskite to the transport material [15]–[19]. The amplitude of each exponential component is usually attributed to the contribution of each process whereas the lifetime as a rate measure of the process [16], [17]. However, this model does not consider the dependence of the recombination processes on the excited charge carrier concentrations in perovskites.

Here, two models considering direct electron-hole recombination as well as trap-mediated recombination in homogeneous perovskite systems are investigated. For most perovskite thin films for solar cells (*i.e.* $< ca.$ 200 nm thick), carrier diffusion can be assumed much faster than recombination such that the charge carriers can be considered homogeneously distributed in the film after photoexcitation [20]. In such films, the photoexcited charge carrier concentration N_0 generated by an excitation pulse of fluence I_0 (in photons/cm²) is [21]:

$$N_0 = \frac{I_0 A}{D} \quad (4.3)$$

where A and D are respectively the film absorptance and thickness. Since the carrier concentration N_0 and the excitation fluence I_0 are proportional, they are used interchangeably here. At room temperature, the excitons quickly dissociate due to their low binding energy [22], leaving Δn_e electrons in the conduction band (CB) and Δn_h holes in the valence band (VB). The total excited electron $n_e(t)$ and hole $n_h(t)$ concentrations in the CB and VB bands at time t are:

$$n_e(t) = \Delta n_e(t) + n_0 \quad (4.4)$$

$$n_h(t) = \Delta n_h(t) + p_0 \quad (4.5)$$

where n_0 and p_0 are respectively the N-type and P-type doping concentrations which may originate from crystal impurities or point defects (intrinsic carriers are ignored due to their low concentration — *ca.* 10^4 cm⁻³ at 300 K [20] — compared to the doping and photoexcited concentrations considered here). Excited carriers can undergo band-to-band recombination (leading to photoluminescence) while the high concentration of trap states in perovskites (see **Section 1.4.2**) is expected to lead to significant non-radiative recombination of the excited carriers. Here, three of the

recombination processes commonly considered in the literature are described: band-to-band, non-radiative bimolecular and trap-mediated recombinations.

4.1.1 Recombination processes

A Bimolecular recombinations

Band-to-band recombination is a radiative process during which an excited electron directly recombines with a hole in the VB (**Figure 4.1a**). Due to the low exciton binding energy in perovskites, excited electrons and holes are uncoupled and their recombination is bimolecular, that is a second order process with a rate dependent on both charge carriers concentrations [23]–[25]. The contribution of this recombination process to the change in the charge carrier concentrations over a small period of time dt , is thus equal to the product of the radiative band-to-band recombination rate constant k_R , and the electron n_e and hole n_h concentrations [23]–[25]:

$$\left[\frac{dn_e}{dt} \right]_R = \left[\frac{dn_h}{dt} \right]_R = -k_R n_e(t) n_h(t) \quad (4.6)$$

As previously discussed in **Section 1.2.2**, direct band-gap semiconductors with a high absorption coefficient and a small Stoke shift such as perovskites can present photon recycling [23], [26]–[28]. As absorption is a much faster process than the recombination processes considered here (\sim fs versus to \sim ns), carriers leading to photon recycling can be assumed to not have recombined. The observed radiative rate constant $\eta_{esc} k_R$ is thus a fraction of the internal radiative rate constant (η_{esc} is the photon escape probability) [23], [26], [29]:

$$\left[\frac{dn_e}{dt} \right]_R = \left[\frac{dn_h}{dt} \right]_R = -\eta_{esc} k_R n_e(t) n_h(t) \quad (4.7)$$

The TRPL intensity measured corresponds to the number of photons emitted by the system studied and is thus equal to:

$$I_{TRPL}(t) = - \left[\frac{dn_e}{dt} \right]_R = \eta_{esc} k_R n_e(t) n_h(t) \quad (4.8)$$

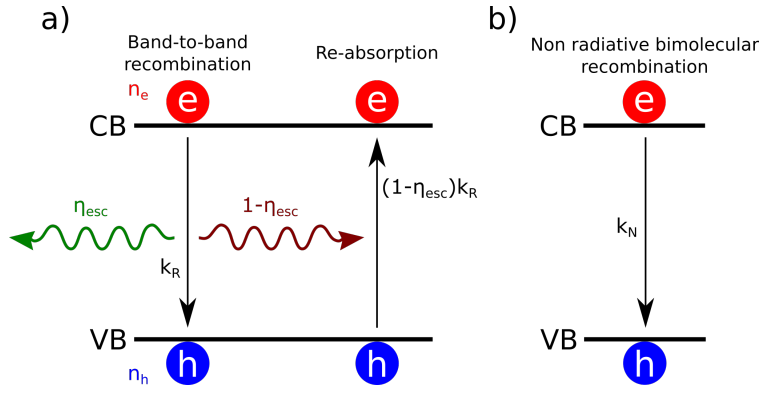


Figure 4.1: **a)** Schematic of band-to-band recombination and re-absorption processes during which charge carriers radiatively recombine at rate constant k_R . A fraction η_{esc} of the emitted photons escape the semiconductor while the rest $(1 - \eta_{esc})$ is re-absorbed. **b)** Schematic of non-radiative bimolecular recombination during which charge carriers recombine non-radiatively at rate constant k_N .

It has been suggested that shallow trap state-mediated recombination and trap-state mediated Auger recombination may lead to non-radiative bimolecular recombination of charge carriers at rate [23], [25], [26] (**Figure 4.1b**):

$$\left[\frac{dn_e}{dt} \right]_N = \left[\frac{dn_h}{dt} \right]_N = -k_N n_e(t) n_h(t) \quad (4.9)$$

where k_N is the non-radiative bimolecular rate constant. As both radiative (**Equation 4.7**) and non-radiative (**Equation 4.9**) bimolecular recombination processes are proportional to the product of the electron and hole concentrations, they can be summed as the bimolecular contribution of rate constant k_B :

$$\left[\frac{dn_e}{dt} \right]_N = \left[\frac{dn_h}{dt} \right]_N = - \underbrace{(\eta_{esc} k_R + k_N)}_{k_B} n_e(t) n_h(t) \quad (4.10)$$

B Trap-mediated recombinations

Trap-mediated recombination, also known as Shockley-Read-Hall recombination can be described as a non-radiative bimolecular process between one carrier type and the available trap states (**Figure 4.2a**) [25], [30]. In the case of electron trapping, the trapping contribution is proportional to the product of free electrons n_e and available trap states concentrations $N_T - n_t$, where N_T is the concentration of trap states and n_t is the concentration of trapped electrons occupying these states [25], [30]:

$$\left[\frac{dn_e}{dt} \right]_T = -k_T n_e(t) [N_T - n_t(t)] \quad (4.11)$$

where k_T is the electron trapping rate constant. The detrapping of an electron through its recombination with a hole in the VB can be described as a non-radiative bimolecular process between trapped electrons and free holes (**Figure 4.2a**) [25], [30]:

$$\left[\frac{dn_t}{dt} \right]_D = -k_D n_t(t) n_h(t) \quad (4.12)$$

where k_D is the detrapping rate constant. In the steady-state regime and if the trap state concentration is much higher than the photoexcited carrier concentration, the electron and hole concentrations can be assumed equal at all time and trap-mediated recombination can be described as a monomolecular processes (**Figure 4.2b**) [31]–[33]:

$$\left[\frac{dn_e}{dt} \right]_T = \left[\frac{dn_h}{dt} \right]_T = -k_T n_e(t) = -k_T n_h(t) \quad (4.13)$$

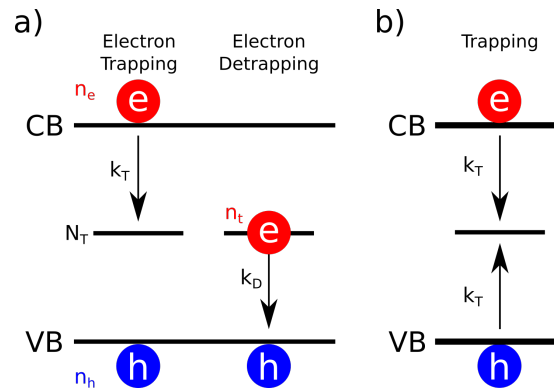


Figure 4.2: Schematic of **a**) bimolecular electron trapping in trap states (concentration N_T) at rate constant k_T and detrapping at rate constant k_D , and **b**) monomolecular trapping at rate constant k_T .

Trimolecular Auger recombination is not discussed here as it has been suggested that it only occurs at very high light fluences (above *ca.* 10 sun illumination) and should therefore be negligible in PSCs under normal operation illumination conditions and in common TRPL measurements conditions [34]. Electron detrapping back to the CB, which has been shown to lead to delayed fluorescence [35], [36] could also influence the decay kinetics, however, the aim here is to highlight complications with

typical analysis found in the literature where commonly delayed fluorescence is not considered.

4.1.2 TRPL kinetic models

In perovskite films, both direct and trap-mediated recombination determine the overall charge recombination dynamics. Here the modelling of the TRPL decays with two possible models is discussed; the bimolecular-trapping (BT) model and the bimolecular-trapping-detrapping (BTD) model. Both models consider bimolecular recombination of charge carriers but differ in their treatment of trap-mediated recombination.

A Bimolecular-trapping model

The BT model assumes the electron and hole concentration equal at all time (*i.e.* $n_e(t) = \Delta n_e(t) = n_h(t) = \Delta n_h(t) = n(t)$) and monomolecular trapping (**Figure 4.3**). The rate equation for the BT model is thus build upon **Equations 4.10 & 4.13** which give [24], [32], [37]:

$$\frac{dn}{dt} = -\underbrace{k_B n^2(t)}_{B_n(t)} - \underbrace{k_T n(t)}_{T_n(t)} \quad (4.14)$$

where $B_n(t)$ and $T_n(t)$ are respectively the bimolecular and trapping contributions to the change in the charge carrier concentration at time t . For TCSPC decay analysis, this differential equation is solved with the condition that each excitation pulse p generates N_0 carriers which add up to any carriers present in the bands just before the pulse. The initial carrier concentration $n^p(t=0)$ of pulse p is thus:

$$n^p(t=0) = N_0 + n^{p-1}(RP) \quad (4.15)$$

where $n^{p-1}(RP)$ is the carrier concentration just before excitation pulse p and RP is the excitation repetition period. It is assumed that TCSPC experiments are started with a film with no free carriers *i.e.* $n^{p=1}(0) = N_0$ (this can be ensured by keeping the sample in the dark for long enough time so that most carriers have recombined). As per **Equation 4.8**, the TRPL intensity measured after excitation pulse p is given by:

$$I_{TRPL}^p(t) = \eta_{esc} k_R (n^p(t))^2 \quad (4.16)$$

Values of the different rate constants from the literature obtained using the BT model are reported in **Table 4.1**.

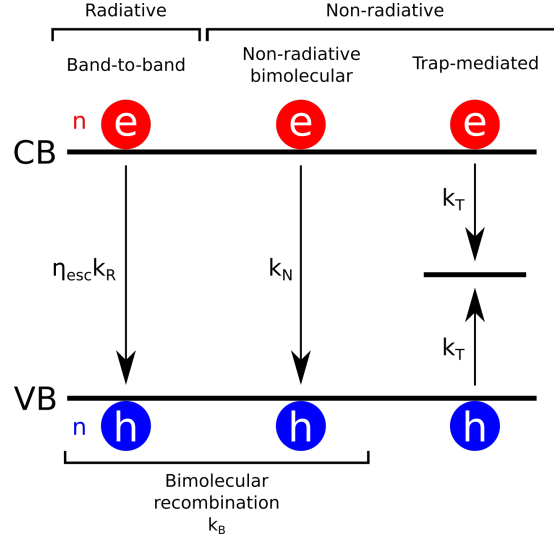


Figure 4.3: Schematic of the recombination processes considered in the bimolecular-trapping model. Excited electrons and holes (concentration n) in the conduction (CB) and valence (VB) bands undergo radiative and non-radiative bimolecular recombinations at rate constants $\eta_{esc}k_R$ and k_N respectively (total rate constant k_B). Electrons and holes can also undergo monomolecular trap-mediated recombination at rate constant k_T .

Table 4.1: Bimolecular k_B and trapping k_T rate constants for different perovskites obtained using the bimolecular-trapping model [$\text{CH}_3\text{NH}_3\text{PbI}_3$ (MAPI), $\text{CH}_3\text{NH}_3\text{PbI}_{3(1-x)}\text{Cl}_{3x}$ (MAPIC), $\text{CH}_3\text{NH}_3\text{PbBr}_3$ (MAPBr)], values taken from literature.

Perovskite	k_B (10^{-20} cm ³ /ns)	k_T (10^{-3} ns ⁻¹)	Ref.
	17	180	[24]
MAPI	51-220	3-28	[38]
	8.1	5	[26]
	92	14	[39]
MAPBr	12-20	2.9-1,100	[40]
	7.0	2.5	[26]
MAPIC	7.9	≤ 0.5	[26]

B Bimolecular-trapping-detrapping model

Contrary to the BT model, the BTD model (depicted in **Figure 4.4**) considers trapping and detrapping as bimolecular processes. The electron and hole concentrations are not always equal and so the rate equations for both carrier types and the trapped carrier concentration needs to be solved. Within this model, trapping and detrapping is believed to be mediated by deep trap states while non-radiative bimolecular recombination is mediated by shallow trap states [23]. In the case of electron trapping and considering P-type doping (*i.e.* $n_e(t) = \Delta n_e(t)$ and $n_h(t) = \Delta n_h(t) + p_0$) (as predicted for MAPI using first principle calculations [41]), **Equations 4.10, 4.11 & 4.12** give the following set of rate equations [23], [25], [30], [42]:

$$\frac{dn_e}{dt} = -\underbrace{k_B \Delta n_e(t) [\Delta n_h(t) + p_0]}_{B_n(t)} - \underbrace{k_T \Delta n_e(t) [N_T - n_t(t)]}_{T_n(t)} \quad (4.17)$$

$$\frac{dn_t}{dt} = \underbrace{k_T \Delta n_e(t) [N_T - n_t(t)]}_{T_n(t)} - \underbrace{k_D n_t(t) [\Delta n_h(t) + p_0]}_{D_n(t)} \quad (4.18)$$

$$\frac{dn_h}{dt} = -\underbrace{k_B \Delta n_e(t) [\Delta n_h(t) + p_0]}_{B_n(t)} - \underbrace{k_D n_t(t) [\Delta n_h(t) + p_0]}_{D_n(t)} \quad (4.19)$$

where $B_n(t)$, $T_n(t)$ and $D_n(t)$ are, respectively, the bimolecular, trapping and detrapping contributions to the change in the carrier concentrations. In TCSPC measurements, the initial carrier concentrations after excitation pulse p generating N_0 carriers are:

$$\Delta n_e^p(t=0) = N_0 + \Delta n_e^{p-1}(RP) \quad (4.20)$$

$$\Delta n_h^p(t=0) = N_0 + \Delta n_h^{p-1}(RP) \quad (4.21)$$

$$n_t^p(t=0) = n_t^{p-1}(RP) \quad (4.22)$$

where $\Delta n_e^{p-1}(RP)$, $\Delta n_h^{p-1}(RP)$ and $n_t^{p-1}(RP)$ are the electron, hole and trapped electron concentrations in the system just before excitation pulse p . As for the BT model, it is assumed that there are no carriers present in the system before the first pulse *i.e.* $\Delta n_e^{p=1}(0) = \Delta n_h^{p=1}(0) = N_0$ and $n_t(0) = 0$. As per **Equation 4.8**, the TRPL intensity measured after an excitation pulse p is given by:

$$I_{TRPL}^p(t) = \eta_{esc} k_R \Delta n_e(t) [\Delta n_h(t) + p_0] \quad (4.23)$$

Values of the rate constants and concentrations obtained from the literature using the BTD model are reported in **Table 4.2**.

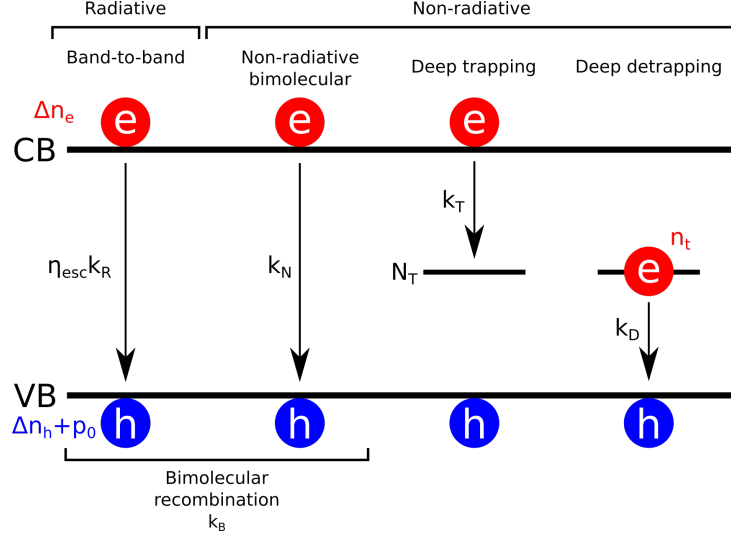


Figure 4.4: Schematic of the recombination processes considered in the bimolecular-trapping-detrapping model. Excited electrons (concentration Δn_e) and holes (concentration $\Delta n_h + p_0$) in the conduction (CB) and valence (VB) band undergo radiative and non-radiative bimolecular recombination at rate constants $\eta_{esc} k_R$ and k_N respectively (total rate constant k_B). Electrons get trapped in trap states (concentration N_T) at rate constant k_T . Trapped electrons (concentration n_t) can then detrapp back to the VB at rate constant k_D .

Table 4.2: Bimolecular k_B , trapping k_T , detrapping k_D rate constants, and deep trap states (N_T) and doping (p_0) concentrations for different perovskites obtained using the bimolecular-trapping-detrapping model [$\text{CH}_3\text{NH}_3\text{PbI}_3$ (MAPI), $\text{CH}_3\text{NH}_3\text{PbI}_{3(1-x)}\text{Cl}_{3x}$ (MAPIC)], values taken from literature.

Perovskite	k_B (10^{-20} cm^3/ns)	k_T (10^{-20} cm^3/ns)	k_D (10^{-20} cm^3/ns)	N_T (10^{12} cm^{-3})	p_0 (10^{12} cm^{-3})	Ref.
MAPI	35	10	5	60,000	10,000	[25]
	26-76	12,000	80	60	65	[23]*
MAPIC	49	~ 0	< 500	1,000	~ 0	[25]

4.1.3 Chapter outline

In this chapter, the use of TRPL for investigating charge carrier recombination in perovskites is discussed. The fluence dependence as well as charge carrier accumulation due to incomplete depopulation of all photoexcited carriers between consecutive excitation pulses are discussed for both BT and BTD models. Recommendations for meaningful measurements of lead halide perovskite thin-films are offered. Finally, the models are used to fit experimentally measured TRPL decays of a MAPI thin film on glass measured at different excitation fluences, and the limitation of these fits are discussed.

4.2 Methodology

In this section, the methods and parameters used to simulate the carrier concentrations and TRPL, details about the fitting of the TRPL decays and experimental details about the measurement of TRPL are described.

4.2.1 Simulations

Carrier concentrations and TRPL intensity were simulated by following the process described in the block diagram in **Figure 4.5**, presented for the BT model only. The same process is valid for the BTD model by replacing the equations with those in **Section 4.1.2B**. Unless otherwise stated, all carrier concentrations and TRPL decays were calculated after the first excitation pulse only (referred to as the single pulse approximation as described in **Section 4.3.1B**).

Parameter values. For the BT model, the carrier concentration was simulated using **Equations 4.14** and **4.15**, and $k_B = 50 \times 10^{-20} \text{ cm}^3/\text{ns}$ and $k_T = 15 \times 10^{-3} \text{ ns}^{-1}$, values consistent with what has been reported for perovskites (**Table 4.1**). The TRPL intensity was then simulated using **Equation 4.16**. For the BTD model, the carrier concentrations were simulated using **Equations 4.17-4.19** and the rate constants and the concentrations reported for a pristine MAPI thin film in [23] (* in **Table 4.2**): $k_B = 26 \times 10^{-20} \text{ cm}^3/\text{ns}$, $k_T = 12,000 \times 10^{-20} \text{ cm}^3/\text{ns}$, $k_D = 80 \times 10^{-20} \text{ cm}^3/\text{ns}$, $p_0 = 65 \times 10^{12} \text{ cm}^{-3}$ and $N_T = 60 \times 10^{12} \text{ cm}^{-3}$. The TRPL intensity was then simulated using **Equation 4.23**.

Simulation

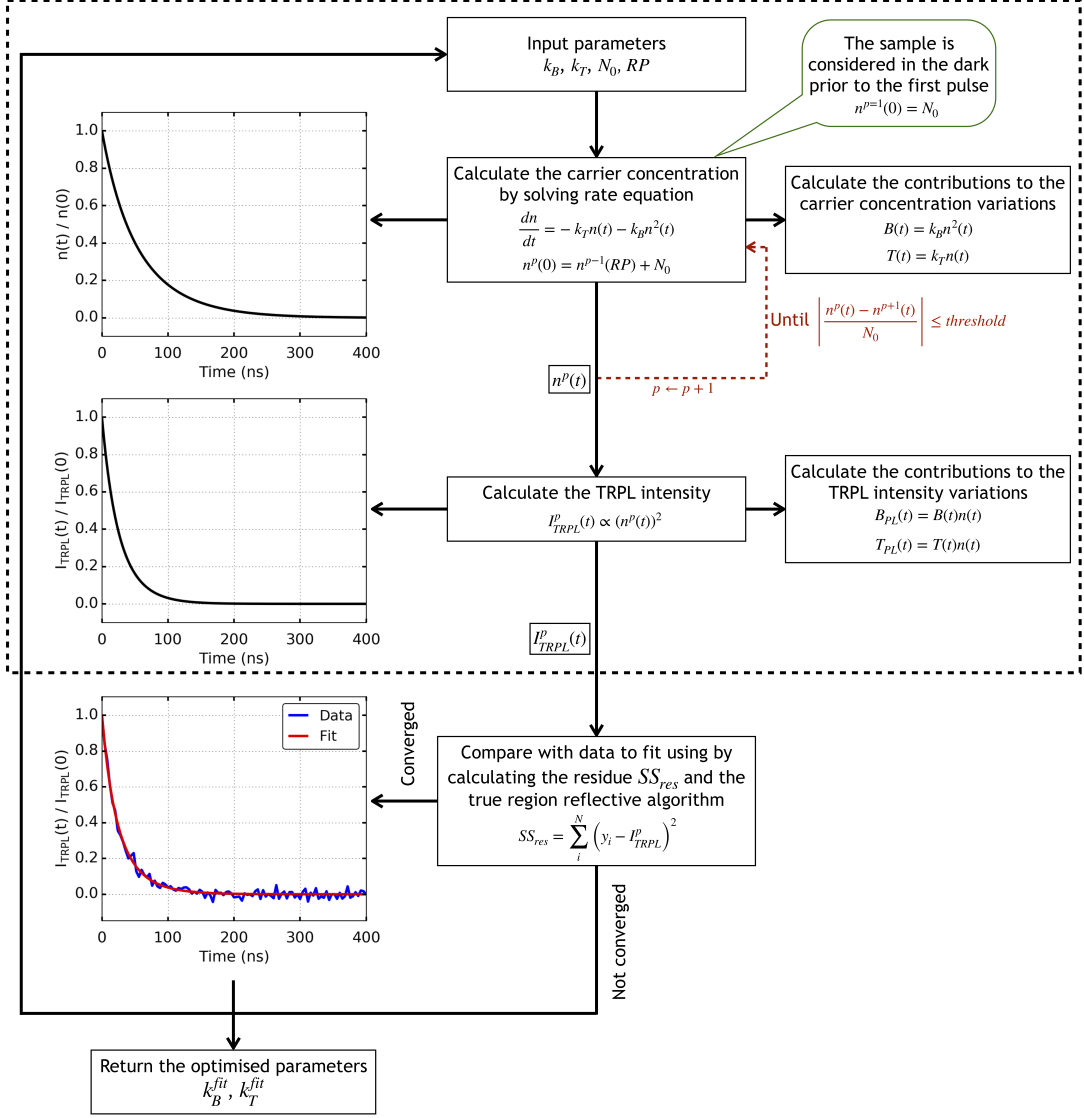


Figure 4.5: Schematic representation of the simulation and fitting procedure exemplified with the bimolecular trapping model. Given a set of parameters k_T , k_B , N_0 and RP , the rate equation is solved to calculate the carrier concentrations after the first excitation pulse $p = 1$. If multiple excitation pulses are simulated (multiple pulse approximation), the carrier concentration $n^{p=1}(RP)$ just before the second pulse $p = 2$ is used to calculate the initial carrier concentration of the second pulse. This iterative process continues until the relative difference between the carrier concentration between a pulse and the next one is lower than a certain threshold. The TRPL intensity is then calculated from the carrier concentration. In the case of fitting, the simulated TRPL intensity is compared to the decay investigated by calculating the residue SS_{res} . If it does not fit, the input parameters are changed and the whole operation is repeated until correct fitting.

The time-scales (repetition period, scale and number of points) used for the simulations were chosen such that the total number of carriers recombined determined

from the sum of the contributions is equal to the carrier concentration N_0 with less than 0.01 % difference (**Figure 4.6**). Time periods of $RP = 1 \mu\text{s}$ for the BT model and $RP = 200 \mu\text{s}$ for the BTD model were found to be suitable while a logarithmic scale with 10^4 points was found to properly define fast processes just after the excitation pulse and slower processes, while keeping the calculation time low.

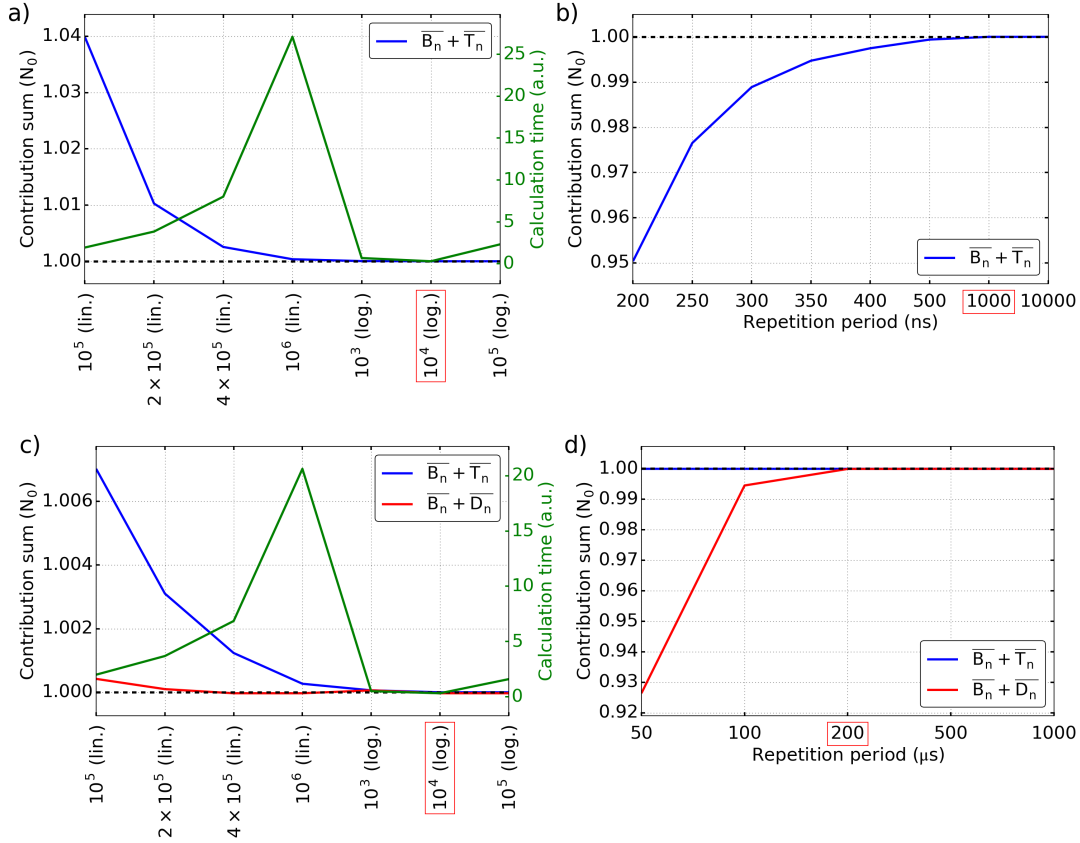


Figure 4.6: Maximum error of the contributions calculated over a range of excitation fluences with the **a)** & **b)** BT ($N_0 \sim 10^{14}—10^{20} \text{ cm}^{-3}$) and **c)** & **d)** BTD ($N_0 \sim 10^{12}—10^{17} \text{ cm}^{-3}$) models, for **a)** & **c)** different time scales (linear or logarithmic) and different number of points (the repetition period is fixed at $RP = 1 \mu\text{s}$ for the BT model and $RP = 200 \mu\text{s}$ for the BTD model) and for **b)** & **d)** different repetition periods (the time scale is fixed at 10^4 points, logarithmic scale). Red boxes indicate the parameters chosen for the simulations allowing fast calculation while maintaining a high level of precision.

Multiple pulse simulations. As discussed in **Section 4.3.1B**, TRPL decays resulting from billions of excitation pulses, as the ones experimentally measured, are simulated with only a few hundred excitation pulses until stabilisation of the carrier concentration(s) after p excitation pulses defined as:

$$\left| n_X^{p-1}(t) - n_X^p(t) \right| \leq 10^{-6} N_0 \quad (4.24)$$

Excitation pulse p is then assumed representative of the carrier concentration in the system after billions of pulses. This method is referred to as the multiple pulse approximation and allows to greatly reduce the calculation cost. As the least square optimisation used for fitting requires multiple simulations of the TRPL intensity, the previous threshold is increased to $10^{-4} N_0$ in order to keep the calculation time reasonable. The effect of carrier accumulation on the carrier concentrations and TRPL intensity is quantified as the absolute difference between the first pulse and the stabilised pulse:

$$\%CA_X = \left| \frac{X^{p=1}}{X^{p=1}(0)} - \frac{X^{p=stabilised}}{X^{p=stabilised}(0)} \right| \quad (4.25)$$

for $X = I_{TRPL}, \Delta n_e, \Delta n_h, n$.

Process contributions. The contribution $C(t)$ of a recombination process (*e.g.* $T_n(t)$ for trapping) corresponds to the rate of charge carriers recombined through such process at a given time t . Over a certain period of time, the total contribution \bar{C} , *i.e.* the total number of carriers recombined through this process, is given by (**Figure 4.7a & b**):

$$\bar{C} = \int C(t) dt \quad (4.26)$$

The relative contribution $\%C(t)$ of a certain process corresponds to the ratio of carriers recombined through this process to the sum $\sum C(t)$ of all carriers recombined at time t ($\sum C(t) = T_n(t) + B_n(t)$ for the BT model and $\sum C(t) = B_n(t) + T_n(t) + D_n(t)$ for the BTD model) (**Figure 4.7c**):

$$\%C(t) = \frac{C(t)}{\sum C(t)} \quad (4.27)$$

Finally, $\%\bar{C}$ is the relative total contribution which corresponds to the percentage of charge carriers recombined through a certain process over a certain period of time (**Figure 4.7d**).

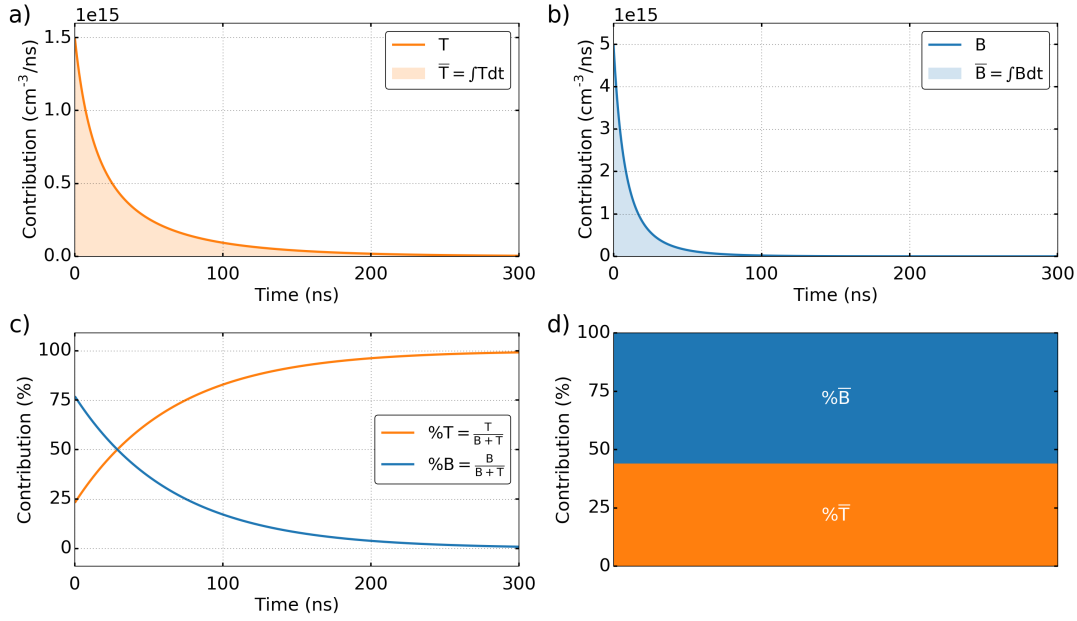


Figure 4.7: Graphical representation of the calculation of the total **a)** trapping \overline{T}_n and **b)** bimolecular \overline{B}_n contributions, **c)** relative contributions ($\%T_n$ & $\%B_n$ respectively) and **d)** relative total contributions ($\%\overline{T}_n$ & $\%\overline{B}_n$ respectively).

As the carrier concentration is not the quantity observed when measuring TRPL, it is necessary to quantify the contribution of each recombination process to the change in the TRPL intensity. In the BT model (**Equation 4.16**), the change in the TRPL intensity over a small period of time dt is:

$$\frac{dI_{TRPL}}{dt} = -\underbrace{2\eta_{esc}k_{RN}(t)B_n(t)}_{B_{PL}(t)} - \underbrace{2\eta_{esc}k_{RN}(t)T_n(t)}_{T_{PL}(t)} \quad (4.28)$$

where $B_{PL}(t)$ and $T_{PL}(t)$ are respectively the bimolecular and trapping contributions to the change in the TRPL intensity. In the BTD model (**Equation 4.23**), the change in the TRPL intensity over a small period of time dt is:

$$\begin{aligned} \frac{dI_{TRPL}}{dt} = & -\underbrace{\eta_{esc}k_R B_n(t) [\Delta n_e(t) + \Delta n_h(t) + p_0]}_{B_{PL}(t)} - \underbrace{\eta_{esc}k_R T_n(t) [\Delta n_h(t) + p_0]}_{T_{PL}(t)} \\ & - \underbrace{\eta_{esc}k_R D_n(t) \Delta n_e(t)}_{D_{PL}(t)} \quad (4.29) \end{aligned}$$

where $B_{PL}(t)$, $T_{PL}(t)$ and $D_{PL}(t)$ are respectively the bimolecular, trapping and detrapping contributions to the change in the TRPL intensity.

4.2.2 Fitting

Fitting optimisation. Fitting was carried using a least-square minimisation of the free parameters (k_B and k_T for the BT model, and k_B , k_T , k_D , p_0 and N_T for the BTD model) as described in **Section 2.6.3**.

Fitting of simulated TRPL decays. In order to investigate the limitations of the models discussed here, fitting was carried out on TRPL decays simulated with the BT and BTD models. In an attempt to reproduce experimental conditions, decays were simulated with 512 points (or channels) with the BT model while 4096 points were used with the BTD model in order to properly resolve the initial fast trapping phase (see **Section 4.3.1A**). For both models, the excitation repetition period used (*i.e.* the time window used) was chosen such that the TRPL intensity reaches $I_{TRPL}(RP)/I_{TRPL}(0) = 10^{-4}$ with both single and multiple pulse approximations (where I_{TRPL} is the TRPL intensity after the first pulse within the single pulse approximation and after the last pulse determined from **Equation 4.24** within the multiple pulse approximation), as TRPL is usually experimentally measured until it reaches “zero”. For the BT model and the multiple pulse approximation, the repetition period was chosen such that $I_{TRPL}(RP)/I_{TRPL}(0) = 0.25$ in order to lead to carrier accumulation. Prior to fitting, noise simulated from a Poisson distribution was added to emulate experimental conditions (an amount of noise reasonably representative of experimental conditions as shown in **Figure 4.8**) and the decays were normalised with respect to their initial intensity.

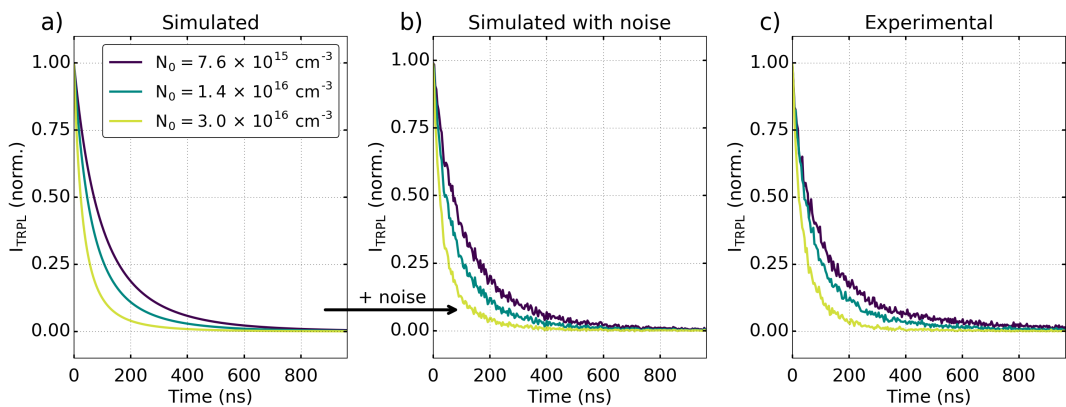


Figure 4.8: Comparison of TRPL decays at different excitation fluencies N_0 **a)** simulated with the bimolecular-trapping model ($k_B = 50 \times 10^{-20} \text{ cm}^3/\text{ns}$, $k_T = 1.7 \times 10^{-3} \text{ ns}^{-1}$), **b)** simulated with Poisson noise and **c)** experimentally measured.

A “best-case scenario” was considered where the same values of the parameters used in the simulated TRPL decays were used as the initial guess values for the fitting optimisation.

Fitting of experimental TRPL decays. Global fitting of experimental TRPL decays measured with different excitation fluences was carried after normalising the decays to their initial intensity and shifting the excitation peak to $t = 0$ (e.g. **Figure 4.8c**). The values previously mentioned and used in the simulations were used as initial guess values.

Initial guess values analysis. In order to ensure that only a unique solution to the fit exists with the BTD model, simulated and experimental TRPL decays were fitted with multiple sets of parameter guess values ($10^{-19}, 10^{-18}, 10^{-17}, 10^{-16}$ cm³/ns for the rate constants and $10^{13}, 10^{14}, 10^{15}, 10^{16}$ cm⁻³ for the concentrations) as graphically described in **Figure 4.9**. In order to keep the number of fits down, only sets of guess values satisfying $k_T > k_B$ and $k_T > k_D$ were considered. This analysis is applied to low ($N_0 = 10^{12}$ cm⁻³), medium ($N_0 = 3.5 \times 10^{14}$ cm⁻³) and high ($N_0 = 10^{17}$ cm⁻³) excitation fluence simulated TRPL decays. Similar solutions (i.e. set of parameters k_B, k_T, k_D, p_0 and N_T) with less than 2 % relative difference are considered identical. It is also assumed that any values below a certain threshold (10^{-23} cm³/ns for the rate constants and 10^{-9} cm⁻³ for the concentrations) are identical.

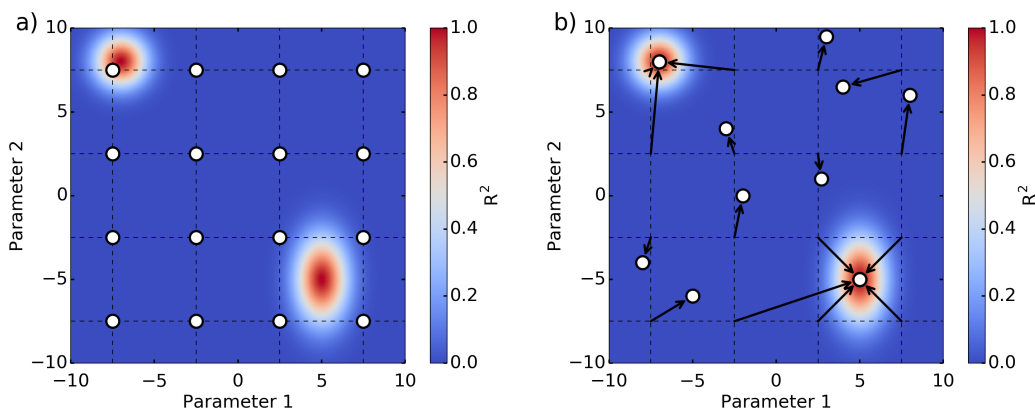


Figure 4.9: Representation of the initial guess value analysis. **a)** A grid of guess values is created. **b)** The fitting optimisation is carried with each set of guess values. Here, 3 and 5 optimisations converge toward 2 distinct solutions while the remaining optimisations yield incorrect solutions as indicated by their low R^2 .

4.2.3 Sample manufacturing & instrumentation

Sample manufacturing. The MAPI perovskite precursor solution was prepared in ambient atmosphere from a 1.25M:1.25M solution of PbI_2 , (*Sigma-Aldrich*, 99 %) and MAI, (*Dyesol*) in 4:1 (v:v) DMF (*Sigma-Aldrich*, ≥ 99.8 %): DMSO (*Sigma-Aldrich*, ≥ 99.9 %). The solution was heated at 60°C until dissolution. Glass substrates were cleaned using *Hellmanex III*, acetone and isopropanol consecutively. The substrates were cleaned with an O_2 plasma for 5 min just before spin-coating to improve the spreading of the solution. 100 μL of perovskite solution was spin-coated at 4500 rpm (4500 rpm/s acceleration) in an ambient atmosphere for 30 s. 200 μL of ethyl acetate was deposited while spinning after 15 s as an anti-solvent treatment to promote crystallisation [43]. The film was then annealed at 100°C for 10 min. In order to hinder degradation by moisture during the measurements, a thin polymethyl methacrylate (PMMA) layer was spin-coated on top of the perovskite layer at 4500 rpm (4500 rpm/s acceleration) for 30 s from a 1.0 M solution of PMMA dissolved in toluene. Finally, the film was annealed at 70°C for 30 min.

Instrumentation. TRPL was measured using an *Edinburgh Instruments Lifespec 2* TCSPC operating in reverse mode (see **Section 2.2.3** for more details). The laser spot size was measured perpendicular to the laser beam using an *Edmund Optics Beam Profiler 4M*. The ellipsoidal spot semi-axis lengths were calculated through gaussian fitting at $1/e^2$ intensity. In order to optimise photon collection, samples were placed at a 45° incidence angle with respect to the laser beam and the measured laser spot size was accordingly corrected, giving a laser fluence of $I_0 = 1.09 \times 10^{12}$ photons/ cm^2 for a laser repetition period of $RP = 1$ μs . The sample emission was measured at $\lambda_{em} = 770$ nm with an emission slitwidth of $\Delta\lambda_{em} = \pm 17.5$ nm.

Absorptance was measured using a *Perkin Elmer Lambda 750* UV/Vis spectrophotometer coupled with a 100 mm integrating sphere (see **Section 2.1** for more details). A 100 % and 0 % transmittance baselines were performed before measurement. The film thickness was measured with a *Dektak 6M* profilometer.

4.3 Results & Discussions

The MAPI film is 295 ± 5 nm thick, and presents a 82 % absorptance at 405 nm (ignoring any reflection or absorption from the PMMA film). Its TRPL was measured

on the film side with three excitation fluences generating the following carrier concentrations N_0 : $7.6 \times 10^{15} \text{ cm}^{-3}$; $1.4 \times 10^{16} \text{ cm}^{-3}$ and $3.0 \times 10^{16} \text{ cm}^{-3}$.

Since only the specular PL was measured and only one or zero photon is measured by a TCSPC after each excitation pulse, the TRPL absolute intensity cannot be used to extract information such as the escape probability η_{esc} and the radiative recombination rate k_r . Therefore, only the normalised TRPL intensity is discussed in this chapter (although the relative TRPL intensity can be used to determine the doping concentration as discussed in **Section 4.3.2A**).

Photobrightening has been previously shown to affect the doping and trap state concentrations along with the recombination rates of MAPI, altering its TRPL intensity and profile [44]–[46]. This can be observed by repeatedly measuring a sample over time leading to an overall increase of the decay lifetime (**Figure 4.10a**). Degradation of the perovskite can also be expected to affect the electronic properties of MAPI and thus its TRPL. This is especially a problem in the case of long measurements which thus require stability of the sample over a long period of time. **Figure 4.10b** shows TRPL decays measured with 3 different excitation fluences and shows significant changes of the TRPL intensity between the first and second run.

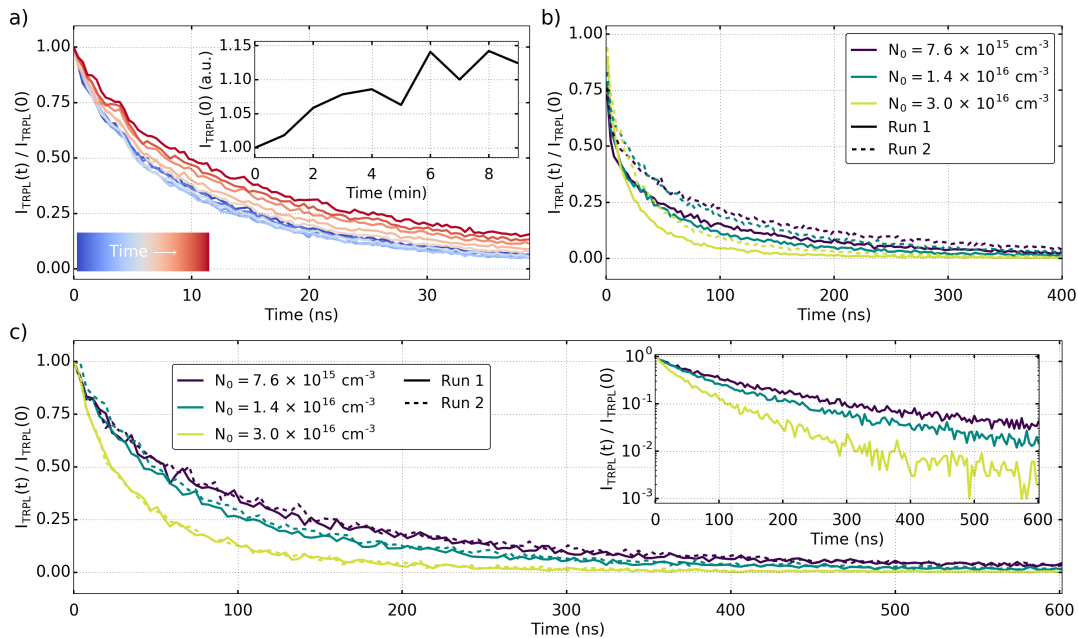


Figure 4.10: TRPL of a MAPI thin film. **a)** Consecutive TRPL decays (excitation repetition period $RP = 50$ ns) measured for 60 s each over 10 min. Inset: evolution of the TRPL initial intensity over time. Set of fluence-dependent measurements with **b)** bad reproducibility ($RP = 500$ ns) and **c)** good reproducibility ($RP = 1 \mu\text{s}$) (inset: logarithmic scale).

As discussed in **Chapter 3**, both photobrightening and degradation can be slowed down by keeping the sample in a N₂ atmosphere. Unfortunately, such experiment was not possible at the time. Instead, the sample was left under illumination until the profile and intensity of the decay remained constant. Photobrightening and degradation were assumed negligible if each set of measurement could be reproduced at least once as in **Figure 4.10c**. In the following sections, the BT and BTD models are used to fit these experimental measurements and the limitation of each model is discussed.

4.3.1 Bimolecular-trapping model

The application of the BT model to describe TRPL decays of perovskite samples is discussed. First discuss the excitation fluence dependence on TRPL after the first excitation pulse (the superscript notation is ignored here for clarity *i.e.* $n^{p=1} = n$). This is an important topic as TRPL decays are usually reported at a variety of fluences in the literature, making comparisons across the literature difficult. The accuracy of the values retrieved from fitting these decays simulated with added noise at different excitation fluences is also discussed. In the second section, the importance of allowing recombination of all photoexcited charge carriers for fitting with a single pulse, advice on how to avoid charge accumulation in the systems measured and multiple pulse fitting are discussed. Finally, the BT model is used to fit the experimental TRPL decays.

A Fluence regimes

The fluence dependence of the BT mode is investigated by simulating the carrier concentration and TRPL for a wide range of initial carrier concentrations N_0 . Within this model, the carrier concentration normalised to its initial value $n(t)/N_0$ (and therefore the normalised TRPL intensity) is observed to decay faster at increasing N_0 (**Figure 4.11a**) [20]. In order to estimate the effect of trapping and bimolecular recombination on the TRPL decay, their contribution to the change in the TRPL intensity, $\% \overline{T_{PL}}$ and $\% \overline{B_{PL}}$ respectively are investigated. In particular, it is noted that $\% \overline{T_{PL}}$ and $\% \overline{B_{PL}}$ are respectively lower and higher than the contributions to the change in the carrier concentrations $\% \overline{T_n}$ and $\% \overline{B_n}$ as the square of the carrier concentration favours bimolecular contribution, which means that bimolecular recombination has a greater effect on the TRPL profile than trapping (**Figure 4.11c**).

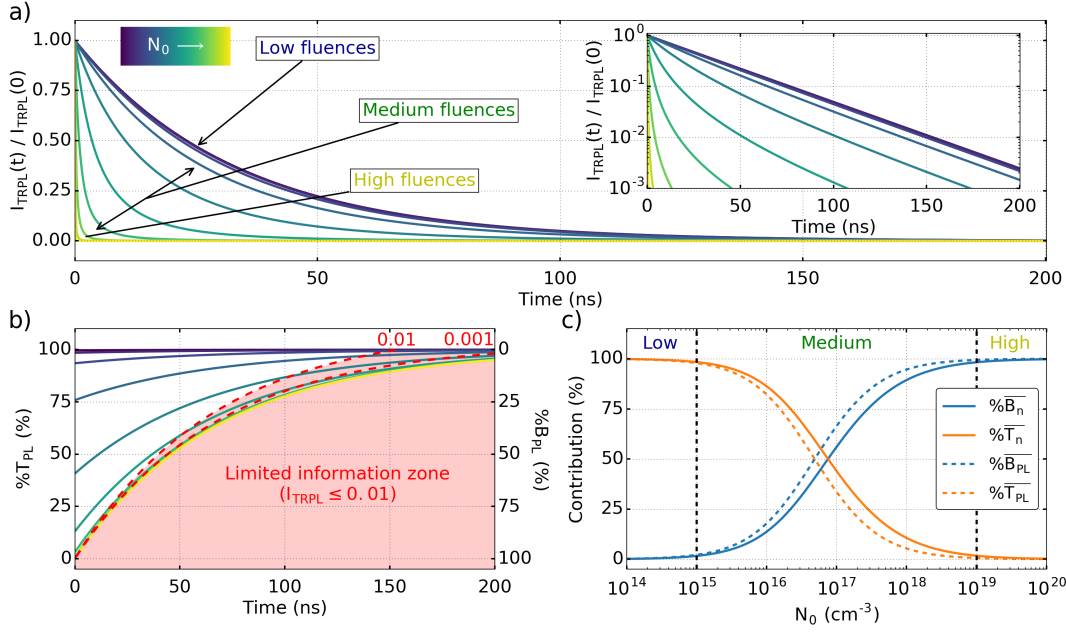


Figure 4.11: Fluence dependence on the recombination process contributions and the determination of their rate constants as predicted by the bimolecular-trapping model. **a)** Simulated TRPL decays (inset: logarithmic scale), **b)** relative trapping $\%T_{PL}$ and bimolecular $\%B_{PL}$ contributions to the change in the TRPL intensity and **c)** total bimolecular and trapping contributions to the change in the carrier concentration ($\%B_n$ and $\%T_n$) and the TRPL intensity ($\%B_{PL}$ and $\%T_{PL}$) at increasing excitation fluences ($N_0 \sim 10^{14} \text{ cm}^{-3} \text{—} 10^{20} \text{ cm}^{-3}$). In **b)** the red dashed lines indicate where the associated normalised TRPL intensity becomes lower than 0.01 and 0.001. The red area defines the time for each excitation fluence over which the TRPL intensity is lower than 0.01 and thus where information about trapping may not be recoverable.

Under low excitation fluence (here $N_0 < 10^{15} \text{ cm}^{-3}$), trapping is the dominant recombination process as $k_T N_0 \gg k_B N_0^2$ as indicated by the dominant trapping contribution $\%T_{PL}$ close to 100 % over the whole time-range in **Figure 4.11b** (blue curves). Consequently, the total trapping contribution $\%T_{PL}$ is close to 100 % while the total bimolecular contribution $\%B_{PL}$ is negligible (**Figure 4.11c**). In this regime, the BT rate equation and TRPL (**Equations 4.14 & 4.16**) can be simplified to:

$$\frac{dn}{dt} \approx -k_T n(t) \Rightarrow I_{TRPL}(t) \propto e^{-2k_T t} \quad (4.30)$$

The TRPL therefore follows a mono-exponential trend dependent only on the trapping rate constant k_T and therefore independent on the initial carrier concentration N_0 (blue curves in **Figure 4.11a**). The low contribution of bimolecular recombination in this regime may lead to inaccurate determination of the bimolecular recombination

rate constant k_B when fitting such TRPL decays. To illustrate this, noise is added to the previous TRPL decays to emulate experimental conditions (**Figure 4.12a**). The decay are then fitted using the BT model using the simulation parameters (k_T and k_B) as guess values to emulate a “best case scenario”. At low fluence, the trapping rate constant k_T is accurately retrieved but not the bimolecular rate constant k_B even though the correct values of the parameters were used as initial guess (**Figure 4.12b**). This highlights well that the BT model may not be able to accurately recover information depending on the fluence. Improving the S/N allows to retrieve k_B at lower fluences as shown in **Figure 4.12d**.

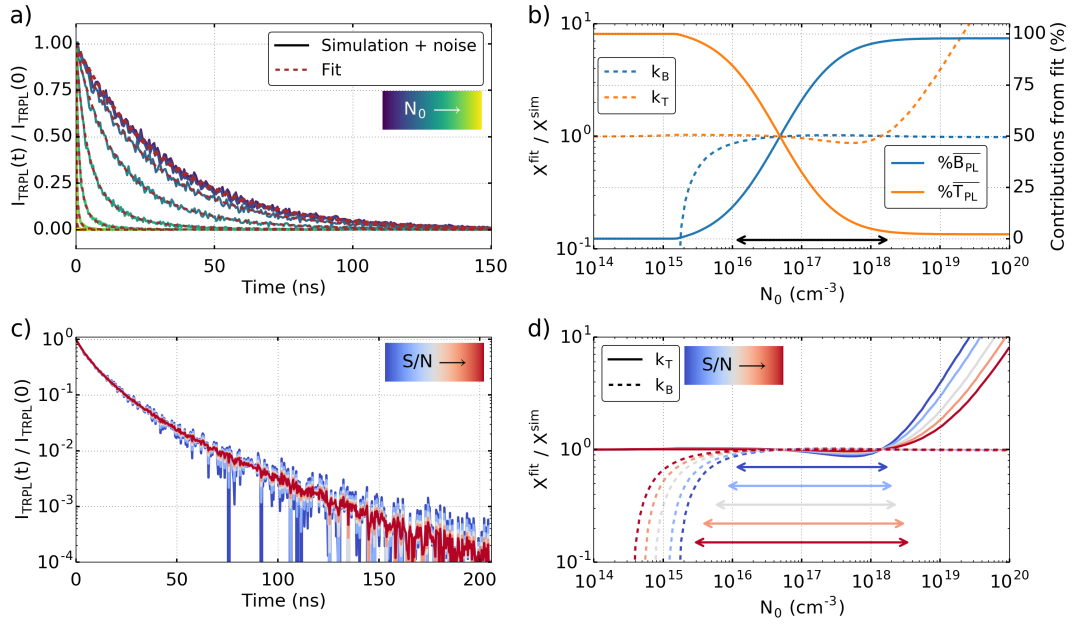


Figure 4.12: Fitting of simulated TRPL decays with added noise with the BT model. **a)** TRPL decays simulated with the bimolecular-trapping model at increasing excitation fluences with added noise and associated fits, and **b)** relative values of the trapping k_T and bimolecular k_B rate constants retrieved from the fits, and trapping $\%T_{PL}$ and bimolecular $\%B_{PL}$ contributions to the TRPL intensity changes calculated from the fits. The double arrow indicates the fluence region where both recombination rate constants can be accurately retrieved with less than 15 % error. **c)** TRPL decays simulated with increasing signal to noise ratio (S/N) ($N_0 = 1.1 \times 10^{17} \text{ cm}^{-3}$) and **d)** relative value of k_T and k_B retrieved from fitting simulated TRPL decays at different excitation fluences with different amounts of noise.

Under medium excitation fluence ($k_T N_0 \sim k_B N_0^2$, here $N_0 \sim 10^{15}—10^{19} \text{ cm}^{-3}$), the bimolecular and trapping contributions are comparable, with bimolecular recombinations dominant in the initial part of the decay and trapping dominant in its tail (green curves in **Figure 4.11b**). The TRPL profile is dependent on the initial

carrier concentration (green curves in **Figure 4.11a**). Since both $\%T_{PL}$ and $\%B_{PL}$ are non-negligible, it is possible to accurately retrieve both recombination rate constants from the fitting of a simulated medium fluence TRPL decays with added noise as shown in **Figure 4.12b**.

Under high excitation fluence ($k_B N_0^2 \gg k_T N_0$, here $N_0 > 10^{19} \text{ cm}^{-3}$), the bimolecular contribution is initially dominant but quickly decreases as the carrier concentration $n(t)$ decreases while the trapping contribution increases (yellow curves in **Figure 4.11b**). It may thus be possible to retrieve the trapping rate constant at the tail of the TRPL decay where the carrier concentration is low and $\%T_{PL}$ is non-negligible. However, the noise present in experimental TRPL decays limits the determination of the trapping rate constant as the S/N is lower at lower TRPL intensity (*i.e.* at the tail of the decay). For example, the time at which the normalised TRPL intensity reach 0.01 is shown as dashed red lines in **Figure 4.11b**. Under high fluence, trapping only contributes a few percent of the total recombinations before the TRPL reaches 0.01 normalised intensity in **Figure 4.11b** (yellow curves). Consequently, fitting TRPL decays simulated at high excitation fluences with added noise yields an accurate value of k_B but not of k_T (**Figure 4.12d**). Improving the S/N (*e.g.* 0.001 curve in **Figure 4.11b**) increases the range of excitation fluences where the trapping rate can be accurately retrieved (**Figure 4.12d**).

It may thus not be possible to accurately retrieve both bimolecular and trapping rate constants when fitting TRPL decays with the BT model depending on the excitation fluence. Global fitting of TRPL decays measured over a wide range of excitation fluences can help improve the accuracy of the values retrieved by preventing all the decays to be within the low or high regime. More generally, the accuracy of the rate constant values retrieved from fitting (at any fluence) can be estimated by calculating the total bimolecular and trapping contributions using these values. For example, in **Figure 4.12b**, the values from fitting become inaccurate when $\%B_{PL}$ and $\%T_{PL}$ get close to zero, respectively at low and high fluence, consistent with the previous observations. It is worth mentioning that the contribution threshold where the rate constant values become inaccurate is dependent upon the S/N ratio. For example, at the lowest S/N used in **Figure 4.12d**, k_B is inaccurate when $\%B_{PL}$ is lower than 17 %, while with the highest S/N used, the rate constant value is inaccurate for $\%B_{PL} < 3 \%$.

B Carrier accumulation

As TCSPC measurements generally require millions to billions excitation pulses to obtain an appropriate S/N, fitting experimentally measured TRPL by simulating only the first excitation pulse (discussed in **Section 4.3.1A** and referred to as the single pulse approximation hereafter) requires that most charge carriers recombine between two consecutive excitation pulses. To illustrate this, the evolution of the carrier concentration after multiple consecutive pulses with excitation repetition periods $RP = 25$ ns and $RP = 200$ ns are compared (**Figure 4.13a**).

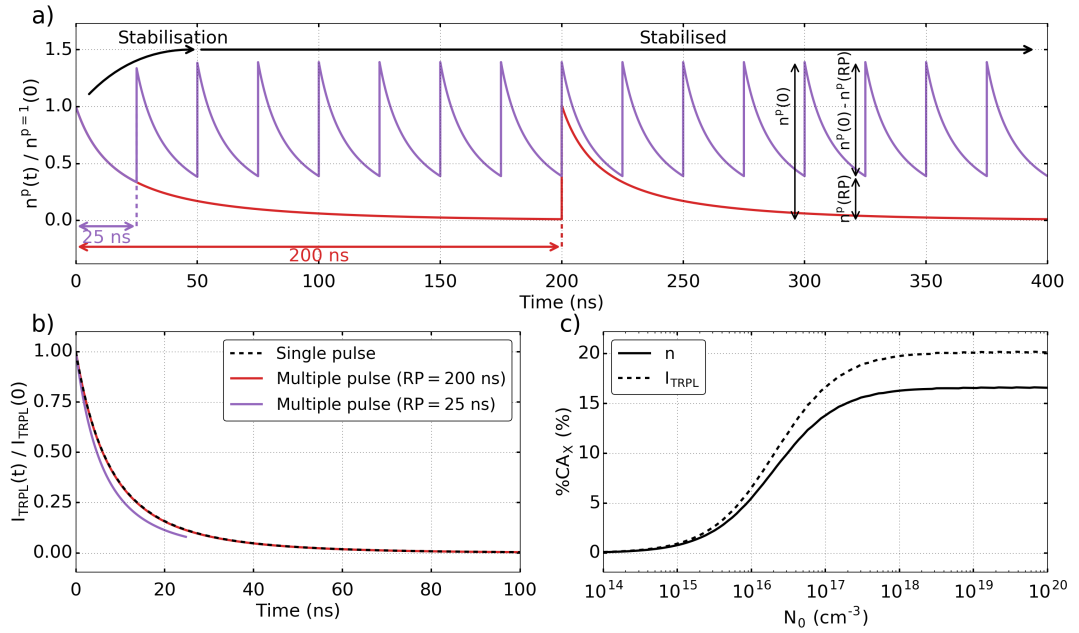


Figure 4.13: Effect of the incomplete depopulation on the carrier concentration and TRPL as predicted by the bimolecular-trapping model at medium fluence excitation ($N_0 = 10^{17}$ cm⁻³) and different excitation repetition periods ($RP = 200$ ns, $RP = 25$ ns). **a)** Carrier concentration $n^p(t)$ normalised to its initial value after the first excitation pulse $n^{p-1}(0)$ over 400 ns and **b)** associated normalised TRPL intensity after 10^9 pulses. The TRPL decay simulated after a single pulse is also shown for comparison. **c)** Normalised difference $\%CA_X$ of the TRPL and carrier concentration between the first and stabilised pulse calculated at different excitation fluences, with a repetition period satisfying $I_{TRPL}(RP)/I_{TRPL}(0) = 0.25$.

In both cases, the first pulse excites $n^{p-1}(0) = N_0$ carriers. When measured with $RP = 200$ ns, $n^{p-1}(RP) = 0.01N_0$ carriers are left in the bands just before the second excitation pulse (red curve). The initial carrier concentration of the second excitation pulse is thus $n^{p-2}(0) = n^{p-1}(RP) + N_0 = 1.01N_0$ leading to a similar variation of the carrier concentration as after the first one (**Figure 4.13a**). The resulting TRPL decay

after 10^9 pulses is thus similar to the TRPL decay simulated with only the first excitation pulse (**Figure 4.13b**). In this case, the system after many excitation pulses can be approximated with the only first excitation pulse, therefore allowing to fit the TRPL decays by simulating a unique excitation pulse. Conversely, with $RP = 25$ ns, $n^{p=1}(RP) = 0.34N_0$ carriers are left in the system before the second excitation pulse (purple curve in **Figure 4.13a**). The higher initial carrier concentration of the second pulse $n^{p=2}(0) = 1.34N_0$ accelerates the recombination due to the higher bimolecular contribution. The TRPL decay obtained after 10^9 pulses is 2.5 times more intense than the single pulse TRPL decay (not shown here) and decays faster due to the higher carrier concentration (**Figure 4.13b**). Such decay cannot be fitted using the single pulse approximation and would require the simulation of all the excitation pulses. The accumulation of charge carriers in the system continues until as many carriers recombine after an excitation pulse as carriers are generated by the latter (**Figure 4.13a**):

$$n^p(0) - n^p(RP) = N_0 \quad (4.31)$$

Assuming that the carrier concentration stabilises over a small fraction of the total number of excitation pulses experimentally required to obtain a good S/N TRPL decay, it is possible to simulate and fit TRPL decays resulting from billions of excitation pulses by only simulating a small fraction and by considering the last simulated pulse to be representative of the system measured (referred to as the multiple pulse approximation hereafter).

The effect of this carrier accumulation (CA) on the carrier concentration and TRPL decays is quantified by calculating the absolute difference between the first and last simulated pulses (**Figure 4.13c**). CA does not affect the profile of the TRPL decay at low fluences as monomolecular recombination does not depend on the carrier concentration (although the increased initial carrier concentration may drive the system in the medium fluence regime where the TRPL profile depends upon the initial carrier concentration). At higher fluence, CA affects the shape of the carrier concentration and TRPL decays due to the non-negligible bimolecular contributions at these fluences.

It is essential to avoid CA in order to use single pulse fitting. This can be ensured by choosing an excitation repetition period such that the TRPL decay reaches zero. The

TRPL decay can only reach zero if the TRPL intensity after each pulse I_{TRPL}^p reaches zero by the end of the repetition period as per **Equation 4.1**:

$$I_{TRPL}(RP) = 0 \Rightarrow I_{TRPL}^p(RP) = 0 \quad (4.32)$$

Since the TRPL intensity is proportional to the square of the carrier concentration, **Equation 4.32** implies that the carrier concentrations also reach zero:

$$I_{TRPL}^p(RP) = 0 \Rightarrow n^p(RP) = 0 \quad (4.33)$$

As per **Equation 4.31**, this means that the initial carrier concentration of each pulse is $n^p(0) = N_0$ and therefore CA is negligible. It is thus straightforward to avoid CA according to the BT model by choosing an excitation repetition period such that the TRPL decay is fully measured (*e.g.* when I_{TRPL} is at least 0.01 % it indicates under 1 % of non-recombined charge carriers as with a $RP = 200$ ns repetition period in **Figure 4.13**).

In the case where CA cannot be avoided, it is possible to fit TRPL decays using the multiple pulse approximation. However, multiple pulse fitting presents multiple disadvantages compared to single pulse fitting. Multiple pulse fitting is much slower due to the requirement of simulating multiple pulses at each step of the least square optimisation. Furthermore, measuring incomplete decays (*i.e.* without their tail) reduces the range of fluences where k_T can be accurately retrieved. Last, the higher initial carrier concentration due to CA drives the system toward the high fluence regime where the accuracy of k_T retrieved from fitting is lower. This is demonstrated by fitting TRPL decays simulated with the multiple pulse approximation, with multiple pulse fitting. TRPL decays are simulated with the multiple pulse approximation over a wide range of excitation fluences. For each fluence, the repetition period is chosen such that the decay obtained after many pulses is incomplete and only reach $I_{TRPL}(RP)/I_{TRPL}(0) = 0.25$, and therefore presents significant CA (dashed curves in **Figure 4.14a**, **Figure 4.14b**). These decays were then fitted using the multiple pulse approximation. Comparing the rate constants obtained from single and multiple pulse fitting show that k_T is not accurately retrieved above $N_0 = 1.1 \times 10^{17} \text{ cm}^{-3}$ with multiple pulse fitting while it can be retrieved up to $N_0 = 1.8 \times 10^{18} \text{ cm}^{-3}$ with single pulse fitting (given a maximum 15 % error) (**Figure 4.14c**). This can be explained by the lower trapping contribution in the

multiple pulse decays due to 1) the absence of the tail of the decays where trapping is more important and 2) the higher initial carrier concentration of the stabilised pulse in the multiple pulse decays, both reducing the trapping contribution (**Figure 4.14d**). In both cases, the bimolecular rate constant k_B can only be accurately retrieved down to $N_0 \approx 10^{16} \text{ cm}^{-3}$. The region where both rate constants can be accurately retrieved is thus much shallower with the multiple pulse approximation than with the single pulse approximation. Measuring TRPL decays reaching zero which can be fitted with the single pulse approximation is thus preferable compared to truncated decays which need to be fitted with the multiple pulse approximation.

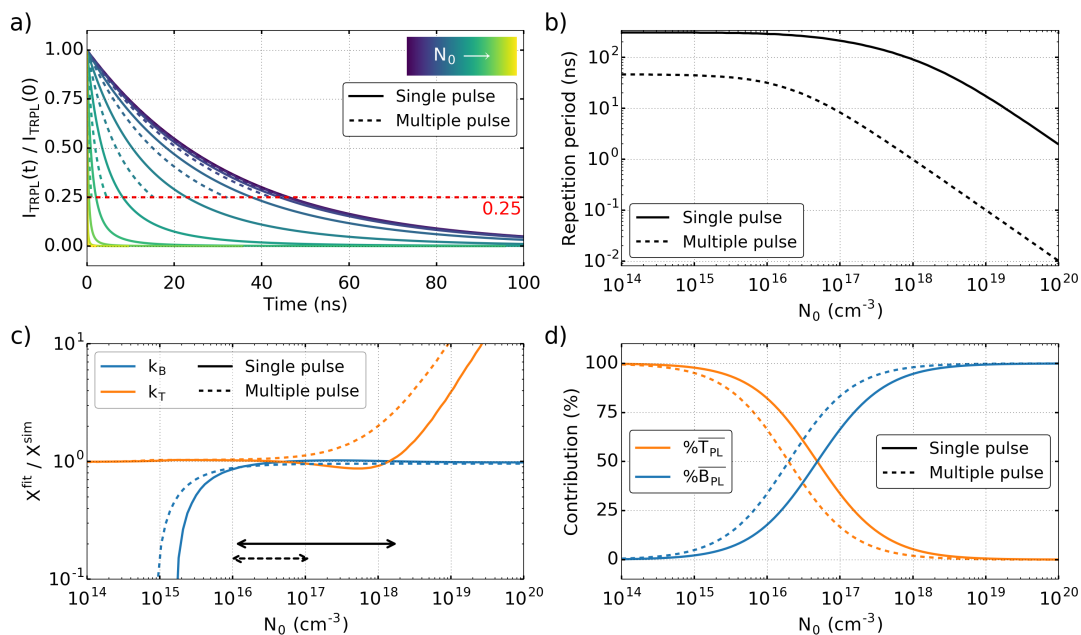


Figure 4.14: Comparison of single pulse and multiple pulse fitting. **a)** TRPL decays calculated using the single pulse (full lines) and multiple pulse (dashed lines) approximations at increasing excitation fluences. For the single pulse decays, the repetition period is chosen such that $I_{TRPL}(RP)/I_{TRPL}(0) = 10^{-4}$, while for the multiple pulse decays it is chosen such that $I_{TRPL}(RP)/I_{TRPL}(0) = 0.25$ and is shown in **b)**. **c)** Relative values of the trapping k_T and bimolecular k_B rate constants retrieved from single pulse and multiple pulse fitting of the corresponding TRPL decays with added Poisson noise ($R^2 > 0.989$). The full and dashed double arrows show the range of fluences for which both rate constant can be accurately retrieved with less than a 15 % error with the single pulse and multiple pulse fits respectively. **d)** Relative total trapping ($\%T_{PL}$) and bimolecular ($\%B_{PL}$) contributions to the change in the TRPL intensity calculated with the single pulse approximation (full curve) and the multiple pulse approximation (dashed curves).

C Experimental decay fitting

All the experimentally measured TRPL decays reach almost zero within the excitation repetition period suggesting negligible CA and therefore the decays can be fitted using the single pulse approximation (**Figure 4.15a**). In order to ascertain this, multiple pulse fitting is also used.

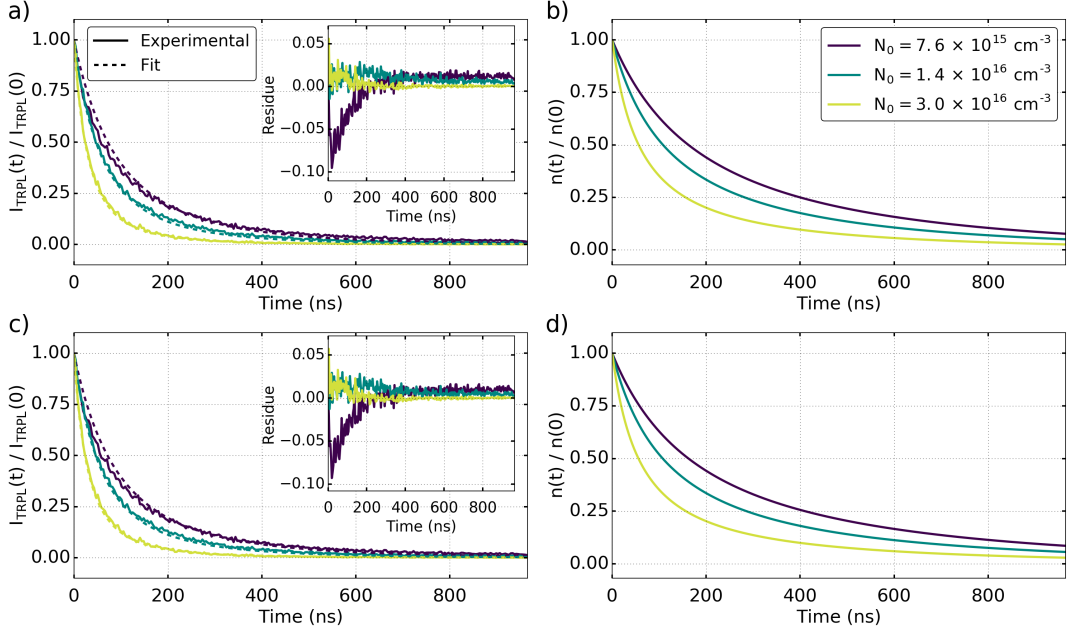


Figure 4.15: Fitting of the experimental TRPL decays using the bimolecular-trapping model and the **a)** single pulse ($R^2 = 0.992$) and **c)** multiple pulse ($R^2 = 0.993$) approximations (insets: residuals), and associated carrier concentration after **b)** the first excitation pulse and **d)** the stabilised pulse calculated from the fits.

The model fits well the experimental TRPL at the two highest excitation fluences used but shows a significant negative residue for the lowest fluence. This indicates that the TRPL decays faster than predicted by the model as this fluence which could be due to fast trapping as predicted by the BTD model (see **Section 4.3.2A**). The single pulse and multiple pulse fits yield similar trapping and bimolecular recombination rate constant values which are within range of values previously reported in the literature (**Table 4.3**).

Table 4.3: Values of the fitting parameters obtained using the bimolecular-trapping model compared to values reported in the literature.

	k_T (10^{-3} ns $^{-1}$)	k_B (10^{-20} cm 3 /ns)
Single pulse	1.55	51.1
multiple pulse	1.30	51.2
[24]	180	17
[38]	3-28	51-220
[26]	5	8.1
[39]	14	92

The accuracy of the values retrieved is estimated by calculating the bimolecular $\% \overline{B_{PL}}$ and trapping $\% \overline{T_{PL}}$ contributions to the change in the TRPL intensity as discussed in **Section 4.3.1A (Figure 4.16a)**. For both single and multiple pulse fits, the higher bimolecular contribution is 84.9 % and 87.2 % while the highest trapping contribution is 39.6 % and 33.7 % respectively. This suggests that bimolecular recombination and trapping are non-negligible here and therefore the values retrieved are accurate. It is also noted that the single pulse and multiple pulse fits respectively predicts a maximum 7 % and 9 % increase of the initial carrier concentration leading to a maximum $\%CA_{PL} = 1.5$ % and $\%CA_{PL} = 1.9$ % difference between the normalised TRPL intensity obtained after the first and stabilised pulses with the excitation fluences used (**Figure 4.16b**). Both fits therefore predict negligible CA in the sample at all the fluences used.

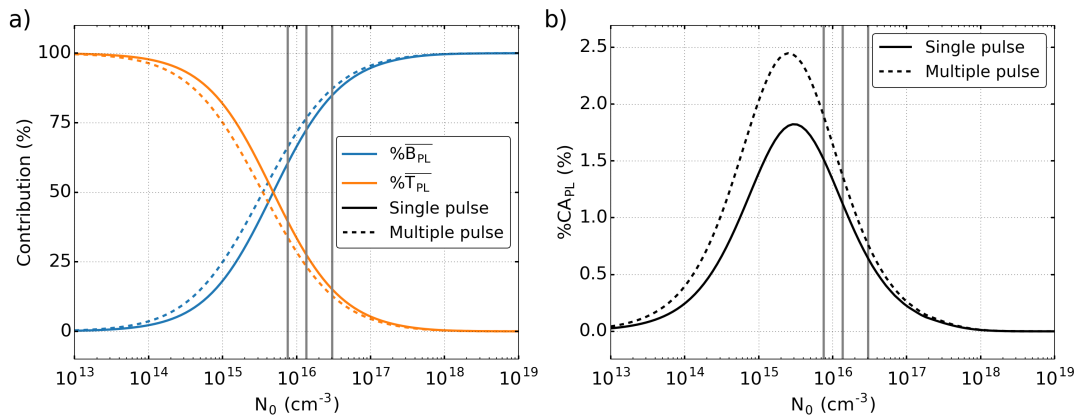


Figure 4.16: **a)** Bimolecular and trapping contributions and **b)** absolute difference between the first and last simulated pulses calculated from the single and multiple pulse fits. Vertical grey lines indicate the excitation fluences experimentally used.

4.3.2 Bimolecular-trapping-detrapping model

Contrary to the BT model, the BTD model does not consider the trap states to remain empty at all time. For the following analysis and discussion, it is assumed that the doping concentration is of the same order of magnitude than the trap state concentration, and that the trapping rate constant is much higher than the bimolecular and detrapping rate constants, consistent with the values reported in [23]. As for the BT model, the excitation fluence dependence after the first excitation pulse is first discussed (the superscript notation is ignored here for clarity *i.e.* $n_X^{p=1} = n_X$). The accuracy of the values retrieved from fitting these decays simulated with added noise at different excitation fluences and with different fitting guess values is also discussed. In the second section, the importance of allowing recombination of all trapped electrons for fitting with a single pulse, advice on how to avoid charge accumulation in the systems measured and multiple pulse fitting are discussed. Finally, the BTD model is used to fit the experimental TRPL decays.

A Fluence regimes

The fluence dependence of the BTD model is investigated by simulating the carrier concentration and TRPL for a wide range of initial carrier concentrations. Contrary to the BT model, the BTD model does not predict a straightforward trend of the TRPL profile (**Figure 4.17a**). It is noted that over the whole fluence range studied, the total trapping $\%T_n$ and detrapping $\%D_n$ contributions are always equal since as many carriers get trapped and detrapped, however, their contribution to the change in the TRPL intensity are different as discussed hereafter (**Figure 4.17c**).

Under low excitation fluence (*i.e.* $N_0 \ll N_T$, here $N_0 < 5 \times 10^{12} \text{ cm}^{-3}$), the hole concentration can be assumed constant and equal to the doping concentration (*i.e.* $\Delta n_h + p_0 \approx p_0$), and therefore the bimolecular contribution has a monomolecular behaviour:

$$B_n(t) \approx k_B \Delta n_e(t) p_0 \quad (4.34)$$

As the photoexcited electron concentration is much lower than the trap states concentration, the trap states can be considered empty at all time (*i.e.* $N_T - n_t \approx N_T$ as $n_t \leq \Delta n_e \ll N_T$) and the trapping contribution has also a monomolecular behaviour:

$$T_n(t) \approx k_T \Delta n_e(t) N_T \quad (4.35)$$

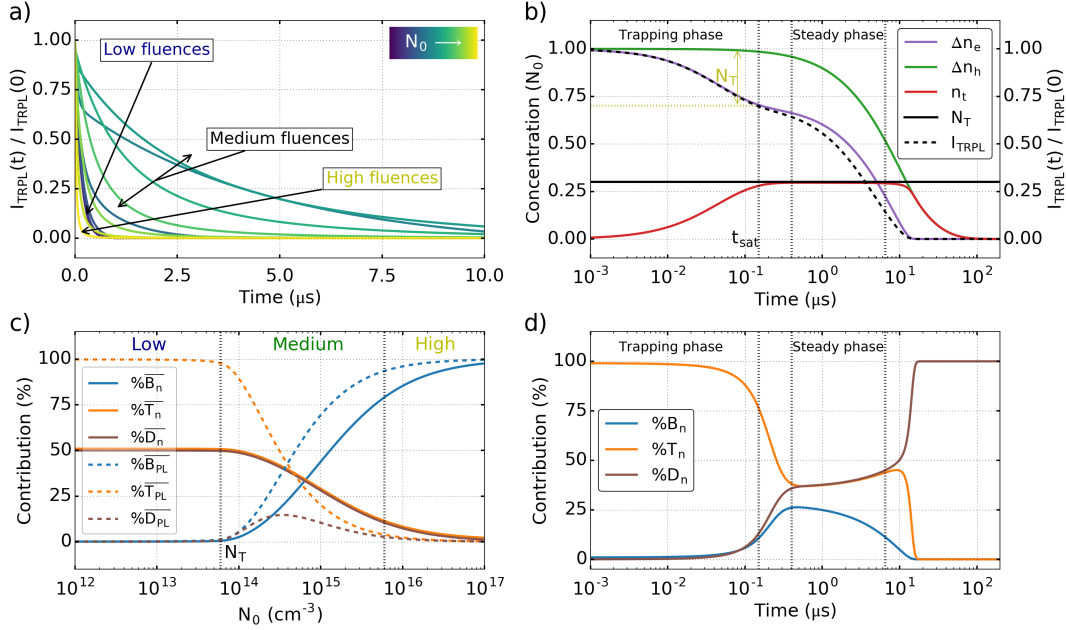


Figure 4.17: Fluence effect on the recombination processes predicted by the bimolecular-trapping-detrapping model. **a)** TRPL decays and **c)** total bimolecular, trapping and detrapping contributions to the change in the carrier concentrations ($\% \overline{B}_n$, $\% \overline{T}_n$ and $\% \overline{D}_n$ respectively, full curves) and TRPL intensity ($\% \overline{B}_{PL}$, $\% \overline{T}_{PL}$ and $\% \overline{D}_{PL}$ respectively, dashed curves) at increasing excitation fluences ($N_0 \sim 10^{12} - 10^{17} \text{ cm}^{-3}$). **b)** Evolution of the photoexcited electron (Δn_e), hole (Δn_h) and trapped electron (n_t) concentrations, and TRPL intensity (I_{TRPL}), and **d)** associated relative bimolecular ($\% B_n$), trapping ($\% T_n$) and detrapping ($\% D_n$) contributions after an excitation pulse generating $N_0 = 2 \times 10^{14} \text{ cm}^{-3}$ (N_T : trap state concentration).

The bimolecular and trapping processes are therefore undistinguishable in this regime. Since the hole concentration is constant, the TRPL intensity follows the same trend as the electron concentration and its shape does not depend on the excitation fluence (blue curve in **Figure 4.17a**):

$$I_{TRPL}(t) \approx p_0 \Delta n_e \propto e^{-(k_B p_0 + k_T N_T)t} = e^{-k_M t} \quad (4.36)$$

where $k_M = k_B p_0 + k_T N_T$. In the present simulations, it is assumed $k_T N_T \gg k_B p_0$ and therefore the TRPL decays only depend on the product $k_T N_T$. This is consistent with the negligible bimolecular $\% \overline{B}_{PL}$ and detrapping $\% \overline{D}_{PL}$ contributions to the change in the TRPL intensity shown in **Figure 4.17c**. As discussed for the BT model, only k_M

can be retrieved from fitting TRPL decays in this regime and therefore any combination of values of k_B , p_0 , k_T and N_T yielding the same value k_M is a solution to the fit. This is demonstrated by fitting TRPL decays simulated with the BTD model at different excitation fluences with added noise. In the low fluence regime, different sets of values of k_B , p_0 , k_T and N_T are retrieved, all yielding the same value k_M (**Figure 4.18a**). Similarly, a low fluence TRPL decay with added noise is fitted with different guess values. A wide range of parameter values are obtained, all yielding the same value k_M (blue lines/crosses in **Figure 4.18c**). Since bimolecular recombination and trapping are indistinguishable in this regime, some fitting solutions yield a dominant bimolecular contribution while other solutions yield dominant trapping leading to the wide range of bimolecular and trapping contributions in **Figure 4.18d**.

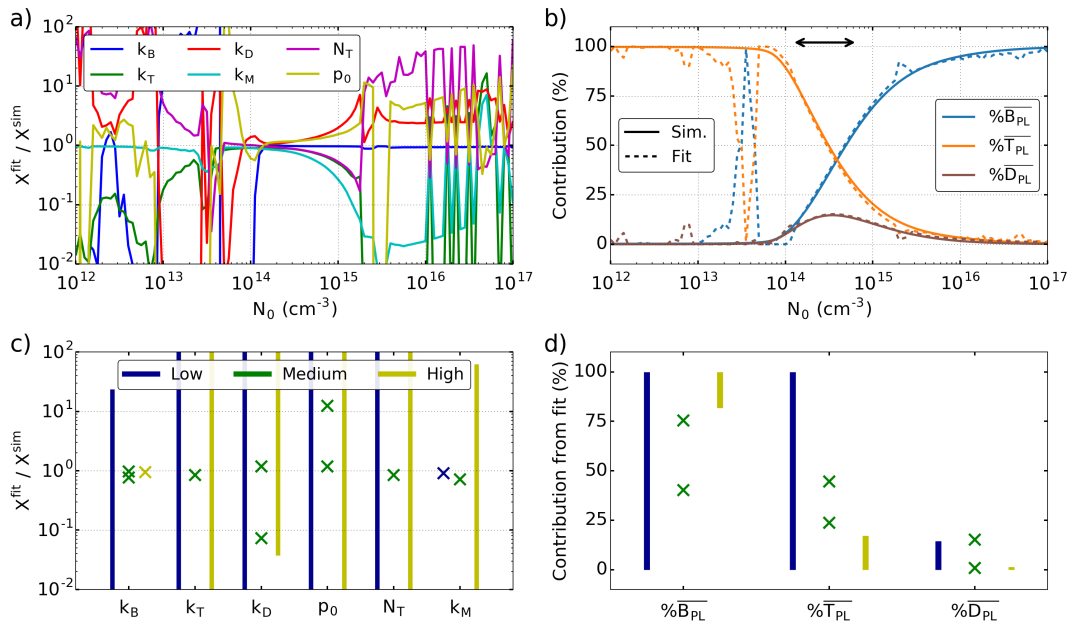


Figure 4.18: Fitting of simulated TRPL decays with added noise using the BTD model **a)** Parameter values obtained from fitting of TRPL decays simulated at different excitation fluences and **b)** corresponding bimolecular $\% \overline{B_{PL}}$, trapping $\% \overline{T_{PL}}$ and detrapping $\% \overline{D_{PL}}$ contributions to the change in the TRPL intensity calculated from the fits (dashed curves) and from the simulated decays (full curves). The double arrow indicates the range of fluences where all the parameters can be accurately retrieved with less than 50 % error. **c)** Range of parameter values obtained from fitting of TRPL decays simulated at low ($N_0 = 10^{12} \text{ cm}^{-3}$), medium ($N_0 = 3.5 \times 10^{14} \text{ cm}^{-3}$) and high ($N_0 = 10^{17} \text{ cm}^{-3}$) fluence with a wide range of initial guess values (crosses are used in the case where less than 2 solutions are found) and **d)** corresponding bimolecular $\% \overline{B_{PL}}$, trapping $\% \overline{T_{PL}}$ and detrapping $\% \overline{D_{PL}}$ contributions.

As the excitation fluence increases and become close to the trap state concentration, the availability of the trap states needs to be considered and trapping has a bimolecular behaviour leading to fluence-dependent non-exponential TRPL profiles.

Under medium excitation fluence (*i.e.* $N_T < N_0 < \sim 100N_T$, here $N_0 \sim 6 \times 10^{13}—6 \times 10^{15} \text{ cm}^{-3}$), the electrons quickly fill the trap states to saturation (**Figure 4.17b**). The trapping then slows down due to the absence of available trap states and the free electrons can only undergo bimolecular recombination while the high trapped electron concentration leads to an increase of the detrapping contribution (**Figure 4.17d**). As these processes are slower than trapping, the TRPL decay decrease slows down after about 100 ns in **Figure 4.17b**. Since the hole concentration can be assumed constant over the initial trapping phase in the low fluence regime (as previously discussed in the low fluence regime) the TRPL intensity can thus be considered proportional to the electron concentration as observed in **Figure 4.17b**. The trap state concentration can thus be roughly estimated from the initial TRPL intensity drop and is equal to the difference between the TRPL initial intensity and its intensity at t_{sat} where the TRPL decrease slows down, multiplied by the initial carrier concentration (**Figure 4.17b**):

$$N_T \approx [I_{TRPL}(0) - I_{TRPL}(t_{sat})] N_0 \quad (4.37)$$

The trapping rate constant can also be extracted from the trapping phase by fitting the initial TRPL decay with a mono-exponential function, as long as it remains mono-exponential (*i.e.* that the trap states remain mostly empty):

$$\frac{I_{TRPL}(t)}{I_{TRPL}(0)} = \frac{\Delta n_e(t)}{\Delta n_e(0)} = e^{-k_T N_T t} \quad t \ll t_{sat} \quad (4.38)$$

As the trap states are filled, the system enters a steady-state during which any electron detrapped gets replaced by another electron and the trap states remain full at all time (as indicated by the equal trapping and detrapping contributions in **Figure 4.17d**). This steady-state continues until the electron concentration becomes low enough that trapping becomes slower than detrapping and the trapped electrons recombine. As for the low fluence regime, detrapping can still happen after the TRPL intensity has reached zero and has therefore a limited contribution $\% \overline{D_{PL}}$ to the change in its intensity as shown in **Figure 4.17c**. Since all the recombination processes are non-negligible in this regime, it is possible to accurately retrieve all the

parameters of the model. However, contrary to the BT model where a set of values gives a very distinct TRPL decay, the BTD model can yield very similar TRPL decays calculated from different sets of values. For example, 2 solutions are found when fitting a TRPL decay simulated at medium fluence with different set of guess values (**Figure 4.18c**). In some cases, two different set of parameter values can even yield similar TRPL decays over a wide range of excitation fluences as shown in **Figure 4.19**.

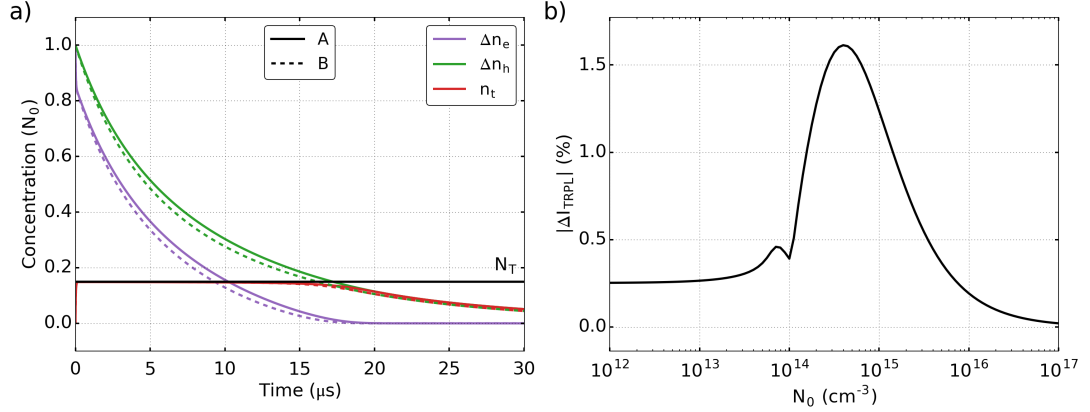


Figure 4.19: a) Carrier concentrations after an excitation pulse generating $N_0 = 3.5 \times 10^{14} \text{ cm}^{-3}$ and calculated from 2 sets of values A ($k_B = 26 \times 10^{-20} \text{ cm}^3/\text{ns}$, $k_T = 12,000 \times 10^{-20} \text{ cm}^3/\text{ns}$, $k_D = 80 \times 10^{-20} \text{ cm}^3/\text{ns}$, $p_0 = 70 \times 10^{12} \text{ cm}^{-3}$ and $N_T = 60 \times 10^{12} \text{ cm}^{-3}$) and B ($k_B = 26 \times 10^{-20} \text{ cm}^3/\text{ns}$, $k_T = 12,000 \times 10^{-20} \text{ cm}^3/\text{ns}$, $k_D = 30 \times 10^{-20} \text{ cm}^3/\text{ns}$, $p_0 = 260 \times 10^{12} \text{ cm}^{-3}$ and $N_T = 60 \times 10^{12} \text{ cm}^{-3}$), and b) Absolute maximum difference between TRPL decays calculated with A and B at different excitation fluences.

Reducing the number of unknown parameters of the model can help limiting the number of solutions fitting the TRPL decays. In particular, the doping concentration can be determined from the initial intensity of the TRPL decays. Assuming negligible CA (see **Section 4.3.2B**), the experimentally measured initial TRPL intensity depends upon the initial carrier concentration N_0 , the doping concentration, and the number of excitation pulses **P** (**Equation 4.23**):

$$I_{TPRL}(0) \propto \mathbf{P}N_0 [N_0 + p_0] \quad (4.39)$$

By measuring the initial TRPL intensity at two or more fluences N_0^A and N_0^B in the medium fluence regime allows the doping concentration to be calculated:

$$\frac{I_{TRPL}^B(0)}{I_{TRPL}^A(0)} = \frac{\mathbf{P}^B N_0^B [N_0^B + p_0]}{\mathbf{P}^A N_0^A [N_0^A + p_0]} \quad (4.40)$$

$$p_0 = \frac{I_{TRPL}^B(0) \mathbf{P}^A (N_0^A)^2 - I_{TRPL}^A(0) \mathbf{P}^B (N_0^B)^2}{I_{TRPL}^A(0) \mathbf{P}^B N_0^B - I_{TRPL}^B(0) \mathbf{P}^A N_0^A} \quad (4.41)$$

where the number of pulses is equal to ratio of the acquisition time and the repetition period. **Figure 4.20** shows the determination of the doping concentration from the TRPL intensity at different excitation fluence, with different N_0^B/N_0^A ratios and S/N. Increasing the ratio N_0^B/N_0^A and increasing the S/N both lead to an increase of the accuracy of the doping value retrieved. If N_0^A and N_0^B are too high, the doping has a negligible contribution to the initial TRPL and cannot be accurately retrieved. At contrary, if N_0^A and N_0^B are too low, the denominator in **Equation 4.41** tends toward zero and the value of p_0 becomes inaccurate.

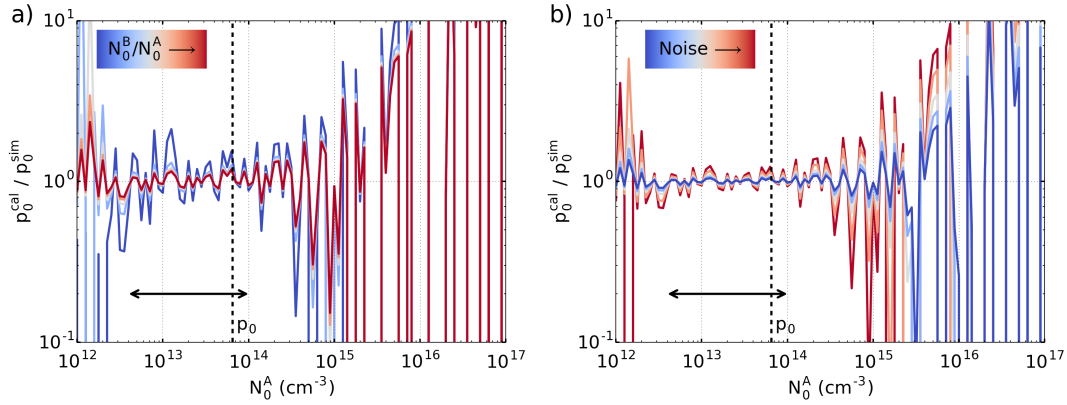


Figure 4.20: Doping concentration calculated from the TRPL initial intensity with added noise as a function of **a)** the ratio of the carrier concentrations N_0^A/N_0^B from 2 to 10 and **b)** noise with a fixed $N_0^A/N_0^B = 5$ ratio (see **Figure 4.12c** for the noise level used). The double arrows indicate the region where the doping concentration is accurately retrieved.

Under high excitation fluences (*i.e.* $N_0 \gg N_T$, here $N_0 > 6 \times 10^{15} \text{ cm}^{-3}$), the trap states are immediately saturated and most carriers undergo bimolecular recombination leading to dominant bimolecular contribution (**Figure 4.17c**). The doping concentration is also negligible compared to the photoexcited carrier concentrations and the hole and electron concentrations can be assumed equal. If the doping concentration is much lower than the photoexcited carrier concentrations, only the bimolecular rate constant can be accurately retrieved (**Figure 4.18a & c**).

It is therefore advised to measure TRPL decays in the medium fluence regime where all the recombination processes are non-negligible. This regime can easily be identified by the fast initial drop of the TRPL intensity followed by a slower decay. TRPL decays measured in the low and high fluence regime can respectively be used to determine the product $k_T N_T$ and k_B . Furthermore, it is recommended to carry out several fittings with different sets of guess values in order to ensure that only a unique set of values can fit the TRPL decay.

B Carrier accumulation

As previously discussed in **Section 4.3.1B**, experimental TRPL can only be fitted with a single excitation pulse by ensuring recombination of all the carriers between consecutive excitation pulses. As for the BT model, CA due to incomplete electron recombination can easily be avoided by ensuring that the TRPL intensity reaches zero. However, the BTD model predicts that trapped electrons can recombine non-radiatively after the free electron concentration, and therefore after the TRPL intensity, has reached zero. For example, in **Figure 4.21b** a $RP = 15 \mu\text{s}$ repetition period does not allow all the trapped electrons and free holes to recombine before the next excitation pulse although the TRPL intensity reaches zero. The resulting TRPL after many consecutive excitation pulses shows a smaller initial decrease due to the presence of the trapped electrons, effectively reducing the available trap state concentration in the model (**Figure 4.21c**). Furthermore, the higher initial hole concentration affects bimolecular recombination and therefore the shape of the steady-state phase following the trapping phase.

Due to the non-radiative nature of trap-mediated recombination, CA of trapped electrons is more complicated to avoid than CA due to incomplete depopulation of the free electrons. The maximum difference between the single and multiple pulse TRPL decays is calculated at different excitation fluences for a repetition period determined such that $I_{TRPL}(RP)/I_{TRPL}(0) = 10^{-4}$ (**Figure 4.21d**). Trap based CA does not affect the TRPL profile in the low fluence regime as the latter does not depend on the initial carrier concentration (although, CA can affect the TRPL profile if the initial carrier concentration becomes comparable to the trap state concentration as observed in **Figure 4.21d**). In the high fluence regime, trap based CA is always negligible as trapping is also negligible compared to bimolecular recombination (**Figure 4.21d**).

The highest difference due to CA is observed in the medium fluence regime. In this regime, it is possible to ensure complete depopulation of all trap states by gradually increasing the repetition period. Doing so allows more and more trapped electrons to detrapp and the TRPL profile converges toward the single-pulse TRPL profile (**Figure 4.21c**). Therefore, measuring identical TRPL decays with different excitation repetition periods in this regime indicates negligible CA.

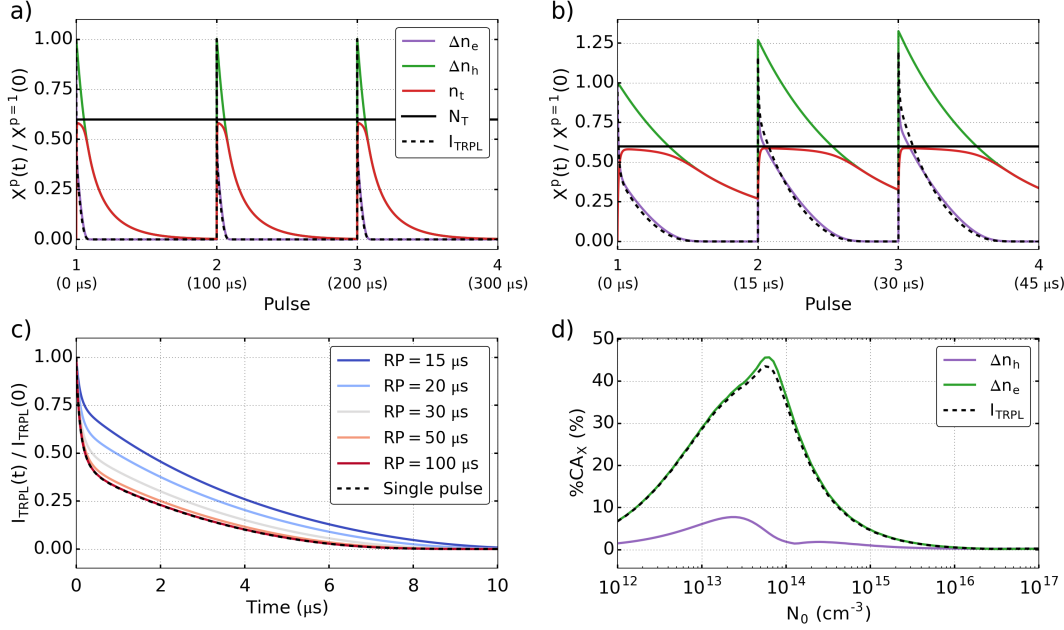


Figure 4.21: Evolution of the photoexcited electron Δn_e , photoexcited hole Δn_h and trapped electron n_t concentrations, and TRPL intensity I_{TRPL} predicted by the bimolecular-trapping-detrapping model ($N_0 = 10^{14} cm^{-3}$) over 3 consecutive excitation pulses for a **a)** repetition period $RP = 100 \mu s$ leading to negligible carrier accumulation and **b)** $RP = 15 \mu s$ leading to non-negligible carrier accumulation ($X = \Delta n_e, \Delta n_h, n_t, I_{TRPL}$). **c)** Normalised TRPL decays after multiple excitation pulses for different excitation repetition periods, compared to the TRPL after the first excitation pulse (single pulse). **d)** Normalised difference $\%CA_X$ of the TRPL and carrier concentrations between the first and stabilised pulse calculated at different excitation fluences, with a repetition period satisfying $I_{TRPL}(RP)/I_{TRPL}(0) = 10^{-4}$.

As for the BT model, the multiple pulse approximation can be used to fit TRPL decays subjected to CA. However, the higher occupation of the trap states limits the trapping contribution and thus may reduce the accuracy of the trapping rate and trap state concentration values retrieved. Fitting using the multiple pulse approximation is carried on TRPL decays simulated at different excitation fluences using the same approximation (**Figure 4.26**). Although the bimolecular rate constant k_B is accurately retrieved in the medium and high fluence regime, the other parameters could not be

accurately retrieved at any of the excitation fluences (**Figure 4.26b**). Although this suggests that the multiple pulse approximation is not adequate to fit decays subjected to CA, this is only an example and therefore it should not be considered as an absolute proof. In particular, it may be necessary to use multiple pulse fitting in the case where detrapping is so slow that CA cannot be avoided.

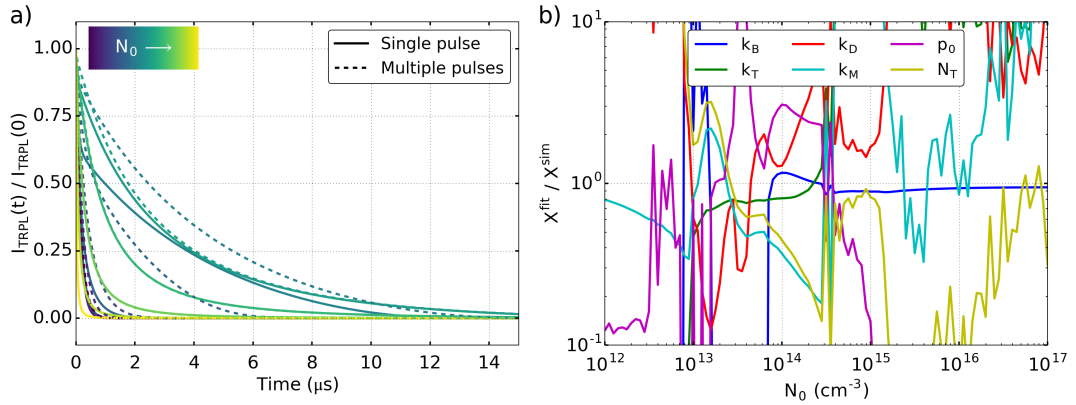


Figure 4.22: a) TRPL decays calculated with the single excitation pulse (continuous lines) and multiple pulse (dashed lines) approximations at increasing excitation fluences ($N_0 \sim 10^{12}$ — 10^{17} cm^{-3}) b) Relative parameter values obtained from the fitting of the decays with added noise ($R^2 > 0.996$).

C Experimental decay fitting

The TRPL of the MAPI thin film was measured at $N_0 = 3.0 \times 10^{16} \text{ cm}^{-3}$ under increasing excitation repetition periods from $0.5 \mu\text{s}$ up to $10 \mu\text{s}$ to observe any potential change due to incomplete trapped electrons depopulation (**Figure 4.23**).

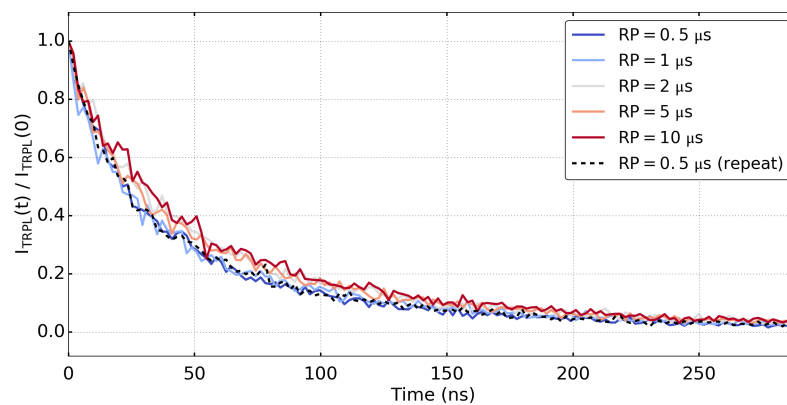


Figure 4.23: TRPL decays measured with increasing excitation repetition periods ($N_0 = 3.0 \times 10^{16} \text{ cm}^{-3}$). The first measurement ($RP = 0.5 \mu\text{s}$) was repeated at the end of the set to ensure that the sample was not affected by photobrightening nor degradation during the measurements.

The small discrepancies observed could be explained by the slight variation of the excitation source fluence at different repetition periods. These results suggest negligible CA in the sample for the specific fluence used. However, this does not imply that CA is negligible at the lower excitation fluences used. The TRPL decays are thus fitted using the single pulse and multiple pulse approximations (**Figure 4.24**).

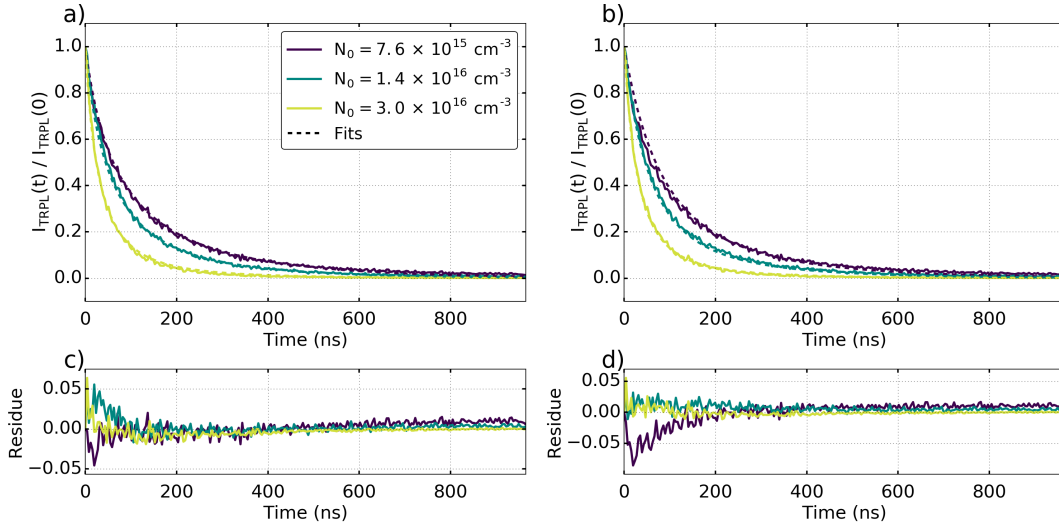


Figure 4.24: a) Fitting of the experimental TRPL decay using the bimolecular-trapping-detrapping model using the a) single pulse ($R^2 = 0.997$) and b) multiple pulse ($R^2 = 0.993$) approximations, and c) & d) corresponding residuals

Compared to the BT model, the single pulse BTD fit shows a much lower absolute residue at the lowest fluence. Both single pulse and multiple pulse approximations give very good fits to the experimental data and the rate and concentrations obtained are within range of values previously reported in the literature (**Table 4.4**).

Table 4.4: Optimised fitting parameter values obtained using the bimolecular-trapping-detrapping model compared to values reported in the literature.

	k_B (10^{-20} cm^3/ns)	k_T (10^{-20} cm^3/ns)	k_D (10^{-20} cm^3/ns)	p_0 (10^{12} cm^{-3})	N_T (10^{12} cm^{-3})
Single pulse	48.6	312.8	32.0	0	2,600
multiple pulse	48.8	20.8	16,041.3	5,800	3,800
[25]	35	10	5	10,000	60,000
[23]	7.6-26	12,000	32-80	20-65	55-60

The evolution of the carrier concentrations after 3 consecutive excitation pulses were simulated using the parameters retrieved from the single pulse and multiple pulse fits (**Figure 4.25**).

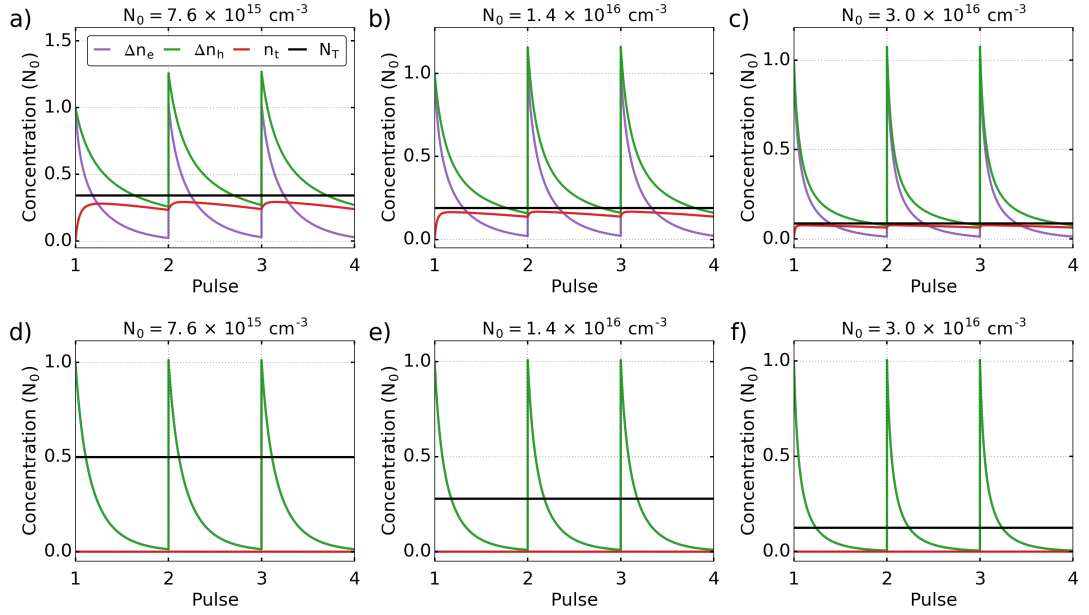


Figure 4.25: Carrier concentrations after 3 consecutive excitation pulses simulated at **a) & d)** $N_0 = 7.6 \times 10^{15} \text{ cm}^{-3}$, **b) & e)** $N_0 = 1.4 \times 10^{16} \text{ cm}^{-3}$ and **c) & f)** $N_0 = 3.0 \times 10^{16} \text{ cm}^{-3}$ using the bimolecular-trapping-detraping model using parameter values obtained from the **a)-c)** single pulse and **d)-f)** multiple pulse fits.

The single pulse fit predicts that the sample is in the medium fluence regime at the lowest excitation fluence (**Figure 4.25a**). The absence of the initial fast TRPL decrease is explained by the fairly low trapping rate such that the bimolecular and trapping contributions are of the same order of magnitude. At the highest fluence used, the single pulse fit predicts that the sample is almost in the high fluence regime (**Figure 4.25c**). At contrary, the multiple pulse fit predicts a very low trapping rate constant and a high detrapping rate constant and doping concentration such that the trap states remain mostly empty (**Figure 4.25d-f**). This is very similar to the assumptions of the BT model (see **Section 4.1.2A**). Indeed, in this case, the trapped electron concentration can be assumed negligible as detrapping is always equal to trapping (*i.e.* $T_n(t) = D_n(t)$). From **Equations 4.17 & 4.19**, the carrier concentration simplifies to:

$$\frac{dn}{dt} = -k_B n^2 - (k_T N_T + k_B p_0) n \quad (4.42)$$

which is identical to the BT rate equation (**Equation 4.14**). As for the low fluence regime, only the sum $k_M = k_T N_T + k_B p_0$ can be retrieved in this regime which shows that the BTD model is not adequate to use in this particular case where the detrapping is high enough to prevent the trap state to be filled.

The TRPL decays after many pulses were simulated from the single pulse fit using the multiple pulse approximation (**Figure 4.26a**). Although, significant CA is predicted from the single pulse fit due to incomplete depopulation of the trap states, especially at the lowest fluence used (**Figure 4.25a**), it only lead to a maximum $\%CA_{PL} = 5\%$ difference between the single and multiple pulse decays. CA decreases as the excitation fluence increase due to the lower trapping contribution compared to the bimolecular contribution. Consequently, little change to the TRPL decay profile is predicted under different excitation repetition periods as experimentally observed in **Figure 4.23** (**Figure 4.26b**). The multiple pulse fit predicts negligible CA as well due to the negligible trapped electron concentration at all fluences, and show little change under different excitation repetition periods (**Figure 4.26c & d**).

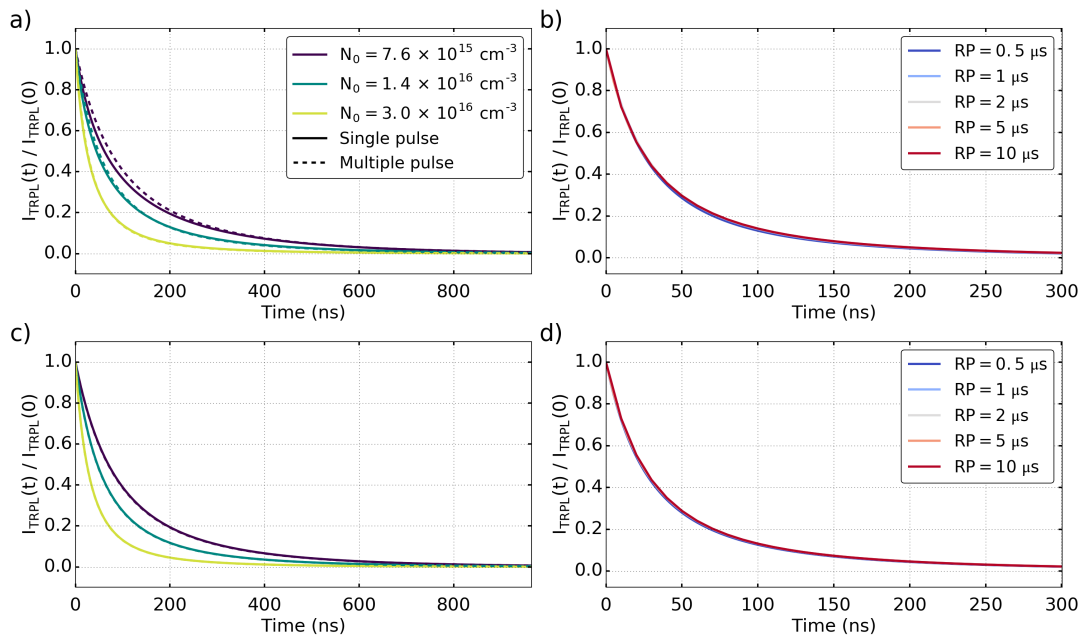


Figure 4.26: TRPL decays calculated from the parameter values obtained from the **a) & b)** single pulse and **c) & d)** multiple pulse fits, at different **a) & c)** excitation fluences and using the single pulse and multiple pulse approximations ($RP = 1\ \mu\text{s}$) and **b) & d)** repetition periods ($N_0 = 3.0 \times 10^{16}\ \text{cm}^{-3}$). Note that the single and multiple pulse decays calculated from the multiple pulse fit are very similar and overlap in **c)**.

In order to ensure that only 1 solution to the fit exists, the TRPL decays are fitted with the single pulse approximation and 224 sets of guess values. Fits yielding similar

solution with less than 2 % relative difference are considered identical, thus yielding 15 different solutions. All the fits yield the same value of k_B suggesting that this parameter is accurately retrieved but different values of k_T , k_D , p_0 and N_T are retrieved (**Figure 4.27a**).

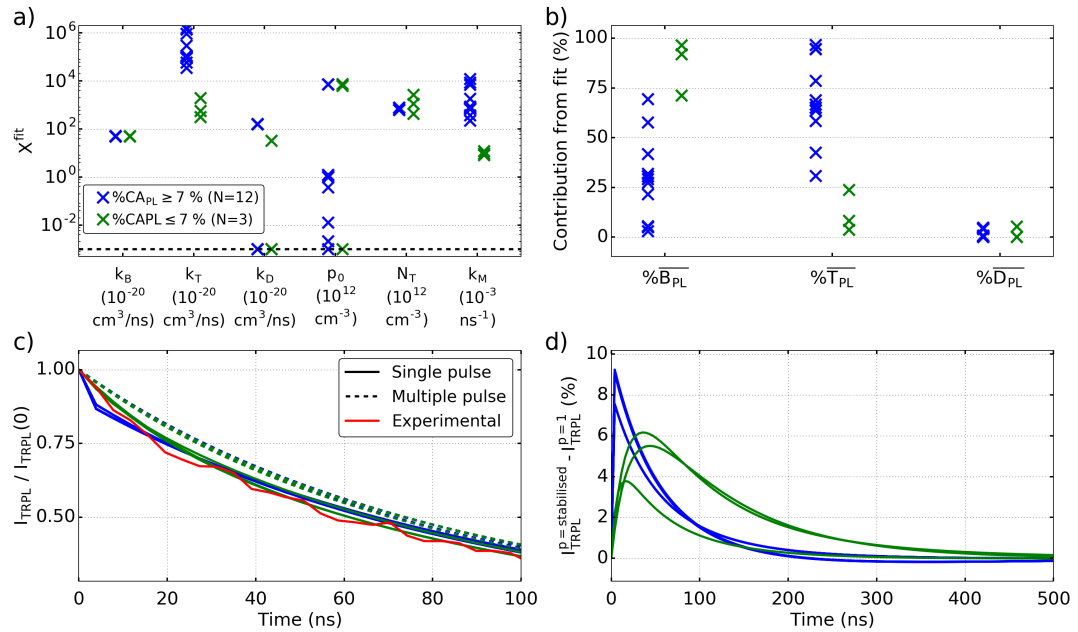


Figure 4.27: a) Parameter values and b) process contributions obtained from the fitting of the experimental TRPL decays using multiple sets of parameters guess values and the single pulse bimolecular-trapping-detraping model ($R^2 > 0.995$). The solutions are grouped depending on the predicted $\%CAPL$. c) Associated single pulse and multiple pulse TRPL decays compared to the experimental decay and d) difference between them.

The solutions are sorted as a function of how much CA affects the TRPL decays: 12 solutions predict a fast trapping rate $k_T > 10^{-16}$ cm⁻³ and that the system is in the medium fluence regime as indicated by the fast drop of the single pulse TRPL intensity (blue curves in **Figure 4.27c**). However, the detrapping predicted by these solutions is too slow to recombine most of the trapped electrons, thus leading to significant CA through the saturation of the trap states. The multiple pulse decay therefore does not show the initial trapping phase and present a $7\% \leq \%CAPL \leq 10\%$ (**Figure 4.27c & d**). 3 solutions predict a lower trapping rate such that the trapping and bimolecular contributions are of the same order of magnitude and no initial trapping phase is observed. Because of that, CA leads to a lower $\%CAPL$ between the single and multiple pulse decays (green curves in **Figure 4.27c & d**). For all solutions, a maximum $\%CAPL = 10\%$ is predicted here and does

not significantly alter the shape of the TRPL decay. Such sanity check should be used to ensure the validity of the solutions obtained from fitting. The multiple solutions found, all yielding the same k_B but different values for k_T , k_D , N_T and p_0 , therefore suggests that the sample was likely in the high fluence regime.

4.3.3 Comparison of the models and discussions

Both BT and BTD models predict dominant bimolecular recombination and trapping at low and high excitation fluence respectively but differ in the medium fluence regime. In order to determine which model describe more adequately the system studied, it is therefore important to measure its TRPL in the medium fluence regime. Since the fluence-position of this regime depends upon the values of the parameters of the models, it is necessary to measure the TRPL with a wide range of excitation fluences such that with the lowest fluence, a mono-exponential is measured while with the high fluence, the decay can be fitted with a simple bimolecular model. In the medium fluence regime, the BT model predicts that the TRPL decay initial decrease is mostly due to bimolecular recombination while trapping is dominant in the tail of the TRPL decay. At contrary, the BTD model predicts that the initial TRPL decay is due to trapping while the tail of the decay is associated with a mix of bimolecular recombination, trapping and detrapping. Therefore, in the case where a fast decrease of the TRPL followed by a slower decrease is observed at a certain excitation fluence (see **Figure 4.17**), the BTD model should be used while if the TRPL intensity is always observed to decrease at increasing excitation fluence (see **Figure 4.11**), the BT model should be used.

In order to extract accurate information from TRPL decays using the BT model and the single pulse approximation, the following protocol is recommended:

1. Measure the TRPL decay at any excitation fluence and with a repetition period allowing the TRPL decay to reach at least 0.01 % of its initial intensity;
2. Fit the decay using the single pulse approximation and ensure that the parameters retrieved are accurate by calculating the total bimolecular and trapping contributions;
3. If the trapping (bimolecular) contribution is too low, decrease (increase) the excitation fluence and repeat the protocol from step (1).

With the BTM model, the following protocol is recommended:

1. Find the excitation fluence such that TRPL decay present a fast initial drop followed by a slower decay;
2. Increase the excitation repetition period until the shape of the TRPL decay stops changing;
3. Optional: estimate the trap state concentration using the TRPL intensity initial drop and the doping concentration by measuring the TRPL decay with a different excitation fluence;
4. Fit the decay and with a range of initial guess values in order to ensure that only 1 solution exists. The parameters retrieved from step (3) can be used as fixed values in the fitting process;
5. Using the multiple pulse approximation, ensure that the CA predicted by the fit solution negligibly affect the TRPL decay shape.

These protocols can be repeated at different excitation fluences, in which case global fitting can be used to further improve the accuracy of the parameters retrieved.

In order to help the fitting of TRPL of perovskite materials, the PERovskite cARrier Recombination Simulator (PEARS) web app was developed and is available at <https://pears-tool.herokuapp.com/> (**Figure 4.28**). This web-app allows to fit sets of TRPL curves measured with different excitation fluences using the BT and BTM models. The user can fix the values of known physical quantities (*e.g.* doping and trap state concentrations). The app can also run a set of parameter guess values to check if multiple solutions to the fit exist such as shown in **Figure 4.27**.

Both models discussed here have advantages and disadvantages: the BT model assumes that the trap states remain empty at all time but is easier to apply, while the BTM model is more complex but requires more complex measurements in order to accurately retrieve the parameter values and avoid trap based carrier accumulation. Coupling TRPL measurements with other techniques could help improve the determination of the parameters of these models. In particular, the TRMC and V_{OC} intensity depend upon the sum of the free carrier concentration and are therefore useful to probe non-radiative recombination processes in perovskite, and therefore interesting techniques to couple with TRPL measurements.

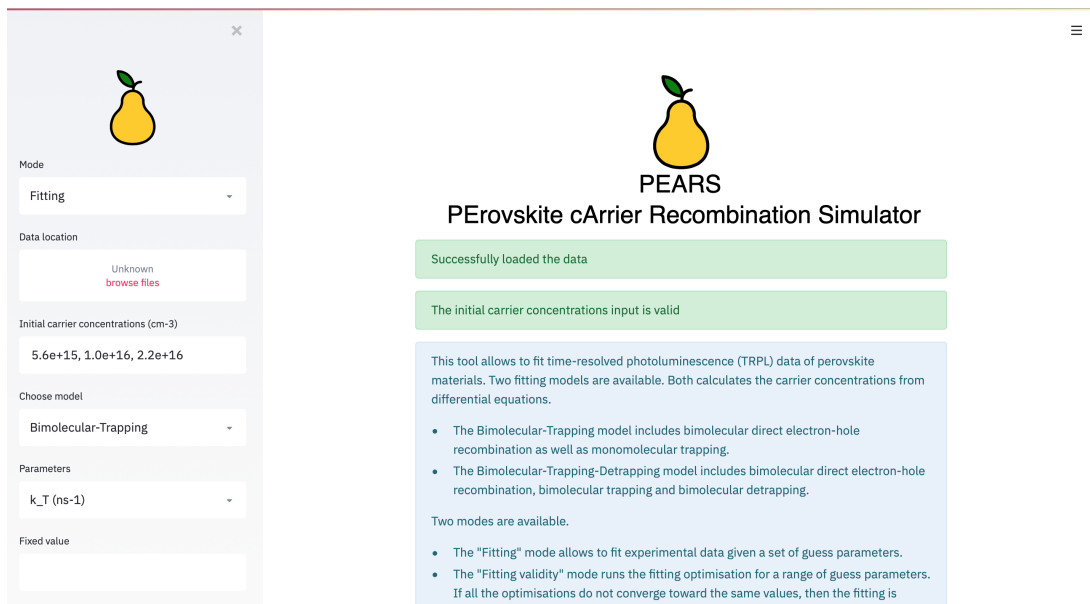


Figure 4.28: Screen shot of the PEARS web app.

4.4 Conclusion

Charge carrier recombination in perovskites is complex and as a result several models for charge dynamics have been used in the literature to extract meaningful data from TRPL decays. In this chapter, the limitation and fluence dependence of the BT and BTM charge carrier recombination models commonly used in the literature were reviewed. These models consider radiative and non-radiative bimolecular recombination, partially responsible for the dependence of the TRPL profile on the carrier concentrations, but differ in their treatment of trap-mediated recombination with the BT model assuming the trap state to remain empty at all time while the BTM model does not.

Both models predict dominant monomolecular trapping at low excitation fluence leading to a mono-exponential TRPL decay. Since other recombination processes are negligible in this regime, only trapping related information can be retrieved (that is the trapping rate constant k_T for the BT model and the product of the trapping rate constant and the trap state concentration $k_T N_T$ for the BTM model). Under high fluence, bimolecular recombination is dominant and only the bimolecular rate constant k_B can be accurately retrieved. Finally, in the medium fluence regime, the BT model predicts non-negligible trapping and bimolecular recombination allowing the accurate measurement of the rate constants of both processes. In the same regime, the BTM model predicts a fast initial trapping phase leading to a fast decrease of the

TRPL intensity followed by a slower decrease, which can be used to roughly determine the trap state concentration and trapping rate constant. As detrapping partially happens after the TRPL intensity becomes negligible, its contribution to the change in the TRPL intensity is limited and it may be complicated to accurately retrieve information related to the detrapping process (that is the detrapping rate constant k_D and the doping concentration p_0). The BTD model can be simplified by determining the values of some parameters beforehand; a method to calculate the doping concentration from the initial TRPL intensity measured in the medium fluence regime is proposed. The validity of the values retrieved from the BT model can be ensured by calculating the contribution of the processes to the change in the TRPL intensity. Due to the higher complexity of the BTD model, it is advised to ensure that only 1 solution to the fit exist by running the fitting optimisation with different parameter guess values. Because of the dependency of the TRPL on the excitation fluence, it is thus therefore important to report this information when reporting TRPL decays.

Incomplete depopulation of all photoexcited charge carriers within the excitation repetition period was shown to lead to the accumulation of charge carriers in the system. This carrier accumulation usually happens over less than a few hundred excitation pulses and can alter the intensity and profile of the resulting TRPL decay. It was shown that such TRPL decays and carrier concentrations can easily be obtained by simulating only a small fraction of the excitation pulses until stabilisation of the carrier concentrations. Carrier accumulation due to incomplete electron recombination was found to be easily avoidable by choosing an excitation repetition period such that the TRPL intensity reaches zero. However, carrier accumulation due to incomplete detrapping as predicted by the BTD model only is harder to avoid as it can happen after the TRPL intensity has reached zero. In the low and high fluence regime, trapped electrons accumulation is negligible while in the medium fluence regime, complete detrapping can be ensured by comparing the TRPL decay profile measured with 2 excitation repetition periods. For both models, fitting TRPL decay subjected to carrier accumulation by simulating multiple pulses is possible but may be more limited than fitting TRPL decays presenting negligible carrier accumulation using single pulse fitting.

The TRPL of a MAPI thin film deposited on glass was measured at different excitation fluences ($7.6 \times 10^{15} \text{ cm}^{-3}$, $1.4 \times 10^{16} \text{ cm}^{-3}$ and $3.0 \times 10^{16} \text{ cm}^{-3}$). Single

pulse and multiple pulse fitting using the BT model yielded a bimolecular rate constant of $k_B = 51.1\text{--}51.2 \times 10^{-20} \text{ cm}^3/\text{ns}$ and a trapping rate constant of $k_T = 1.30\text{--}1.55 \times 10^{-3} \text{ ns}^{-1}$, consistent with values previously reported in the literature. These values were found to be accurate and the sample was found to be in the medium fluence regime by calculating the bimolecular and trapping contributions to the change in the TRPL intensity. The single pulse fit predicted some CA but negligibly affecting the TRPL decay shape. The TRPL decay measured at the highest excitation fluence and with different repetition periods showed similar shapes suggesting negligible trap based CA at this fluence. However, CA could have affected the TRPL shape at the lower fluence used and therefore the TRPL decays were fitted using the single pulse and multiple pulse approximation of the BT model in order to account for possible CA. Single pulse fitting predicted that the sample was in the medium fluence regime at the lowest excitation fluence used and in the high fluence regime at the highest fluence used, while multiple pulse fitting predicted that the trap states remained empty at all time similar to the BT model assumptions. The single pulse fit predicted noticeable CA at the lowest fluence used but a negligible effect on the TRPL decay shape. Both fits predicted negligible change to the TRPL decay shape at different excitation repetition periods consistent with the experimental measurements. Single pulse fitting using multiple sets of guess values showed that the sample was likely in the high fluence regime and that only the bimolecular recombination rate constant of $k_B \sim 49 \times 10^{-20} \text{ cm}^3/\text{ns}$ was accurately retrieved.

Finally, recommendations and protocols on which model to use and how to measure TRPL of perovskite materials are given.

These models are the corner stone of better understanding perovskite materials. Further processes can be considered *e.g.* electron detrapping back the CB, Auger recombination, carrier diffusion and carrier extraction, however, they will likely increase the complexity of these models and may require more complex measurements.

4.5 References

- [1] S. D. Stranks *et al.*, “Electron-hole diffusion lengths exceeding 1 micrometer in an organometal trihalide perovskite absorber”, *Science*, vol. 342, no. 6156, pp. 341–344, Oct. 2013. DOI: 10.1126/science.1243982.

- [2] S. G. Motti *et al.*, “Controlling competing photochemical reactions stabilizes perovskite solar cells”, *Nature Photonics*, p. 1, May 2019. DOI: 10.1038/s41566-019-0435-1.
- [3] J. S. Godding *et al.*, “Oxidative passivation of metal halide perovskites”, *Joule*, vol. 3, no. 11, pp. 2716–2731, 2019. DOI: 10.1016/j.joule.2019.08.006.
- [4] Z. Andaji-Garmaroudi *et al.*, “Photobrightening in lead halide perovskites: Observations, mechanisms, and future potential”, *Advanced Energy Materials*, vol. 10, no. 13, p. 1903109, 2020. DOI: 10.1002/aenm.201903109.
- [5] N. Aristidou *et al.*, “Fast oxygen diffusion and iodide defects mediate oxygen-induced degradation of perovskite solar cells”, *Nature Communications*, vol. 8, p. 15218, May 2017. DOI: 10.1038/ncomms15218.
- [6] A. Leguy *et al.*, “Reversible hydration of $\text{CH}_3\text{NH}_3\text{PbI}_3$ in films, single crystals and solar cells”, *Chemistry of Materials*, vol. 27, pp. 3397–3407, 2015. DOI: 10.1021/acs.chemmater.5b00660.
- [7] U. Noomnarm *et al.*, “Fluorescence lifetimes: fundamentals and interpretations”, *Photosynthesis Research*, vol. 101, no. 2-3, pp. 181–194, Sep. 2009. DOI: 10.1007/s11120-009-9457-8.
- [8] T. Kirchartz *et al.*, “Photoluminescence-Based Characterization of Halide Perovskites for Photovoltaics”, *Advanced Energy Materials*, p. 1904134, May 2020. DOI: 10.1002/aenm.201904134.
- [9] J. R. Lakowicz, *Principles of fluorescence spectroscopy*. Boston, MA: Springer US, 2006. DOI: 10.1007/978-0-387-46312-4.
- [10] J. S. S. De Melo *et al.*, “Photophysics of fluorescently labeled oligomers and polymers”, *Photochemistry*, vol. 41, pp. 59–126, 2013. DOI: 10.1039/9781849737722-00059.
- [11] Z. Y. Zhang *et al.*, “The role of trap-assisted recombination in luminescent properties of organometal halide $\text{CH}_3\text{NH}_3\text{PbBr}_3$ perovskite films and quantum dots”, *Scientific Reports*, vol. 6, no. 1, p. 27286, Jul. 2016. DOI: 10.1038/srep27286.
- [12] T. Du *et al.*, “Elucidating the origins of subgap tail states and open-circuit voltage in methylammonium lead triiodide perovskite solar cells”, *Advanced Functional Materials*, vol. 28, no. 32, p. 1801808, Aug. 2018. DOI: 10.1002/adfm.201801808.
- [13] J. Yang *et al.*, “Effects of aromatic ammoniums on methyl ammonium lead iodide hybrid perovskite materials”, *Journal of Nanomaterials*, vol. 2017, pp. 1–6, Jan. 2017. DOI: 10.1155/2017/1640965.

- [14] P. Caprioglio *et al.*, “High open circuit voltages in pin-type perovskite solar cells through strontium addition”, *Sustainable Energy and Fuels*, vol. 3, no. 2, pp. 550–563, Jan. 2019. DOI: 10.1039/c8se00509e.
- [15] W.-J. Yin *et al.*, “Unusual defect physics in CH₃NH₃PbI₃ perovskite solar cell absorber”, *Applied Physics Letters*, vol. 104, no. 6, p. 063 903, Feb. 2014. DOI: 10.1063/1.4864778.
- [16] P.-W. Liang *et al.*, “Additive enhanced crystallization of solution-processed perovskite for highly efficient planar-heterojunction solar cells”, *Advanced Materials*, vol. 26, no. 22, pp. 3748–3754, Jun. 2014. DOI: 10.1002/adma.201400231.
- [17] K.-C. Hsiao *et al.*, “Enhancing Efficiency and Stability of Hot Casting p-i-n Perovskite Solar Cell via Dipolar Ion Passivation”, *ACS Applied Energy Materials*, vol. 2, no. 7, pp. 4821–4832, Jul. 2019. DOI: 10.1021/acsaem.9b00486.
- [18] J. Tao *et al.*, “Enhanced efficiency in perovskite solar cells by eliminating the electron contact barrier between the metal electrode and electron transport layer”, *Journal of Materials Chemistry A*, vol. 7, no. 3, pp. 1349–1355, Jan. 2019. DOI: 10.1039/C8TA10630D.
- [19] Z. Yao *et al.*, “CH₃NH₃PbI₃ grain growth and interfacial properties in meso-structured perovskite solar cells fabricated by two-step deposition”, *Science and Technology of Advanced Materials*, vol. 18, no. 1, pp. 253–262, 2017. DOI: 10.1080/14686996.2017.1298974.
- [20] E. Péan *et al.*, “Interpreting time-resolved photoluminescence of perovskite materials”, *Phys. Chem. Chem. Phys.*, 2020. DOI: 10.1039/D0CP04950F.
- [21] Y. Yang *et al.*, “Observation of a hot-phonon bottleneck in lead-iodide perovskites”, *Nature Photonics*, vol. 10, no. 1, pp. 53–59, Jan. 2016. DOI: 10.1038/nphoton.2015.213.
- [22] L. M. Herz, “Charge-carrier dynamics in organic-inorganic metal halide perovskites”, *Annual Review of Physical Chemistry*, vol. 67, no. 1, pp. 65–89, May 2016. DOI: 10.1146/annurev-physchem-040215-112222.
- [23] R. Brenes *et al.*, “Metal halide perovskite polycrystalline films exhibiting properties of single crystals”, *Joule*, vol. 1, no. 1, pp. 155–167, Sep. 2017. DOI: 10.1016/j.joule.2017.08.006.
- [24] Y. Yamada *et al.*, “Photocarrier recombination dynamics in perovskite CH₃NH₃PbI₃ for solar cell applications”, *Journal of the American Chemical Society*, vol. 136, no. 33, pp. 11 610–11 613, Aug. 2014. DOI: 10.1021/ja506624n.

- [25] E. M. Hutter *et al.*, “Charge carriers in planar and meso-structured organic-inorganic perovskites: Mobilities, lifetimes, and concentrations of trap states”, *Journal of Physical Chemistry Letters*, vol. 6, no. 15, pp. 3082–3090, Aug. 2015. DOI: 10.1021/acs.jpcllett.5b01361.
- [26] J. M. Richter *et al.*, “Enhancing photoluminescence yields in lead halide perovskites by photon recycling and light out-coupling”, *Nature Communications*, vol. 7, no. 1, p. 13941, Dec. 2016. DOI: 10.1038/ncomms13941.
- [27] D. W. DeQuilettes *et al.*, “Charge-carrier recombination in halide perovskites”, *Chemical Reviews*, pp. 11007–11019, Sep. 2019. DOI: 10.1021/acs.chemrev.9b00169.
- [28] T. W. Crothers *et al.*, “Photon reabsorption masks intrinsic bimolecular charge-carrier recombination in CH₃NH₃PbI₃ perovskite”, *Nano Letters*, vol. 17, no. 9, pp. 5782–5789, Sep. 2017. DOI: 10.1021/acs.nanolett.7b02834.
- [29] L. M. Pazos-Outón *et al.*, “Photon recycling in lead iodide perovskite solar cells”, *Science*, vol. 351, no. 6280, pp. 1430–1433, Mar. 2016. DOI: 10.1126/SCIENCE.AAF1168.
- [30] S. D. Stranks *et al.*, “Recombination kinetics in organic-inorganic perovskites: Excitons, free charge, and subgap states”, *Physical Review Applied*, vol. 2, no. 3, p. 034007, Sep. 2014. DOI: 10.1103/PhysRevApplied.2.034007.
- [31] Y. Yamada *et al.*, “Photocarrier recombination dynamics in highly excited SrTiO₃ studied by transient absorption and photoluminescence spectroscopy”, *Applied Physics Letters*, vol. 95, no. 12, p. 121112, Sep. 2009. DOI: 10.1063/1.3238269.
- [32] T. Handa *et al.*, “Charge injection mechanism at heterointerfaces in CH₃NH₃PbI₃ perovskite solar cells revealed by simultaneous time-resolved photoluminescence and photocurrent measurements”, *Journal of Physical Chemistry Letters*, vol. 8, no. 5, pp. 954–960, Mar. 2017. DOI: 10.1021/acs.jpcllett.6b02847.
- [33] A. R. S. Kandada *et al.*, “Chapter 4 photophysics of hybrid perovskites”, in *Unconventional Thin Film Photovoltaics*, The Royal Society of Chemistry, 2016, pp. 107–140. DOI: 10.1039/9781782624066-00107.
- [34] A. Alnuaimi *et al.*, “Performance of planar heterojunction perovskite solar cells under light concentration”, *AIP Advances*, vol. 6, no. 11, p. 115012, Nov. 2016. DOI: 10.1063/1.4967429.
- [35] V. S. Chirvony *et al.*, “Delayed luminescence in lead halide perovskite nanocrystals”, *The Journal of Physical Chemistry C*, vol. 121, no. 24, pp. 13381–13390, Jun. 2017. DOI: 10.1021/acs.jpcc.7b03771.

- [36] V. S. Chirvony *et al.*, “Trap-limited dynamics of excited carriers and interpretation of the photoluminescence decay kinetics in metal halide perovskites”, *The Journal of Physical Chemistry Letters*, vol. 9, no. 17, pp. 4955–4962, Sep. 2018. DOI: 10.1021/acs.jpcllett.8b01241.
- [37] Y. Yamada *et al.*, “Temperature dependence of photoluminescence spectra of nondoped and electron-doped SrTiO₃: Crossover from auger recombination to single-carrier trapping”, *Physical Review Letters*, vol. 102, no. 24, p. 247 401, Jun. 2009. DOI: 10.1103/PhysRevLett.102.247401.
- [38] Y. Li *et al.*, “Direct observation of long electron-hole diffusion distance in ch₃nh₃pbi₃ perovskite thin film”, *Scientific Reports*, vol. 5, no. 1, p. 14 485, Nov. 2015. DOI: 10.1038/srep14485.
- [39] C. Wehrenfennig *et al.*, “High charge carrier mobilities and lifetimes in organolead trihalide perovskites”, *Advanced Materials*, vol. 26, no. 10, pp. 1584–1589, Mar. 2014. DOI: 10.1002/adma.201305172.
- [40] B. Wu *et al.*, “Discerning the surface and bulk recombination kinetics of organic-inorganic halide perovskite single crystals”, *Advanced Energy Materials*, vol. 6, no. 14, p. 1 600 551, Jul. 2016. DOI: 10.1002/aenm.201600551.
- [41] D. Meggiolaro *et al.*, “Modeling the interaction of molecular iodine with mapbi₃: A probe of lead-halide perovskites defect chemistry”, *ACS Energy Letters*, vol. 3, no. 2, pp. 447–451, Feb. 2018. DOI: 10.1021/acsenerylett.7b01244.
- [42] T. J. Savenije *et al.*, “Quantifying charge-carrier mobilities and recombination rates in metal halide perovskites from time-resolved microwave photoconductivity measurements”, *Advanced Energy Materials*, vol. 10, no. 26, p. 1 903 788, Feb. 2020. DOI: 10.1002/aenm.201903788.
- [43] J. Troughton *et al.*, “Humidity resistant fabrication of CH₃NH₃PbI₃ perovskite solar cells and modules”, *Nano Energy*, vol. 39, pp. 60–68, Sep. 2017. DOI: 10.1016/J.NANOEN.2017.06.039.
- [44] R. Brenes *et al.*, “The impact of atmosphere on the local luminescence properties of metal halide perovskite grains”, *Advanced Materials*, vol. 30, no. 15, p. 1 706 208, Apr. 2018. DOI: 10.1002/adma.201706208.
- [45] D. W. DeQuilettes *et al.*, “Photo-induced halide redistribution in organic-inorganic perovskite films”, *Nature Communications*, vol. 7, no. May, p. 11 683, May 2016. DOI: 10.1038/ncomms11683.
- [46] Y. Tian *et al.*, “Mechanistic insights into perovskite photoluminescence enhancement: Light curing with oxygen can boost yield thousandfold”, *Physical Chemistry Chemical Physics*, vol. 17, no. 38, pp. 24 978–24 987, Sep. 2015. DOI: 10.1039/c5cp04410c.

Chapter 5

Superoxide formation and stability in mesoporous carbon perovskite solar cells with an aminovaleric acid additive

Contents

5.1	Introduction	146
5.2	Methodology	148
5.2.1	Sample fabrication	148
5.2.2	Microscopy and morphology	149
5.2.3	Ultraviolet-Visible spectrophotometry	149
5.2.4	X-ray diffractometry measurements	150
5.2.5	Photoluminescence measurements	151
5.2.6	Superoxide yield measurements	152
5.3	Results and discussions	154
5.3.1	Properties of MAPI and AVA-MAPI perovskites on different substrates	154
A	Morphology properties	154
B	Optical properties	159
C	Photoluminescence properties	163
D	Crystallographic properties	169
5.3.2	Stability of MAPI and AVA-MAPI perovskites on different substrates	171
A	Ambient stability under illumination	171
B	Superoxide formation in MAPI and AVA-MAPI perovskites	173
5.4	Conclusion	183
5.5	Bibliography	185

5.1 Introduction

First presented by Z. Ku *et al.* in 2013, mesoporous carbon perovskite solar cells (mCPSCs) present better stability and a potentially easier fabrication process than conventional halide perovskite cell architectures using spiro-OMeTAD and gold [1]. mCPSCs consist of 3 printed mesoporous layers, deposited on top of each other: a mesoporous titanium oxide (TiO_2) layer as the ETL, a porous carbon (C) layer as the HTL and back contact of the cell, and an insulating zirconia oxide (ZrO_2) layer in between the two aforementioned layers, hindering electron-hole recombination (**Figure 5.1**). A perovskite solution is then infiltrated through the stack and annealed to induce crystallisation.

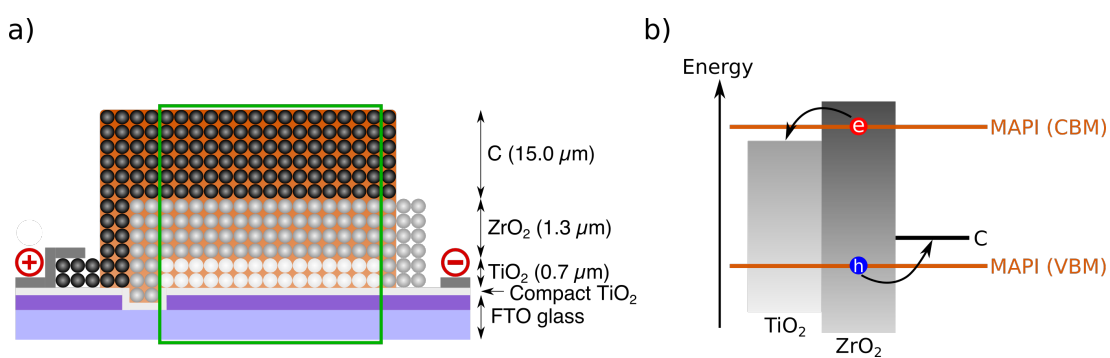


Figure 5.1: a) Schematic of a mesoporous carbon perovskite solar cell (the photoactive area is highlighted in green) and b) corresponding band diagram.

The absence of an expensive organic HTL such as spiro-OMeTAD and the lack of a metal back contact, usually thermally evaporated silver or gold, make these devices potentially low cost [2]. It has also been demonstrated that it is possible to screen print these devices on large areas making them suitable for large-scale production [1], [3]. Z. Ku *et al.* obtained 6.6 % PCE stable for over 840 h in the dark using the MAPI perovskite. This reasonable stability is likely due to the hydrophobic character of the carbon layer hindering moisture infiltration in the perovskite and therefore hindering moisture-mediated degradation [4]. In 2014, A. Mei *et al.* mixed MAPI with 5-aminovaleric acid [5-AVA, $\text{NH}_2(\text{CH}_2)_4\text{CO}_2\text{H}$] forming $(5\text{-AVA})_x(\text{MA})_{1-x}\text{PbI}_3$ and improving the penetration and distribution of the perovskite within the stack which resulted in an improved PCE of 12.8 % [5]. It was also suggested that this improved penetration and surface contact resulted in lower defect concentration [5]. 5-AVA is believed to form hydrogen bonds between the iodide anions of MAPI and its carboxyl (COOH) and ammonia (NH_3^+) groups [5]. These devices showed promising stability

with no performance drop over 1008 h under simulated sunlight without encapsulation. In 2015, X. Li *et al.* presented a 12.8 % PCE $(5\text{-AVA})_x(\text{MA})_{1-x}\text{PbI}_3$ mCPSC stable over 1000 h tested in air, at constant 1 sun illumination and at a temperature of 80°C [6]. The following year, G. Grancini *et al.* demonstrated an impressive 100 cm² mCPSC with 3 % 5-aminovaleric acid iodide [5-AVAI, $\text{NH}_2(\text{CH}_2)_4\text{CO}_2\text{HI}$] and with zero PCE loss over more than 10,000 h in *ISOS* standard conditions [7]. Their results suggested the presence of a very thin 2D $[\text{HOOC}(\text{CH}_2)_4\text{NH}_3]_2\text{PbI}_4$ perovskite layer within the TiO_2 scaffold with a 3D tetragonal phase of MAPI capping layer [7]. Density functional theory calculations and PL measurements suggested the presence of a 2D/3D hybrid between the 2D and 3D phases with a slightly wider band-gap than the 3D perovskite (1.7 eV and 1.6 eV for the 2D/3D and 3D perovskites respectively) [7]. The improved stability of aminovaleric acid methylammonium lead iodide (AVA-MAPI) mCPSCs was hypothesised to originate from the presence of this 2D perovskite layer which acting as a protective layer against moisture [7]. The addition of 5-AVA or 5-AVAI to the perovskite precursor solution enhances the stability and efficiency of mCPSCs. The improvement of the PCE has been explained in terms of enhanced penetration and crystallization of the perovskite, however, the stability improvement origins are less clear. [5].

In this chapter, the morphological, optical, fluorescence, crystallographic and stability properties of MAPI and AVA-MAPI in complete mCPSCs and combinations of its mesoporous layers are investigated. Sample manufacturing and experimental details are first discussed. The morphology of the two perovskite solutions drop-cast onto (i) glass, (ii) fluorine doped tin oxide (FTO) glass, (iii) ZrO_2 , (iv) TiO_2 , (v) $\text{TiO}_2/\text{ZrO}_2$ and (vi) $\text{TiO}_2/\text{ZrO}_2/\text{C}$ substrates is compared using optical, PL and electron microscopy, profilometry and EDX. Their transmittance, reflectance and absorptance measured using UV-Vis spectrophotometry are then discussed. The PL properties of the perovskites is then investigated using fluorescence spectroscopy and imaging. The stability in ambient condition under illumination is then investigated using *in situ* XRD. Finally, superoxide formation in these samples is assessed by monitoring the fluorescence of 2-hydroxyethidium, reaction product of the dihydroethidium probe and superoxide [8].

5.2 Methodology

A description of the samples, as well as the experimental procedures used in this chapter is given here. More details about the instruments used can be found in **Chapter 2**.

5.2.1 Sample fabrication

The samples were fabricated following the method reported in [3]. MAPI precursor solutions were prepared from a 1:1 M solution of lead iodide (*TCI*) and MAI, (*Dyesol*) in gamma-butyrolactone (GBL, *Sigma-Aldrich*). AVA-MAPI precursor solutions were prepared as above for MAPI with the replacement of 4 % molar ratio of MAI with 5-AVAI, (*Dyesol*). The ZrO_2 , TiO_2 and C mesoporous layers were screen-printed on fluorine doped tin oxide (FTO) glass substrates (**Figure 5.2a**).

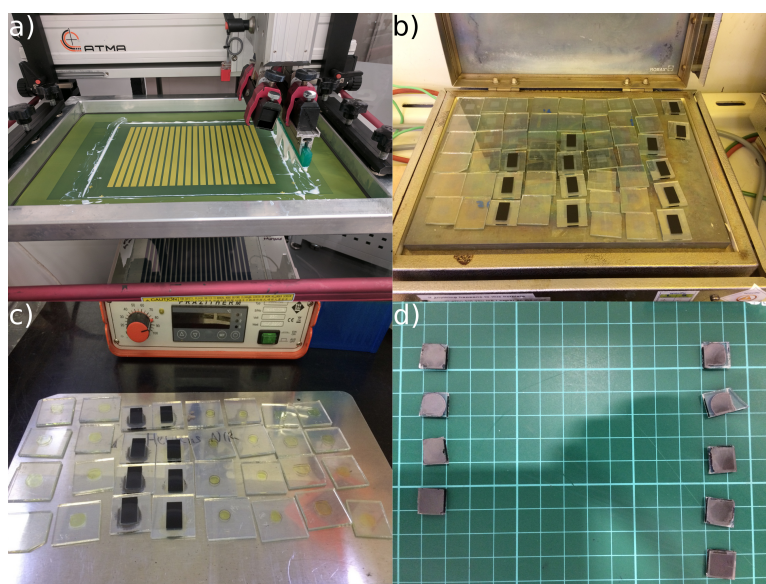


Figure 5.2: Fabrication process of the mesoporous samples. **a)** Screen-printing of the mesoporous layers **b)** annealing at 400°C for 30 min **c)** perovskite infiltration and **d)** final samples after removing the excess of glass.

ZrO_2 paste (*Solaronix*), 30NRD TiO_2 paste (*Dyesol*) mixed with terpineol (2:3 weight) and carbon paste (*Gwent Electronic Materials*) were used to print 1.3 μm , 0.7 μm and $\sim 15 \mu\text{m}$ layers respectively by Jenny Baker, Francesca De Rossi and Simone Meroni at Swansea University. The substrates were annealed at 400°C for 30 min (substrates including a TiO_2 layer were annealed at 550°C prior to this). Different combinations of layers shown in **Figure 5.3** were studied in order to understand their respective role in the complete device properties.

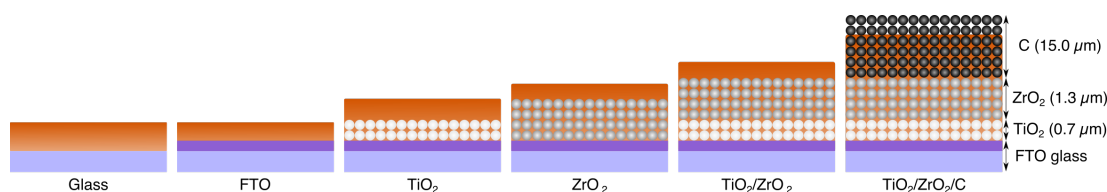


Figure 5.3: Representation of the substrates studied. The perovskite is shown in brown.

Mesoporous samples (TiO_2 , ZrO_2 , $\text{TiO}_2/\text{ZrO}_2$ and $\text{TiO}_2/\text{ZrO}_2/\text{C}$) were heated to at least 150°C for 30 min prior to infiltration of the perovskite in order to remove any moisture present (**Figure 5.2b**). For superoxide measurements, $10\ \mu\text{L}$ of solution was drop-cast on glass substrates while $1\ \mu\text{L}$ and $2\ \mu\text{L}$ were needed for mesoporous substrates measured with illumination through the film and glass side respectively. $1\ \mu\text{L}$ and $2\ \mu\text{L}$ were used for UV-Vis spectroscopy and PL measurements. The samples were left for 10 min in a low humidity atmosphere to allow infiltration of the perovskite solutions and were then annealed at 50°C for 1 h in a closed oven (**Figure 5.2c & d**).

5.2.2 Microscopy and morphology

Perovskite spreading was calculated using the *ImageJ* software [9]. Bright-field microscopy was carried using *Olympus BH2* (40 X objective) *BX51* (20 X objective) optical microscopes. PL images were obtained using the fluorescence microscopy setup described in **Section 2.2.2** (20 X objective, power $P \sim 19\ \text{W}/\text{cm}^2$). SEM and EDX were carried using a *Zeiss Evo LS25* with an acceleration voltage of 20 kV and a probe current between 400 pA and 500 pA. The surface coverage of large and small grains was calculated using the *Zeiss trainable image segmentation* software (see **Section 2.3** for more details). *In situ* annealing was carried in ambient atmosphere using a *Linkam THMS600* temperature controller and a *Linkam THMS600* environmental chamber.

5.2.3 Ultraviolet-Visible spectrophotometry

Total reflectance and transmittance of the films were measured between 500 nm and 855 nm (1 nm step) using a *Perkin Elmer Lambda 750* with a 100 mm integrating sphere (see **Section 2.1** for more details). Due to the small size of the samples used, *spectralon* masks were used to narrow the integrating sphere aperture. 0 % and 100 % transmittance baselines were carried prior to the measurements. Due to the low

reflectance of the sample and thus low S/N, absorbance and reflectance were smoothed using a Savitzky-Golay filter.

The band-gap energy was determined using the Tauc relation between the absorption coefficient α and the band-gap energy E_g :

$$\frac{\alpha h\nu}{\lambda} \propto \frac{h\nu}{\lambda} - E_g \quad (5.1)$$

where h is the Planck constant, ν is the speed of light in air and λ is the photon wavelength. Assuming no internal reflections in the film (which is obviously incorrect for mesoporous samples and makes the previous equation more of a qualitative than quantitative measure of the band-gap energy), α can be calculated from **Equation 2.2** of **Section 2.1**. Considering that MAPI presents a direct band-gap, its energy is determined from fitting a linear function to $(\log_e(\frac{T}{1-R}) h\nu)^2$ with respect to energy.

Absorbance measurement of dihydroethidium solutions were carried using a *Perkin Elmer 750* and a *Lambda 9 UV-Vis* spectrophotometers. The molar attenuation coefficient ε was calculated using the linear relation between the solution absorbance **A**, the light path length l and the solution concentration c as per the Beer-Lambert law:

$$\mathbf{A}(\lambda) = \varepsilon(\lambda)cl \quad (5.2)$$

5.2.4 X-ray diffractometry measurements

XRD patterns were measured between 12.0° and 14.5° with a 0.01° step and a 1.5 s integration time, and between 27.5° and 29.5° with a 0.02° step and a 1 s integration time with a *Bruker D8 Discover* (see **Section 2.4** for more details). The patterns were smoothed with a Savitzky-Golay filter. Background was removed using a linear baseline calculated at the two extreme of the patterns (see **Section 2.6.4** for more details). The intensity, FWHM and position of the overlapping (004) and (220) diffraction peaks between 27.5° and 29.5° were extracted by fitting the background-corrected XRD pattern using a double-Gaussian model:

$$I = A_1 \exp\left(-\frac{4\log_e(2)(\theta - \theta_1)^2}{FWHM_1^2}\right) + A_2 \exp\left(-\frac{4\log_e(2)(\theta - \theta_2)^2}{FWHM_2^2}\right) \quad (5.3)$$

In situ XRD patterns under illumination with a *LedLenser M7R* torch (power $P \sim 19 \text{ mW/cm}^2$) were measured between 12.0° and 14.5° every 12.4 min (0.01° step and 1.5 s integration time).

5.2.5 Photoluminescence measurements

PL measurements were carried using an *Edinburgh instruments FS5*, an *Olympus BX51* fluorescence microscope and a *Horiba Fluoromax-4* (see **Section 2.2.1** for more details).

Samples measured with the *FS5* fluorometer were excited with photons of wavelength $\lambda_{exc} = 600 \text{ nm}$ ($\Delta\lambda_{exc} = \pm 6 \text{ nm}$, $P \sim 2.4 \text{ mW/cm}^2$). Their emission was measured between 660 nm and 900 nm with a 1 nm step, a 0.1 s integration time and an emission slitwidth of $\Delta\lambda_{em} = \pm 6 \text{ nm}$. A 520 nm bandpass and a 665 nm longpass filter were used to remove any undesired excitation peak from the fluorometer lamp. The background intensity due to overcorrection of the PMT sensitivity was corrected using a linear baseline calculated at 660 nm and 865 nm (see **Section 2.6.4** for more details).

A 50 X magnification objective ($P \sim 33 \text{ W/cm}^2$) was used with the fluorescence microscope. Emission spectra were measured with an *OceanOptics USB2000+* spectrophotometer with a 2 s scan integration time. Timelapse spectra were measured every 6 s with an integration time of 6 s. The background intensity of the PL spectra was corrected using an averaged baseline calculated between 400 nm and 500 nm (see **Section 2.6.4** for more details). The spectra were then corrected with the fluorescence microscope filter transmittance and smoothed using a Savitzky-Golay filter. The PL of one sample was measured under decreasing fluence using a set of neutral density filters. For each excitation fluence, the spectrum was quickly measured with a 1 s integration time to avoid any undesired change to the sample properties due to degradation or photobrightening. Timelapse spectra at low and high excitation fluence were measured every 1 s with an integration time of 1 s. The intensity of the spectra was normalised using the excitation fluence used. The background intensity of the PL spectra was corrected using an averaged baseline calculated between 400 nm and 500 nm. The spectra were smoothed with a Savitzky-Golay filter. In order to distinguish the two overlapping PL peaks between 650 nm and 850 nm, and extract

their intensity, FWHM and position, the normalised background-corrected spectra were fitted on the energy scale using a double-Gaussian model:

$$I = A_1 \exp\left(-\frac{4 \log_e(2) (\lambda - \lambda_1)^2}{\text{FWHM}_1^2}\right) + A_2 \exp\left(-\frac{4 \log_e(2) (\lambda - \lambda_2)^2}{\text{FWHM}_2^2}\right) \quad (5.4)$$

The PL of samples with the *Fluoromax-4* was measured between 650 nm and 850 nm (1 nm step, 0.1 s integration time, $\Delta\lambda_{em} = \pm 5$ nm) with a $\lambda_{exc} = 560$ nm excitation wavelength ($\Delta\lambda_{exc} = \pm 3.5$ nm, $P \sim 1.3$ mW/cm², **Figure 5.38**).

5.2.6 Superoxide yield measurements

The superoxide yield was monitored by measuring the fluorescence of 2-hydroxyethidium, product of the reaction of dihydroethidium and superoxide [10]–[13]. 1.1 ± 0.1 mg of dihydroethidium (*Sigma-Aldrich*, $\geq 95\%$) was dissolved in 100 mL of toluene (*Sigma-Aldrich*, 99.8 % or 99.9 %) in order to obtain a 34.9 μM probe stock solution. Samples were immersed into 10 mL of 3.49 μM dihydroethidium solution. In order to generate excited carriers, the samples were illuminated with a *Sylvania FVT 12v GY6,35* halogen lamp coupled with a 530 nm high pass filter and a near infrared low pass filter to avoid degradation of the probe by heat ($P \sim 1.5$ mW/cm²) (**Figure 5.4a**). Superoxide formation was studied with illumination through the glass substrate and through the film (**Figure 5.4b**).

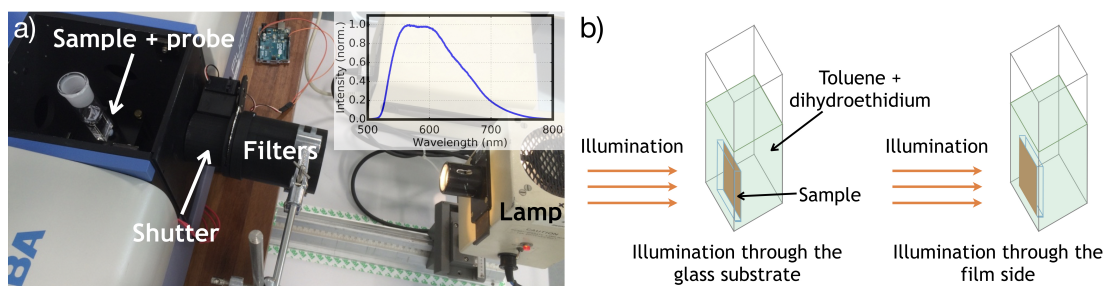


Figure 5.4: Superoxide setup: **a)** An halogen lamp filtered with a 530 nm high pass and NIR filters is used to generate excited carriers in the sample. The sample is placed in a cuvette with 10 mL of dihydroethidium probe solution. The fluorescence of the probe solution is periodically measured using a fluorometer coupled with an automatic shutter. Inset: lamp emission spectrum **b)** Schematic of the superoxide experiments during which samples were illuminated through the glass or through the film (*i.e.* the perovskite infiltration side).

The fluorescence spectra of 2-hydroxyethidium was measured with a *Horiba FluoroMax-4* spectrofluorometer ($\lambda_{exc} = 520$ nm, $\Delta\lambda_{exc} = \pm 3.5$ nm, $P \sim 1.6$ mW/cm²). For superoxide yield measurements with illumination through the film and baseline measurements, the emission spectrum of the solution was measured between 550 nm and 750 nm (1 nm step, 0.2 s integration time, $\Delta\lambda_{em} = \pm 3.5$ nm). The emission spectra range was later narrowed between 600 nm and 700 nm (1 nm step, 0.05 s integration time, $\Delta\lambda_{em} = \pm 10$ nm) allowing measurement of the solution fluorescence every 2 min (compared to every 5 min previously), for superoxide yield measurements illuminated through the glass layer. The spectra were smoothed using Savitzky-Golay smoothing to improve the S/N. The emission of dihydroethidium was measured between 390 nm and 500 nm (1 nm step, 0.1 s integration time, $\lambda_{exc} = 370$ nm, $\Delta\lambda_{exc} = \pm 2.5$ nm, $\Delta\lambda_{em} = \pm 0.25$ nm, $P \sim 1.0$ mW/cm², **Figure 5.33**), as well as between 300 nm and 500 nm (1 nm step, 0.1 s integration time, $\lambda_{exc} = 289$ nm, $\Delta\lambda_{exc} = \pm 0.5$ nm, $\Delta\lambda_{em} = \pm 2.5$ nm, **Figure 5.26**). The 2-hydroxyethidium emission intensity ratio at 660 nm $I(t)/I(t = 0)$ was used to monitor the superoxide yield. The slope obtained was corrected for the number of excited states in the sample [14]:

$$\left[\frac{I(t)}{I(0)} \right]_{corr} = 1 + \frac{I(t) - I(0)}{\beta \cdot I(0)} \quad (5.5)$$

where β is a correction factor calculated from the number of absorbed photons by the sample:

$$\beta = \frac{\int I_0(\lambda) \cdot A(\lambda) \cdot d\lambda}{S} \quad (5.6)$$

with $I_0(\lambda)$ the intensity of the lamp and $A(\lambda)$ the absorbance of the sample at wavelength λ , and S the area of the sample. The corrected superoxide yield is simply referred as $I(t)/I(0)$ hereafter.

5.3 Results and discussions

5.3.1 Properties of MAPI and AVA-MAPI perovskites on different substrates

A Morphology properties

Macro-morphology. The images of 36 films prepared show the degree of spreading of the drop-cast MAPI and AVA-MAPI perovskite solutions (the full stack is not discussed here as the thick carbon layer did not allow the formation of a capping layer on top of it and thus prevented investigation of the perovskite morphology) (**Figure 5.5**); little spreading is seen on glass and FTO glass, increased spreading is seen when infiltrated in TiO_2 , and the highest spreading is observed when infiltrated in substrates with a ZrO_2 layer (*i.e.* ZrO_2 and $\text{TiO}_2/\text{ZrO}_2$). AVA-MAPI spreads more than MAPI in substrates with a ZrO_2 layer while no significant difference is observed between the two perovskite solutions in the TiO_2 , glass or FTO samples.

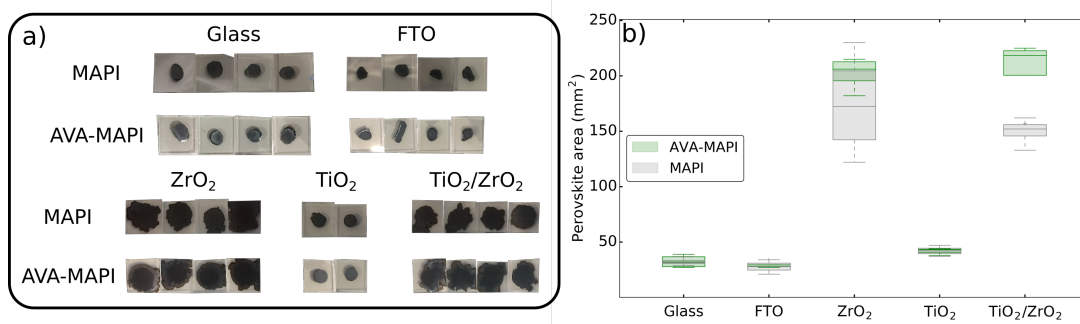


Figure 5.5: Macro-morphology of MAPI and AVA-MAPI perovskites drop-cast on different substrates. **a)** Pictures of the samples and **b)** perovskite spreading area calculated from **a)**.

Micro-morphology. In addition to different wetting/spreading properties, the perovskites form films with different morphologies depending on the substrate used (**Figure 5.6**). When drop-cast onto glass, the MAPI solution creates a film with large grains while smaller grains are obtained with the AVA-MAPI solution, both leaving many pinholes in the films with 52 % and 56 % grain surface coverage respectively (8 % more surface coverage in Glass/AVA-MAPI). On FTO glass, MAPI forms smaller grains compared to those on glass while AVA-MAPI forms a compact layer with few pinholes.

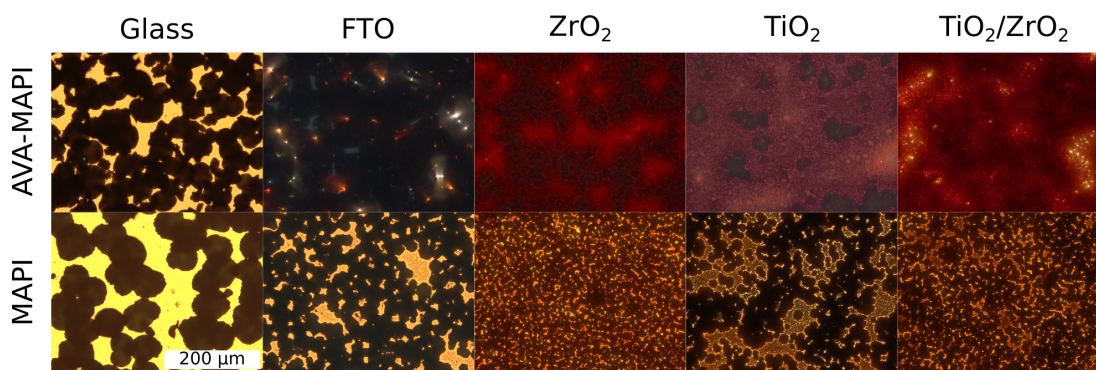


Figure 5.6: Bright field microscopy images of MAPI and AVA-MAPI drop-cast on different substrates.

When drop-cast on mesoporous substrates (*i.e.* ZrO_2 , TiO_2 and TiO_2/ZrO_2), the samples present lighter and darker areas suggesting inhomogeneous perovskite distribution in the mesoporous scaffold most likely due to inhomogeneous solution infiltration (**Figure 5.6**). Assuming an homogeneous mesoporous layer, if all the mesopores were filled with perovskites, a homogeneous dark layer should be observed with optical microscopy (**Figure 5.7**). AVA-MAPI forms large homogeneous areas likely due to good solution infiltration (note that AVA-MAPI mesoporous sample presents dark spots that are associated with large grains located on top of the layer and are thus not representative on the perovskite infiltration as discussed below). The perovskite grains are sparser in MAPI, forming a homogeneous network in ZrO_2 and TiO_2/ZrO_2 and a very inhomogeneous distribution in TiO_2 suggesting poor infiltration of the perovskite in the later (**Figure 5.7**).

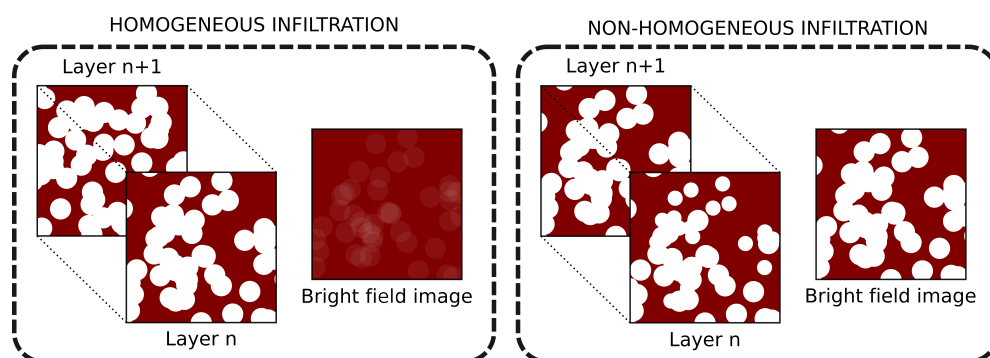


Figure 5.7: Schematic of the expected perovskite infiltration in a mesoporous layer. The brown areas correspond to the perovskite while the lighter areas correspond to poor infiltration (the mesoporous layer is not shown). Homogeneous infiltration leads to a homogeneous bright field image while inhomogeneous infiltration leads to images with high contrast.

All the mesoporous samples present capping layers with similar morphologies with the presence of larger ($> 10 \mu\text{m}$) and smaller ($< 10 \mu\text{m}$) grains (**Figure 5.8a-d**). In the case of AVA-MAPI, the smaller grains are about $3 \mu\text{m}$ and form an almost continuous and smooth capping layer on top of the mesoporous layers.

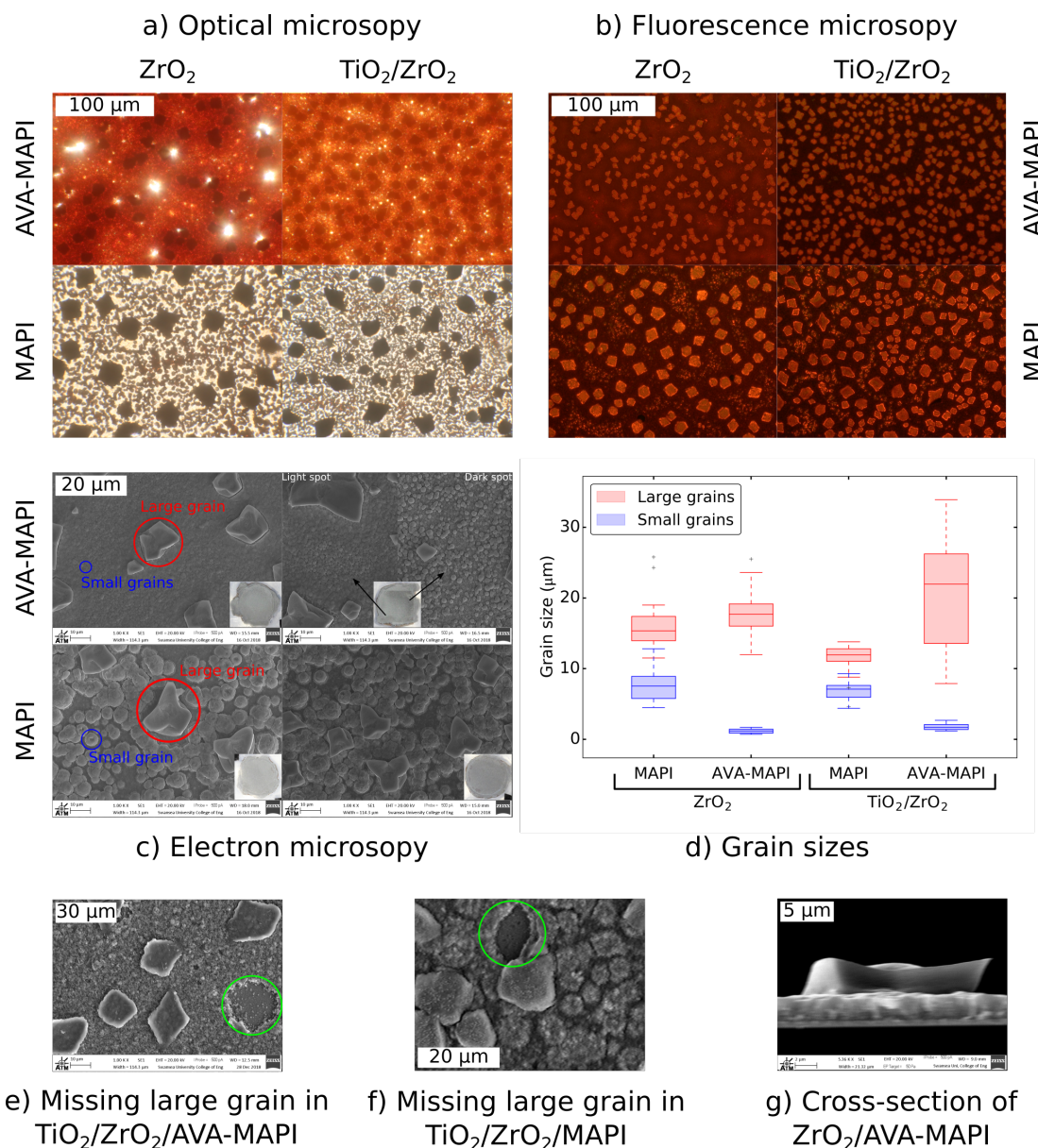


Figure 5.8: a) Optical, b) fluorescence, c) electron microscopy images of the capping layer of MAPI and AVA-MAPI infiltrated in ZrO₂ and TiO₂/ZrO₂. d) Grain size calculated from SEM images. Electron microscopy image of a e) TiO₂/ZrO₂/AVA-MAPI and f) TiO₂/ZrO₂/MAPI samples showing the absence of large grains (red circle) and g) cross-section electron microscopy image of a ZrO₂/AVA-MAPI sample.

The smaller grains in MAPI samples are bigger ($\sim 7 \mu\text{m}$) and do not form a smooth layer, with the presence of many pinholes (**Figure 5.8a & c**). The larger grains are a few μm thick and appear to be partially inside the capping layer formed by the smaller

grains and not sitting on top of it (**Figure 5.8e & f**). $\text{TiO}_2/\text{ZrO}_2/\text{AVA-MAPI}$ is the only sample presenting lighter and darker areas by eye. The darker spot shows a higher surface roughness than the lighter spot, consistent with more stronger scattering which is the likely cause of the darker appearance.

EDX imaging of a $\text{TiO}_2/\text{ZrO}_2/\text{MAPI}$ sample shows the presence of lead and iodide where the large and small grains are situated confirming that these are indeed perovskite grains while little to none of these elements are measured in the pinholes (**Figure 5.9**). Zirconium and oxygen are measured where the small grains and the pinholes are located and likely originates from the ZrO_2 layer located below. These two chemical elements are not measured where the large grains are observed, likely due to their relatively large thickness ($\sim \mu\text{m}$, **Figure 5.8g**), preventing the electrons from reaching the ZrO_2 layer below. Similarly, titanium is only measured where pinholes are located as the cumulative thickness of the ZrO_2 and the perovskite is likely too high to allow the electrons to reach the TiO_2 layer.

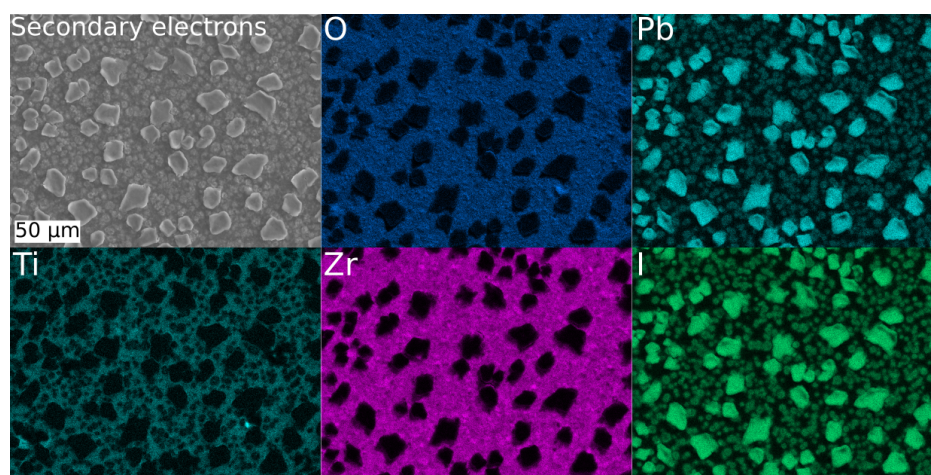


Figure 5.9: Energy dispersive X-ray images of a $\text{TiO}_2/\text{ZrO}_2/\text{MAPI}$ sample (top to bottom, left to right: SEM image, oxygen, lead, titanium, zirconium and iodide).

Annealing and grain growth. The transmittance and optical microscopy images of a $\text{TiO}_2/\text{ZrO}_2/\text{AVA-MAPI}$ sample were recorded during annealing at 50°C (**Figure 5.10**). The bimodal grain distribution in these mesoporous samples can be explained by abnormal grain growth during which some grains grow faster than others.

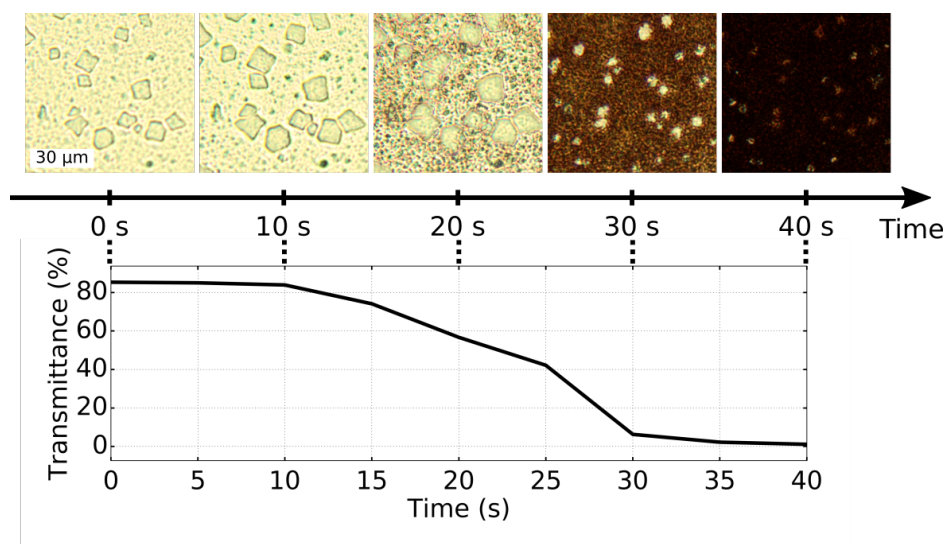


Figure 5.10: Bright field microscopy images and transmittance at 600 nm of AVA-MAPI infiltrated in $\text{TiO}_2/\text{ZrO}_2$ substrate and heated at 50°C .

Large grains and small grains are initially observed. This is likely due to the quick growth of the grains and the time difference between the sample put on the hot plate and the start of the subsequent measurement as well as possible room temperature annealing during the perovskite solution infiltration. The large grains quickly grow while more small grains are observed. The perovskite starts to darken after ~ 20 s and becomes almost entirely black after a minute. No change to the large grain size or the transmittance is observed after the initial minute of annealing.

In order to further investigate the growth process of the perovskite grains, the morphology of MAPI and AVA-MAPI infiltrated in $\text{TiO}_2/\text{ZrO}_2$ was studied at increasing annealing temperatures. Both MAPI and AVA-MAPI perovskites show a decrease of the large grain surface coverage and an increase of the small grain surface coverage for increasing annealing temperature (MAPI also shows a decrease of the pinhole surface coverage) (**Figure 5.11a & d**). In AVA-MAPI samples, such decrease of the large grains surface coverage is explained by fewer large grains at higher temperature (**Figure 5.11b**) without significant size change (**Figure 5.11c**). This suggests that higher temperatures prevent the growth of small grains into large grains but does not affect the final size of the latter. On the other hand, increased number of smaller large grains are obtained at higher temperatures with the MAPI perovskite (**Figure 5.11b & c**). This is consistent with the stronger coarsening of the grains at low temperature, during which smaller grains can merge with larger grains, hence increasing their size and preventing the growth of small grains into large grains. At

higher temperatures, coarsening is more limited and it appears that it is more energetically favourable for the smaller grains to grow into large ones instead of merging with existing ones.

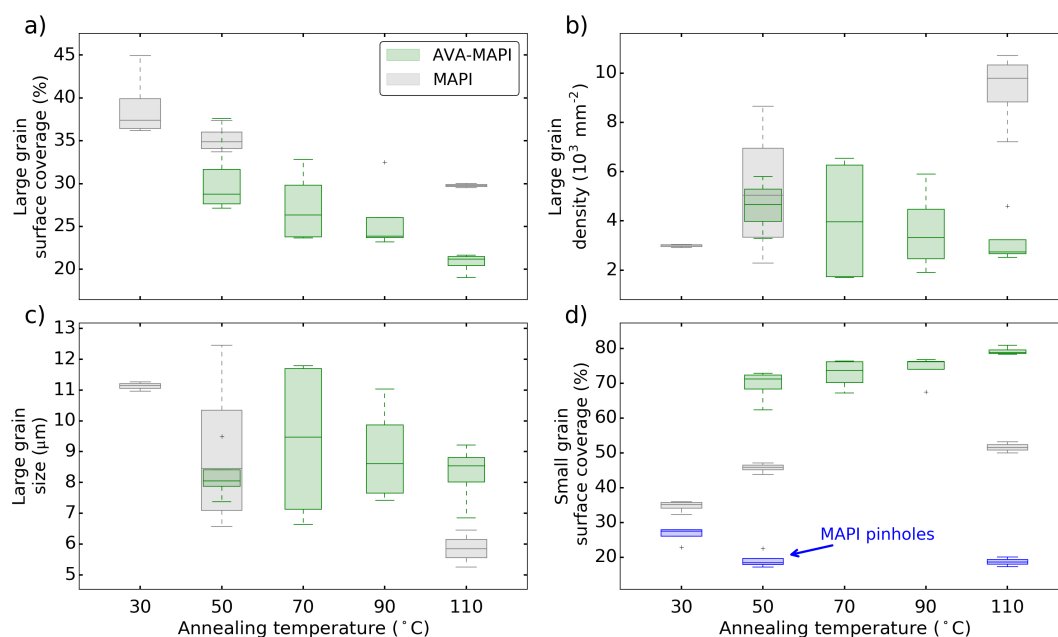


Figure 5.11: a) Surface coverage, b) density and c) size of large grains and d) surface coverage of small grains and pinholes in MAPI and AVA-MAPI infiltrated in $\text{TiO}_2/\text{ZrO}_2$ and annealed at different temperatures. The large grain size was calculated from the surface coverage and the density of grains assuming square grains.

MAPI and AVA-MAPI thus present very different morphologies from each other which is also dependent on the substrate used. These morphological differences are likely responsible for the differences in the optical, crystallographic and PL properties of these samples.

B Optical properties

The total transmittance and reflectance of MAPI and AVA-MAPI drop-cast on glass, FTO glass, ZrO_2 , TiO_2 , $\text{TiO}_2/\text{ZrO}_2$ and $\text{TiO}_2/\text{ZrO}_2/\text{C}$ substrates are shown in **Figures 5.12 & 5.13**. The transmittance of the full stack $\text{TiO}_2/\text{ZrO}_2/\text{C}$ is almost zero over the whole range of wavelengths studied due to the high scattering of the carbon layer. $\text{TiO}_2/\text{ZrO}_2/\text{C}$ samples are therefore not discussed in the following (consequences on the superoxide yield correction factor are discussed in **Section 5.2.6**). Periodic variations of the reflectance measured on the glass side due to thin-film interferences

are observed (**Figures 5.12b & 5.13b**). These are light constructive and destructive interferences due to the delays created by the different layers refraction indexes.

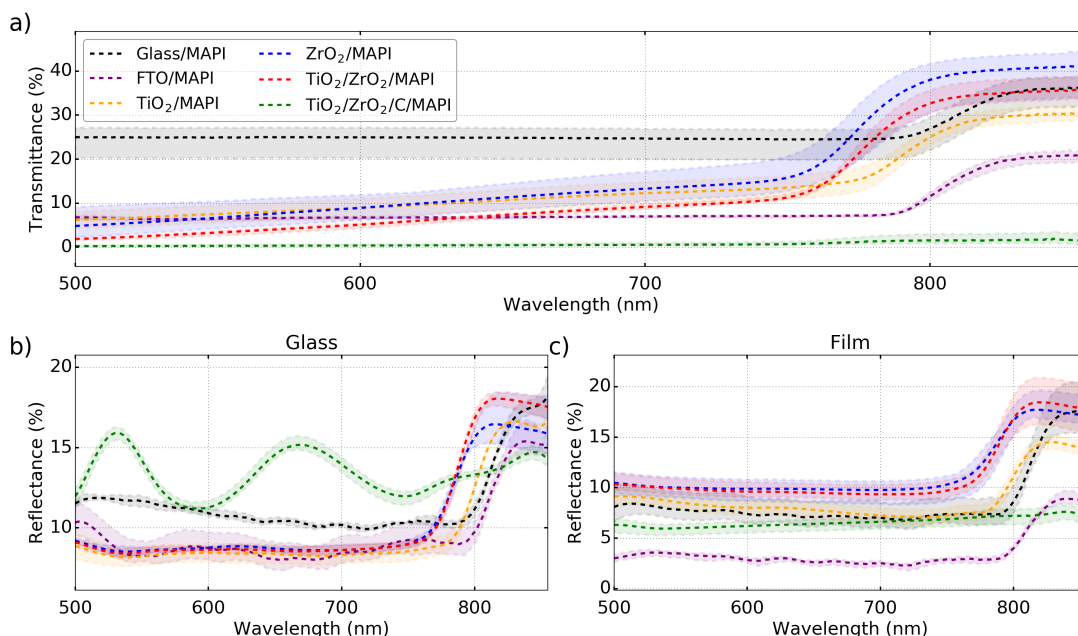


Figure 5.12: Total **a)** transmittance, and **b)** glass-side and **c)** film-side reflectance of MAPI drop-cast on different substrates (4 samples per condition).

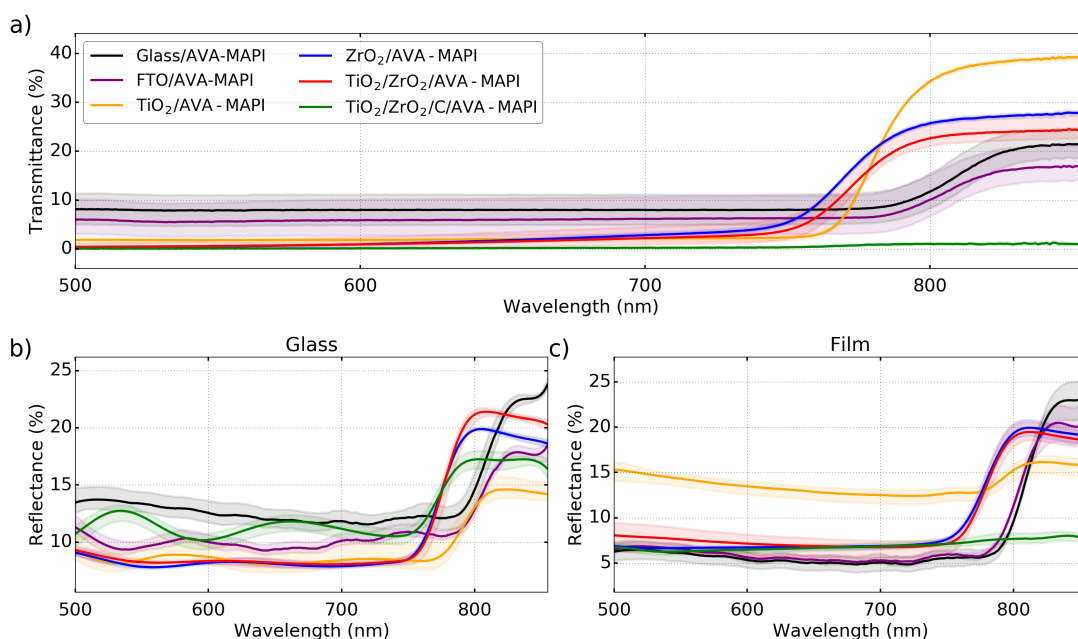


Figure 5.13: Total **a)** transmittance, and **b)** glass-side and **c)** film-side reflectance of AVA-MAPI drop-cast on different substrates (4 samples per condition).

AVA-MAPI samples absorb light more than (or equally as much in the case of the FTO substrate) as their MAPI counterpart (**Figure 5.14 & 5.15**). On glass, MAPI has a lower absorbance than in the other substrates likely due to the many pinholes

previously observed on this substrate (**Figures 5.6**). Glass/AVA-MAPI samples absorb *ca.* 25 % (23 % and 27 % through the glass and film respectively) more light at 700 nm than MAPI while only an 8 % increase of the grain surface coverage was measured for AVA-MAPI (**Figure 5.15**). On FTO glass, the two perovskites have similar absorption spectra. AVA-MAPI absorbs 14 % to 17 % more light than MAPI in ZrO_2 , 6 % to 13 % more in TiO_2 and 9 % to 12 % more in TiO_2/ZrO_2 . Non-zero absorbance is measured above the band-gap energy (*i.e.* $>\sim 840$ nm) likely due to light scattering. Scattering of shorter wavelength is stronger and decreases for lower wavelength which makes it complex to correct for.

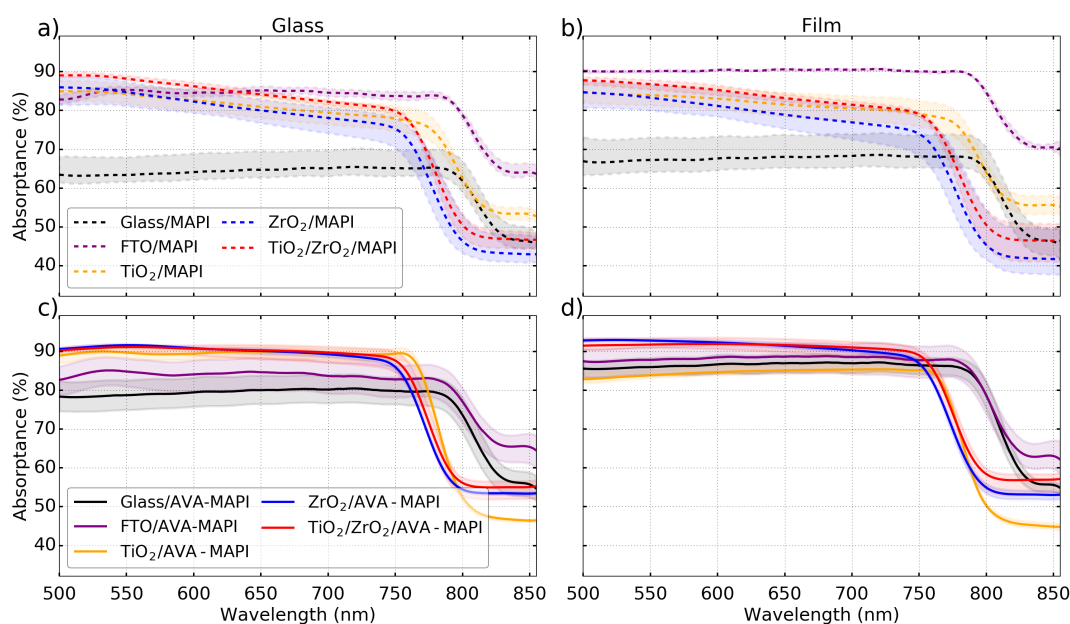


Figure 5.14: Total absorbance at the **a)** & **c)** glass and **b)** & **d)** film interface of **a)** & **b)** MAPI and **c)** & **d)** AVA-MAPI drop-cast on different substrates (4 samples per condition).

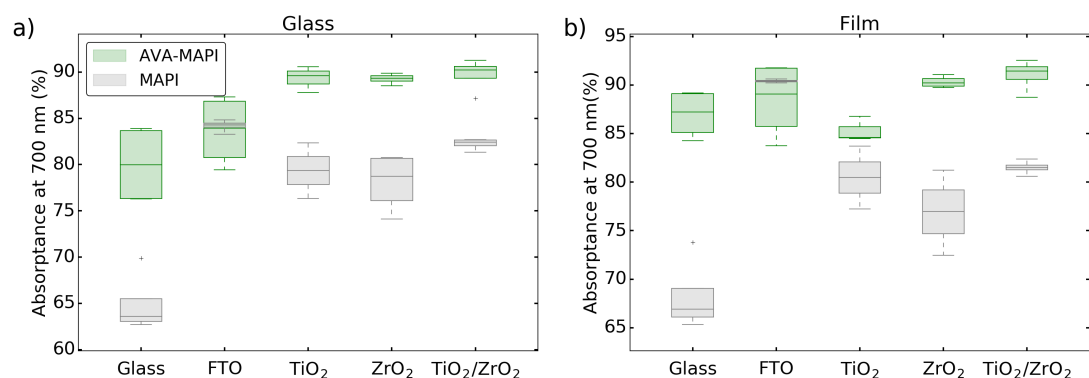


Figure 5.15: Absorbance of MAPI and AVA-MAPI deposited on different substrates at 700 nm and measured through the **a)** glass and **b)** film side (4 samples per condition).

The band-gap energy was calculated from the Tauc method (**Figure 5.16**). Due to the important scattering previously mentioned, the absorption coefficient α was corrected using an average baseline calculated above the band-gap energy (see **Section 2.6.4**). This is a fair assumption as the region of interest here (the absorption front) is localised over a shallow range of wavelength and therefore scattering can be assumed to uniformly affect this region (**Figure 5.16a**). The band-gap energy of both perovskites shifts from ~ 810 nm when deposited on glass and FTO glass down to ~ 770 nm when infiltrated in a mesoporous architecture. As previously discussed in **Chapter 3**, such blue-shift could be explained by the presence of smaller grains in the mesoporous architectures, consistent with the expected constriction of the grain growth within the mesoporous layer pores [15]–[17]. The smaller band-gap energy of TiO₂/MAPI compared to other mesoporous samples would then suggest bad infiltration of the perovskite within the TiO₂ pores. The MAPI perovskite always present a smaller band-gap than AVA-MAPI (or equal in the case of FTO glass). This is consistent with the previous observations made using optical and electron imaging showing the formation of smaller grains in AVA-MAPI samples (at least in the capping layer for mesoporous samples). The band-gap energy of ZrO₂ samples is very similar to TiO₂/ZrO₂ while TiO₂ samples present a lower energy. Consistent with the previous morphology observations, this suggests that the ZrO₂ layer affects more the perovskite morphology than the TiO₂ layer. Depending on the perovskite solution and substrate, a slight shift of the band-gap energy was noted between the perovskite and glass sides (**Figure 5.16b**). This could be explained by the expected different grain sizes at the substrate/perovskite interface and in the capping layer.

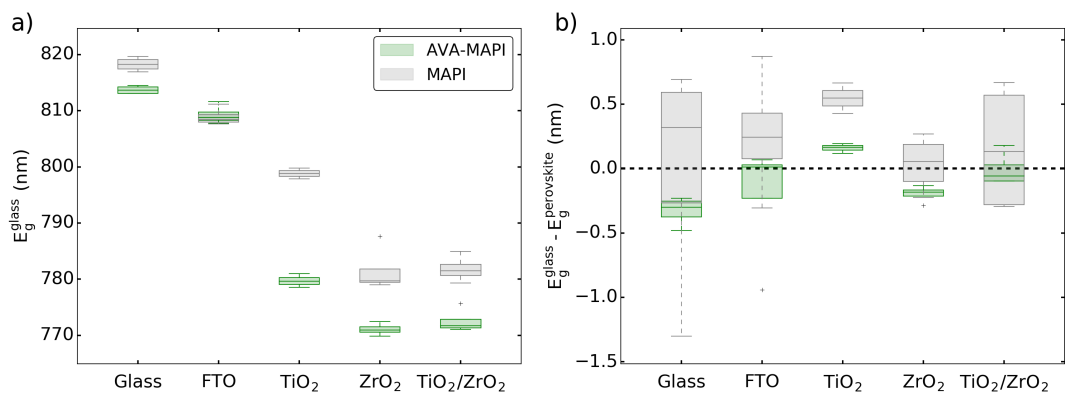


Figure 5.16: **a)** Band-gap energy calculated from the transmittance and reflectance measured from glass side E_g^{glass} and **b)** difference of band-gap energy between the glass and perovskite side $E_g^{perovskite}$ (4 samples per condition).

MAPI and AVA-MAPI present significant differences in their absorbance spectra with different band-gap energies which could be partially explained by the presence of smaller grains in the mesoporous substrates and different infiltration of the perovskites. This can be related to the very different fluorescence properties of these perovskites.

C Photoluminescence properties

The steady-state PL spectra of MAPI and AVA-MAPI drop-cast on glass, FTO glass, ZrO₂, TiO₂, TiO₂/ZrO₂ and TiO₂/ZrO₂/C was measured through the glass side and film side using spectrofluorometry and fluorescence microscopy (**Figure 5.17**).

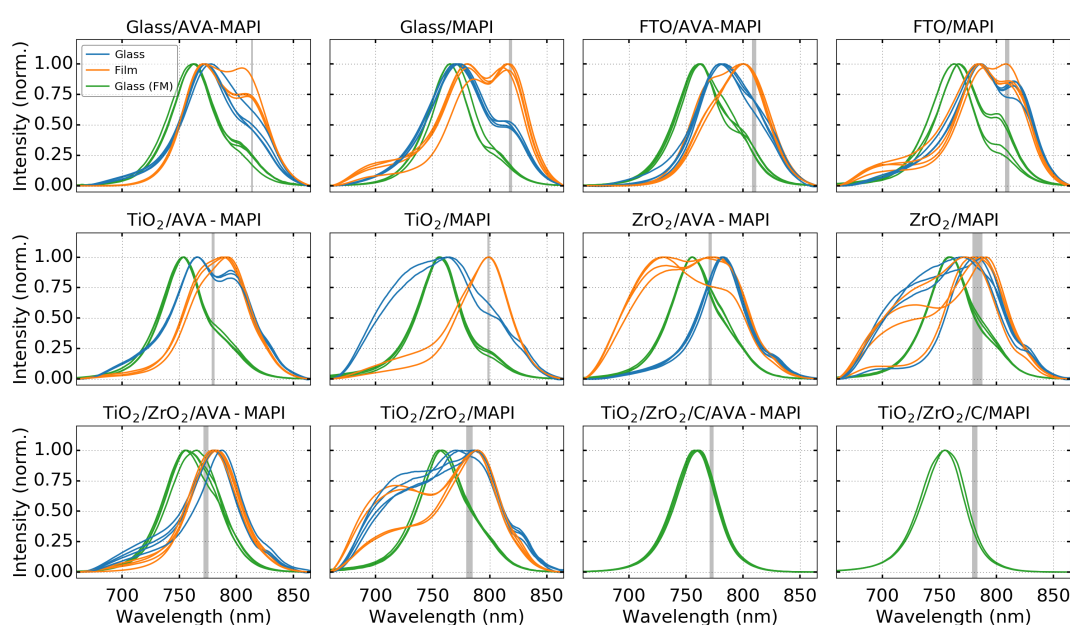


Figure 5.17: PL spectra of MAPI and AVA-MAPI drop-cast on different substrates (4 samples per condition, some spectra are not shown due to saturation of the detector) and measured through the glass (blue) and film (orange) side with a spectrofluorometer (TiO₂/ZrO₂/C samples were not measured with the spectrofluorometer due to their low emission) and through the glass with a fluorescence microscope (FM - green). The range of band-gap energies calculated from UV-Vis spectroscopy is shown as grey areas.

The emission spectra measured with the fluorometer are first discussed. Three peaks are distinguished in the emission spectra of MAPI and AVA-MAPI which have not been observed before [7], [18]: between 700 – 750 nm, 750 – 775 nm and 775 – 825 nm. Their relative intensities and positions appear to depend on the substrate and perovskite solution used but also on the side measured and the repeat sample (*e.g.* ZrO₂/MAPI repeat samples show significant variations of their PL

intensity). The presence of an emission peak around 730 nm has been previously associated with the 2D/3D perovskite phase formed when AVA-MAPI is infiltrated in a TiO₂ mesoporous layer [7]. The 700 – 750 nm peak is located around the same wavelength in AVA-MAPI samples, but is also present in MAPI samples thus suggesting that this peak does not correspond to the 2D/3D phase (**Figure 5.17**).

When the perovskites are drop-cast on glass and FTO glass substrates to mesoporous substrates, all the peaks shift to lower wavelengths. This could be due to a change of the relative intensity between the peaks, although the consistent shift of the band-gap energy calculated from UV-Vis spectroscopy suggests a change of the grain electronic properties due to *e.g.* strain or smaller grains in the mesoporous layers as previously discussed (Section **5.3.1B**). On glass and FTO glass, the 750 – 775 nm peak is more intense than the 775 – 825 nm peak when measured through the glass while the opposite is observed when measured through the film. This suggests the presence of smaller grains at the substrate-perovskite interface [15]–[17]. When drop cast on mesoporous substrates, the 700 – 750 nm peak emission increases consistent with the presence of smaller grains with a higher band-gap energy in these samples. These 3 peaks could thus originate from different grain type of different sizes in the samples.

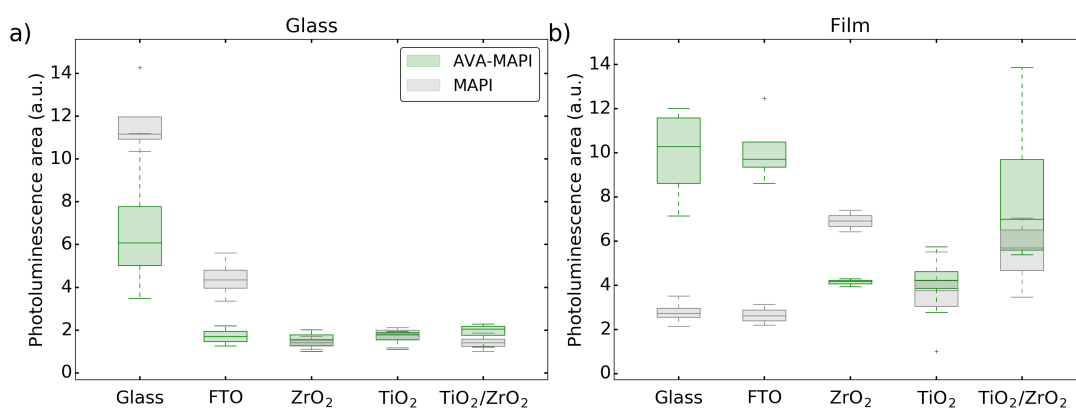


Figure 5.18: PL spectra area of MAPI and AVA-MAPI drop-cast on different substrates and measured on the **a)** glass and **b)** perovskite sides (4 samples per condition).

When measured through the glass side, AVA-MAPI is less emissive than MAPI on glass (**Figure 5.18a**) while the opposite is observed on the film side (**Figure 5.18b**). Compared to the glass substrate, the emission of both perovskites decreases from when drop-cast on FTO glass and when measured through the glass side but is

unaffected on the perovskite side, suggesting that these two substrates affect the grain formation at the substrate/perovskite interface but not on the film side. On the glass side, the emission of AVA-MAPI and MAPI is similar when infiltrated in ZrO₂, TiO₂ and TiO₂/ZrO₂. However, on the film side, the emission of AVA-MAPI decreases in ZrO₂ and TiO₂ compared to FTO glass, suggesting that the perovskite capping layer is affected by the mesoporous layer, consistent with the previous electron microscopy observations. The emission of MAPI in ZrO₂ is similar to FTO, increases in TiO₂ and slightly decreases in TiO₂/ZrO₂.

When measured with the fluorescence microscope, the 700 – 750 nm peak is not noticeable and the positions of the 750 – 775 nm and 775 – 825 nm peaks show much less variations depending on the substrate and perovskite. Such blue-shift can be partially explained by the different excitation fluences of the fluorescence microscope and the fluorometer (2.4 mW/cm² and 33 W/cm² respectively). In ZrO₂/AVA-MAPI, the large grains are more emissive than the small ones under high excitation fluence ($P \sim 33 \text{ mW/cm}^2$) (**Figure 5.19d**). This is still valid even if the sample is prior illuminated (for a few seconds) with low excitation fluence ($P \sim 2 \text{ mW/cm}^2$) and little difference is observed between the grain behaviours over time due to the previous illumination condition (**Figure 5.19b & f**). Under low fluence, emission from the small grains is more intense and both small and large grains photodarken over time (**Figure 5.19a & e**). However, emission from the large grains becomes dominant at low excitation fluence if the samples is exposed for a few seconds to high excitation fluence beforehand (**Figure 5.19c & e**) with persistence of the effect over at least 1 hour. In this case, the small grains photobrighten over a few seconds and then photodarken while the small grains photobrighten and quickly stabilise, without reaching the emission intensity of the large grains (**Figure 5.19e**). Such non-reversible change of the PL properties of the perovskite due to short exposition to high excitation fluence could be explained by irreversible photodarkening (due to *e.g.* degradation) and photobrightening (due to trap state passivation by oxygen and moisture) of the grains.

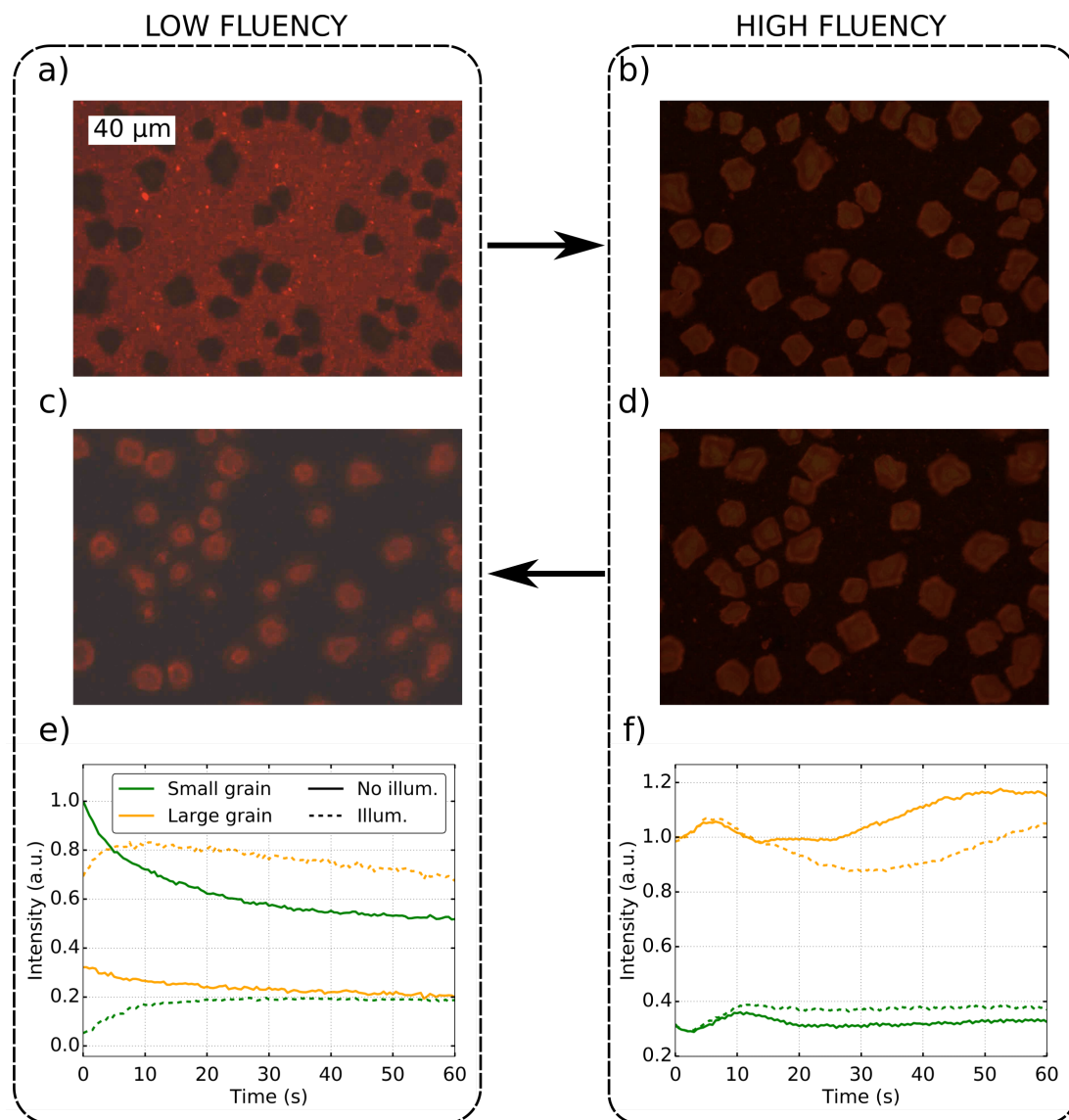


Figure 5.19: Fluorescence microscopy images of 2 spots of the capping layer of a $\text{ZrO}_2/\text{AVA-MAPI}$ sample. The first spot was sequentially measured with first **a)** low and second **b)** high excitation fluence ($P_{low} \sim 0.06P_{high}$) while the second spot was measured with first **c)** high and second **d)** low excitation fluence. **e)** Evolution of the intensity of the small (green) and large (orange) grains under low excitation fluence, with (dashed curves) and without (continuous curves) prior high fluence illumination and **f)** evolution of the intensity of the grains under high excitation fluence, with and without prior low fluence illumination.

The intensity of the fluence-normalised PL spectra obtained with low excitation fluence was estimated 11 (sequentially high and low fluences illumination) to 18 (sequentially low and high fluences illumination) times higher than the high fluence measurement. This could be explained by a higher contribution of Auger recombination at high excitation fluence. This is consistent with the report that Auger recombinations are non-negligible above 10 suns intensity

(1 sun = 1.4×10^8 photons/ns/cm² for a 1.6 eV band-gap semiconductor) while a maximum 9.3×10^{10} photons/ns/cm² is used here [19]. The lower intensity at higher fluence could as well be explained by very fast photodarkening of the sample when excited with high fluence.

Independent of the previous illumination condition, the low fluence PL spectra presents a peak around 765 nm while the high fluence peak is located at 750 nm and is broader (the slight difference observed between the illumination conditions likely originates from variation in the film) (**Figure 5.20a**).

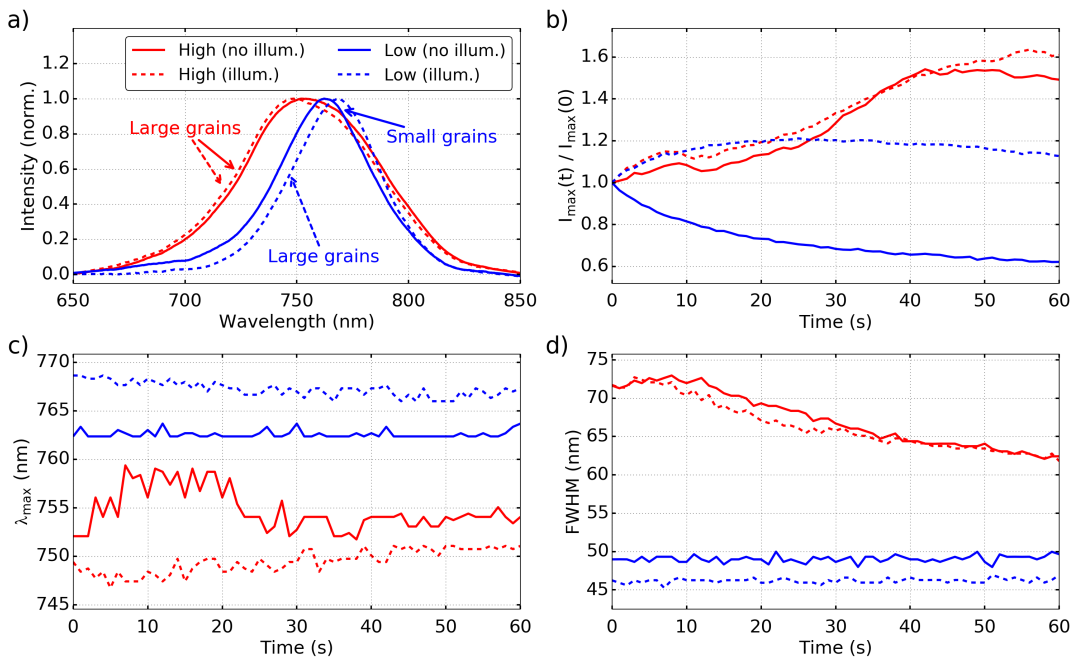


Figure 5.20: Evolution of the PL properties of ZrO₂/AVA-MAPI under high and low excitation fluence measured at 2 spots with and without prior illumination. **a)** PL spectra, **b)** evolution of the maximum intensity I_{max} , **c)** emission wavelength λ_{max} and **d)** FWHM.

With or without prior illumination, similar PL spectra are obtained at low excitation fluence while PL images show exclusively large and small grains emission respectively (**Figure 5.19**). This suggests that both large and small grains have similar emission position and shape although their intensity is different and behave differently over time (**Figures 5.19 & 5.20**). This is inconsistent with the previous observation explaining the origin of different emission peaks from different grain sizes. However, the emission measured here likely originates from the capping layer and it is possible that grains located within the mesoporous layers have a different emission spectrum. The sample photobrightens under high excitation fluence independent of the previous illumination

condition (**Figure 5.20b**). This is associated with a decrease of its FWHM (such as observed in **Chapter 3**) and negligible change to the emission wavelength (**Figure 5.20c & d**). Conversely, the sample only photodarkens under low excitation fluence if not previously illuminated, and initially photobrightens and then photodarkens if prior illuminated with high fluence without noticeable change of the emission wavelength nor the FWHM (**Figure 5.20b-d**). The PL spectra was measured for fluences between 2 W/cm^2 and 33 W/cm^2 at different spots to avoid photobrightening and degradation (**Figure 5.21**).

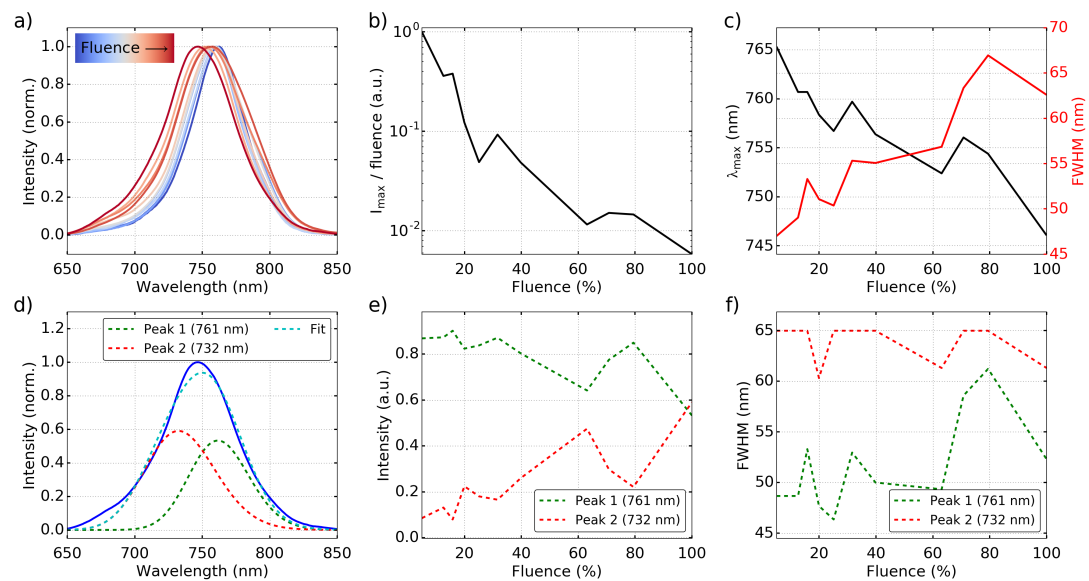


Figure 5.21: Evolution of the PL properties of $\text{ZrO}_2/\text{AVA-MAPI}$ depending on the excitation fluence (measured at different spots). **a)** PL spectra, **b)** fluence-normalised maximum intensity $I_{max}/fluence$, **c)** emission wavelength λ_{max} and FWHM. **d)** Fitting of the 100 % fluence spectrum with a double-Gaussian model, and **e)** intensity and **f)** FWHM of the fitted Gaussians ($R^2 = 0.994$).

As previously discussed, a large decrease of the PL intensity is observed and may be linked to increased Auger recombination or faster photodarkening of the perovskite as the excitation fluence is increased. This is associated with a blue-shift of the emission peak and an increase of its FWHM. Assuming that the high fluence peak is composed of 2 peaks, a double-Gaussian model was used to fit the normalised PL spectra. The positions of the 2 Gaussians were assumed independent of the excitation fluence and the fit was performed on an energy scale [20]. One peak was found at the same wavelength ($\sim 760 \text{ nm}$) as the low excitation fluence peak (**Figure 5.20a**) while the second peak was found at 732 nm (**Figure 5.21d**). The lower energy peak intensity decreases as the excitation fluence is increased while the intensity of the

higher energy peak increases (**Figure 5.21e**). Variations of the FWHMs is noted but no trend is noticeable (**Figure 5.21f**). Such dependency of the emission spectra shape on the excitation fluence may explain why the PL spectra obtained with the fluorescence microscope is blue-shifted with respect to the fluorometer spectra as the fluorometer lamp power is much lower than the fluorescence microscope (**Figure 5.17**).

MAPI and AVA-MAPI therefore present complex photoluminescence properties with multiple emission peaks whose position, intensity and FWHM appear to depend on the excitation fluence and substrate.

D Crystallographic properties

The XRD pattern of MAPI and AVA-MAPI infiltrated in ZrO_2 , TiO_2/ZrO_2 and $TiO_2/ZrO_2/C$ was measured between 12° and 14.5° as well as between 27.5° and 29° (**Figure 5.22**).

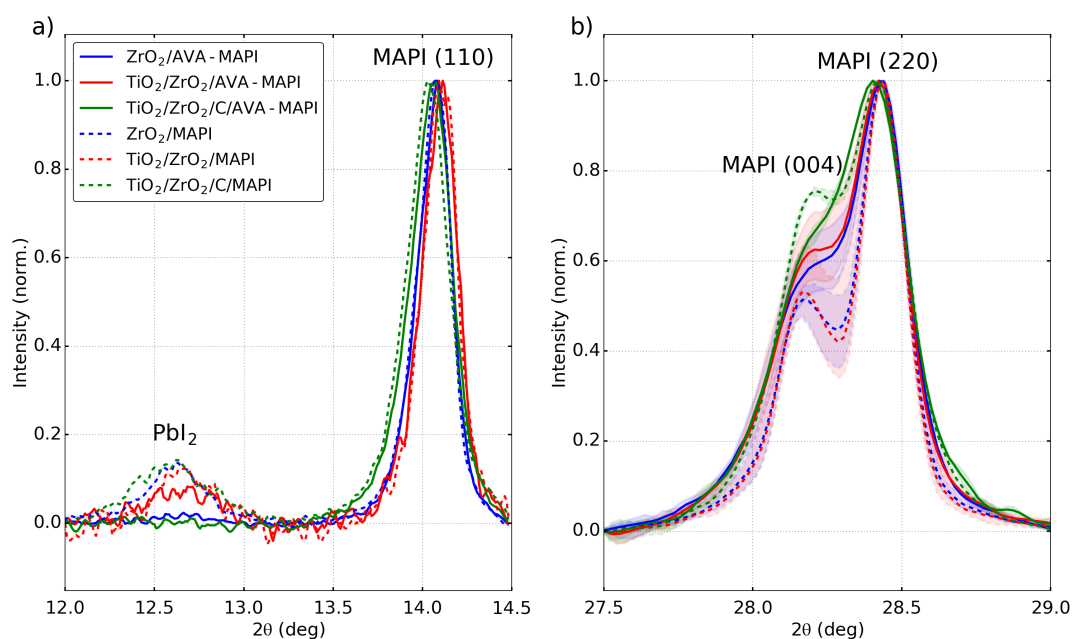


Figure 5.22: X-ray diffraction pattern of MAPI and AVA-MAPI in different substrates between **a)** 12° and 14.5° , and **b)** 27.5° and 29.0° (3 samples per condition).

Both perovskites present diffraction peaks at 14.1° ((002) & (110)), 28.2° (004) and 28.3° (220) that match the tetragonal phase of MAPI (see **Chapter 3** for a more detailed discussion about the crystallographic phase of MAPI at room temperature). All MAPI samples show a low intensity peak at 12.6° corresponding to lead iodide. This can be related to the instability of the MAPI solution which tends to precipitate

at room temperature. Since 10 min of infiltration is required during the samples manufacturing, the solution may precipitate during the infiltration hence explaining the presence of lead iodide in fresh samples. $\text{TiO}_2/\text{ZrO}_2/\text{AVA-MAPI}$ is the only AVA-MAPI sample to present lead iodide after annealing. Differences in the (004) and (220) peak intensity ratio has been previously observed between MAPI and AVA-MAPI [7]. Here, the ratio of the (004) and (220) peaks are extracted by fitting the diffraction pattern with a double-Gaussian distributions. The position of the peaks were assumed independent of the substrate and perovskite used (**Figure 5.23**).

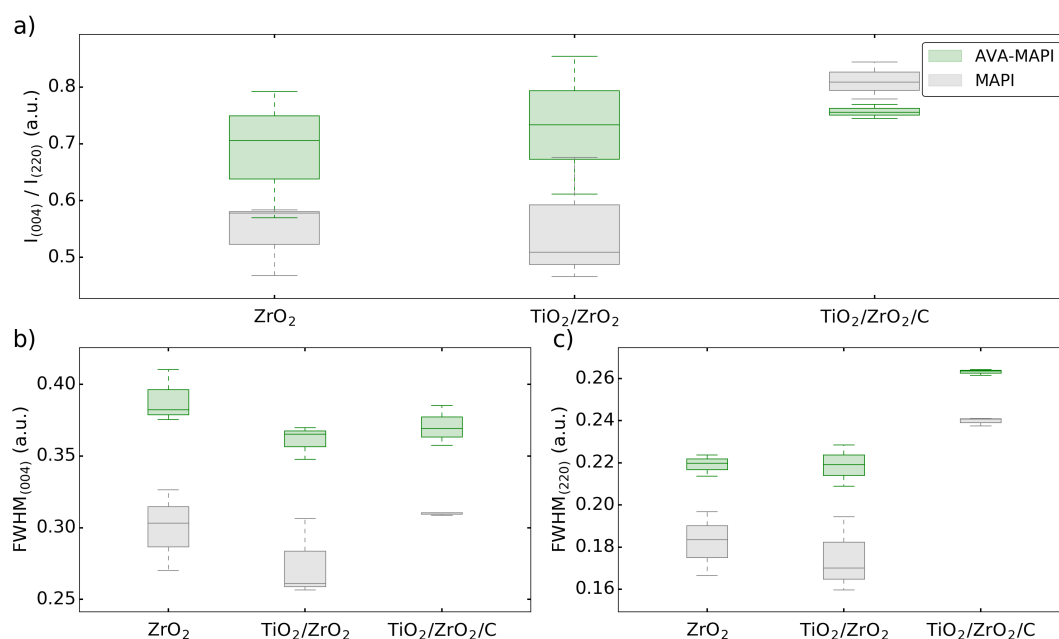


Figure 5.23: Results of the fitting of the XRD patterns ($R^2 > 0.981$). **a)** Gaussians intensity ratio and FWHM of the Gaussians associated with peaks **b)** (004) and **c)** (220).

The crystal mean domain size is inversely proportional to the FWHM according to the Scherrer equation. AVA-MAPI thus presents smaller crystal sizes in the substrates studied, consistent with the previous observations using optical and electron microscopy (**Figure 5.23b & c**). In ZrO_2 and $\text{TiO}_2/\text{ZrO}_2$, a higher fraction of grains have a (004) orientation in AVA-MAPI than in MAPI as indicated by the higher $I_{(004)}/I_{(220)}$ ratio while the opposite is observed in $\text{TiO}_2/\text{ZrO}_2/\text{C}$ (**Figure 5.23a**). In comparison, a lower fraction of (004) grains has been previously reported in $\text{TiO}_2/\text{AVA-MAPI}$ compared to TiO_2/MAPI [7]. As previously discussed regarding the photoluminescence properties of these samples, TiO_2 and ZrO_2 substrates appear to

affect differently the perovskite. Hence it is therefore not surprising to observe a preferred (004) orientation when infiltrated in ZrO_2 than in TiO_2 .

5.3.2 Stability of MAPI and AVA-MAPI perovskites on different substrates

A Ambient stability under illumination

AVA-MAPI has been previously shown to be more stable than MAPI when infiltrated in mCPSCs [21]. In order to further understand the stability improvement of AVA-MAPI compared to MAPI, the XRD pattern of these perovskites infiltrated in ZrO_2 , $\text{TiO}_2/\text{ZrO}_2$ and $\text{TiO}_2/\text{ZrO}_2/\text{C}$ substrates was measured under illumination in an ambient atmosphere over time (**Figure 5.24**).

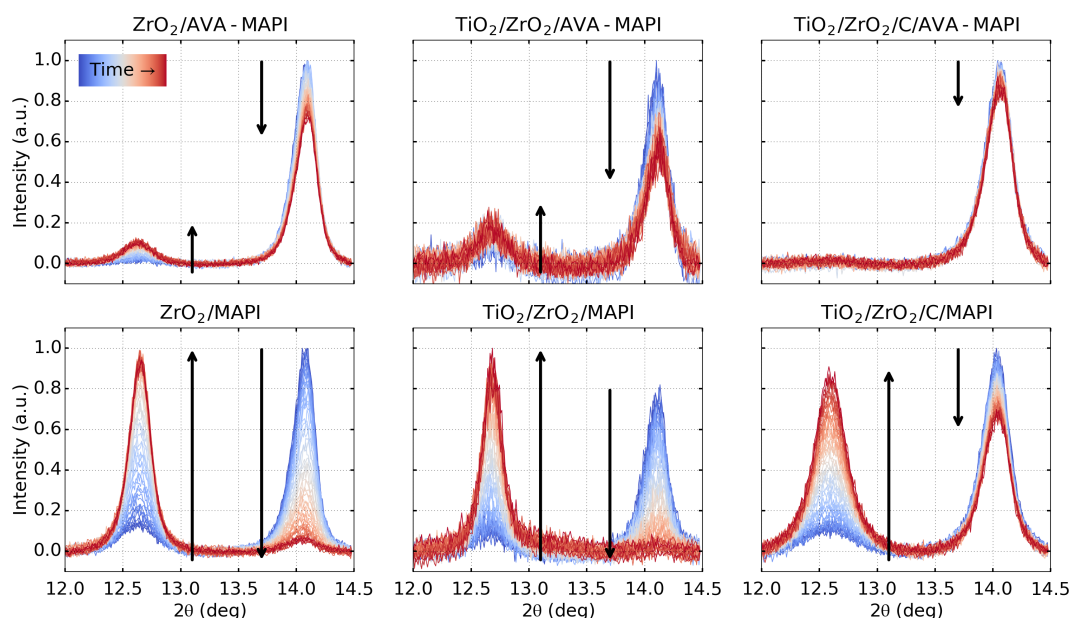


Figure 5.24: Evolution of the diffraction pattern between 12.0° and 14.5° of MAPI and AVA-MAPI in different substrates under illumination in ambient atmosphere for 12 hours.

ZrO_2/MAPI and $\text{TiO}_2/\text{ZrO}_2/\text{MAPI}$ completely degrades to lead iodide after 12 hours as indicated by the disappearance of the (110) perovskite peak at 14° and the appearance of the lead iodide peak at 12.6° . Lower degradation is observed in $\text{TiO}_2/\text{ZrO}_2/\text{C}/\text{MAPI}$ which could be explained by the hydrophobic properties of the carbon layer, thus preventing infiltration and degradation of the perovskite by water.

AVA-MAPI shows much lower degradation in all the substrates studied, especially in $\text{TiO}_2/\text{ZrO}_2/\text{C}$.

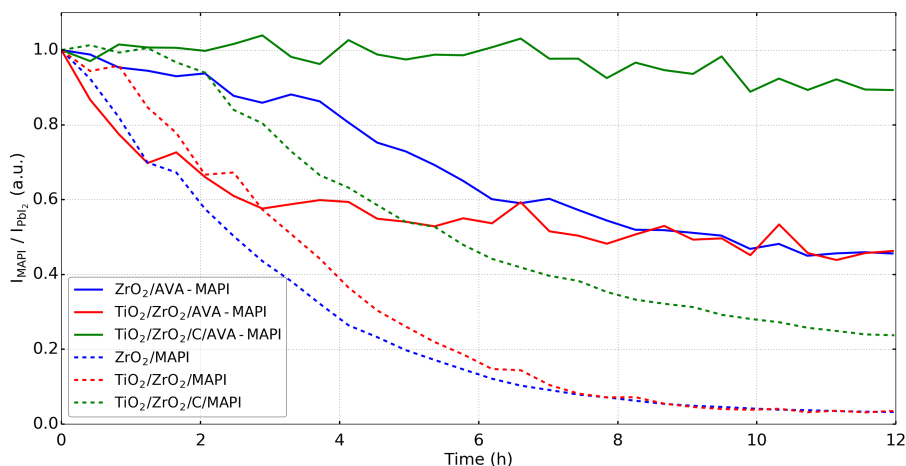


Figure 5.25: Evolution of the intensity ratios of the MAPI and PbI_2 peaks over 12 hours illumination.

MAPI infiltrated in ZrO_2 presents the highest degradation rate with the perovskite being almost entirely converted to lead iodide after 12 h (**Figure 5.25**). The same substrate using AVA-MAPI is much more stable in comparison with an $I_{\text{MAPI}}/I_{\text{PbI}_2}$ ratio of 0.45 after 12 h indicating a significant amount of non-degraded perovskite. $\text{TiO}_2/\text{ZrO}_2/\text{MAPI}$ is initially slightly more stable than ZrO_2/MAPI but is also fully degraded after 12 h. $\text{TiO}_2/\text{ZrO}_2/\text{AVA-MAPI}$ is initially less stable than $\text{ZrO}_2/\text{AVA-MAPI}$ and displays a similar initial decay to $\text{TiO}_2/\text{ZrO}_2/\text{MAPI}$ which slows down after the first 2 hours. $\text{TiO}_2/\text{ZrO}_2/\text{C}$ stacks present higher stabilities than other samples using the same perovskite, likely thanks to inhibition of moisture degradation by the carbon layer. In particular, $\text{TiO}_2/\text{ZrO}_2/\text{C}/\text{AVA-MAPI}$ shows the lowest degradation rate, demonstrating the higher stability of AVA-MAPI compared to MAPI. AVA-MAPI infiltrated in any of the substrates studied here is therefore more stable than MAPI. It is particularly striking that AVA-MAPI infiltrated in ZrO_2 is less degraded after 11 hours than MAPI infiltrated in the full stack of $\text{TiO}_2/\text{ZrO}_2/\text{C}$. This is somewhat surprising as it is expected that the thick carbon layer offers significant protection to the perovskite film. This highlights the significant stability benefit of the 5-AVAI additive in ambient atmosphere. The higher stability observed between AVA-MAPI and MAPI in their respective substrates suggest it could originate from the different perovskite morphologies previously observed, although an active effect

of the 5-AVAI molecule should not be ignored. However, it is not clear whether this improved stability is due to hindered moisture or oxygen degradation.

B Superoxide formation in MAPI and AVA-MAPI perovskites

Properties of the dihydroethidium fluorescence probe. The dihydroethidium fluorescence probe was used to measure superoxide formation in MAPI and AVA-MAPI samples. When dissolved in toluene, dihydroethidium presents an absorption peak centred around 360 nm and an emission peak around 390 nm. When dihydroethidium reacts with superoxide, it forms 2-hydroxyethidium which has an absorption peak around 525 nm and an emission peak around 660 nm (**Figure 5.26**).

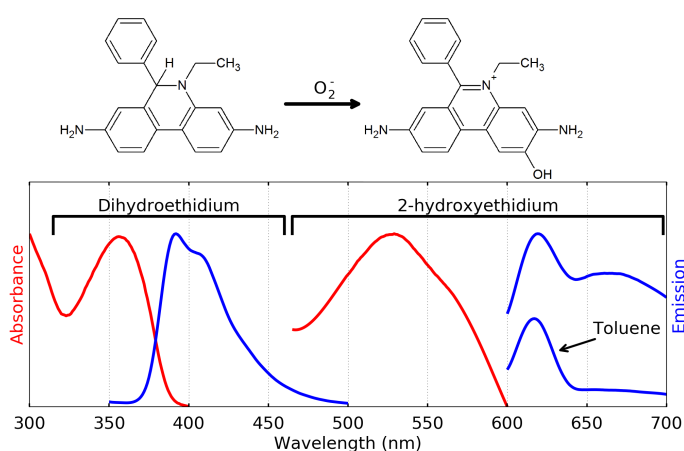


Figure 5.26: Absorption (red) and fluorescence (blue) spectra of dihydroethidium and 2-hydroxyethidium in toluene. The emission of toluene is also shown.

The sharp peak in the 2-hydroxyethidium emission spectra at 620 nm corresponds to a Raman peak of the toluene solvent as suggested by the dependence of its position on the excitation wavelength (**Figure 5.27**).

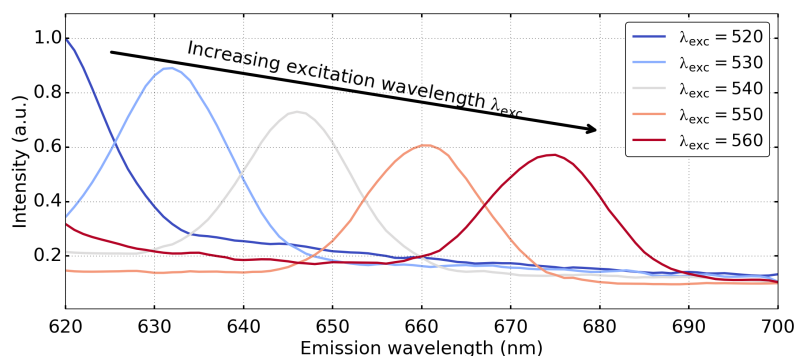


Figure 5.27: Emission spectrum of toluene measured with different excitation wavelengths λ_{exc} .

The molar attenuation coefficient of dihydroethidium was measured using the relation between its absorbance and concentration as per the Beer-Lambert law. An average value of $7632 \pm 25 \text{ M}^{-1}\text{cm}^{-1}$ at 357 nm was obtained through 3 measurements and 9 dilutions (comparable to the value of $9750 \text{ M}^{-1}\text{cm}^{-1}$ at 345 nm reported for DMSO [22]) (**Figure 5.28**).

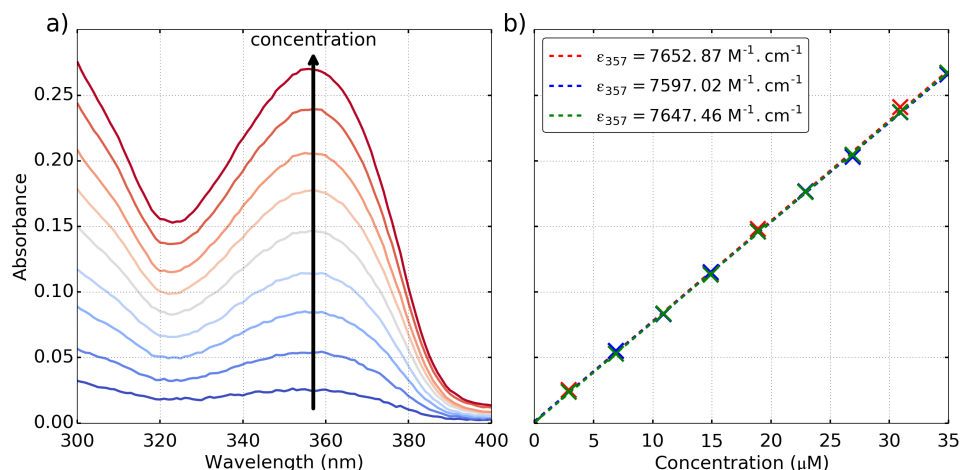


Figure 5.28: Determination of the molar attenuation coefficient at 357 nm (ϵ_{357}) of dihydroethidium in toluene. **a)** Absorption spectra at different concentrations and **b)** linear fitting of the absorbance at 357 nm as a function of the concentration.

Superoxide yield of MAPI and AVA-MAPI drop-cast on glass and mesoporous substrates. The superoxide yield correction factor β calculated for illumination through the glass and film is shown in **Figure 5.29a & b**. As previously noted, the presence of mesoporous layers leads to important light scattering leading to non-zero absorbance above the band-gap energy. This was corrected by shifting the absorbance above the band-gap wavelength to zero (**Figure 5.29c & d**). Due to the high scattering of the carbon layer, the transmittance of $\text{TiO}_2/\text{ZrO}_2/\text{C}$ was assumed the same as of $\text{TiO}_2/\text{ZrO}_2$ samples. The superoxide yield are further corrected using the size of each sample according to **Equation 5.6**.

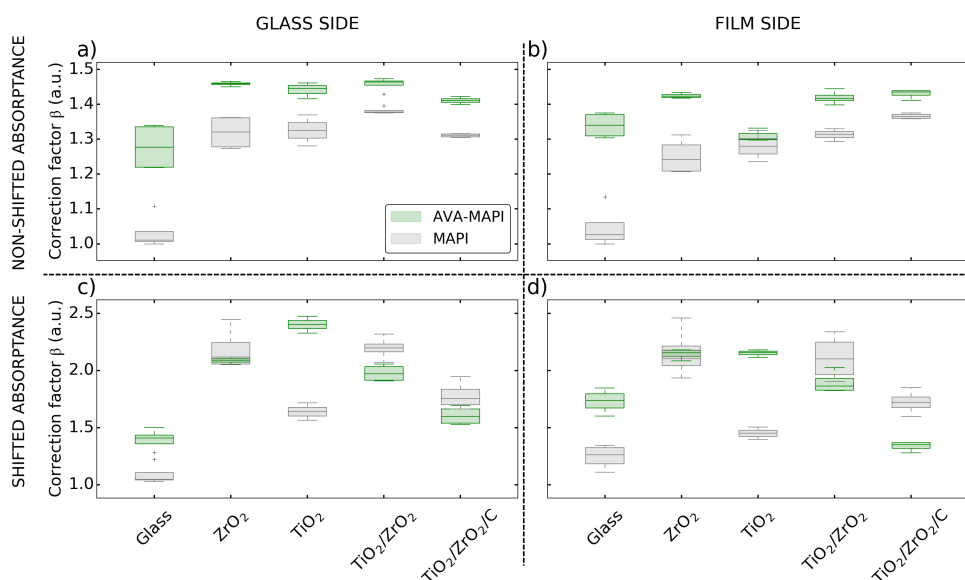


Figure 5.29: Correction factor for the superoxide yield measurement for illumination through the **a)** & **c)** glass and **b)** & **d)** film using the **a)** & **b)** absorbance and the **c)** & **d)** shifted absorbance.

Figure 5.30 shows the evolution of the fluorescence of dihydroethidium in toluene in the presence of a $\text{ZrO}_2/\text{AVA-MAPI}$ sample under illumination.

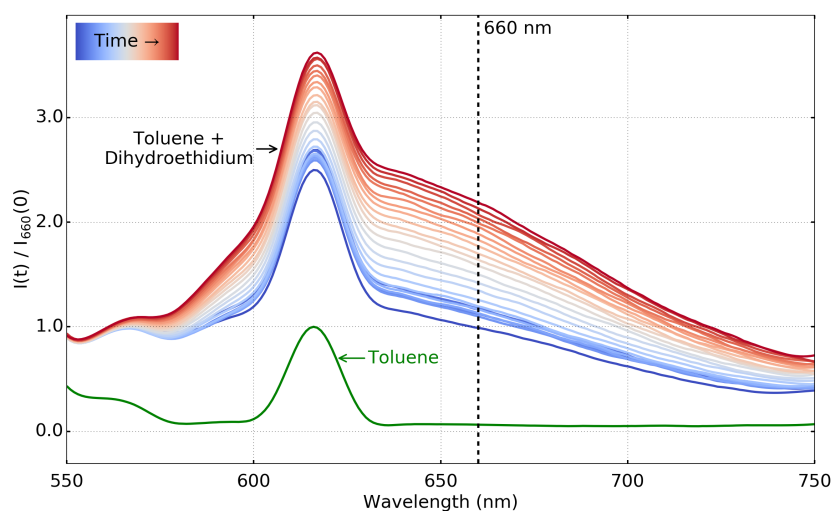


Figure 5.30: Evolution of the emission spectra of dihydroethidium in toluene in the presence a $\text{ZrO}_2/\text{AVA-MAPI}$ samples under illumination over 2 hours.

The emission intensity increases with time indicating the formation of 2-hydroxyethidium from the reaction of dihydroethidium with superoxide. The superoxide yield was taken at 660 nm which gives the highest ratio $I(t)/I(0)$ and where the toluene Raman peak does not affect the emission spectra of the probe.

Figure 5.31 shows the evolution of the superoxide yield of MAPI and AVA-MAPI drop-cast on glass.

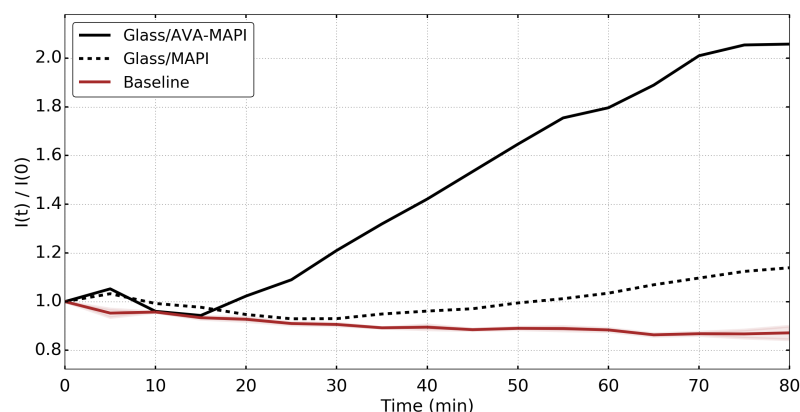


Figure 5.31: Superoxide yield of MAPI and AVA-MAPI drop-cast on glass over 80 min. The evolution of the intensity ratio without a sample is shown in brown.

The corrected superoxide yield $I(t)/I(0)$ at 660 nm shows that glass/AVA-MAPI generates more superoxide than glass/MAPI within the experiment timescale, consistent with the work of C.T. Lin *et al.* [18]. Although AVA-MAPI has been reported to have a lower defect concentration than MAPI [18], the smaller size of the crystals of AVA-MAPI lead to a higher surface/volume ratio which may increase the overall defect concentration of AVA-MAPI compared to MAPI and thus may explain the higher superoxide yield measured in AVA-MAPI. The variations of the probe fluorescence without a sample present were recorded twice as a baseline (**Figure 5.31**). A slight decrease of the fluorescence intensity is observed over time which may be explained by the degradation of 2-hydroxyethidium by light. The superoxide yield of MAPI and AVA-MAPI infiltrated in ZrO_2 , TiO_2/ZrO_2 and $TiO_2/ZrO_2/C$ substrates was measured with illumination through the glass and film sides (**Figure 5.32**).

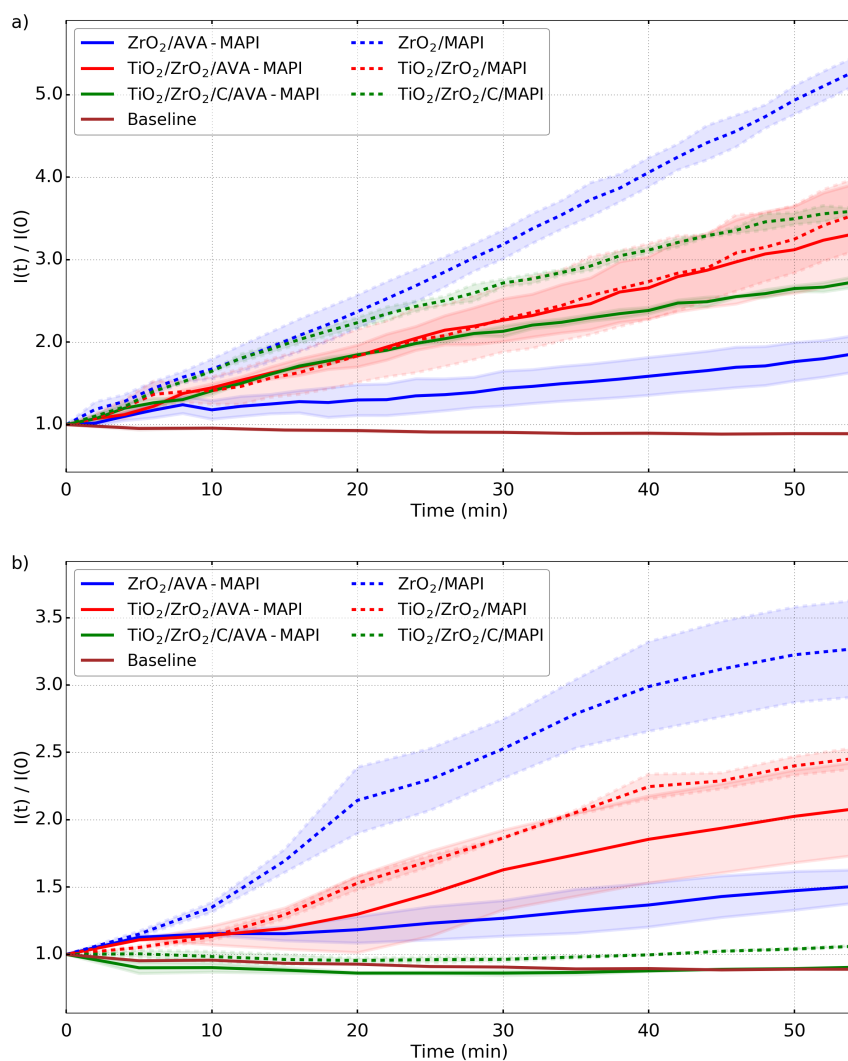


Figure 5.32: Superoxide yields of MAPI and AVA-MAPI infiltrated in different substrates and illuminated through **a)** the glass and **b)** the film over 55 min (each curve is the average of 2 samples). Note: these two batches were measured with slightly different experimental setups and hence are not comparable.

Similar trends are observed independently of the direction of illumination (*i.e.* glass side or film side) other than for TiO₂/ZrO₂/C samples. While superoxide formation is measured in these samples when illuminated through the glass, no or very little superoxide formation is observed when illuminated through the film side as the carbon top layer prevents the creation of excited carriers in the perovskite. TiO₂/ZrO₂/C samples illuminated through the film are thus ignored for the rest of the discussion. It is also noted that the fluorescence intensity increase is not linear when the samples are illuminated through the film and this is likely due to exhaustion of the dihydroethidium probe as suggested by the almost absent emission of dihydroethidium at the end of the experiment (**Figure 5.33**).

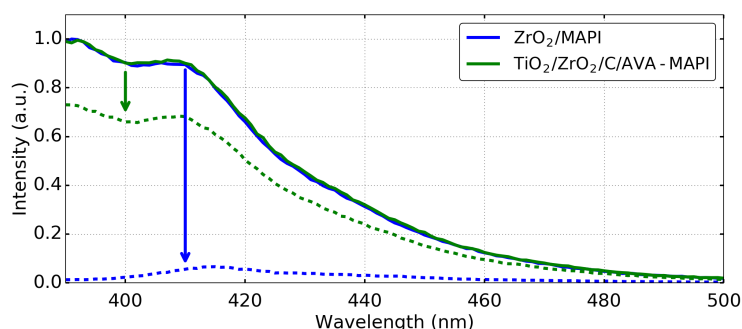


Figure 5.33: Dihydroethidium fluorescence emission spectrum before (full lines) and after illumination (dotted lines) through the perovskite layer with a ZrO_2/MAPI sample.

Independently of the direction of illumination, ZrO_2/MAPI generates more superoxide compared to the other samples studied (**Figure 5.32**). When infiltrated in $\text{TiO}_2/\text{ZrO}_2$, the superoxide yield of MAPI decreases likely due to the possibility of charge injection into the mesoporous TiO_2 . Little difference is observed between the superoxide yield of MAPI infiltrated in $\text{TiO}_2/\text{ZrO}_2/\text{C}$ and $\text{TiO}_2/\text{ZrO}_2$ when illuminated through the glass. AVA-MAPI infiltrated in ZrO_2 generates the lowest amount of superoxide of all the samples studied independently of the illumination direction. $\text{TiO}_2/\text{ZrO}_2/\text{AVA-MAPI}$ presents a higher superoxide yield than $\text{ZrO}_2/\text{AVA-MAPI}$ and similar to $\text{TiO}_2/\text{ZrO}_2/\text{MAPI}$. This is quite surprising as a reduction in the superoxide yield may be expected due to the presence of the mesoporous TiO_2 layer as observed with MAPI. Independent measurements also showed that AVA-MAPI generates less superoxide than MAPI when infiltrated in mesoporous TiO_2 (**Figure 5.34**). Finally, when illuminated through the glass substrate, $\text{TiO}_2/\text{ZrO}_2/\text{C}/\text{AVA-MAPI}$ generates slightly less superoxide than in $\text{TiO}_2/\text{ZrO}_2$ but more than in ZrO_2 only.

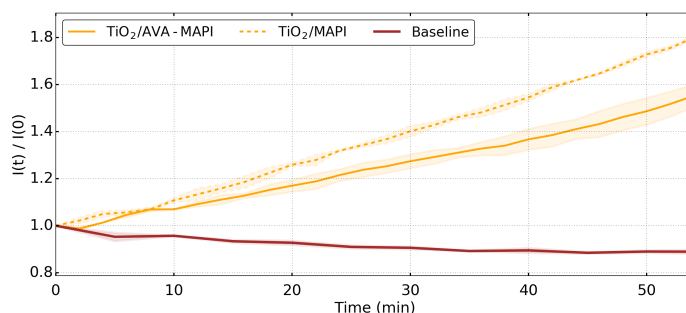


Figure 5.34: Superoxide yields of MAPI and AVA-MAPI infiltrated in TiO_2 and illuminated through the glass over 55 min (each curve is the average of 2 samples).

Little to no differences are observed between the superoxide yield after 55 min with and without shifting of the absorbance (**Figure 5.35**).

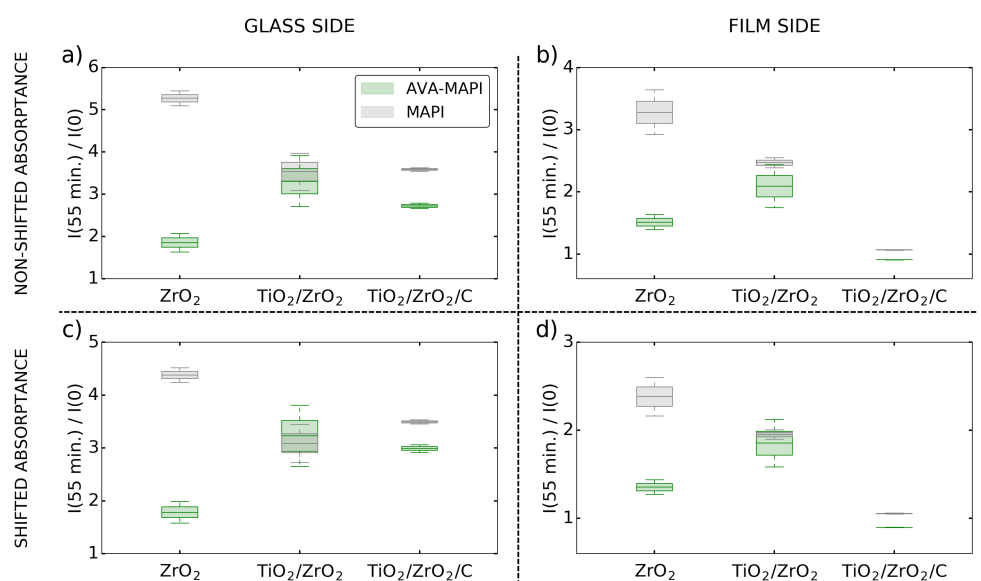


Figure 5.35: Comparison of the superoxide yield of MAPI and AVA-MAPI samples illuminated through a) & b) the glass and c) & d) the film after 55 min, a) & c) with and b) & d) without absorbance shift.

Given the difference in lamp power used during the superoxide yield measurements ($P \sim 1.5 \text{ mW/cm}^2$) and the XRD experiment ($P \sim 19 \text{ mW/cm}^2$), the results obtained in **Figure 5.32** over 55 min are consistent with the ones obtained in **Figure 5.25** during the first few min: AVA-MAPI samples present the lowest superoxide yield / highest stability, $\text{TiO}_2/\text{ZrO}_2/\text{MAPI}$ is slightly more stable than ZrO_2/MAPI while $\text{TiO}_2/\text{ZrO}_2/\text{AVA-MAPI}$ is less stable than $\text{ZrO}_2/\text{AVA-MAPI}$. The only difference with the superoxide experiment is observed for $\text{TiO}_2/\text{ZrO}_2/\text{C}$ substrates which are more stable than the other stacks and which can be explained by the presence of the carbon layer which prevents moisture infiltration and moisture-mediated degradation of the perovskite due to its hydrophobic properties.

The superoxide yields measured in mesoporous substrates can be partially explained by the morphology of the samples (**Figure 5.8**). As previously discussed in **Section 5.3.1A**, the small grains in MAPI samples are bigger and do not form a smooth layer leaving many pinholes. Since AVA-MAPI forms smaller grains with ergo a higher defect concentration, a higher superoxide yield than in MAPI samples would be expected (as observed on glass). However, pinholes observed in MAPI samples are believed to allow increased oxygen diffusion into the samples while the compact capping layer formed in AVA-MAPI samples limits oxygen diffusion. This

may explain the higher superoxide yield observed in ZrO_2/MAPI and $\text{TiO}_2/\text{ZrO}_2/\text{MAPI}$ compared to $\text{ZrO}_2/\text{AVA-MAPI}$. The higher superoxide yield measured in $\text{TiO}_2/\text{ZrO}_2/\text{AVA-MAPI}$ compared to $\text{ZrO}_2/\text{AVA-MAPI}$ could be explained by the increased surface roughness of $\text{TiO}_2/\text{ZrO}_2/\text{AVA-MAPI}$ (especially for the observed dark spot) resulting in increased surface area to react with oxygen thus counterbalancing the reduction in the concentration of excited electrons from charge extraction. The PL peak of $\text{ZrO}_2/\text{AVA-MAPI}$ is slightly narrower (FWHM ~ 44 nm) than $\text{TiO}_2/\text{ZrO}_2/\text{AVA-MAPI}$ (FWHM ~ 50 nm) indicating a lower trap states concentration in the former. 5-AVAI has been previously shown to slow down the movement of perovskite iodide ions in the $\text{TiO}_2/\text{ZrO}_2$ substrate [23]. This may then limit trap state passivation (*e.g.* iodide Frenkel pair passivation) leaving more trap states to react with oxygen to form superoxide. This is consistent with the slower photobrightening observed in $\text{TiO}_2/\text{ZrO}_2/\text{AVA-MAPI}$ samples compared to $\text{ZrO}_2/\text{AVA-MAPI}$ (**Figure 5.36**).

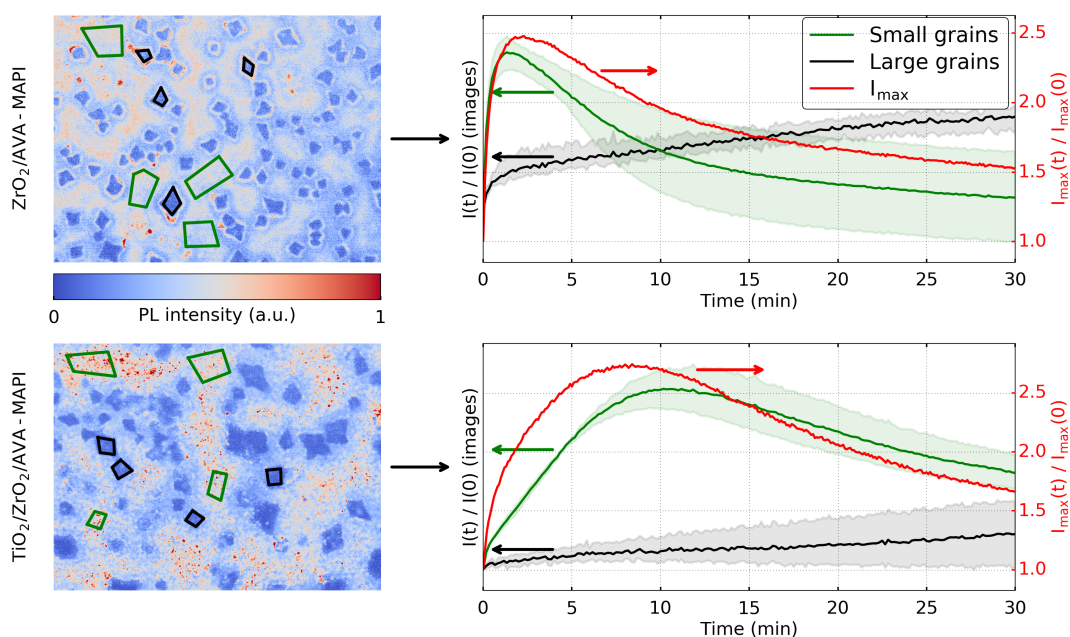


Figure 5.36: PL images of $\text{ZrO}_2/\text{AVA-MAPI}$ and $\text{TiO}_2/\text{ZrO}_2/\text{AVA-MAPI}$ samples and evolution of the intensity of the small grains (green), large grains (black) and the maximum spectral PL intensity over 30 min.

This needs to be put in perspective with passivation of trap states (and thus photobrightening) by superoxide and moisture. The photobrightening observed in **Figure 5.36** is the result of ion migration, superoxide and moisture. Ignoring the contribution of moisture, the slower photobrightening of the $\text{TiO}_2/\text{ZrO}_2/\text{AVA-MAPI}$

sample indicates that the stronger passivation of trap states by superoxide (as more superoxide is generated in this sample) is not enough to balance the slow ion migration. In both samples, large grains emit much less and photobrighten much slower than the small grains. Photodarkening of the small grains is observed in both samples and hints that the greater photobrightening in these grains is not due to higher enhanced trap state passivation by ion migration but rather trap state passivation by superoxide as the superoxide then degrades the perovskite. This is consistent with the higher defect concentration of small grains compared to large ones.

To further assess superoxide formation with respect to illumination direction, further 8 samples, namely MAPI and AVA-MAPI infiltrated in $\text{TiO}_2/\text{ZrO}_2$ were studied (2 samples of each, note fresh samples were used for each illumination direction) (**Figure 5.37**).

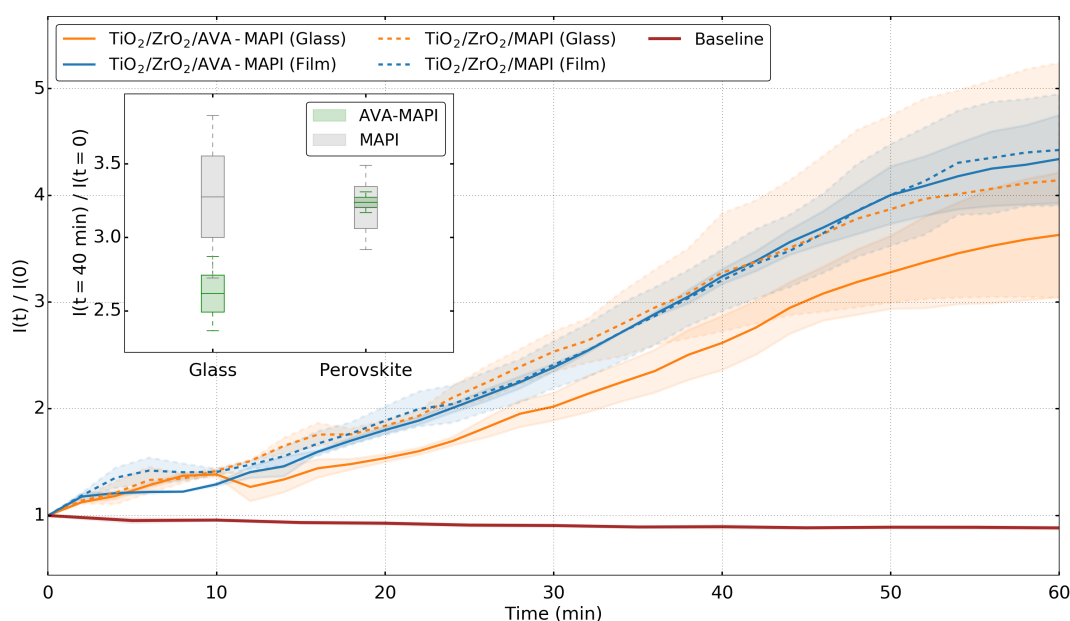


Figure 5.37: Superoxide yield of MAPI and AVA-MAPI infiltrated in the $\text{TiO}_2/\text{ZrO}_2$ substrate and illuminated through the glass or film side. Inset: superoxide yield after 40 min (2 repeats per condition).

Most excited charge carriers are localized within a few hundred nm in the film with respect to the illumination direction [24]. The superoxide yield does not change for MAPI depending on the illumination direction as oxygen can easily diffuse in the film and reacts where the excited charges were created (**Figure 5.37**). Conversely, less superoxide is formed when illuminating through the glass layer of AVA-MAPI than when illuminating from the film since the seemingly dense perovskite capping layer

limits the rate of oxygen diffusion into the film. This provides strong evidence for the increased oxygen diffusion in the MAPI samples and highlights the importance of the morphology in prevention of oxygen diffusion and hence superoxide formation.

An increase of the PL intensity of MAPI samples before and after the superoxide experiment is noted whilst the AVA-MAPI samples present a decrease of their PL intensity (**Figure 5.38a**). This consistent with previous observations that showed that superoxide more likely reacts with the MA cation rather than be extracted from the crystal and react with dihydroethidium [11]. However, little to no change of the absorption spectra as well as the sample morphology are observed (**Figure 5.38b - d**).

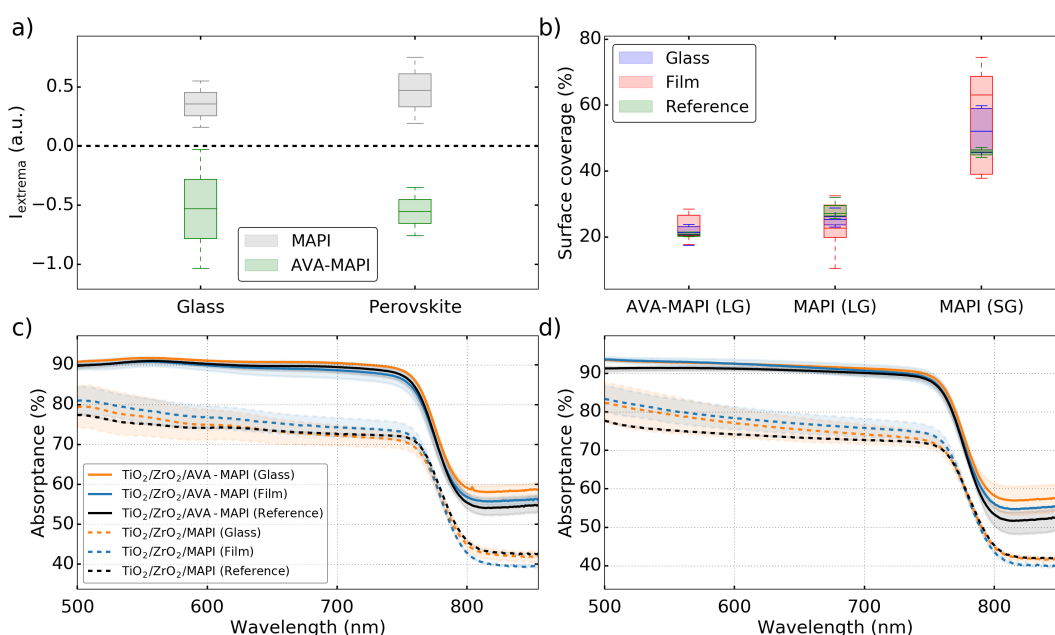


Figure 5.38: **a)** Extremum intensity of the difference of the PL of MAPI and AVA-MAPI infiltrated in $\text{TiO}_2/\text{ZrO}_2$ before and after the superoxide experiment with illumination through the glass and film side, **b)** surface coverage of the large grains (LG) and small grains (SG) of samples subjected to the superoxide experiment and reference samples (3 images per sample, 2 samples per sample type – 1 for MAPI (Reference)). Absorbance of the samples measured through the **c)** glass and **d)** film.

The superoxide yield experiment thus does not seem to affect the sample morphology apart from a few missing large grains due to the sample handling (**Figure 5.8**). The processes and factors affecting superoxide formation in MAPI and AVA-MAPI infiltrated in ZrO_2 and $\text{TiO}_2/\text{ZrO}_2$ are summarized in **Figure 5.39**.

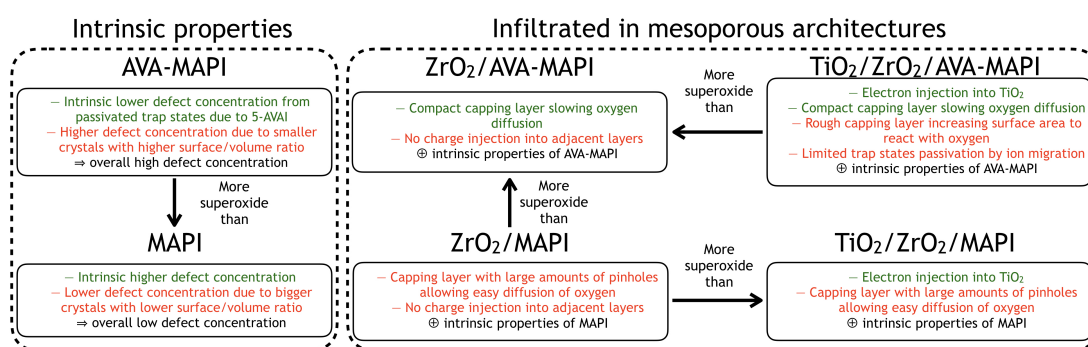


Figure 5.39: Summary of the processes happening in MAPI and AVA-MAPI on glass and infiltrated in ZrO_2 , TiO_2/ZrO_2 mesoporous substrates (green: inhibiting effect, red: catalytic effect).

5.4 Conclusion

The role of 5-AVAI in improving the ambient stability of the MAPI perovskite in mCPSCs and different combination of mesoporous layers has been studied.

On glass, AVA-MAPI presents a higher surface coverage as well as smaller grains than MAPI. When infiltrated in mesoporous layers, MAPI shows very inhomogeneous perovskite distribution likely from bad solution infiltration compared to AVA-MAPI. The mesoporous samples present a perovskite capping layer with thick large grains incorporated in a layer of smaller grains. In the case of MAPI, the smaller grains present numerous pinholes while AVA-MAPI forms a smooth continuous layer. The growth of these grains in the TiO_2/ZrO_2 substrates happens over a period of about a minute and their morphology can be controlled by changing the annealing temperature. Increasing the temperature leads to a lower surface coverage of large grains and a higher surface coverage of small grains in both perovskites.

The PL spectra of MAPI and AVA-MAPI are complex and present 3 different peaks closely packed between 700 nm and 825 nm. Their positions, intensity and FWHM were found to depend upon the perovskite solution, the substrate and the excitation fluence. An overall blue-shift was observed when infiltrating the perovskite into the mesoporous substrates compared to glass or FTO glass, consistent with a blue-shift of the perovskite band-gap calculated from transmittance and reflectance measurements, and was suggested to originate from the presence of smaller grains in the mesoporous substrates. The relative peak intensities were found to depend upon the excitation fluence.

Changes in the perovskite and lead iodide XRD peak intensities under illumination showed higher degradation rates for MAPI samples than AVA-MAPI samples. In all the architectures studied, MAPI displays significant degradation after 12 h, with $\text{TiO}_2/\text{ZrO}_2/\text{C}/\text{MAPI}$ being more stable than ZrO_2/MAPI and $\text{TiO}_2/\text{ZrO}_2/\text{MAPI}$ likely due to the hydrophobic property of the carbon layer, hindering moisture degradation. AVA-MAPI shows lower degradation after 12 h for all architectures compared to the most stable MAPI sample $\text{TiO}_2/\text{ZrO}_2/\text{C}/\text{MAPI}$, highlighting the great stability improvement brought by 5-AVAI. $\text{TiO}_2/\text{ZrO}_2/\text{C}/\text{AVA-MAPI}$ presents very little degradation after 12 h compared to the other samples consistent with the reported higher stability of mCPSCs with AVA-MAPI.

Using dihydroethidium as a probe, superoxide formation in MAPI and AVA-MAPI has been measured. AVA-MAPI deposited on glass presented a higher superoxide yield than MAPI. However, when drop-cast on ZrO_2 , $\text{TiO}_2/\text{ZrO}_2$ and $\text{TiO}_2/\text{ZrO}_2/\text{C}$ mesoporous substrates, AVA-MAPI presented significantly lower formation of superoxide than MAPI. Superoxide formation in these samples has been shown to be the result of a combination of multiple factors including oxygen diffusion, grain morphology and defect concentration. AVA-MAPI samples have smaller grains with higher surface/volume ratio and therefore more surface defects which is counterbalanced by an overall lower defect concentration through the binding of 5-AVAI to iodide vacancies, and poor oxygen diffusion into the film due to the compact perovskite layer, resulting in an overall lower superoxide yield. MAPI samples have larger grains with lower surface/volume ratio and thus less surface defects which is balanced by higher defect concentration compared to AVA-MAPI and the increased oxygen diffusion in the film caused by the very porous perovskite capping layer, leading to a higher superoxide formation yield. The lower superoxide yield measured when MAPI is infiltrated in the $\text{TiO}_2/\text{ZrO}_2$ substrate compared to the ZrO_2 substrate was explained by the improved charge injection into the former substrate. Conversely, a higher superoxide yield in $\text{TiO}_2/\text{ZrO}_2/\text{AVA-MAPI}$ compared to ZrO_2/MAPI was observed and is believed to be due to the higher perovskite porosity as well as more limited trap states passivation in the former substrate. All these factors are heavily influenced by the sample morphology and thus better understanding and control of morphology is required to help to lower superoxide formation and thus increase the device stability.

5.5 Bibliography

- [1] Z. Ku *et al.*, “Full printable processed mesoscopic $\text{CH}_3\text{NH}_3\text{PbI}_3/\text{TiO}_2$ heterojunction solar cells with carbon counter electrode.”, *Scientific reports*, vol. 3, no. 1, p. 3132, Dec. 2013. DOI: 10.1038/srep03132.
- [2] Y. Cai *et al.*, “Promise of commercialization: Carbon materials for low-cost perovskite solar cells”, *Chinese Physics B*, vol. 27, no. 1, 2018. DOI: 10.1088/1674-1056/27/1/018805.
- [3] J. Baker *et al.*, “High throughput fabrication of mesoporous carbon perovskite solar cells”, *Journal of Materials Chemistry A*, vol. 5, no. 35, pp. 18 643–18 650, Sep. 2017. DOI: 10.1039/C7TA05674E.
- [4] S. Ito *et al.*, “Light stability tests of $\text{CH}_3\text{NH}_3\text{PbI}_3$ perovskite solar cells using porous carbon counter electrodes”, *Physical Chemistry Chemical Physics*, vol. 18, no. 39, pp. 27 102–27 108, Oct. 2016. DOI: 10.1039/C6CP03388A.
- [5] A. Mei *et al.*, “A hole-conductor-free, fully printable mesoscopic perovskite solar cell with high stability”, *Science*, vol. 345, no. 6194, pp. 295–298, Jul. 2014. DOI: 10.1126/science.1254763.
- [6] X. Li *et al.*, “Outdoor performance and stability under elevated temperatures and long-term light soaking of triple-layer mesoporous perovskite photovoltaics”, *Energy Technology*, vol. 3, no. 6, pp. 551–555, Jun. 2015. DOI: 10.1002/ente.201500045.
- [7] G. Grancini *et al.*, “One-year stable perovskite solar cells by 2D/3D interface engineering”, *Nature Communications*, vol. 8, p. 15 684, Jun. 2017. DOI: 10.1038/ncomms15684.
- [8] J. Zielonka *et al.*, “Detection of 2-hydroxyethidium in cellular systems: A unique marker product of superoxide and hydroethidine”, *Nature Protocols*, vol. 3, no. 1, pp. 8–21, Jan. 2008. DOI: 10.1038/nprot.2007.473.
- [9] C. T. Rueden *et al.*, “ImageJ2: ImageJ for the next generation of scientific image data”, *BMC Bioinformatics*, vol. 18, no. 1, p. 529, Dec. 2017. DOI: 10.1186/s12859-017-1934-z.
- [10] D. Bryant *et al.*, “Light and oxygen induced degradation limits the operational stability of methylammonium lead triiodide perovskite solar cells”, *Energy & Environmental Science*, vol. 9, no. 5, pp. 1655–1660, 2016. DOI: 10.1039/C6EE00409A.
- [11] N. Aristidou *et al.*, “Insights into the increased degradation rate of $\text{CH}_3\text{NH}_3\text{PbI}_3$ solar cells in combined water and O_2 environments”, *Journal of Materials Chemistry A*, vol. 5, no. 48, pp. 25 469–25 475, Dec. 2017. DOI: 10.1039/c7ta06841g.

- [12] N. Aristidou *et al.*, “Fast oxygen diffusion and iodide defects mediate oxygen-induced degradation of perovskite solar cells”, *Nature Communications*, vol. 8, p. 15 218, May 2017. DOI: 10.1038/ncomms15218.
- [13] N. Aristidou *et al.*, “The role of oxygen in the degradation of methylammonium lead trihalide perovskite photoactive layers”, *Angewandte Chemie - International Edition*, vol. 54, no. 28, pp. 8208–8212, Jul. 2015. DOI: 10.1002/anie.201503153.
- [14] S. Pont *et al.*, “Tuning $\text{CH}_3\text{NH}_3\text{Pb}(\text{I}_{1-x}\text{Br}_x)_3$ perovskite oxygen stability in thin films and solar cells”, *Journal of Materials Chemistry A*, vol. 5, no. 20, pp. 9553–9560, 2017. DOI: 10.1039/C7TA00058H.
- [15] G. Grancini *et al.*, “The impact of the crystallization processes on the structural and optical properties of hybrid perovskite films for photovoltaics”, *The Journal of Physical Chemistry Letters*, vol. 5, no. 21, pp. 3836–3842, Nov. 2014. DOI: 10.1021/jz501877h.
- [16] M. R. Filip *et al.*, “Steric engineering of metal-halide perovskites with tunable optical band gaps.”, eng, *Nat Commun*, vol. 5, p. 5757, Dec. 2014. DOI: 10.1038/ncomms6757.
- [17] V. D’Innocenzo *et al.*, “Tuning the light emission properties by band gap engineering in hybrid lead halide perovskite”, *Journal of the American Chemical Society*, vol. 136, no. 51, pp. 17 730–17 733, Dec. 2014. DOI: 10.1021/ja511198f.
- [18] C.-T. Lin *et al.*, “Evidence for surface defect passivation as the origin of the remarkable photostability of unencapsulated perovskite solar cells employing aminovaleric acid as a processing additive”, *Journal of Materials Chemistry A*, vol. 7, no. 7, pp. 3006–3011, Feb. 2019. DOI: 10.1039/C8TA11985F.
- [19] A. Alnuaimi *et al.*, “Performance of planar heterojunction perovskite solar cells under light concentration”, *AIP Advances*, vol. 6, no. 11, p. 115 012, Nov. 2016. DOI: 10.1063/1.4967429.
- [20] J. Mooney *et al.*, “Get the basics right: Jacobian conversion of wavelength and energy scales for quantitative analysis of emission spectra”, *The Journal of Physical Chemistry Letters*, vol. 4, no. 19, pp. 3316–3318, Oct. 2013. DOI: 10.1021/jz401508t.
- [21] E. V. Péan *et al.*, “Investigating the superoxide formation and stability in mesoporous carbon perovskite solar cells with an aminovaleric acid additive”, *Advanced Functional Materials*, p. 1909 839, Feb. 2020. DOI: 10.1002/adfm.201909839.

- [22] J. Zielonka *et al.*, “Mechanistic similarities between oxidation of hydroethidine by Fremy’s salt and superoxide: Stopped-flow optical and EPR studies”, *Free Radical Biology and Medicine*, vol. 39, no. 7, pp. 853–863, Oct. 2005. DOI: 10.1016/j.freeradbiomed.2005.05.001.
- [23] A. Pockett *et al.*, “Origin of exceptionally slow light soaking effect in mesoporous carbon perovskite solar cells with aVA additive”, *Journal of Physical Chemistry C*, vol. 123, no. 18, pp. 11 414–11 421, May 2019. DOI: 10.1021/acs.jpcc.9b01058.
- [24] R. Kerremans *et al.*, “On the electro-optics of carbon stack perovskite solar cells”, *Solar RRL*, p. 1 900 221, Jul. 2019. DOI: 10.1002/solr.201900221.

Chapter 6

Conclusions

In this work, the photochemistry of the methylammonium lead iodide (MAPI) perovskite for solar cell applications has been investigated using a wide range of techniques including; fluorescence microscopy, secondary electron microscopy, X-ray diffractometry (XRD), superoxide yield measurements using the dihydroethidium fluorescence probe, steady state photoluminescence (PL) and time-resolved photoluminescence (TRPL). Great care was taken in ensuring reproducibility of the results through careful control of the fabrication and experimental conditions, as well as measuring multiple identical samples. **Chapter 3** discusses photobrightening, photodarkening and degradation of MAPI thin-film through the monitoring of their PL and XRD pattern. **Chapter 4** examines two models to simulate charge carrier recombination and TRPL of perovskite materials. Finally, in **Chapter 5**, superoxide formation in MAPI and 5-aminovaleric acid iodide-modified MAPI (AVA-MAPI) in mesoporous carbon perovskite solar cells (mCPSCs) is investigated.

6.1 Optical properties of methylammonium lead iodide thin-films

The PL and crystallographic properties of MAPI thin-films deposited on glass were studied in ambient and N₂ atmospheres. Observed photobrightening and photodarkening happen sequentially in ambient atmosphere under illumination. The photobrightening observed in N₂ atmosphere is slower and little to no photodarkening is observed over the time scale of the experiments. Photobrightening is associated with the passivation of defect-induced trap states through light-mediated iodide

Frenkel pair annihilation, aided by oxygen, moisture and lead iodide (PbI_2), consistent with the decrease of the linewidth of the PL emission peak. Photodarkening is likely caused here by the degradation of the perovskite by oxygen and moisture, although other phenomenon such as iodide Frenkel pair formation and iodide migration should not be overlooked and could explain the very small photodarkening observed in N_2 . By monitoring the diffraction pattern and PL of a MAPI thin-film under illumination in ambient atmosphere, it is evident that degradation occurs at the same time as photobrightening when illuminated, and that at the point of maximum photobrightening there had been a significant degradation of the perovskite into PbI_2 .

Photobrightening and photodarkening are thus competing processes in a MAPI thin-film with common origins: oxygen passivates iodide vacancies through its conversion to superoxide. Superoxide then can react with the methylammonium cation to form an hydroperoxyl radical, PbI_2 and iodine (I_2). The hydroperoxyl radical can form hydrogen peroxide and passivate uncoordinated lead defects. On the other hand, I_2 can migrate toward the surface of the film acting as a quencher, and leading to the formation of defects in the bulk due to the imbalance of iodide in the film. If the excitation wavelength allows it (*ca.* $\lambda < 500$ nm), PbI_2 and I_2 can be photolysed leading to the formation of more defects. Moisture passivates the surface of grains which are rich in reactive defects through its degradation.

In a perovskite solar cell (PSC), the passivation of such trap states would improve the efficiency by limiting non-radiative recombination of electron and holes. It would thus be beneficial to maximise passivation and photobrightening whilst preventing the degradation pathways, or indeed produce pristine films with high PL and minimal trap states. Great care should be taken when measuring PL of perovskite samples as photobrightening and photodarkening may happen differently between samples depending, amongst other things, on their defect concentration and grain morphology. Measuring the PL of perovskites over time should thus be preferred to single measurements as these are more sensitive to previous conditions (*e.g.* illumination, storage atmosphere). Measurement in inert atmosphere (*e.g.* N_2) inhibits both photobrightening and stops oxygen and moisture degradation producing more reliable results, however, depending on final solar cell architecture/design, such measurements may not be as relevant to device conditions.

6.2 Modelling charge carrier recombination and time-resolved photoluminescence of methylammonium lead iodide perovskite

Charge carrier recombination in perovskites is complex and as a result several models for charge dynamics have been used in the literature to extract meaningful data from TRPL decays. In this work, two charge carrier recombination models were investigated, both considering radiative and non-radiative bimolecular recombination of the charge carriers but differing in their treatment of trap-mediated recombination. The bimolecular-trapping-detrapping (BTD) model considers trapping as a bimolecular process between the free carriers and the available trap states and detrapping as a bimolecular process between the trapped carriers and the associated free carriers. The bimolecular-trapping (BT) model assumes that the detrapping rate and/or the trap state concentration is high enough such that the trap state remain mostly empty at all time, allowing to merge trapping and detrapping of the BTD model into a simple monomolecular process and to consider the electron and hole concentrations equal at all time.

The BT and BTD models behave similarly at low and high fluence with dominant monomolecular trapping at low fluence and bimolecular recombination at high fluence. However, they differ at medium fluence with the BT model predicting dominant bimolecular recombination in the initial phase of the TRPL decay and dominant trapping in its tail, while the BTD model predicts a fast initial trapping phase leading to a fast decrease of the TRPL, followed by a slower decrease due to a mix of bimolecular recombination, trapping and detrapping. The accuracy of the model parameter values retrieved from fitting were shown to depend on the fluence regime with only parameters associated with a non-negligible recombination process can be extracted (*e.g.* the bimolecular rate constant at high fluence). Within the BT model, the accuracy of the values retrieved can be ensured by calculating the contribution of the recombination processes to the change in the TRPL intensity. For the BTD model, it was shown that the trap state concentration can easily be estimated from the fast initial decrease of the TRPL intensity without fitting. It was also suggested that the doping concentration can be estimated from the initial TRPL intensity measured at different fluences.

Fitting TRPL decays by simulating a single excitation pulse was shown to require that all photoexcited carriers have recombined within the excitation source repetition period. Remaining carriers in the system affect the recombination after the next excitation pulse, leading to charge accumulation (CA). As per the BT model, CA can easily be avoided by allowing the TRPL intensity to reach at least 0.01 % of its initial intensity indicating that less than 1 % of the carriers are left in the bands. Because the BT model predicts that trapped electrons can recombine after the TRPL intensity has reached zero, CA is much harder to avoid. As per this model, increasing the excitation repetition period in the medium fluence regime lead to an increase of the initial TRPL decrease due to trapping as more trapped electrons are allowed to recombine. Measuring identical decays with 2 excitation repetition periods suggests that all carriers have recombined. The use of multiple pulses fitting of TRPL decays of systems subjected to CA was also investigated and was found less suitable than single pulse fitting of systems not subjected to CA.

The two models were used to fit TRPL decays of a MAPI thin film deposited on glass measured with fluences between $7.5 \times 10^{15} \text{ cm}^{-3}$ and $3.0 \times 10^{16} \text{ cm}^{-3}$. Fitting with the BT model yielded a bimolecular recombination rate constant of $k_B = 51.1\text{--}51.2 \times 10^{-20} \text{ cm}^3/\text{ns}$ and a trapping rate constant of $k_T = 1.30\text{--}1.55 \times 10^{-3} \text{ ns}^{-1}$. The accuracy of these values was ensured through the calculation of the bimolecular and trapping contributions to the change in the TRPL intensity, and are consistent with values previously reported in the literature. Fitting with the BT model with different sets of guess values yielded multiple solutions, all with the same bimolecular recombination rate constant $k_B = 48.6 \times 10^{-20} \text{ cm}^{-3}$, suggesting that this parameter was accurately retrieved and that the sample was in the high fluence regime. The sample should thus have been measured at lower fluence in order to observe trapping and detrapping.

These models are the corner stone of better understanding perovskite materials. This work highlights their limitations and requirements and can be used to measure more complex perovskites such as triple cation perovskites. Considering more complex processes such as Auger recombinations, detrapping back to the conduction band and charge carrier diffusion should be aimed to improve the accuracy of these models. However, it is important to acknowledge that TRPL by itself may not be suitable to determine all the parameter value of these more complex models (as shown for the BT model where multiple set of parameter values can yield very similar

TRPL decay shapes over a wide range of excitation fluences). Coupling TRPL with other techniques such as open-circuit voltage measurement and time-resolved microwave conductivity may allow to solve this flaw.

6.3 Superoxide formation and stability in mesoporous carbon perovskite solar cells with an aminovaleric acid additive

The role of 5-aminovaleric acid iodide (5-AVAI) in improving the stability of MAPI perovskite in mCPSCs was studied. AVA-MAPI and MAPI precursor solutions present different spreading and crystallisation on the different substrates studied. When drop-cast on glass, AVA-MAPI forms smaller grains with a higher surface coverage compared to MAPI. When infiltrated in mesoporous layers, the two perovskites present a bimodal grain distribution with large and small grains. The small grains in AVA-MAPI form a continuous and smooth capping layer in which larger grains are incorporated, while the capping layer in MAPI sample presents numerous pinholes. Transmittance and reflectance measurements showed that AVA-MAPI generally absorbs more light than MAPI, with greater differences observed on glass and in mesoporous substrates. The PL spectra of MAPI and AVA-MAPI are complex and present 3 different peaks closely packed between 700 nm and 825 nm. Their positions, intensity and FWHM were found to depend upon the perovskite solution, the substrate and the excitation fluence. The 10–30 nm blue-shift of the perovskite band-gap calculated from transmittance and reflectance measurements as well as the fluorescence was associated with the emission of smaller grains in the mesoporous layers.

XRD and the dihydroethidium superoxide probe were used to measure MAPI and AVA-MAPI infiltrated in ZrO_2 , $\text{TiO}_2/\text{ZrO}_2$ and $\text{TiO}_2/\text{ZrO}_2/\text{C}$ mesoporous layers. Changes in the perovskite and lead iodide XRD peak intensities under illumination show higher degradation rates for MAPI samples than AVA-MAPI samples. In all the architectures studied, MAPI displays significant degradation after 12 h, with $\text{TiO}_2/\text{ZrO}_2/\text{C}/\text{MAPI}$ being more stable than ZrO_2/MAPI and $\text{TiO}_2/\text{ZrO}_2/\text{MAPI}$ likely due to the hydrophobic property of the carbon layer, hindering moisture degradation. AVA-MAPI shows lower degradation after 12 h for all architectures compared to the

most stable MAPI sample $\text{TiO}_2/\text{ZrO}_2/\text{C}/\text{MAPI}$, highlighting the great stability improvement brought by 5-AVAI. $\text{TiO}_2/\text{ZrO}_2/\text{C}/\text{AVA-MAPI}$ presents very little degradation after 12 h compared to the other samples consistent with the reported higher stability of mCPSCs with AVA-MAPI. AVA-MAPI deposited on glass displays a higher superoxide yield than MAPI. However, when infiltrated in the mesoporous architectures, AVA-MAPI presents significantly lower formation of superoxide than MAPI. Superoxide formation in these samples is believed to be the result of a combination of multiple factors including oxygen diffusion, grain morphology and defect concentration. AVA-MAPI samples have smaller grains with higher surface/volume ratio and therefore more surface defects, counterbalanced by an overall lower defect concentration through the binding of 5-AVAI to iodide vacancies. MAPI samples present larger grains with lower surface/volume ratio and thus less surface defects which is balanced by a higher defect concentration compared to AVA-MAPI due to the absence of 5-AVAI, resulting in a lower superoxide yield than AVA-MAPI when deposited on glass. The compact capping layer formed in AVA-MAPI samples on top of the mesoporous layers hinders oxygen diffusion and limits reaction sites for superoxide formation. Conversely, the porous capping layer in MAPI mesoporous samples results in a higher superoxide yield. The lower superoxide yield measured when MAPI is infiltrated in the $\text{TiO}_2/\text{ZrO}_2$ architecture compared to the ZrO_2 architecture is explained by the improved charge extraction in the presence of the TiO_2 layer. A surprising higher superoxide yield is measured in $\text{TiO}_2/\text{ZrO}_2/\text{AVA-MAPI}$ compared to ZrO_2/MAPI and is believed to be due to the higher porosity of the capping layer of $\text{TiO}_2/\text{ZrO}_2/\text{AVA-MAPI}$ as well as limited trap state passivation by ion migration in this sample. All these factors are heavily influenced by the sample morphology and thus better understanding and control of morphology is required to help lower superoxide formation and thus increase the device stability. Passivation of trap states is thus a crucial step in improving the stability of mCPSCs and PSCs in general. The addition of 5-AVAI to MAPI is a good pathway to do so and could be improved by controlling the perovskite morphology to limit oxygen diffusion and superoxide formation sites.

Perovskites are extremely promising materials for solar cell applications. However, their relative poor stability in ambient atmosphere as well as complex photochemistry hinders their development. Here, MAPI has been used as a relatively

simple model material to study the photochemistry of perovskites. Point defect-induced trap states in the perovskite band-gap are found to be partially responsible for the particular photochemistry of MAPI; photobrightening due to passivation of such trap states by Frenkel pair annihilation, superoxide formation, uncoordinated lead passivation by hydrogen peroxide and moisture degradation can highly affect the PL, and is intrinsically linked to degradation. TRPL is a powerful technique to investigate and extract information related to these trap states as well as recombination processes in perovskites. However, it requires measurements performed with carefully selected excitation fluences while avoiding carrier accumulation due to incomplete carrier depopulation of the free and trapped carriers between consecutive excitation pulses. Superoxide formation in MAPI infiltrated in mCPSCs, and more generally in mesoporous layers, is the result of a combination of multiple factors including oxygen diffusion, grain morphology and defect concentration. The addition of 5-AVAI improves the stability of the perovskite in ambient atmosphere, partially by limiting oxygen diffusion in the device thanks to improved morphology of the perovskite layer. It is hoped these studies can be used as a starting point and have helped improve our understanding of perovskite materials, developed accurate determination of their properties and helped understand the causes and consequences of their instability. Further work should be carried on more complex system such as the triple cation perovskite $\text{Cs}_{0.05}(\text{MA}_{0.17}\text{FA}_{0.83})_{0.95}\text{Pb}(\text{I}_{0.83}\text{Br}_{0.17})_3$ which has been shown to be very promising for higher efficiency and more stable devices.